OPTIMAL STEERING OF A SECOND STAGE BOOST VEHICLE SUBJECT TO LOADING AND ROLL RATE CONSTRAINTS

by

Gilbert Mark Brown
B.S., Massachusetts Institute of Technology
(1985)

SUBMITTED IN PARTIAL FULFILLMENT
OF THE REQUIREMENTS FOR THE
DEGREE OF
MASTER OF SCIENCE
IN AERONAUTICS AND ASTRONAUTICS
at the
MASSACHUSETTS INSTITUTE OF TECHNOLOGY
September 1987

Signature of Author _____
Department of Aeronautics and Astronautics
September 21, 1987

Certified by ___
Gilbert S. Stubbs
Technical Advisor
C.S. Draper Lab.

Certified by ___
H. Philip Whitaker
Thesis Advisor

Accepted by ____
Professor Harold Y. Wachman
Chairman, Departmental Graduate Comittee

OPTIMAL STEERING OF A SECOND STAGE BOOST VEHICLE SUBJECT TO LOADING AND ROLL RATE CONSTRAINTS

by

Gilbert Mark Brown

Submitted to the Department of Aeronautics and Astronautics on September 21, 1987 in partial fulfillment of the requirements for the Degree of Master of Science in Aeronautics and Astronautics

ABSTRACT

This thesis examines new approaches to steering and roll rate limiting control in the second stage of a multistage solid rocket gimballed engine boost vehicle. The second stage trajectory is designed to carry the vehicle through the upper layers of the Earth's atmosphere to a desired intermediate staging altitude, and to minimize the velocity to be gained by the upper stages of the spacecraft. The second stage vehicle follows the desired trajectory using a steering algorithm that commands the orientation of the thrust vector with respect to inertial space. Since the boost vehicle achieves the commanded thrust orientation through autopilot control of its attitude, performance constraints associated with the vehicle structure and/or its flight control hardware may constrain the second stage trajectory. Studies in this thesis consider the effects of a structurally-imposed aerodynamic loading limit and an IMU-imposed roll rate limit on the optimal performance of the second stage trajectory. It is shown that both limits are necessitated by undesirable effects of the forces which act on the vehicle when it develops an angle of attack.

The thesis provides a detailed vehicle description, and also presents a baseline flight control system that uses attitude control in combination with an exponential steering law. The performance of this flight control system is analyzed for nominal and off-nominal flight conditions in the first and second stage flight phases. It is shown that forces applied to the vehicle during the first stage flight phase and at stage separation can cause the vehicle to develop a high roll rate. When the vehicle then develops an angle of attack to follow the second stage exponential steering commands, the specified roll rate limit can be exceeded.

An alternative steering system employing a linear tangent steering law is introduced in the second stage flight control software. A performance comparison is made between this alternative steering system, the baseline steering algorithm, and the theoretically optimal thrust direction history in the second stage. An alternative autopilot is then implemented to indirectly limit the second stage roll rate through feedback control of the vehicle's angle of attack. It is shown that this alternative autopilot can be used in conjunction with the linear tangent steering system to effectively limit the roll rate of the vehicle without severely compromising the second stage trajectory goals.

Thesis Advisor: H. Philip Whitaker
Title: Emeritus Professor of Aeronautics and Astronautics

ACKNOWLEDGEMENT

This report was prepared at The Charles Stark Draper Laboratory, Inc. under Contract F04704-85-C-8081 with the Ballistic Missile Office of the Air Force Systems Command.

TABLE OF CONTENTS

Table of Contents (Cont.)

Table of Contents (Cont.)

Table of Contents (Cont.)

Table of Contents (Cont.)

LIST OF FIGURES

List of Figures (Cont.)

List of Figures (Cont.)

List of Figures (Cont.)

LIST OF TABLES

CHAPTER 1

INTRODUCTION

1.1 Background

In the boost phase of any space mission, the purpose of the boost vehicle is to transport the upper stage, or payload, of the spacecraft out of the Earth's atmosphere to specified position and velocity end conditions. The specified position is usually a desired altitude at which an orbit can be established. In order to successfully establish an orbit, it is necessary for the spacecraft to reach the desired orbital altitude with a large horizontal velocity component. Thus, the boost trajectory must be "shaped", so that the spacecraft acquires velocity in the downrange direction as it gains altitude. The shaping of the boost trajectory may or may not be tightly constrained, depending on the performance boundaries of the boost vehicle. A considerable volume of research has been dedicated to the development of trajectory shaping methodologies. Since the goal of trajectory shaping is to make the commanded trajectory optimal in some sense (e.g., minimum fuel expended, minimum time to orbit, maximum velocity achieved), this area of research is also referred to as trajectory optimization. Readers interested in the general background and theory of trajectory optimization may wish to refer to Lawden [9] or Lietmann [10].

This thesis examines the effects of performance constraints on trajectory optimization techniques in the second stage of a multistage solid rocket gimballed-engine boost vehicle. The objective of the second stage trajectory, which transports the spacecraft through the upper

layers of the Earth's atmosphere, is to boost the vehicle to a desired intermediate staging altitude, while reducing the remaining velocity to be gained by the upper stages. The second stage trajectory must be able to accomplish this objective from a variety of staging conditions inherited from the first stage flight phase.

1.2 The Required Velocity Vector

During the boost flight phase, the boost vehicle must supply the required velocity to the payload. If the boost vehicle achieves the required velocity at the targeted altitude, it is assumed that the payload will then be able to reach orbital insertion conditions via a freefall path. In order that the required velocity vector, $\bar{V}_{REQ}$, contain the large horizontal velocity component necessary for orbital insertion, this vector is typically oriented only a small angle above the local horizontal, as shown in Figure 1-1. A multistage boost vehicle produces $\bar{V}_{REQ}$ as the summation of velocity vector increments from its individual stages. Figure 1-1 shows velocity vector increments from three different boost stages summed in velocity space, where V_X is the horizontal or downrange velocity component, and V_Z is the vertical velocity component. The velocity vector increments, designated $\Delta\bar{V}_i$ (i is the stage index), represent the total velocity added to the vehicle during the burn time of that stage, including velocity losses due to gravity and atmospheric drag. Note that the required velocity vector may be achieved via many combinations of velocity vector increments.

1.3 The Velocity to be Gained Vector

At any time during the boost flight, the velocity to be gained, $\bar{V}_{TBG}$, may be specified as the difference between the required velocity and the current velocity:

$$\bar{V}_{TBG} = \bar{V}_{REQ} - \bar{V} \qquad (1.1)$$

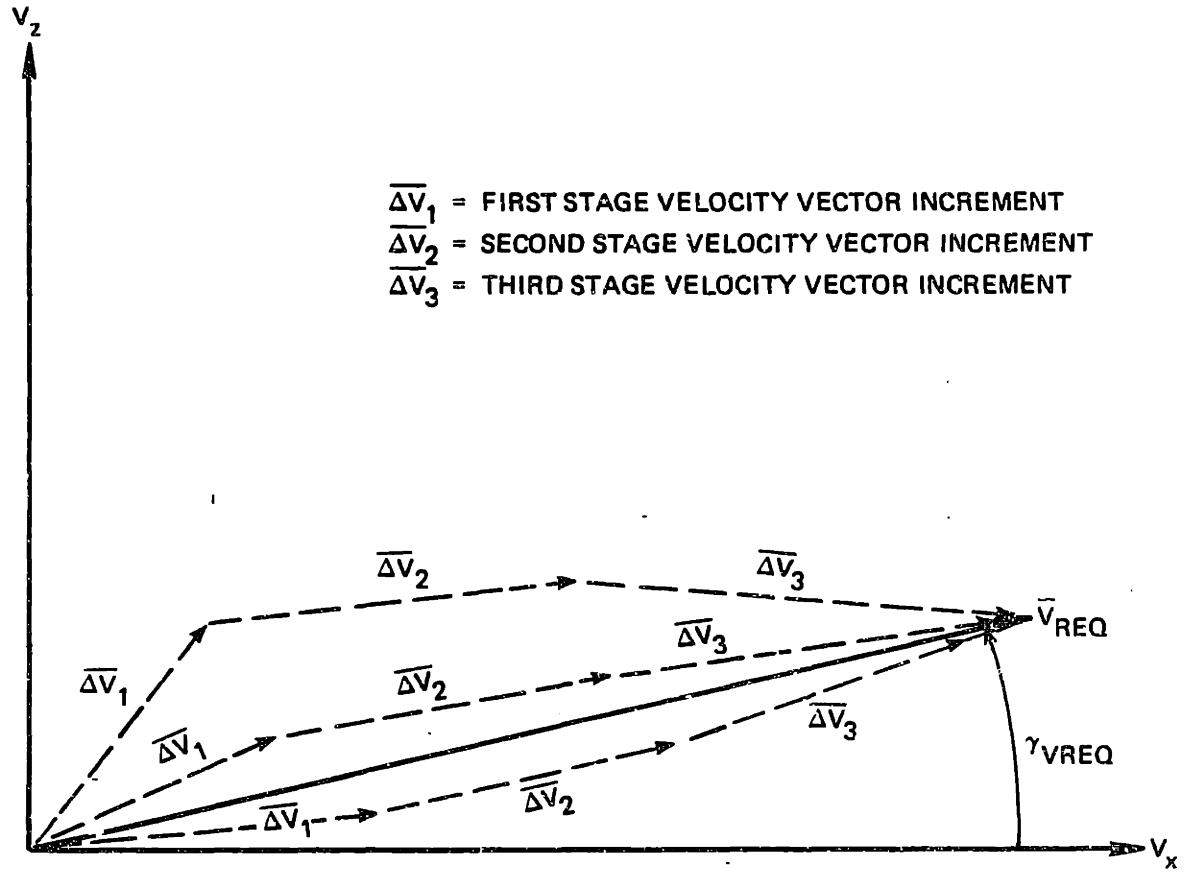

Figure 1-1. Achieving the required velocity vector.

In the above equation, $\bar{V}_{TBG}$ includes the effects of gravity. The velocity to be gained through thrust application alone, $\bar{V}_{GO}$, may be defined as:

$$\bar{V}_{GO} = \bar{V}_{TBG} - \int_{t}^{t + t_{BURN}} \bar{g}\, dt \qquad (1.2)$$

where $\bar{g}$ is the local gravity vector and t_{BURN} is the remaining burn time in the boost flight. If it is assumed that all the thrust in the boost vehicle can be applied impulsively, then t_{BURN} is zero, and $\bar{V}_{GO}$ is equal to $\bar{V}_{TBG}$ as shown in Figure 1-2 (a). If the thrust is applied during a known finite burn time, then the value of t_{BURN} determines the inclination of $\bar{V}_{GO}$ with respect to $\bar{V}_{TBG}$, as shown in Figure 1-2 (b).

1.4 Introduction to the Thesis Problem

The problem addressed in this thesis is the determination of an optimal thrust direction profile in the second stage flight phase of a boost vehicle with three propulsive stages. In order to limit the number of design variables in the thesis, the flight conditions at the initiation of the second stage flight phase will be fixed as a function of the first stage trajectory. In the first stage flight phase, the boost vehicle is transported rapidly to the upper atmosphere, for the following two reasons:

(1) By carrying the boost vehicle quickly out of the dense, lower regions of the atmosphere, velocity losses due to drag are reduced.

(2) In order to prevent large aerodynamic forces from driving the vehicle to an uncontrollable attitude following stage separation, the boost vehicle must reach an altitude where the local dynamic pressure is sufficiently small.

It is necessary to modify the commanded first stage trajectory as a function of the thrust level in order to reach the desired dynamic pressure at staging. In order to propel the boost vehicle quickly through the atmosphere during the first stage flight phase, this stage must apply much of its thrust in the vertical direction, resulting in a velocity vector at I/II staging which is inclined with respect to the required velocity vector, as shown in Figure 1-3. The second stage thrust direction commands must then be programmed to satisfy two categories of concern: steering and control. These concerns are discussed in the following subsections.

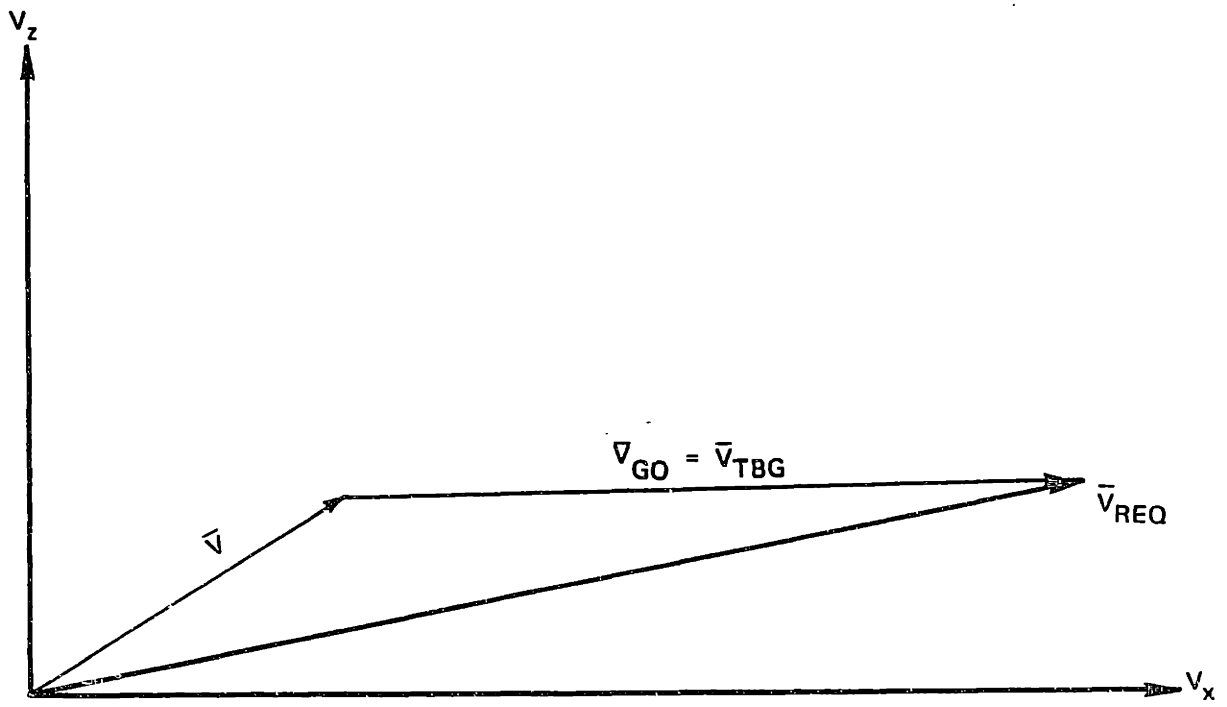

(a) THRUST APPLIED IMPULSIVELY

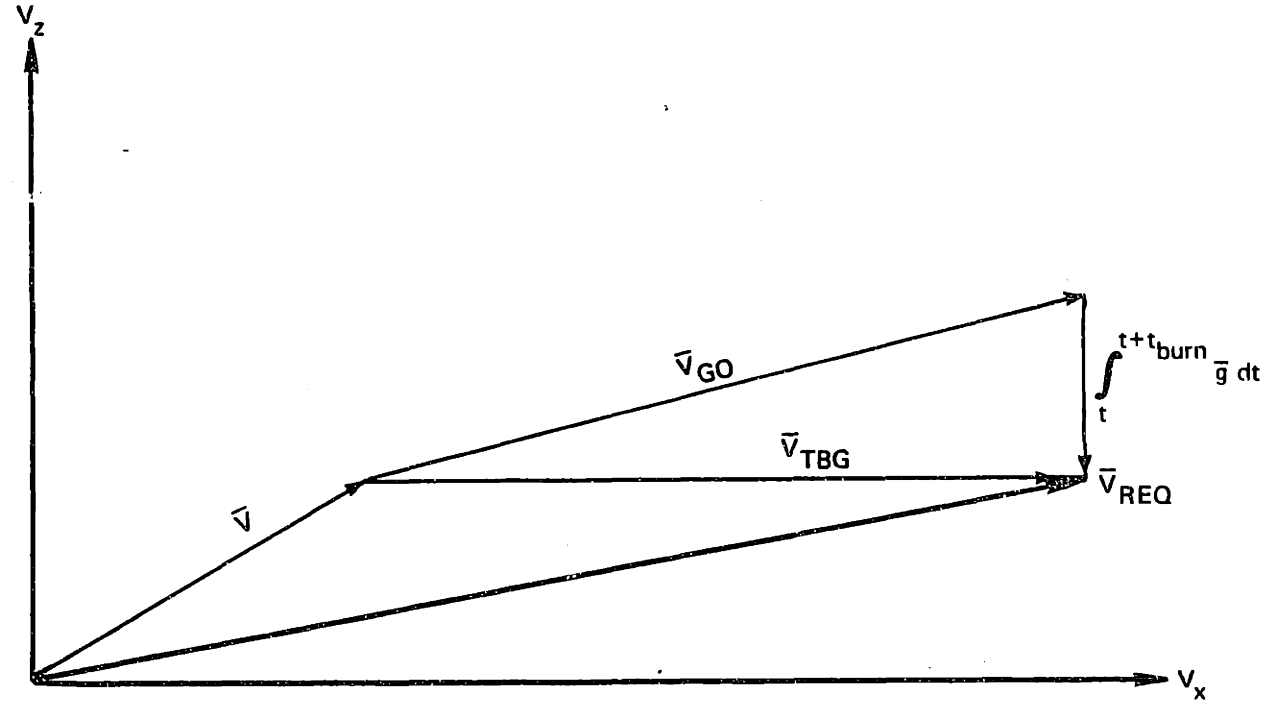

(b) THRUST APPLIED OVER FINITE BURN TIME

Figure 1-2. Definitions of $\bar{V}_{TBG}$ and $\bar{V}_{GO}$.

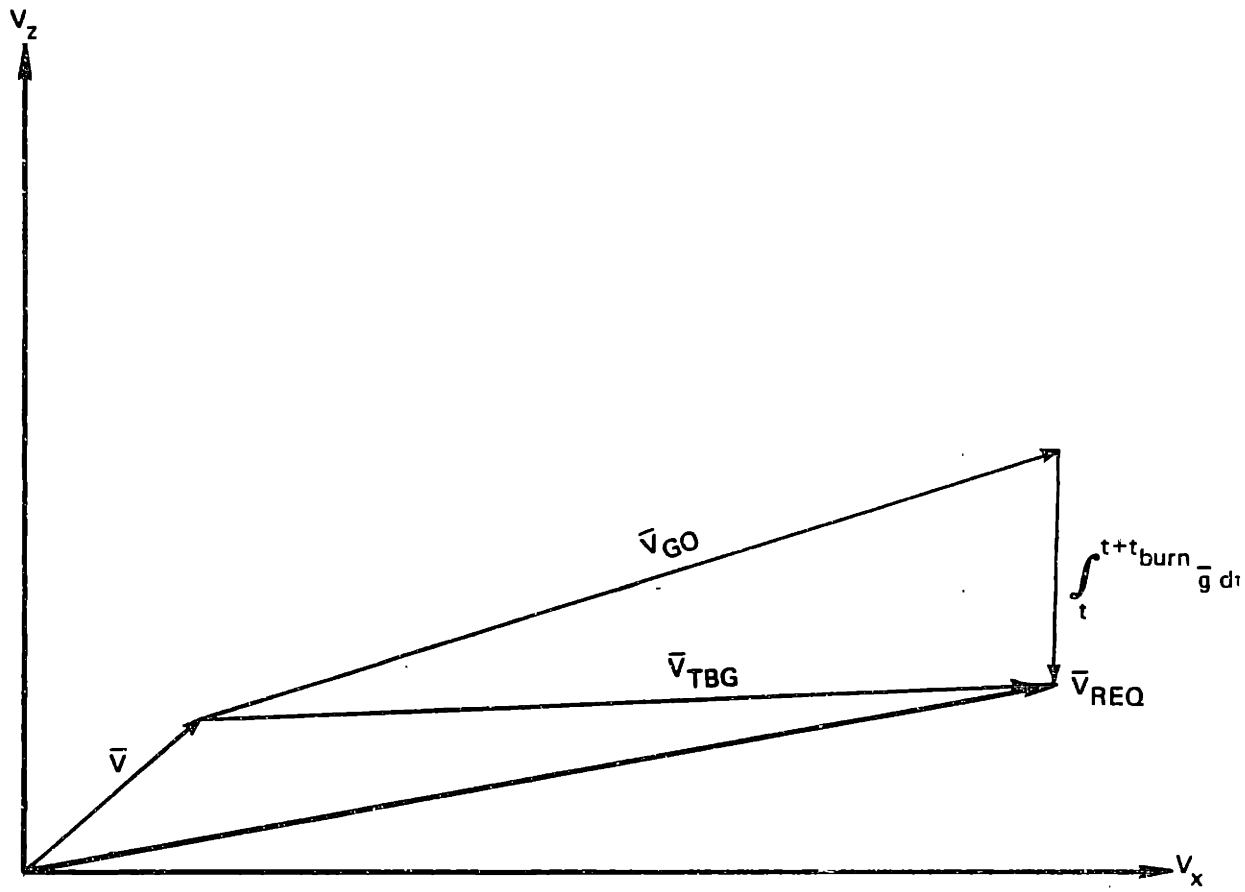

Figure 1-3. Velocity conditions at I/II staging.

1.4.1 Steering Concerns

There are two steering goals in the second stage flight phase:

(1) Achieving the required intermediate altitude at second stage burnout

(2) Minimizing the magnitude of the velocity to be gained through thrust application in the third stage

The staging altitude goal will be considered a "hard" constraint, not to be violated. The best, or optimal, trajectory is the one which carries the vehicle to the staging altitude while minimizing the magnitude of $\bar{V}_{GO}$ for the third stage flight phase.

A constant thrust rocket booster controls its trajectory by varying the thrust direction as a function of time. In the second stage flight phase, the two above-mentioned steering concerns combine to dictate the best thrust direction. It is generally desirable to thrust in the direction of $\bar{V}_{GO}$, because this results in the largest reduction in the magnitude of $\bar{V}_{GO}$. However, in order to achieve the desired staging altitude, it may not be possible to thrust in the direction of $\bar{V}_{GO}$. The second stage thrust direction program should then be formulated to apply as much thrust as possible in the direction of $\bar{V}_{GO}$, while deviating away from $\bar{V}_{GO}$ as necessary to produce a vertical velocity history which carries the vehicle to the desired staging altitude.

In a gimballed engine boost vehicle, the thrust vector must generally be directed through the center of gravity of the vehicle, so that the applied thrust will not produce a large rotational moment on the vehicle. When a change in the thrust direction is commanded, the vehicle must reorient itself to keep the thrust vector directed through the center of gravity. If the commanded thrust direction is not colinear with the vehicle velocity vector, the second stage vehicle must rotate its longitudinal axis away from the velocity vector, developing an angle of attack. The angle of attack, α, is defined as the angle between the air-relative velocity vector and the vehicle's longitudinal axis. Figure 1-4 shows a second stage vehicle which has developed a negative angle of attack in order to thrust in the direction of $\bar{V}_{GO}$.

1.4.2 Control Concerns

The determination of the optimal second stage trajectory is not solely a steering problem. In addition to satisfying the steering goals, the commanded trajectory must not cause the vehicle to violate performance constraints for satisfactory control system performance. In the second stage flight phase, the two most important performance constraints affecting the shape of the trajectory are those imposed on the allowable aerodynamic normal force and vehicle roll rate. The reasons for these constraints are discussed below:

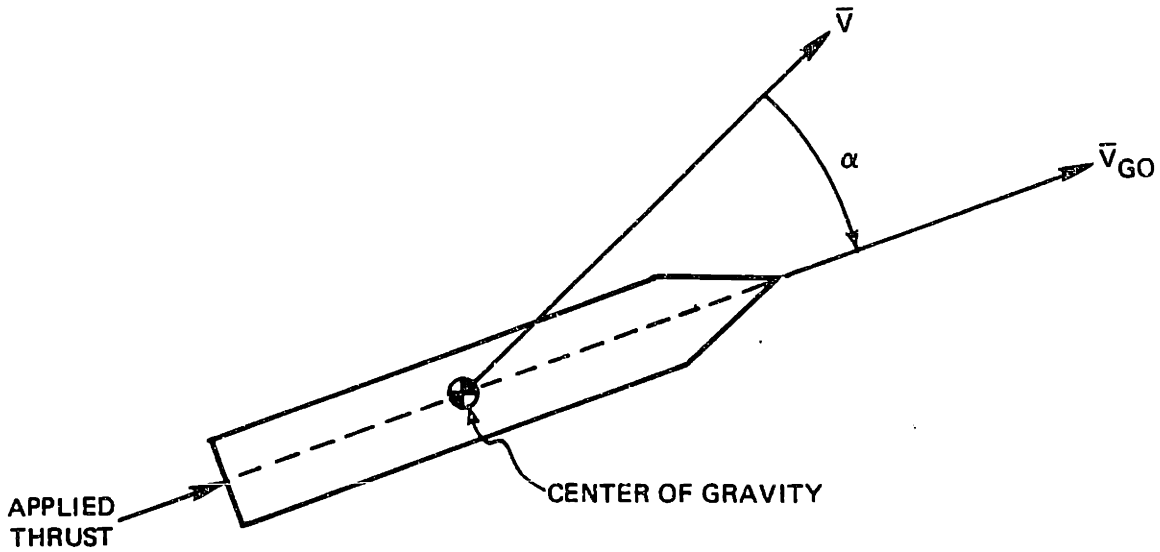

Figure 1-4. Negative angle of attack flight condition.

(1) Aerodynamic normal force constraint

A large aerodynamic normal force can cause severe bending deformation of the vehicle structure. Furthermore, if the torque produced by the aerodynamic normal force exceeds the torque that the engine can produce, then attitude control cannot be maintained.

(2) Vehicle roll rate constraint

The flight control system relies on accurate measurements from its Inertial Measurement Unit (IMU). Large angular rates of the vehicle can introduce dynamic problems in some

types of IMUs, affecting the navigation performance of the instrument. Specification of pitch and yaw rate constraints has very little effect on the trajectory, because the flight control system commands only small sustained rates about the pitch and yaw axes. However, the forces that shape the trajectory of the vehicle during the atmospheric boost phase can have an appreciable accumulated effect on the vehicle's uncontrolled roll rate. As a consequence, it may be necessary to constrain the trajectory plane steering in order to satisfy the IMU-imposed roll rate limit.

These two performance constraints are very different in character, but both are related to undesirable effects of the same flight condition: angle of attack. First of all, a non-zero angle of attack flight condition results in a component of the aerodynamic force which acts perpendicular to the vehicle's longitudinal axis. The larger the angle of attack, the larger is the normal component of the aerodynamic force. Secondly, when the vehicle develops an angle of attack, lateral engine forces are required to balance the aerodynamic moment applied to the vehicle. If an offset exists between the vehicle's center of gravity and its longitudinal axis, the normal aerodynamic force and the lateral engine force can produce a net roll torque. This roll torque causes angular acceleration about the vehicle roll axis.

The aerodynamic normal force is approximately proportional to the product of the dynamic pressure, Q, and the angle of attack, α. Therefore, the aerodynamic loading limit may be specified in terms of a maximum allowable value of $Q\alpha$, $(Q\alpha)_{LIM}$. The corresponding limit on the instantaneous magnitude of α is then:

$$\alpha_{LIM} = \frac{(Q\alpha)_{LIM}}{Q} \tag{1.3}$$

The specification of a roll rate limit does not constrain the instantaneous angle of attack in the manner of the aerodynamic loading

limit. The angle of attack limit associated with the roll rate constraint will depend on both the current roll rate and the predicted time history of Q during the remainder of the boost flight.

The current flight conditions determine which of the two performance limits constrains the angle of attack. For example, if the vehicle has reached the region of maximum dynamic pressure with a low roll rate, a small angle of attack perturbation will not immediately cause the vehicle to exceed its roll rate limit, but the angle of attack may violate the $Q\alpha$ limit. Alternatively, if the vehicle has reached the upper atmosphere with a high roll rate, it may be able to develop a large angle of attack without exceeding the $Q\alpha$ limit, but even a small angle of attack perturbation could cause a large enough roll rate increase to violate the vehicle's roll rate limit.

1.4.3 Resolution of Steering and Control Concerns in the Second Stage Trajectory Design

As illustrated in the two previous subsections, the steering and control concerns in the selection of a desirable second stage trajectory can place conflicting requirements on the orientation of the vehicle. To satisfy the second stage steering concerns for the best end conditions on velocity and altitude, it might be desirable for the vehicle to develop a large angle of attack. The second stage control concerns, however, may dictate that the angle of attack remain small as long as the vehicle is still in the atmosphere.

In resolving these conflicting interests, steering goals must be compromised to satisfy control concerns. Although it may mean flying a less optimal trajectory, the vehicle performance boundaries must not be exceeded. In this thesis, therefore, the second stage trajectory will be formulated to achieve the steering goals as best it can, with the control concerns acting as constraints that may not be violated.

When formulating an optimization problem, it is desirable to first attempt to explore and/or reduce the effects of any constraints upon the optimization. For a vehicle with a given aerodynamic loading limit,

Equation (1.3) provides an explicit constraint on the second stage trajectory; however, the effect of the roll rate limit on the second stage trajectory is not immediately quantifiable. Therefore, although the primary focus of this thesis is the optimization of the second stage trajectory subject to given constraints, this thesis will also explore the roll dynamics of the boost vehicle. If the conditions which contribute to the vehicle roll rate are understood, it may be possible to reduce the effect of the roll rate constraint on the trajectory optimization. The body of the thesis will be divided into two broad categories, which will be examined chronologically as they occur in a boost mission:

(1) In the first and second stage flight phases, roll torque sources will be examined, to determine how to minimize the effect of the roll rate constraint on the second stage trajectory.

(2) In the second stage flight phase, constrained optimal trajectories will be formulated as a function of the vehicle roll rate, the aerodynamic loading limit, the staging altitude requirement, and the required velocity vector.

1.5 Thesis Overview

Chapter 2 introduces the vehicle model, coordinate frame definitions, the flight environment, and the flight control system. This chapter also describes the simulation techniques used to generate the quantitative results of this thesis. Chapter 3 describes the roll dynamics of the boost vehicle, and examines the sources of roll torque in atmospheric flight. Chapter 4 discusses the specific control problems that arise when a boost vehicle stages in the atmosphere. This chapter also demonstrates how the staging conditions can produce a significant increase in roll rate during the second stage flight phase. In Chapter 5, second stage trajectory optimization techniques are presented and applied to problems with a specified aerodynamic loading limit. Chapter 6 then discusses the effect of a roll rate limit on the optimal second stage trajectory, and presents a modified flight control system which can

be used to indirectly limit the second stage roll rate. Chapter 7 presents the conclusions of this thesis, and makes recommendations for further research.

CHAPTER 2

SYSTEM DESCRIPTION, MODELLING, AND SIMULATION

2.1 Vehicle Model

The boost vehicle simulated in this thesis consists of four vertically stacked booster stages, as shown in Figure 2-1. The four stages are connected mechanically through interstage fairings, which also protect the inactive engine nozzles. When the vehicle "stages" (i.e., transfers propulsive authority from a lower stage to an upper stage), explosive bolts are detonated within the involved fairing, effectively separating the upper stages from the expended lower stage. The stages interact electrically with the flight computer through cables housed in a long conduit, or raceway. The raceway lies parallel to the longitudinal axis along the outside of the vehicle.

Each stage is powered by a single high thrust gimballed solid rocket engine. The thrust of each stage is modelled as a constant value, T, for the majority of the burn time, except for constant-slope buildup and tailoff characteristics. A sample thrust profile is shown in Figure 2-2. The value of the constant thrust level is assumed to be a known function of the temperature of the propellant at liftoff. The specific impulse of each stage is modelled as a constant over that stage's burn time. The specific impulse is assumed to be independent of the propellant temperature. Each engine possesses a limited thrust vector control capability, implemented by two single-degree-of-freedom nozzle actuators.

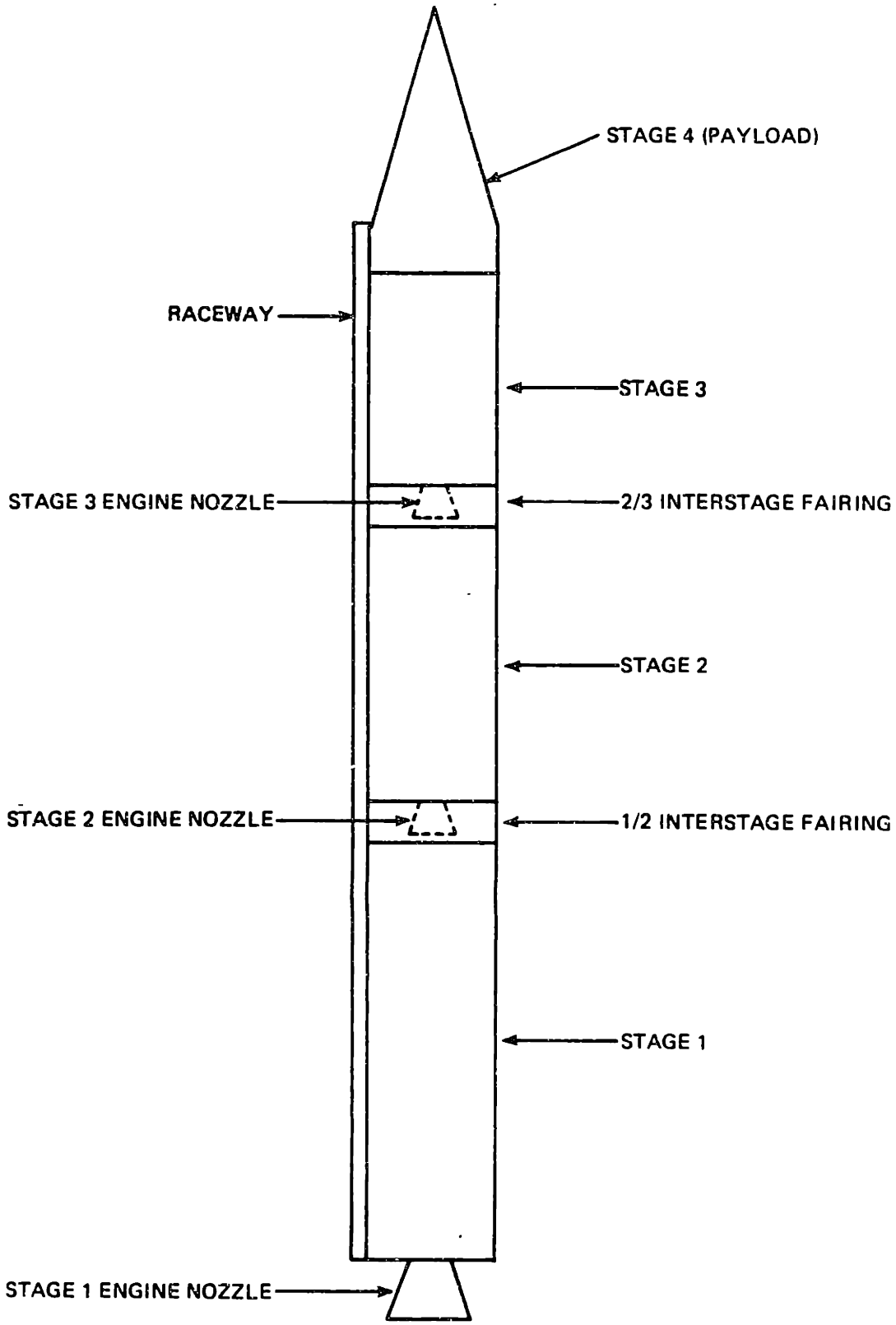

Figure 2-1. Launch configuration of four-stage boost vehicle.

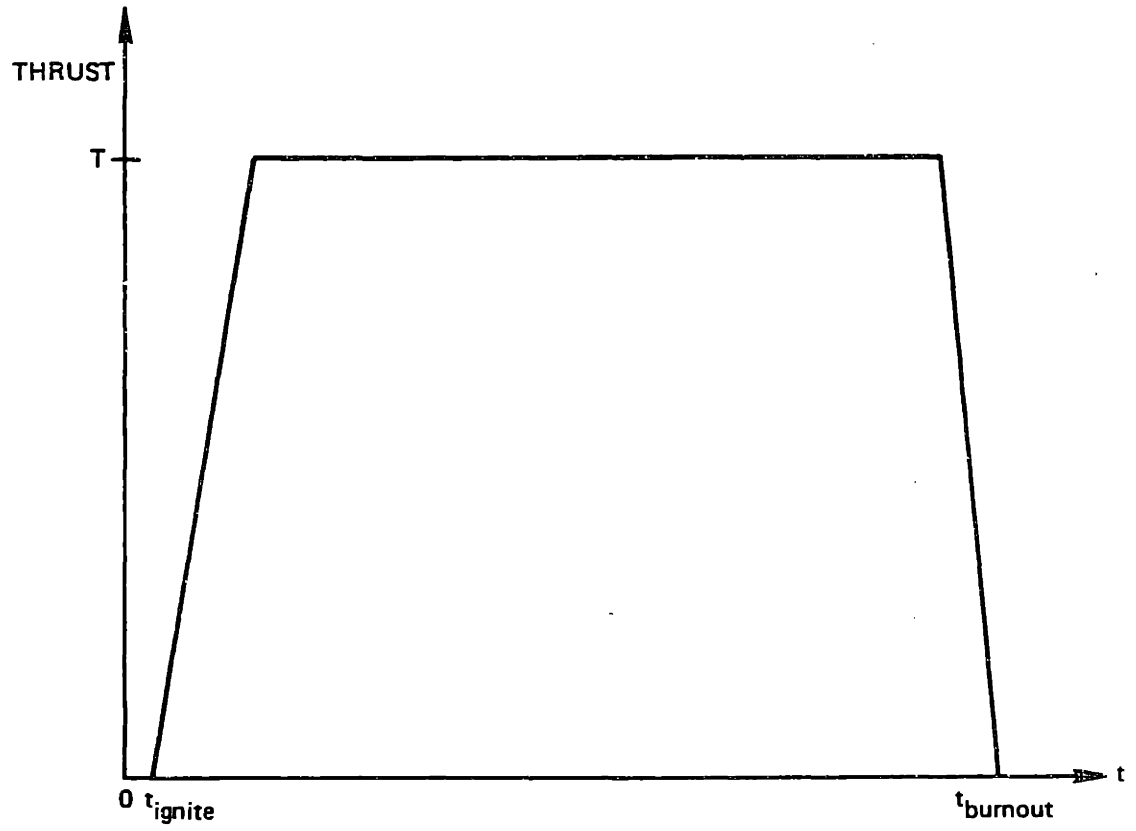

Figure 2-2. Typical single-stage thrust profile.

The boost vehicle is modelled as a symmetric cylindrical rigid body, with the effects of the raceway superimposed. The model without the raceway employs the following assumptions:

(1) The vehicle moments of inertia are known functions of the expended mass.

(2) The vehicle products of inertia are zero.

(3) The transverse moment of inertia is independent of the roll orientation of the vehicle.

(4) The center of gravity position along the longitudinal axis is a known function of the expended mass.

(5) The aerodynamic cross-sectional reference area remains constant through all flight phases.

(6) The aerodynamic center of pressure lies on the vehicle center line.

(7) The motion of the vehicle can be completely described by a translation of the center of gravity and a rotation about the center of gravity.

The complete model of the boost vehicle includes the asymmetric effects of the raceway. The size and mass of the raceway is quite small relative to the total boost vehicle, so that the effect of the raceway on the vehicle mass properties is negligible. However, the raceway does produce significant asymmetry in the aerodynamic properties of the vehicle. The effect of the raceway is to move the aerodynamic center of pressure away from the vehicle centerline. An aerodynamic force applied at this offset center of pressure causes a rolling moment about the vehicle's center of gravity. For this reason, the raceway is modelled as a roll torque source. The magnitude and direction of the roll torque produced will vary with the vehicle's roll orientation, angle of attack, and Mach number. More specifics of the raceway roll torque model will be discussed in Chapter 3.

2.2 Coordinate Frame Definitions

Five distinct coordinate frames will be referenced in this thesis. Four of the coordinate frames are updated and stored in the digital flight computer, and may be used by the flight computer for computational purposes. These frames will also be used to present steering and control concepts, and to present simulation results. The fifth coordinate frame is used purely for theoretical development. The five coordinate frames, presented with their accompanying notational conventions, are as follows:

(1) AIRS IMU Platform Frame $(X_{PLAT}, Y_{PLAT}, Z_{PLAT})$

This frame is defined by the orientation of the inertially stabilized IMU platform. During an initialization procedure

prior to launch, the platform is aligned so that each of its three coordinate axes makes an equal angle with the local gravity vector.

(2) Earth-Fixed Reference Frame (X_E, Y_E, Z_E)

This frame remains fixed with respect to the Earth. This frame is initialized according to the azimuth of the commanded trajectory plane. Defining $+Z_E$ to point toward the center of the Earth, $+X_E$ is defined as the downrange direction, so that X_E-Z_E is the commanded trajectory plane. $+Y_E$ is then chosen to form a right-handed set.

(3) Body-Fixed Coordinate Frame (X_B, Y_B, Z_B)

This frame remains fixed in the body of the vehicle. To permit decoupling of the autopilot commands, this frame is defined with the $+Y_B$ and $+Z_B$ axes each parallel to one of the engine nozzle actuator axes, and the $+X_B$ axis along the vehicle longitudinal axis. Applying airplane terminology to the vehicle, the Y_B axis is referred to as the pitch axis, and the Z_B axis is called the yaw axis.

(4) Unrolled-Body Coordinate Frame (X_U, Y_U, Z_U)

This frame remains fixed with respect to the unrolled body. The $+X_U$ axis is always aligned with the $+X_B$ axis, but the Y_U and Z_U axes remain fixed relative to an initial roll orientation of the vehicle. The transformation between the unrolled frame and the body-fixed frame can then be expressed, in effect, by a rotation about the roll axis through the roll angle, ϕ. The reference roll orientation is chosen such that the Y_U axis is initially aligned with the Y_E axis.

(5) Velocity Direction Coordinate Frame (X_V, Y_V, Z_V)

This coordinate frame is completely specified by the current vehicle velocity direction. The $+X_V$ axis is aligned with the Earth-relative velocity vector, and $+Y_V$ is in the

direction of the cross product of the gravity vector with X_V. $+Z_V$ is then chosen to form a right-handed set.

A graphical description of these five coordinate frames is given in Figure 2-3.

2.3 Flight Control Hardware

2.3.1 Digital Flight Computer

A digital flight computer, located in the payload stage of the vehicle, performs all the necessary navigation, guidance, control, and sequencing functions during the boost phase. The flight computer is programmed in a low-level language, so that it may perform high-speed real-time computations. For the purposes of this thesis, an IBM 3080 mainframe computer has been utilized to simulate the digital flight computer as part of the vehicle simulation. Necessary constants and functionalized variables are stored in accessible computer memory. All the necessary flight program computational routines have been programmed in MAC, a CSDL-developed high-level language. The flight computer simulation is allowed to sample the available sensor data every 10 msec. The flight computer simulation then processes this data, performs computations, and outputs control signals at one of three predetermined frequencies. The cycle times associated with these frequencies are:

- 10 msec, referred to as the minor cycle or control cycle
- 100 msec, referred to as the intermediate cycle
- 500 msec, referred to as the major cycle or steering cycle

In real-time flight computers, small computation delays may cause lags between the time at which the sensors are sampled and the time at which the resulting control signals are generated. In this thesis, these computation delays are assumed to be negligible, and are not modelled.

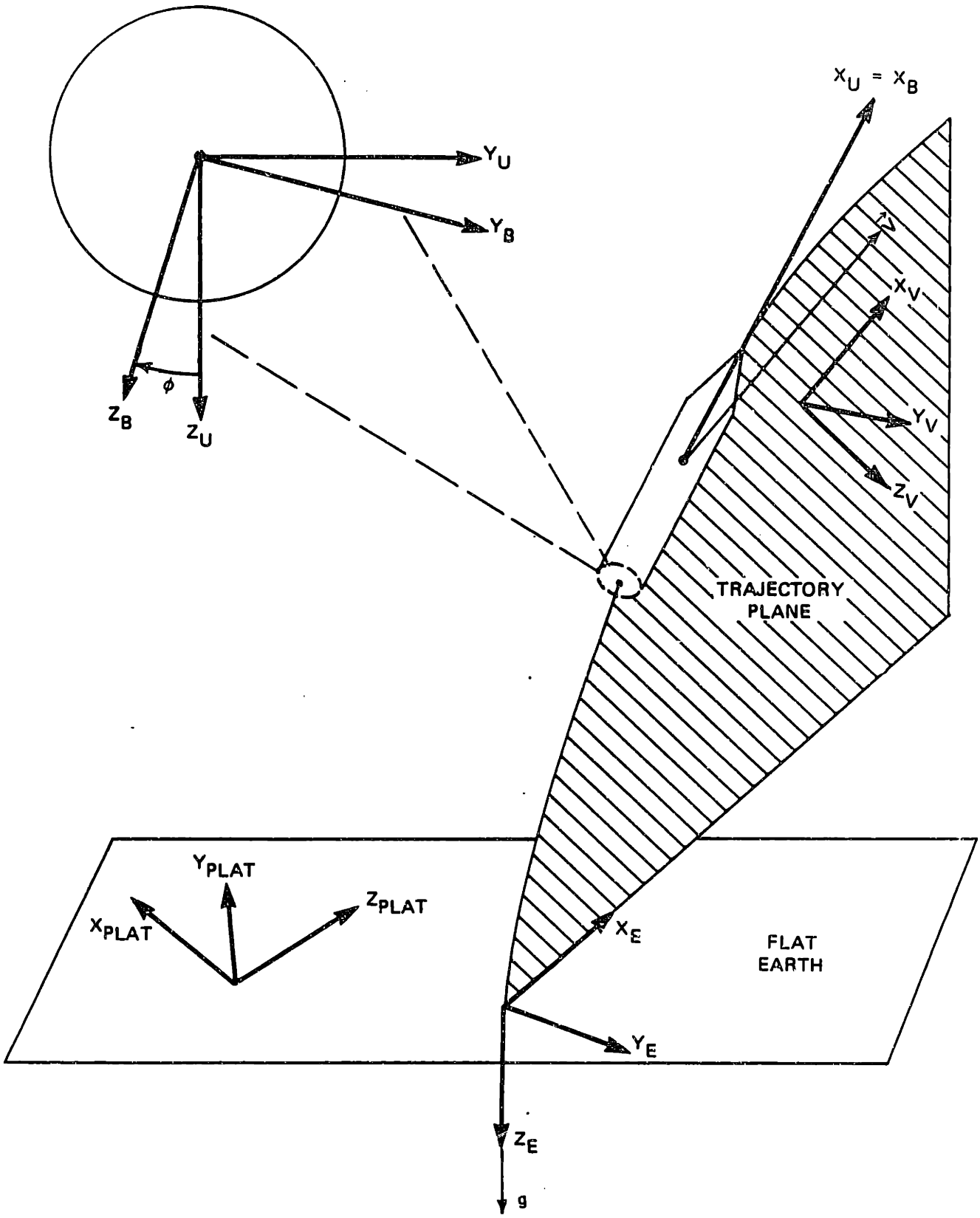

Figure 2-3. Definitions of coordinate frames and the trajectory plane.

2.3.2 Inertial Measurement Unit

The inertial measurement unit (IMU) is the primary sensor on any spacecraft. The IMU provides accurate measurement of the vehicle attitude, referenced to an inertially stabilized platform. The IMU also measures all non-gravitational accelerations of the body. These measured accelerations can then be integrated from known initial conditions to provide "sensed" velocity information.

For use in this thesis, a simulation of the CSDL-developed AIRS (Advanced Inertial Reference Sphere) IMU has been integrated into the vehicle model. Detailed description of the inner workings of this IMU is beyond the scope of this thesis. For further information on the AIRS, consult Reference [12]. For simulation purposes, the AIRS has been coded as a subroutine of the vehicle simulation. The AIRS subroutine receives information of the vehicle's actual motion, and generates data representing the AIRS measurement of that motion. The AIRS subroutine will return imperfect measurements to the flight computer simulation, according to models of the deterministic errors, random noise characteristics, and quantization effects of the actual instrument.

2.3.3 Engine Nozzle Actuators

In each booster stage, the position of the engine nozzle relative to the longitudinal axis of the vehicle is controlled by the motion of two actuators. Each actuator has only one degree of freedom. However, by operating the actuators at right angles to each other, the engine nozzle can be deflected to any commanded angular orientation in the Y_B-Z_B plane. The body axes are defined such that each actuator produces an engine nozzle deflection purely about one body axis. For this reason, one actuator is termed the pitch actuator, and the other is called the yaw actuator. The configuration of the two actuators is shown in Figure 2-4. The physical design of each actuator mechanism limits both the total angular deflection of the engine nozzle, and the speed at which the nozzle can be repositioned.

For analysis in this thesis, each engine actuator has been modelled as a moderately damped second order system, with an undamped natural frequency of 10 Hz (62.8 rad/sec), and a damping ratio of 0.5. The rate at which the nozzle may be moved is limited to 40 deg/sec. In the first stage engine, the limit on the total nozzle deflection is six degrees. For the second stage engine, the nozzle deflection limit is five degrees.

Each engine nozzle actuator is equipped with an accurate sensor, which interprets the motion of the actuator as an angular deflection of the nozzle which that motion produces. Every control cycle, the digital flight computer receives two sensor measurements, δ_Y and δ_Z, indicating the angular deflection of the engine nozzle about the pitch (Y_B) and yaw (Z_B) axes.

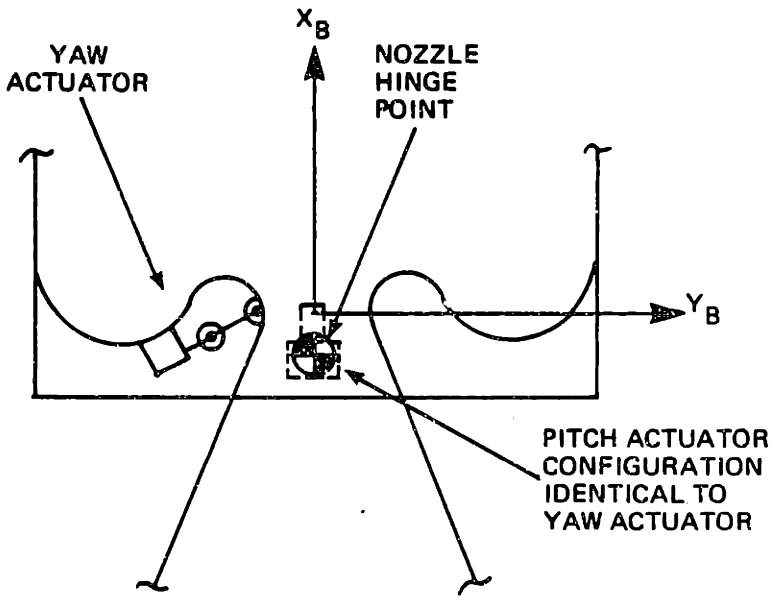

Figure 2-4. Configuration of engine nozzle actuators.

2.4 Flight Control Software

In this section, a set of baseline flight control software routines is presented to illustrate the different functions performed by the flight control system. In later chapters of this thesis, this baseline software will be modified, in an attempt to improve the performance of the flight control system in the second stage flight phase.

2.4.1 Steering

The purpose of the steering loop is to control the orientation of the vehicle velocity vector in the trajectory plane, so that the vehicle simultaneously reaches the desired position and velocity end conditions. In most applications, the orientation of the vehicle velocity vector is expressed in terms of the flight path angle, γ, defined as the angle between the velocity vector and the local horizontal plane. Steering algorithms attempt to command the vehicle to fly a predetermined trajectory that has been specified by a desired time history of γ. A typical profile of γ versus time is shown in Figure 2-5. The steering algorithm produces the desired γ profile by supplying attitude commands to the autopilot. These attitude commands are formulated so that when the autopilot drives the vehicle to the commanded flight condition, the resultant forces acting on the vehicle will produce the desired rate of change in γ.

2.4.1.1 Steering Algorithms

For use in this thesis, several algorithms have been developed to command the attitude of the vehicle, producing a desired orientation of the thrust vector relative to inertial space. There are two distinct advantages to using thrust vector orientation as the steering variable:

(1) For well-known gravitational and aerodynamic effects, the flight path angle profile $\gamma(t)$ can be predetermined as an integrated function of the applied thrust direction.

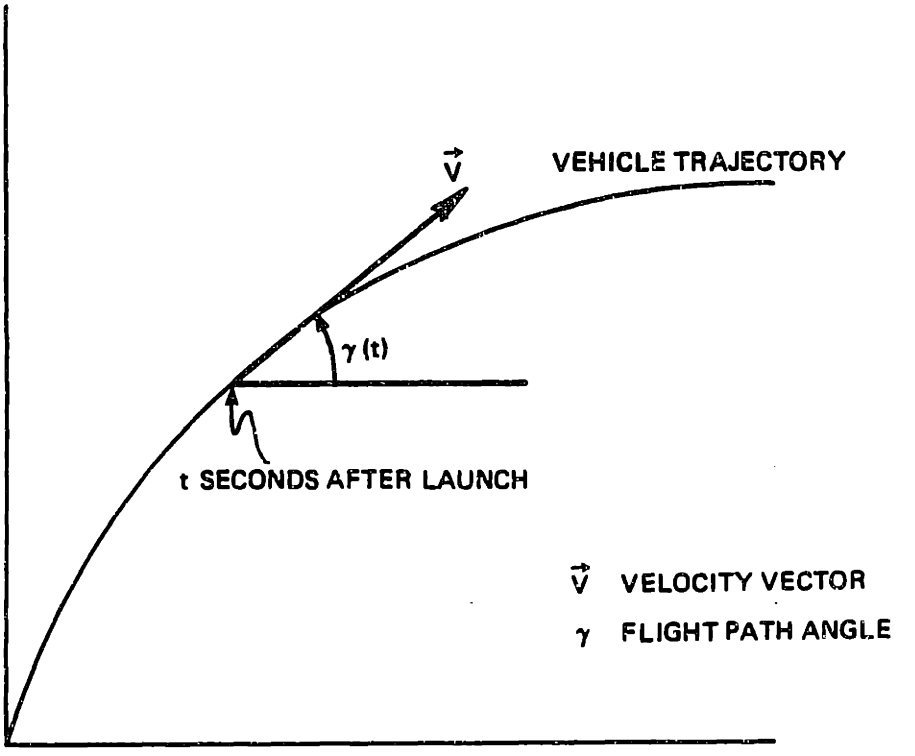

Figure 2-5. Profile of γ vs time along a typical trajectory.

(2) Since a gimballed solid rocket engine has very limited thrust deflection capability, the direction of the applied thrust lies close to the vehicle's longitudinal axis. Reorientation of the thrust vector can therefore be accomplished directly through autopilot control of the vehicle attitude.

Stage I Steering

Two distinctly different steering algorithms are implemented during the two different phases of the first stage boost flight. They are discussed in the following paragraphs.

Stage I Launch Maneuver Steering

The purpose of the launch maneuver is to rapidly rotate the vehicle's velocity vector to an intermediate command direction. Because

the magnitude of the velocity vector is still small following launch, its direction can be rapidly rotated by changing the applied thrust direction. During the launch maneuver, rapid reorientation of the vehicle may result in a large angle of attack excursion. However, this excursion does not cause a severe aerodynamic load on the vehicle because the dynamic pressure, which is a function of velocity, is still small. The intermediate commanded velocity direction is computed as a function of the estimated thrust level. If the intermediate commanded velocity direction is achieved at the end of the launch maneuver, the remainder of the first stage trajectory may be flown with near-zero angle of attack. A number of methods have been developed to command effective launch maneuvers, as discussed by Fader [5] and Bonnice [1].

In this thesis, the launch maneuver is implemented with the same algorithm employed by Dailey [4] and Ozaki [13]. This algorithm, which was originally developed by James Herner of Autonetics, rotates the vehicle to a commanded attitude, achieving an approximately zero angle of attack twelve seconds after launch. The commanded attitude is a function of the thrust estimate, λ_{EST}, discussed in Section 2.5.1.

Stage I Exponential Steering

During the first stage exponential steering phase, the vehicle passes through a region of very high dynamic pressure. In order to prevent large aerodynamic loads, the angle of attack must be limited during this flight phase. As previously discussed, the launch maneuver rotates the vehicle to an intermediate attitude, from where it is assumed that the vehicle will be able to reach the desired end conditions along a zero angle of attack trajectory. An efficient trajectory which allows the vehicle to fly with near-zero angle of attack can be realized by commanding the thrust direction to vary exponentially with time, according to the relation:

$$\beta(t) = \beta_{FINAL} + e^{-K_{EXP}t}(\beta_0 - \beta_{FINAL}) \qquad (2.1)$$

where β is the commanded angle between the thrust vector and the local horizontal, β_{FINAL} is a final reference value of β, and β_0 is the initial value of β at initiation of the exponential steering flight phase.

To allow the flight computer to implement the above profile as a steering command, this function must be transformed to a difference equation. It can be shown that if the time constant of the exponential steering function, $1/K_{EXP}$, is much greater than the steering cycle time, ΔT_{STR}, the difference equation representing Equation (2.1) is:

$$\beta(t_K) = \beta(t_{K-1}) + K_{EXP}\,\Delta T_{STR}(\beta_{FINAL} - \beta(t_{K-1})) \qquad (2.2)$$

For a given steering cycle time, such as the 500 msec period used in this thesis, the exponential steering algorithm is dependent on two constants, K_{EXP} and β_{FINAL}. These two constants can be determined prior to flight to yield the approximately zero angle of attack trajectory which best carries the vehicle from the conditions at the end of the launch maneuver to the desired conditions at I/II staging. Referring to Equation (2.1), note that $\beta(t)$ will only reach β_{FINAL} as t goes to infinity, so it is best to select a β_{FINAL} which lies below the actual desired β at the end of the first stage steering phase. For a known first stage burn time, K_{EXP} can then be selected to effect a predetermined percentage of the difference between β_0 and β_{FINAL} over the course of the flight.

It is important to recognize that the flight control system is only able to achieve approximately the commanded thrust direction, for the following two reasons:

(1) There are inherent lags and error sources in the steering and control loops.

(2) Load relief feedback signals modify the attitude errors at the input of the autopilot.

Stage II Steering

The second stage steering algorithm is implemented using the same difference equation as the first stage exponential steering algorithm. However, the constants K_{EXP} and β_{FINAL} may be altered for the second stage steering computations, depending on the desired second stage end conditions. Since the dynamic pressure is relatively low during the second stage flight phase, it is permissible to command a second stage exponential thrust direction history which causes the vehicle to develop an angle of attack.

2.4.1.2 Autopilot Interface

As outlined so far, the purpose of the steering loop is to command the orientation of the thrust vector. In order to interface with the autopilot, however, the steering commands must be transformed into body attitude angle commands. Since the thrust vector will generally lie close to the X_B axis, this fact can be used to simplify the transformation.

A complete block diagram of the pitch channel steering system is shown in Figure 2-6. At the beginning of each steering cycle, the steering algorithm outputs a new commanded thrust angle, β. It is important to note that β is calculated open loop as a function of time; it is independent of both the current vehicle orientation and the current thrust angle. The difference between the new β and the previous β, $\Delta\beta$, represents the change in the thrust angle which the autopilot must attempt to achieve over the next steering cycle. $\Delta\beta$ is resolved into body coordinates by a transformation about the roll axis. Prior to this calculation, the thrust vector is assumed to lie along the X_B axis. In order to compensate for the effects of the engine nozzle deflection, an estimate of the change in the steady-state nozzle deflection over the previous steering cycle is subtracted from the previously determined attitude command, to produce the commanded body attitude increment, $\Delta\theta_{STR}$, for the next steering cycle.

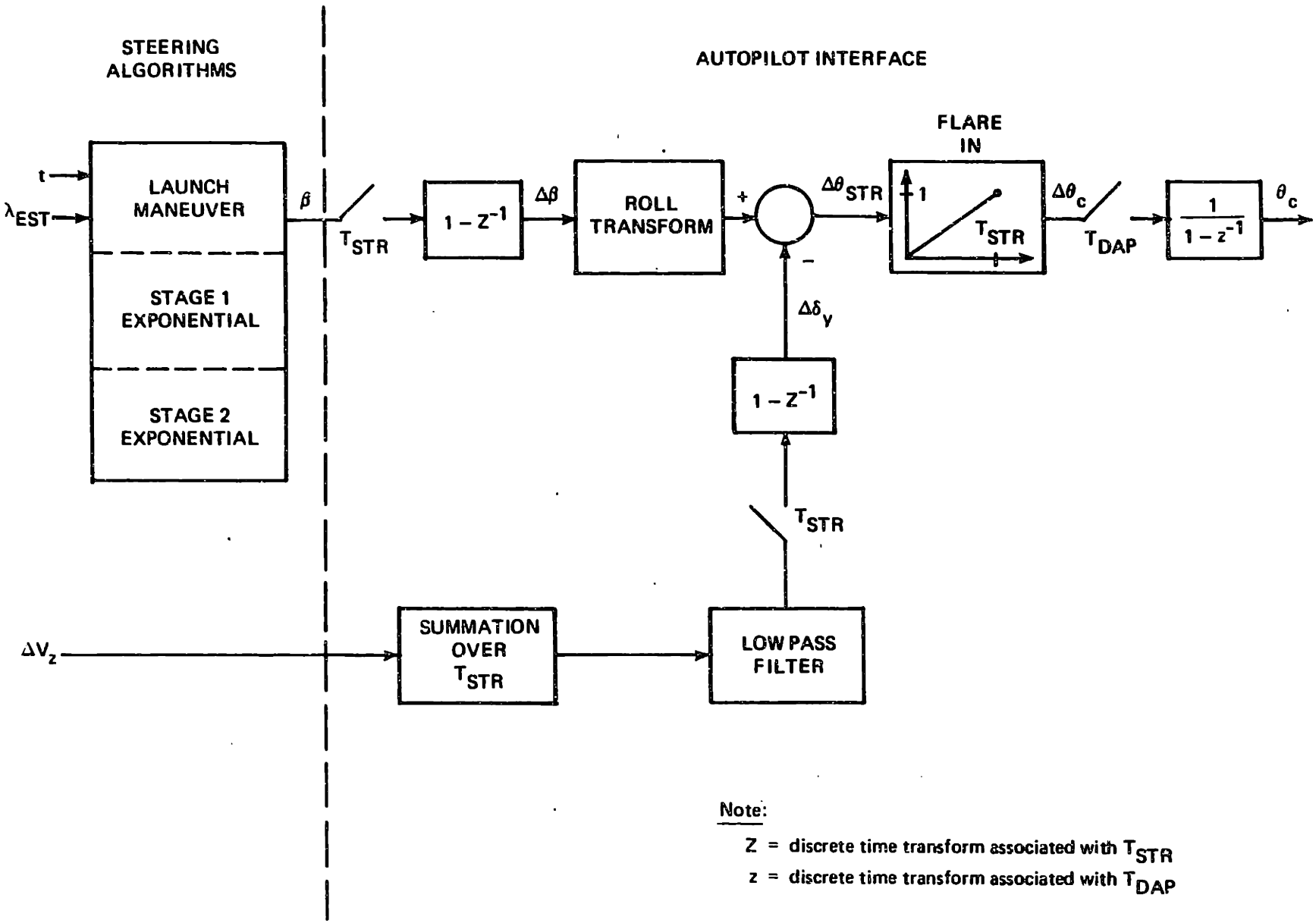

Figure 2-6. Pitch channel steering system block diagram.

Since β is only recomputed every 500 msec, the magnitude of $\Delta\beta$ can be relatively large. To prevent the steering commands from saturating the autopilot with large step inputs, the commanded body angle increment $\Delta\theta_{STR}$ is gradually "flared in" to the autopilot as a function of time. Every control cycle (10 msec), 1/50 of the total command increment is introduced at the input of the autopilot.

Referring to Figure 2-6, note that the form of the autopilot interface is the same, no matter which steering algorithm is used. The steering algorithms all make use of the estimated thrust ratio, λ_{EST}, defined as the ratio of the estimated thrust level to the nominal thrust level. A complete development of the thrust estimator is given in Section 2.5.1.

It is important to recognize that there is also a steering command which controls the angle between the thrust vector and the trajectory plane. This out-of-plane steering command is generated by the steering algorithms in the same manner as β, but it is important to note that the final commanded velocity direction is always parallel to the trajectory plane. Thus, it is the β command which controls the rotation of the velocity vector in the trajectory plane. The out-of-plane channel serves solely to command the velocity vector back towards the trajectory plane when the vehicle encounters external disturbance inputs.

2.4.2 Autopilot

A boost vehicle in atmospheric flight has its aerodynamic center of pressure forward of the center of gravity, as shown in Figure 2-7. Without any control system compensating the motion of a vehicle in this flight configuration, a perturbation in the vehicle's angle of attack leads to an increased angular acceleration in the same direction as the perturbation. Thus, an uncontrolled boost vehicle is inherently unstable. The purpose of the autopilot is to stabilize the vehicle in the presence of disturbance inputs, while simultaneously driving the vehicle to the orientation commanded by the steering loop.

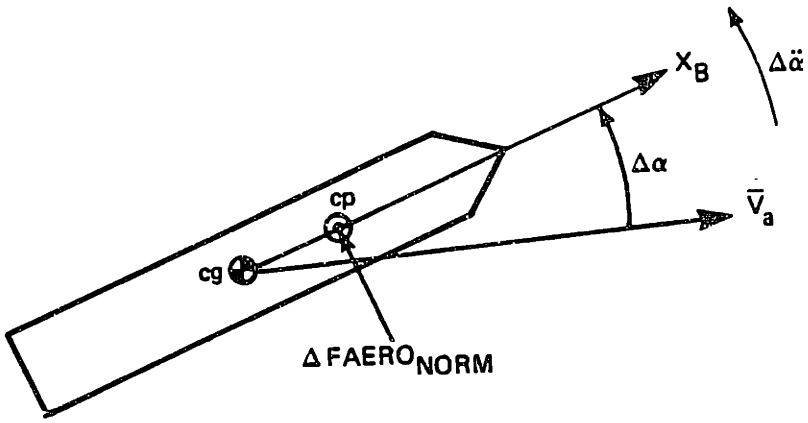

X_B = LONGITUDINAL AXIS

$\bar{V}_a$ = AIR-RELATIVE VELOCITY VECTOR

cg = CENTER OF GRAVITY

cp = CENTER OF PRESSURE

$\Delta\alpha$ = ANGLE OF ATTACK PERTURBATION

$\Delta FAERO_{NORM}$ = PERTURBATION IN AERODYNAMIC NORMAL FORCE

$\Delta\ddot{\alpha}$ = PERTURBATION IN ANGULAR ACCELERATION

Figure 2-7. Unstable flight configuration of uncontrolled boost vehicle.

In this thesis, a digital autopilot is employed to calculate discrete-time engine deflection commands for the engine nozzle actuators. The deflection of the engine thrust produces a control moment that counters the aerodynamic torques on the vehicle, and also provides any additional torque momentarily required to rotate the vehicle to a new commanded orientation. The autopilot generates new command signals every 10 msec, based on sampled and estimated data from the previous control cycle. The digital autopilot operates through two lightly coupled

control channels. Because each control channel drives one engine nozzle actuator, it is convenient to define these channels in body coordinates. The autopilot pitch channel controls the vehicle motion about the pitch axis by commanding δ_Y, the deflection of the nozzle about the pitch axis. Similarly, the yaw channel commands the nozzle deflection δ_Z. To establish a convention on the polarity of the nozzle deflection, positive nozzle deflection will be defined to produce positive angular acceleration of the vehicle about the control axis.

Figure 2-8 presents the block diagram of the pitch channel autopilot. The input to the autopilot is the commanded body orientation about the pitch axis, which is calculated by the steering loop. The autopilot also receives measurements from the IMU of the vehicle attitude and change in velocity along all three axes. The first autopilot function is to form an attitude error signal from the difference between the commanded and measured body angles. A load relief signal then augments this attitude error, so that the attitude correction does not cause a large angle of attack. The augmented error signal is passed through a magnitude limiter. A rate estimate is subtracted from the limited error signal to obtain a signal that is first multiplied by a constant gain factor, then passed through a bending filter to produce the pitch actuator command. The pitch actuator command is sent, along with the yaw actuator command, into a "bucket" limiter. The bucket function limits the total commanded engine deflection to the physical saturation limit of the actuator system. The pitch output of the bucket limiter is the commanded pitch nozzle deflection, which is sent to the pitch channel actuator through a zero-order hold (ZOH) circuit. The ZOH circuitry holds the command signal constant until a new command signal is generated 10 msec later.

As mentioned in Chapter 2, this thesis treats the boost vehicle as a rigid body. Under this assumption, the bending filter transfer function can be set to a unity gain without affecting the stability of the autopilot.

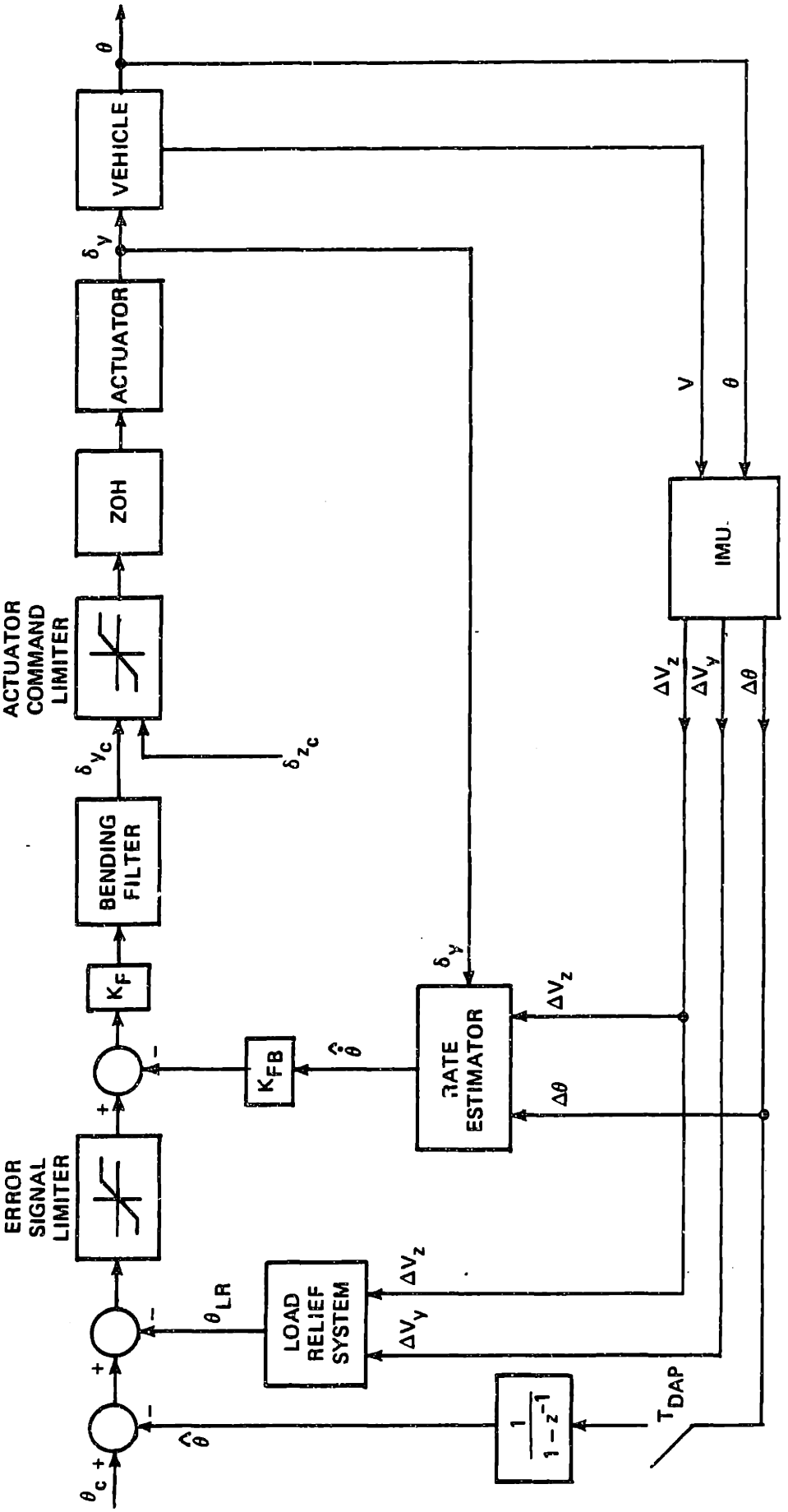

Figure 2-8. Pitch channel autopilot block diagram.

2.4.3 Load Relief

As the boost vehicle accelerates through the atmosphere, it is subjected to very large aerodynamic forces during portions of its flight. The magnitudes of these aerodynamic forces are directly proportional to the dynamic pressure, Q, defined as:

$$Q = 1/2\ \rho\ V_A^2 \tag{2.3}$$

where ρ is the local air density, and V_A is the magnitude of the vehicle velocity vector with respect to the atmosphere.

If the vehicle is following a prescribed zero angle of attack trajectory, the dynamic pressure produces a purely axial aerodynamic force. The axial force opposes the acceleration of the vehicle along its longitudinal axis, and does not produce a bending moment on the booster. However, if the vehicle develops an angle of attack, the aerodynamic force will contain a component acting normal to the vehicle longitudinal axis. The combination of this aerodynamic normal force, acting effectively at the center of pressure, and the compensating lateral thrust component, acting at the engine hinge point, can produce a large bending moment that could structurally damage the vehicle. Figure 2-9 shows a boost vehicle subjected to a large aerodynamic normal force, or "load". The magnitude of the aerodynamic normal force is approximately proportional to both the dynamic pressure and the total angle of attack:

$$FAERO_{NORM} = S\ Q\ CN_\alpha\ \alpha \tag{2.4}$$

where S is the aerodynamic reference area of the vehicle, and CN_α is the local normal force stability derivative.

The purpose of the load relief system is to minimize the aerodynamic loads that produce bending moments on the vehicle. Referring to Equation (2.4), S is a vehicle constant, and Q and CN_α cannot be directly controlled. Thus, an effective load relief system must keep the

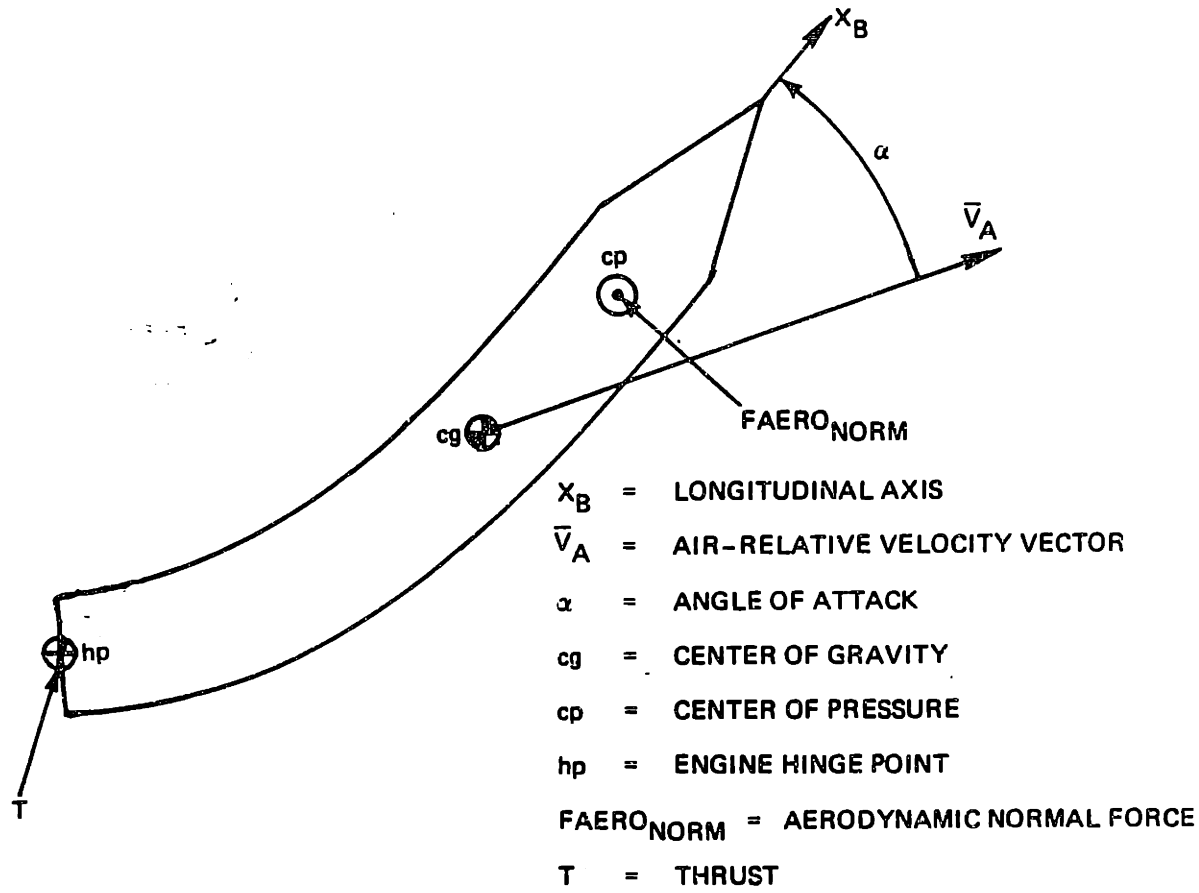

Figure 2-9. Boost vehicle subjected to large aerodynamic load.

magnitude of α small during portions of the flight when the dynamic pressure is large.

For the purposes of this thesis, a load relief system is introduced to augment the attitude errors acted upon by the digital autopilot. The load relief system receives the sensed velocity increments ΔV_Y and ΔV_Z from the IMU, and uses these measurements to generate low frequency estimates of the angle of attack components. The angle of attack estimates are then subtracted from the attitude errors generated by the steering command. This load relief correction causes the vehicle to rotate into the wind to reduce its angle of attack.

Because the need for load relief varies with the potential for aerodynamic loading due to Q, load relief is implemented in varying degrees during the first and second stage flight phases. In this thesis, there are four different load relief periods of interest, which are discussed in the following paragraphs.

Launch Maneuver Load Relief

During the launch maneuver, the velocity of the vehicle is still small, the dynamic pressure is low, and the vehicle is allowed to develop a large angle of attack, as commanded by the launch maneuver steering routine. No load relief is necessary during the launch maneuver, so the load relief feedback signals are zeroed during this flight phase.

Stage I Exponential Steering Phase Load Relief

Midway through the first stage flight phase, the vehicle passes through the region of maximum dynamic pressure. In this region, great care must be taken to limit the angle of attack that could produce severe bending moments. Upon entry into the first stage exponential steering phase, the load relief system begins to compute load relief signals based upon the measured ΔV's over two different time intervals:

(1) Minor cycle (10 msec) ΔV measurements

(2) Major cycle (500 msec) ΔV measurements

The minor cycle load relief, based on low-pass filtered ΔV measurements, provides rapid load relief response to wind disturbances. The major cycle load relief, based on numerical integration of 500 ms ΔV increments, provides slow control action to orient the vehicle to an approximately zero angle of attack.

A complete block diagram of the pitch channel load relief system is shown in Figure 2-10. It is important to note that the ΔV measurements enter the load relief loop and are immediately transformed to the unrolled body coordinates. This allows the load relief system to decouple its compensation into angle of attack corrections in and out of the commanded trajectory plane. The load relief signals must then be transformed back to body coordinates before being fed back to the autopilot.

Both load relief paths make use of a low frequency angle of attack estimator, which is outlined in Section 2.5.3. The major cycle integral load relief is weighted differently in the total signal, according to the

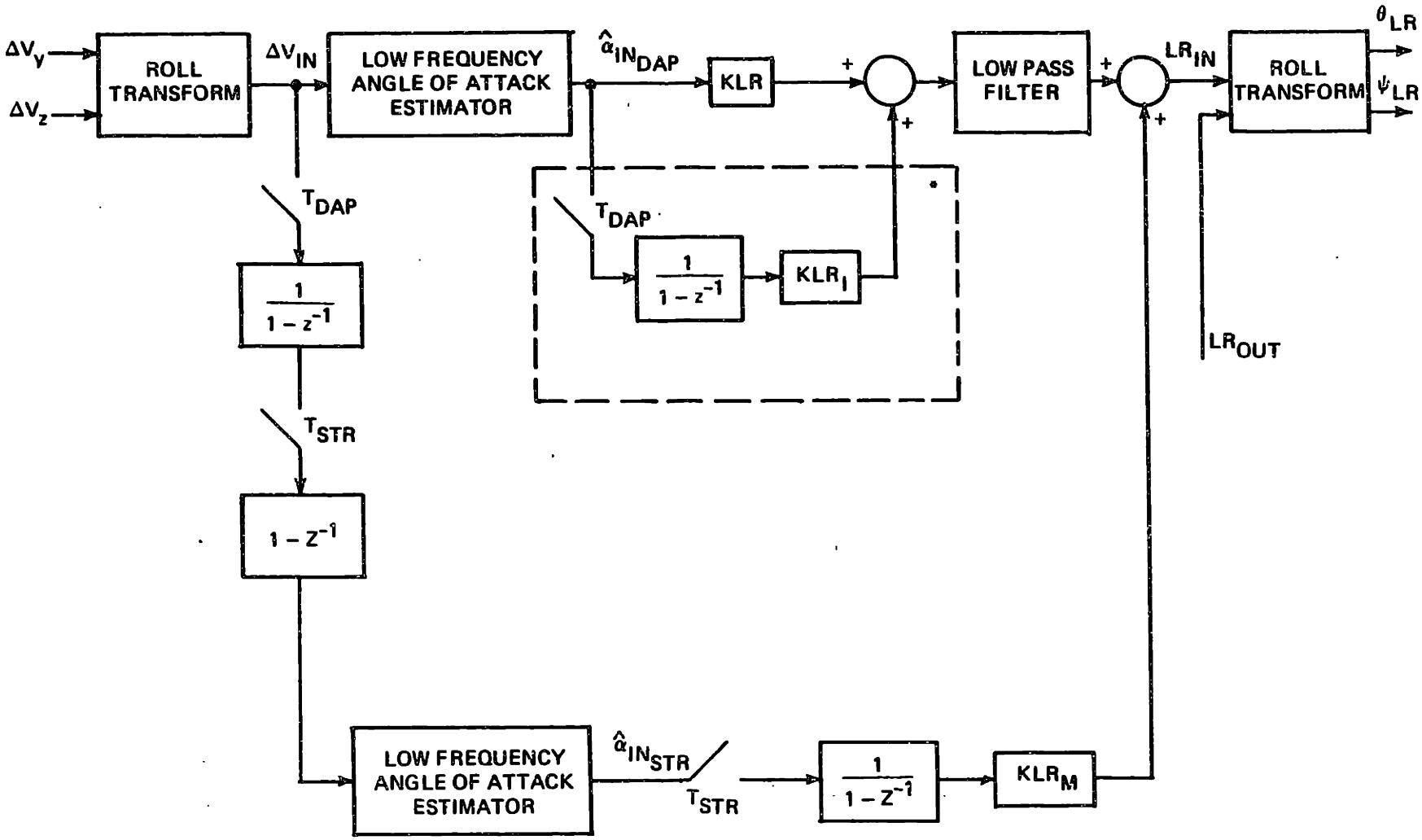

NOTE:

Z = discrete time transform associated with T_{STR}

z = discrete time transform associated with T_{DAP}

*Minor cycle integral load relief used only during Stage 1 tailoff.

Figure 2-10. Pitch channel load relief block diagram.

value of KLR_M. In the time preceding the predicted thrust tailoff, the system weights major cycle ΔV readings more heavily by increasing KLR_M.

Stage I Tailoff Load Relief

Near the end of the first stage thrusting phase, the thrust produced by the first stage engine begins to decrease, or "tailoff". With the engine producing a lower thrust level, the control system lacks the capability to stabilize the vehicle in the presence of large aerodynamic normal forces. In order to prevent the buildup of large angles of attack during this uncontrolled interval, it is necessary to minimize the angle of attack and angular velocity of the vehicle prior to staging. Specific limits on the angle of attack at stage separation are presented in Chapter 4. In order to reduce the angle of attack before staging, the load relief system adds an integral of the minor cycle load relief signal to the proportional signal used earlier in flight. The formation of this integral load relief signal is shown in Figure 2-10.

Stage II Load Relief

As previously discussed, the effect of the first stage load relief is to modify the attitude error signal to cause the vehicle to rotate into the wind, thereby reducing the angle of attack. A consequence of the load relief correction is that an attitude error develops between the actual attitude and the attitude commanded by the steering loop. This attitude error may continue to grow throughout the first stage flight, and does not disappear upon transfer to second stage steering. Therefore, although aerodynamic loading problems are much less severe at the second stage altitudes, the load relief signals are held constant following stage separation, to prevent a large step in the autopilot error signal. As the boost vehicle exits the atmosphere, the load relief signals are then gradually phased out in order to avoid large transients.

2.5 Estimation Algorithms

2.5.1 Thrust Estimator

In a solid rocket booster, the burn characteristics of the propellant vary somewhat with the propellant temperature. The range of possible temperature deviations, while not extreme, can still result in thrust levels as much as ±10% off the nominal value. The accuracy of the boost steering system can be improved if the actual thrust can be estimated following launch, and then used to modify the commanded trajectory.

This thesis uses a method developed by James Herner of Autonetics to compute a thrust estimate from measurements of the axial ΔV and an approximate functionalization of the sensed axial acceleration time profile. The sensed axial acceleration profile is derived for a vehicle with a constant thrust level and a constant specific impulse. Under these assumptions, the vehicle mass M may be expressed in terms of the applied thrust T, the specific impulse I_{SP} and the constant gravitational acceleration g:

$$M = M_o - \frac{T\,t}{I_{SP}g} \tag{2.5}$$

where M_o is the initial mass of the vehicle and t is the time from engine ignition.

The x-axis acceleration of the vehicle, neglecting effects of the axial aerodynamic force, the atmospheric pressure, and the engine nozzle deflection, is given by:

$$ACC_{FIT} = \frac{T}{M} \tag{2.6}$$

Substituting the expression for M from Eq. (2.5) gives:

$$ACC_{FIT}(t) = \frac{T}{M_o - \frac{T\,t}{I_{SP}g}} \tag{2.7}$$

Factoring out M_o:

$$ACC_{FIT}(t) = \frac{T/M_o}{1 - \frac{T\,t}{M_o I_{SP} g}} \qquad (2.8)$$

If the fractional change in mass over t seconds is small, then the above expression may be approximated by:

$$ACC_{FIT}(t) \cong \frac{T}{M_o}\left[1 + \frac{T\,t}{M_o I_{SP} g} + \left(\frac{T\,t}{M_o I_{SP} g}\right)^2\right] \qquad (2.9)$$

If the ratio between the actual thrust and the nominal thrust T_{NOM} is given by λ, then ACC_{FIT} becomes:

$$ACC_{FIT}(t) \cong \frac{\lambda\, T_{NOM}}{M_o}\left[1 + \left(\frac{\lambda\, T_{NOM}\, t}{M_o I_{SP} g}\right) + \left(\frac{\lambda\, T_{NOM}\, t}{M_o I_{SP} g}\right)^2\right] \qquad (2.10)$$

In the thrust estimator, this functionalization is implemented in the form:

$$ACC_{FIT}(t) = \lambda\,[CA1 + CA2(\lambda t) + CA3(\lambda t)^2] \qquad (2.11)$$

where:

$$CA1 = \frac{T_{NOM}}{M_o} \qquad (2.12a)$$

$$CA2 = \frac{1}{I_{SP} g}\left(\frac{T_{NOM}}{M_o}\right)^2 \qquad (2.12b)$$

$$CA3 = \left(\frac{1}{I_{SP}g}\right)^2 \left(\frac{T_{NOM}}{M_o}\right)^3 \qquad (2.12c)$$

In order that the assumptions of a small relative change in mass and negligible aerodynamic force be valid, it is desirable to make the thrust estimate as soon as possible following engine ignition, for the following reasons:

- The contribution of drag to the sensed axial acceleration is negligible following launch, because the dynamic pressure is small.
- The change in mass during the launch maneuver is very small compared to the total mass of the vehicle at launch.

A thrust estimate is therefore calculated only during the launch maneuver. To make the necessary assumption of constant thrust during the estimation period, thrust estimation is limited to the interval $2.0 < t < 9.0$ seconds. During this interval, the thrust estimate is updated every intermediate cycle (100 msec) using an iterative algorithm which attempts to reduce the effects of measurement noise. This algorithm is implemented in the following steps:

(1) Set the initial estimate of λ, λ_{EST}, equal to 1.0.

(2) Calculate ACC_{FIT} using the current values of t and λ_{EST} in Equation (2.11).

(3) Calculate the derivative of the quadratic curvefit with respect to λ_{EST}:

$$\frac{\partial ACC_{FIT}}{\partial \lambda_{EST}} = CA1 + 2\,CA2(\lambda_{EST}t) + 3\,CA3(\lambda_{EST}t) \qquad (2.13)$$

(4) Calculate the average measured axial acceleration over the intermediate cycle:

$$\bar{ACC}_{MEAS} = \frac{\Delta V_{INT}}{T_{INT}} \tag{2.14}$$

where T_{INT} is the intermediate cycle time and ΔV_{INT} is the summation of the IMU ΔV_X measurements over the intermediate cycle.

(5) Calculate the error in λ_{EST} indicated by the measured acceleration using the following approximation:

$$\Delta\lambda_{EST} = \frac{\Delta ACC_{FIT}}{\partial ACC_{FIT}/\partial\lambda_{EST}} = \frac{\bar{ACC}_{MEAS} - ACC_{FIT}}{ACC_{FIT}/\partial\lambda_{EST}} \tag{2.15}$$

(6) Update λ_{EST} according to:

$$\lambda_{EST}(t_K) = \lambda_{EST}(t_{K-1}) + K_\lambda \Delta\lambda_{EST} \tag{2.16}$$

where t_K is the Kth discrete value of time, and K_λ is the appropriate estimator gain.

(7) If $t < 9.0$ seconds, return to Step #2 at the next intermediate cycle.

The estimator gain K_λ must be chosen large enough to allow the estimation process to converge during the short estimation interval, but not so large that it will heavily weight noisy measurements in the final estimate. In this implementation, a value of 0.40 was selected for K_λ.

2.5.2 Angular Rate Estimator

As shown in Figure 2-8, the digital autopilot requires feedback of angular rate estimates to form the error signals necessary for autopilot control of the vehicle. The angular rate estimator used for this thesis employs a complementary filter. The low-frequency components of the rate estimates are computed from IMU-measured body angle increments:

$$\hat{\dot{\theta}}_{LOW} = \left(\frac{\Delta\theta}{T_{DAP}}\right)$$

$$\hat{\dot{\Psi}}_{LOW} = \left(\frac{\Delta\Psi}{T_{DAP}}\right) \qquad (2.17)$$

$\hat{\dot{\theta}}_{LOW}$ and $\hat{\dot{\Psi}}_{LOW}$ are termed the derived angular rates about the Y_B (pitch) and Z_B (yaw) axes, respectively. T_{DAP} is the autopilot loop sampling interval.

To remove the large fluctuations in the derived rate signals caused by noise and quantization effects, the derived rate signals are passed through a first-order low-pass filter. The low-pass filter, however, introduces an undesirable lag into the rate estimates. In the complementary filter approach, the effects of this lag are compensated by the addition of another signal that provides, in effect, the high-frequency component of the rate estimates. The high-frequency signals, which represent the change in the angular rates over the previous control cycle, are calculated from solution of the rigid body equations of motion. As an example of one of the high-frequency rate estimate calculations, the equations of motion about the vehicle pitch axis are:

$$M\, a_{CG} = FAERO_Z - T\, \delta_Y$$

$$I\, \ddot{\theta} = T\, L_{CG}\, \delta_Y + FAERO_Z\, L_{CP} \qquad (2.18)$$

$$a_{IMU} = a_{CG} + L_{IMU}\ddot{\theta}$$

where all symbols are as defined in Figure 2-11. Eliminating a_{CG} and $FAERO_Z$ from the above set of equations and solving for $\ddot{\theta}$:

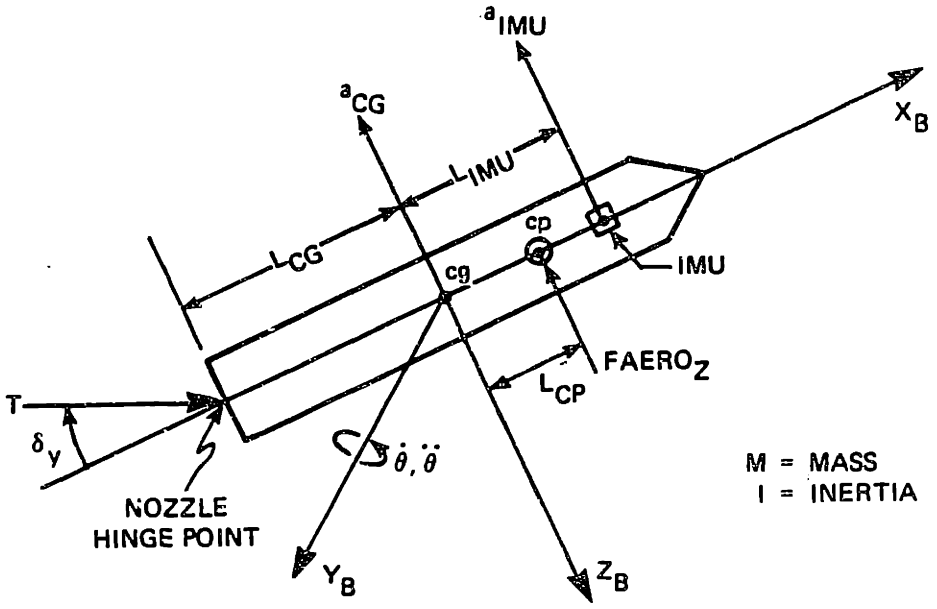

X_B, Y_B, Z_B	BODY-FIXED COORDINATE FRAME
$\dot{\theta}, \ddot{\theta}$	ANGULAR VELOCITY AND ACCELERATION OF THE VEHICLE ABOUT THE Y_B AXIS
cp	CENTER OF PRESSURE
cg	CENTER OF GRAVITY
L_{CP}	DISTANCE BETWEEN cg AND cp
L_{CG}	DISTANCE BETWEEN NOZZLE HINGE POINT AND cg
L_{IMU}	DISTANCE BETWEEN cg AND IMU
T	THRUST
δ_y	NOZZLE DEFLECTION ABOUT THE $-Y_B$ AXIS
$FAERO_Z$	COMPONENT OF AERODYNAMIC FORCE PARALLEL TO $-Z_B$ AXIS
a_{CG}	COMPONENT OF cg ACCELERATION PARALLEL TO $-Z_B$ AXIS
a_{IMU}	COMPONENT OF IMU ACCELERATION PARALLEL TO $-Z_B$ AXIS

Figure 2-11. Vehicle schematic for derivation of pitch axis equations of motion.

$$\ddot{\theta} = C1\ \delta_Y + C2\ a_{IMU} \tag{2.19}$$

where the constants C1 and C2 are defined by

$$C1 = \frac{T\ (L_{CP} + L_{CP})}{I + M\ L_{IMU}\ L_{CP}} \qquad C2 = \frac{M\ L_{CP}}{I + M\ L_{IMU}\ L_{CP}} \tag{2.20}$$

For a known thrust profile, the parameters L_{CG}, L_{IMU}, I, and M can all be specified as known functions of time. The aerodynamic parameter L_{CP} can also be well-defined, although its time history varies somewhat with the specific trajectory flown. From these parameter time histories, the coefficients C1 and C2 can be functionalized vs time. This functionalization vs time, however, tends to be in error if the thrust profile deviates from the nominal. In this case, it is more accurate to functionalize C1 and C2 vs sensed velocity, as has been done in this thesis. The coefficients are stored in the digital flight computer and then used every cycle to form an estimate of $\dot{\theta}$ which is accurate at high frequencies. This estimate is obtained by first integrating Equation (2.19) to obtain an expression for the change in $\dot{\theta}$ over the control cycle time:

$$\Delta\dot{\theta} = C1\ \delta_Y\ T_{DAP} - C2\ \Delta V_Z \tag{2.21}$$

where δ_Y is the average δ_Y over the interval T_{DAP}.

The high-frequency rate estimate is then formed as the sum of the previous estimate and the estimated change in rate:

$$\hat{\dot{\theta}}_{HIGH}(t_K) = \hat{\dot{\theta}}_{HIGH}(t_{K-1}) + \Delta\hat{\dot{\theta}}(t_K) \tag{2.22}$$

where t_K represents the Kth discrete value of time.

The high-frequency rate estimate is passed through a first-order high-pass filter whose characteristics complement those of the low-pass filter. The total output of the complementary filter is a good approximation of the true angular rate, without any filtering lags. For further discussion and analysis of complementary filters, see Bonnice [1].

An analogous development could be used to illustrate the calculation of the high-frequency yaw rate estimate. A block diagram of the complete rate estimator is shown in Figure 2-12.

2.5.3 Low Frequency Angle of Attack Estimator

As shown in Figure 2-10, the load relief system requires angle of attack estimates in unrolled body axes to form the load relief feedback feedback signals. In this section, it will be shown that ΔV measurements from the IMU, transformed into the unrolled body axis system, can be used to form estimates of the in-plane (i.e., trajectory plane) and out-of-plane angle of attack components. These estimates neglect the effects of angular acceleration on the lateral ΔV measured by the IMU, and therefore are valid only for quasi-steady state or low frequency conditions where these effects can be neglected.

For the in-plane angle of attack, an estimate can be derived from the vehicle's equations of motion in the trajectory plane:

$$\begin{aligned} M\, a_{CG} &= FAERO_{IN} - T\, \delta_{IN} \\ I\, \ddot{\theta}_{IN} &= FAERO_{IN}\, L_{CP} + T\, \delta_{IN}\, L_{CG} \\ a_{IMU} &= a_{CG} + L_{IMU}\, \ddot{\theta}_{IN} \end{aligned} \tag{2.23}$$

where all symbols are as defined in Figure 2-13. The subscript IN defines the component of its argument in the trajectory plane. To obtain an estimate of angle of attack which is accurate at low frequencies, a steady state condition is assumed in which the angular acceleration,

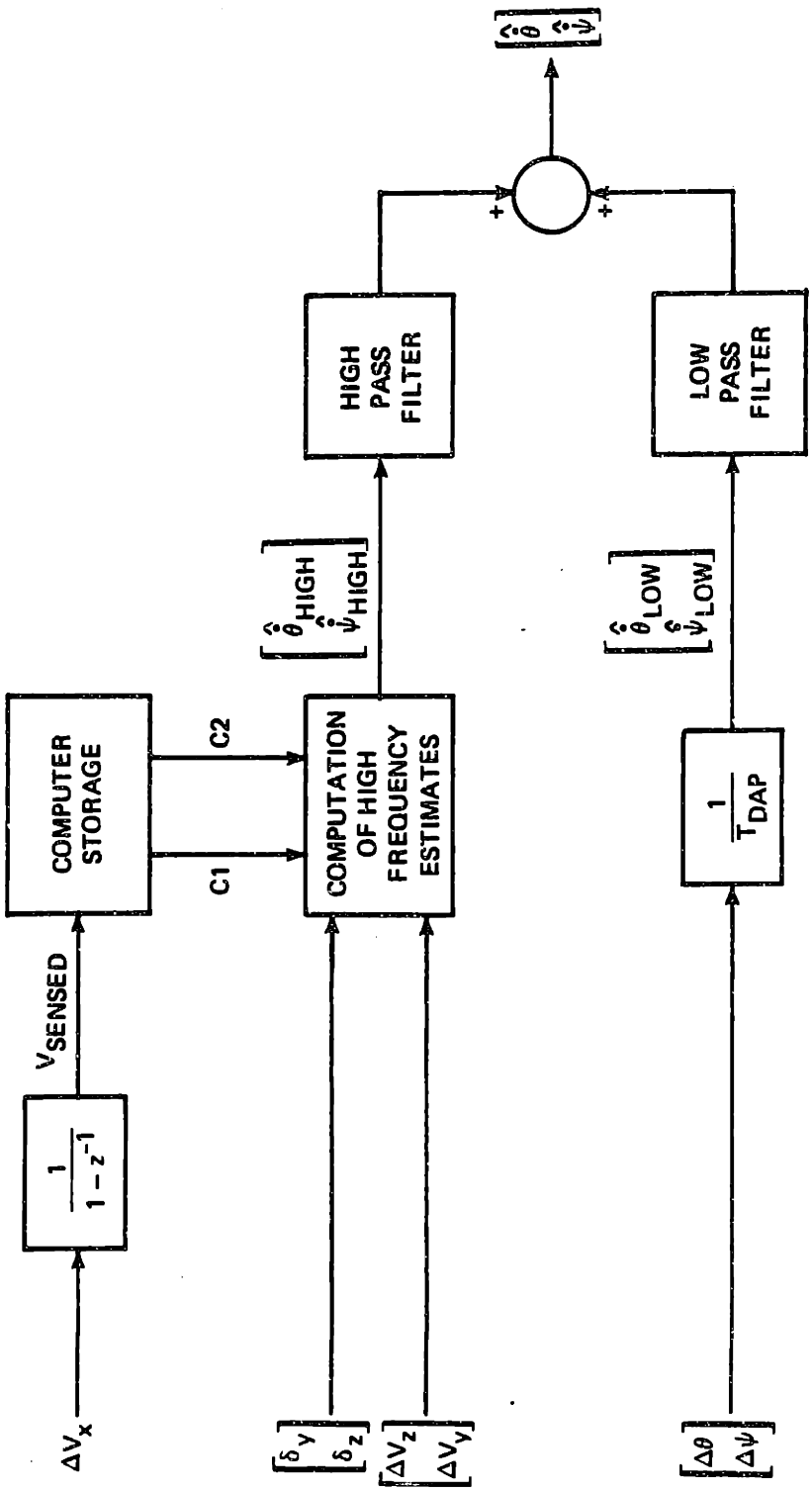

Figure 2-12. Angular rate estimator block diagram.

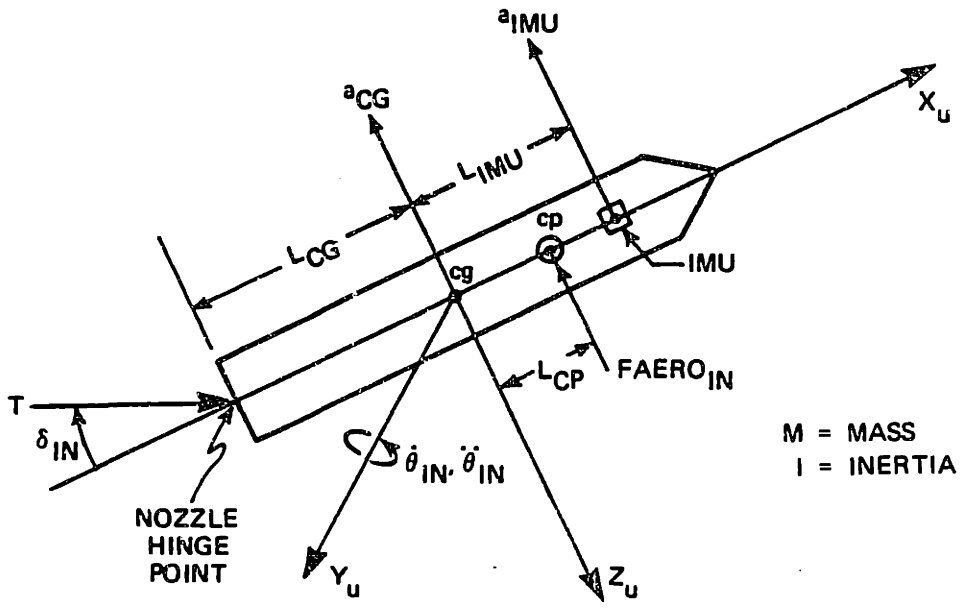

X_u, Y_u, Z_u	UNROLLED BODY COORDINATE FRAME
$\dot{\theta}_{IN}, \ddot{\theta}_{IN}$	ANGULAR VELOCITY AND ACCELERATION OF THE VEHICLE ABOUT THE Y_u AXIS
cp	CENTER OF PRESSURE
cg	CENTER OF GRAVITY
L_{CP}	DISTANCE BETWEEN cg AND cp
L_{CG}	DISTANCE BETWEEN NOZZLE HINGE POINT AND cg
L_{IMU}	DISTANCE BETWEEN cg AND IMU
T	THRUST
δ_{IN}	NOZZLE DEFLECTION ABOUT THE $-Y_u$ AXIS
$FAERO_{IN}$	COMPONENT OF AERODYNAMIC NORMAL FORCE PARALLEL TO $-Z_u$ AXIS
a_{CG}	COMPONENT OF cg ACCELERATION PARALLEL TO $-Z_u$ AXIS
a_{IMU}	COMPONENT OF IMU ACCELERATION PARALLEL TO $-Z_u$ AXIS

Figure 2-13. Vehicle schematic for derivation of trajectory plane equations of motion.

$\ddot{\theta}_{IN}$, is zero. Given this assumption, and eliminating δ_{IN} and a_{CG} from the above set of equations:

$$a_{IMU} = FAERO_{IN} \frac{L_{CP} + L_{CG}}{M\ L_{CG}} \tag{2.24}$$

The aerodynamic force $FAERO_{IN}$ is approximately proportional to α_{IN} through the relationship:

$$FAERO_{IN} \cong S\ Q\ CN_{\alpha}\ \alpha_{IN} \tag{2.25}$$

Also, at low frequencies:

$$a_{IMU} \cong \frac{\Delta V_{IN}}{T_{DAP}} \tag{2.26}$$

Substituting the approximate expressions for $FAERO_{IN}$ and a_{IMU} into Equation (2.24):

$$\frac{\Delta V_{IN}}{T_{DAP}} = \frac{S\ Q\ CN_{\alpha}\left(L_{CG} + L_{CP}\right)\ \alpha_{IN}}{M\ L_{CG}} \tag{2.27}$$

Rearranging and solving for α_{IN}:

$$\alpha_{IN} = C_{LR} \frac{\Delta V_{IN}}{T_{DAP}} \tag{2.28}$$

where the coefficient C_{LR} is defined as:

$$C_{LR} = \frac{M\ L_{CG}}{S\ Q\ CN_{\alpha}\ \left(L_{CG} + L_{CP}\right)} \tag{2.29}$$

In a method similar to that used to determine the rate estimator coefficient, the coefficient C_{LR} may be stored in the digital flight computer as a functionalized variable of time.

An analogous development could be used to illustrate the calculation of the out-of-plane angle of attack estimate, α_{OUT}. The same coefficient C_{LR} can be used to calculate both angle of attack estimates.

2.6 Flight Environment

The trajectories presented in this thesis are generated using a flat, non-rotating, constant gravity Earth model. Under these assumptions, no distinction need be made between an Earth-fixed and an inertially-fixed reference frame. The Earth-fixed frame shall be defined such that the commanded boost trajectory takes place in the X_E-Z_E plane, as shown in Figure 2-3. Note that gravity always accelerates the vehicle in the $+Z_E$ direction.

A standard atmosphere has been modelled by making piecewise-exponential curvefits to the 1967 U. S. Standard Atmosphere Tables. The atmospheric model outputs air pressure and density as a function of altitude. The effect of atmospheric temperature deviations on the air pressure and density have not been modelled.

In this thesis, wind speed is the only atmospheric disturbance introduced into the flight environment. A wind model has been developed which outputs horizontal wind speed as a function of altitude. The model is based on a 99th percentile wind speed boundary vs altitude; that is, at any given altitude, the probability of the wind speed exceeding the boundary value is 0.01. To use the wind model for a simulated trajectory, it is necessary to specify two parameters:

- Wind spike altitude
- Wind direction

The wind spike altitude determines the altitude at which the maximum wind speed occurs. The rate of change of the wind speed in the range of the wind spike altitude ±5000 feet is then determined from tabled data in the memory of the simulation computer. The remainder of the wind model is characterized by a decrease in wind speed with altitude, down to a wind speed of zero at sea level, and a wind speed of zero at twice the altitude of the wind spike.

Examples of the 99% wind speed boundary and a 99% wind spike model are shown in Figure 2-14. Notice that the wind speed at the wind spike altitude is defined to be the wind speed of the 99% wind speed boundary at that altitude.

The effects of wind disturbances on the trajectory of the vehicle will vary greatly, depending on the wind direction. To make analysis simpler, in this thesis the specification of wind direction will be limited to one of three possibilities: a headwind (wind velocity along the $-X_E$ axis), a tailwind (wind velocity along the $+X_E$ axis), or a crosswind (wind along the $+Y_E$ axis). All winds are assumed to travel parallel to the Earth's surface, with no vertical velocity component.

2.7 Flight Performance Specifications

To properly define "satisfactory" performance by the flight control software, it is necessary to define flight performance specifications for the boost vehicle. Although many of the following specifications will be presented and discussed elsewhere in this thesis, all relevant specifications are included here for ease of reference.

Steering Specifications

The first stage steering algorithms shall be designed to guide the vehicle to end conditions in the dynamic pressure range:

$$1200 \text{ psf} < Q < 1600 \text{ psf}$$

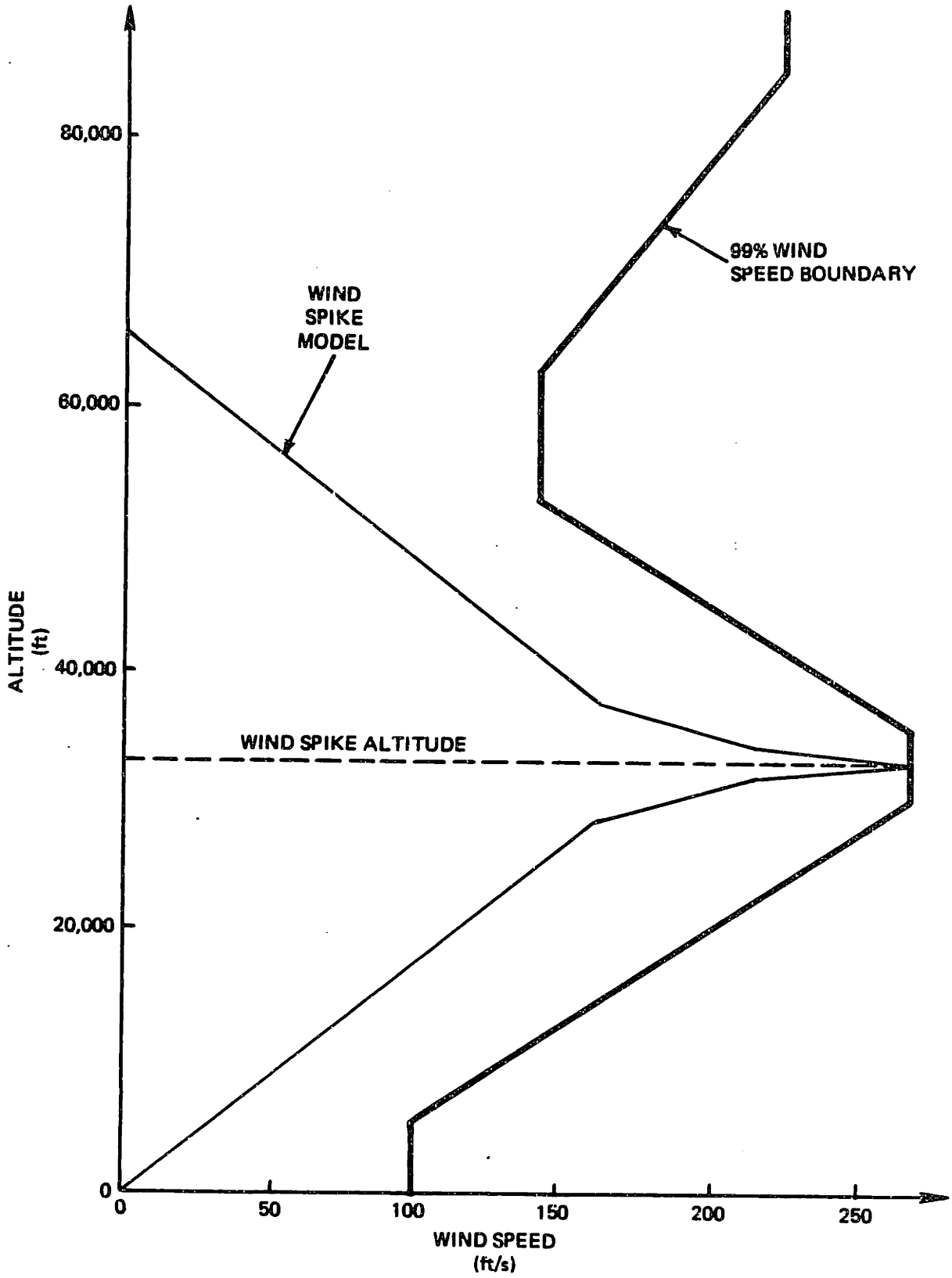

Figure 2-14. Example 99th percentile wind model.

Launch Specifications

(1) The first stage steering algorithms shall be designed to compensate for off-nominal launch angles in the region:

$$\theta_{LAUNCH} = 90 \pm 29 \text{ degrees}$$

(2) The magnitude of the roll rate at launch shall be restricted:

$$\left|\dot{\phi}\right| \leq 10 \text{ deg/sec}$$

Maneuvering Limits

(1) The vector sum of the body rates about its control axes shall be limited, according to the condition:

$$\sqrt{(\dot{\theta}^2 + \dot{\psi}^2)} \leq 28 \text{ deg/sec}$$

(2) The magnitude of the vehicle roll rate shall be restricted to:

$$\left|\dot{\phi}\right| \leq 50 \text{ deg/sec}$$

Aerodynamic Loading Limits

(1) The magnitude of the product of dynamic pressure and angle of attack, $Q\alpha$, shall be kept below 10,000 psf deg during the first stage flight phase.

(2) The magnitude of the $Q\alpha$ product shall be kept below 6000 psf deg during the second stage flight phase.

2.8 System Simulation

The flight of the boost vehicle modelled in this thesis is simulated in non-real time using an IBM 3080 mainframe computer. This computer simultaneously simulates the motion of the vehicle and the action

of the digital flight computer. The computer makes use of both the flight control software routines and the flight control hardware models to compute the commanded thrust direction and the resulting engine nozzle deflection as a function of time. The simulation also generates the local environmental conditions. Using a numerical integration routine, the simulation updates the position, velocity, and orientation of the vehicle according to the computed engine, aerodynamic, and gravitational forces. The numerical iterations are performed using a fourth-order Runge-Kutta routine with a time step of 0.005 seconds. Because this simulation describes the motion of the vehicle through translations along each of the three body axes as well as rotations about those axes, the simulation is termed a six-degree-of-freedom simulation.

CHAPTER 3

BOOST VEHICLE ROLL DYNAMICS DURING FIRST AND SECOND STAGE FLIGHT PHASES

3.1 Introduction

Thrust and aerodynamic forces acting on the boost vehicle can produce moments about all three body axes: roll, pitch, and yaw. The resulting angular accelerations about the pitch and yaw axes are large, but they are controlled through feedback. Although the angular acceleration produced about the roll axis is small, it is not directly controlled by the flight control system. Over the appreciable time intervals of the first and second stage flight phases, the accumulated effects of these roll accelerations can result in an unacceptably high roll rate.

In this chapter, the forces which can contribute to the applied roll torque are identified. This chapter also explores the conditions under which the applied forces will or will not contribute an increase in the roll rate. A simulation method is introduced to determine maximum roll rates produced under worst-case conditions along selected reference trajectories. It will be shown that when the vehicle is allowed to roll freely without any limits on the forces that produce roll moments, it is possible to exceed the specified roll rate limit.

3.2 Effect of Manufacturing Imperfections on Boost Vehicle Roll Dynamics

3.2.1 Offsets Caused by Manufacturing Imperfections

In order for an applied force to produce a roll torque, an offset must exist between the point of application and the vehicle's center of

gravity, in a direction normal to the force. In the boost vehicle there are two offsets which are created by manufacturing imperfections:

(1) Center of Gravity Offset

(2) Engine Hinge Point Offset

These two offsets, caused by inaccuracies in the construction of the solid rockets, are present in the vehicle at launch and throughout the boost flight. Thus, their effects on the roll motion of the vehicle must be understood.

Center of Gravity Offset

An offset may exist between the boost vehicle's center of gravity (cg) and the vehicle center line. The cg offset is a result of manufacturing imperfections and asymmetric packing of the propellant into the rocket booster. This offset cannot be accurately measured prior to flight, and may change as propellant is expelled from the rocket. The cg offset may also shift when the vehicle's mass properties change following stage separation. In this thesis, the small deterministic component of the cg offset is neglected; the cg offset is modelled as a two-dimensional random variable. The magnitude of the offset is represented by a Gaussian distribution with a 3σ value of 0.20 inches. The direction of the offset is represented by a uniform distribution over ± 180 degrees.

Engine Hinge Point Offset

An offset may exist between the engine hinge point and the vehicle center line. The engine hinge point offset results from inaccurate installation of the engine solid rocket booster. The engine hinge point offset is constant during the burn time of each stage, but can be expected to change when a new engine is ignited following stage separation. In this thesis, the hinge point offset is modelled as a two-dimensional random variable. The magnitude of the offset is represented by a Gaussian distribution with a 3σ value of 0.16 inches. The direction of the offset is represented by a uniform distribution over ± 180 degrees.

3.2.2 Relation Between Manufacturing Imperfections and Applied Roll Torques

During atmospheric flight, there are three places on the boost vehicle where applied forces can contribute to an applied roll torque on the body:

(1) Lateral engine forces act at the engine hinge point.

(2) Aerodynamic normal forces act effectively at the center of pressure.

(3) Aerodynamic normal forces act on the vehicle raceway.

The relations between these forces, the manufactured offsets, and the resultant roll torques will be discussed in the following subsections.

3.2.2.1 Lateral Engine Forces at Engine Hinge Point

When the engine nozzle deflects the thrust vector away from the X_B axis, a lateral thrust component is created. The lateral component of thrust exerts a force on the vehicle at the engine hinge point, as shown in Figure 3-1. If a lateral offset exists between the engine hinge point and the vehicle's center of gravity (cg), a torque is produced about the roll axis. Defining the coordinates of the engine hinge point and center of gravity in the Y_B-Z_B plane as two-dimensional vectors:

$$\bar{CG} = (CG_Y, CG_Z) \quad , \quad \bar{HNG} = (HNG_Y, HNG_Z) \tag{3.1}$$

the position of the hinge point in the Y_B-Z_B plane relative to the center of gravity can be defined as:

$$\bar{R}_{HNG} = \bar{HNG} - \bar{CG} \tag{3.2}$$

The torque produced by the lateral engine force is:

$$\bar{TORQ}_{ENG} = \bar{R}_{HNG} \times \bar{F}_{ENG} \tag{3.3}$$

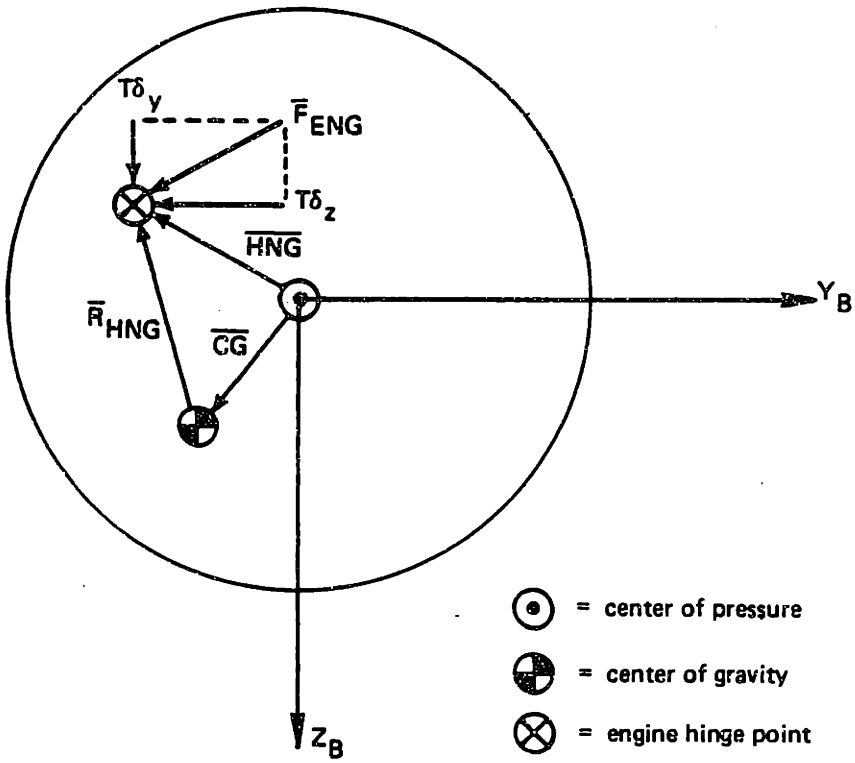

Figure 3-1. Engine forces in the Y_B-Z_B plane.

The roll component of $\bar{TORQ}_{ENG}$ is defined by the scalar equation:

$$ROLLTORQ_{ENG} = T\,\delta_Y\,R_{HNGY} + T\,\delta_Z\,R_{HNGZ} \qquad (3.4)$$

where T is the applied thrust, δ_Y and δ_Z are the components of the engine deflection about the body pitch and yaw axes, and R_{HNGY} and R_{HNGZ} are the Y and Z components of $\bar{R}_{HNG}$.

3.2.2.2 Aerodynamic Normal Forces at Center of Pressure

Neglecting the effects of the raceway, which will be considered separately, the vehicle is aerodynamically symmetric. Because of this

symmetry, the effective point of application of the aerodynamic normal force, termed the center of pressure (cp), lies on the vehicle centerline, as shown in Figure 3-2. If a lateral offset exists between the cg and the centerline, the aerodynamic normal force acting at the center of pressure will produce a roll torque. The vector $\overline{CP}$ defines the position of the center of pressure in the Y_B-Z_B plane:

$$\bar{CP} = (0, 0) \tag{3.5}$$

The position of the center of pressure in the Y_B-Z_B plane relative to the center of gravity can then be defined with the vector $\bar{R}_{CP}$:

$$\bar{R}_{CP} = \bar{CP} - \bar{CG} = -\bar{CG} \tag{3.6}$$

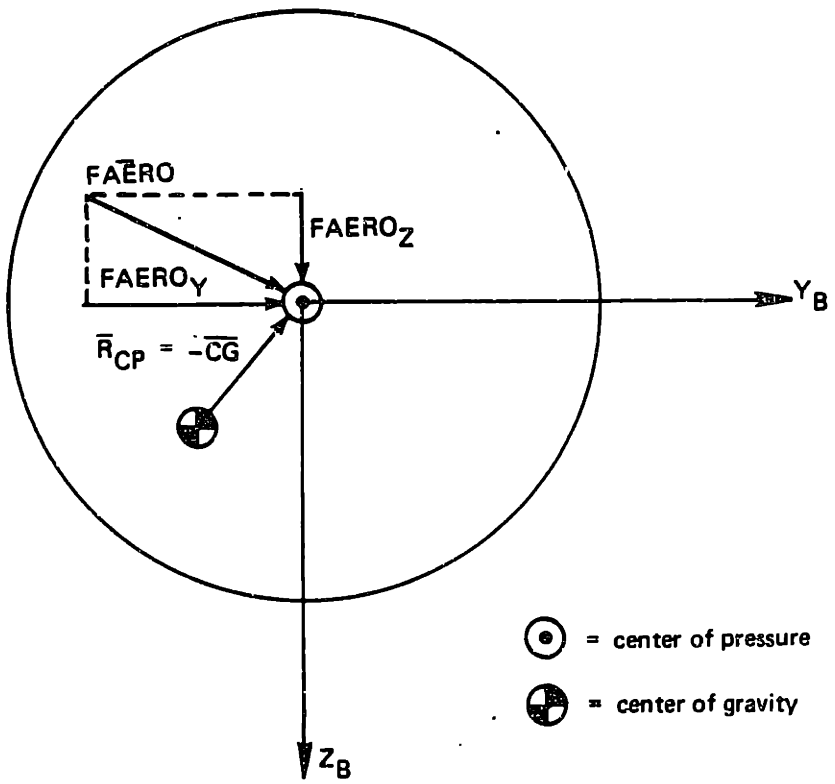

Figure 3-2. Aerodynamic forces in the Y_B-Z_B plane.

The torque produced by the lateral aerodynamic force is:

$$\bar{TORQ}_{AERO} = \ddot{\bar{R}}_{CP} \times \bar{FAERO} = -\overline{CG} \times \bar{FAERO} \qquad (3.7)$$

The roll torque is defined by the scalar equation:

$$ROLLTORQ_{AERO} = FAERO_Y \, CG_Z - FAERO_Z CG_Y \qquad (3.8)$$

3.2.2.3 Aerodynamic Normal Forces at Raceway

The aerodynamic normal force not only affects the translational and rotational motion of the boost vehicle, but also determines the flow of air around the vehicle. Since the raceway protrudes from the smooth surface of the vehicle, flow of air around the body exerts pressure on the raceway. This applied pressure causes the vehicle to roll, as shown in Figure 3-3. Wind tunnel testing has shown that the direction and magnitude of the pressure on a raceway can be accurately represented by a rolling moment coefficient, C_R. The rolling moment is a function of the Mach number, the total angle of attack, and the body angle between the raceway and the aerodynamic normal force. This body angle, ϕ_{CR}, is defined in Figure 3-3. Qualitative graphs of C_R versus Mach, α, and ϕ_{CR} are shown in Figure 3-4.

For a given value of C_R, the aerodynamic force acting on the raceway is defined as:

$$F_{RCWY} = C_R \, S \, Q \qquad (3.9)$$

Since the raceway is located at the outer surface of the booster, the roll torque produced by the aerodynamic force on the raceway is:

$$ROLLTORQ_{RCWY} = F_{RCWY} \, r_{BOOSTER} \qquad (3.10)$$

where $r_{BOOSTER}$ is the radius of the boost vehicle.

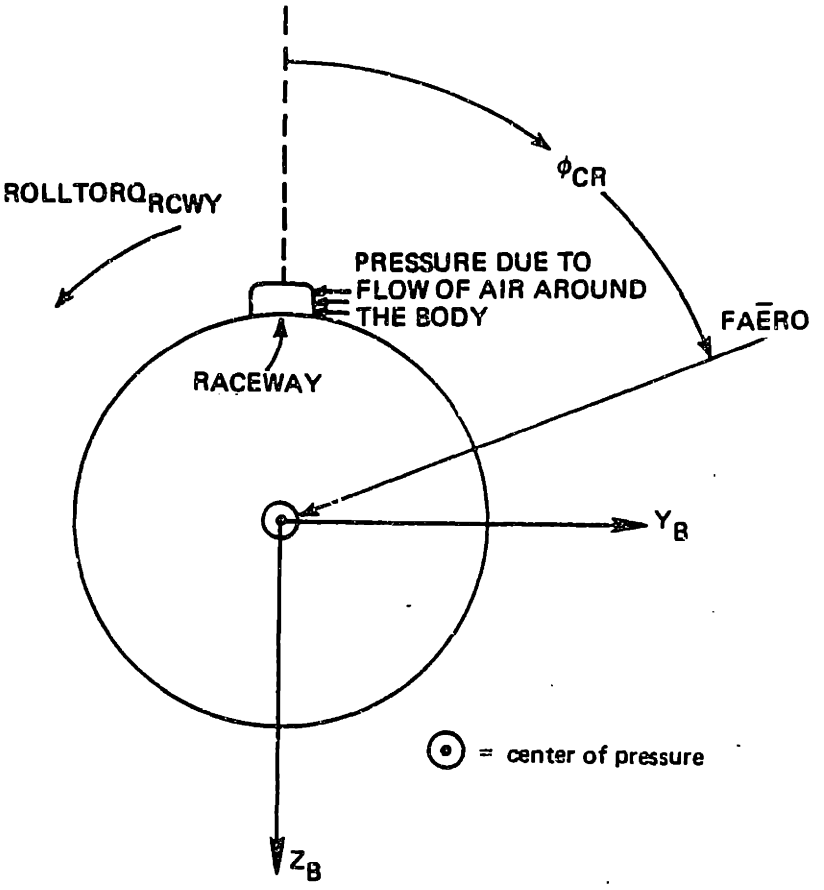

Figure 3-3. Aerodynamic forces at vehicle raceway.

3.2.2.4 Total Applied Roll Torque

At any given time, the total roll torque applied to the vehicle is the sum of the three roll torque components:

$$ROLLTORQ = ROLLTORQ_{ENG} + ROLLTORQ_{AERO} + ROLLTORQ_{RCWY} \quad (3.11)$$

The instantaneous roll angular acceleration of the vehicle is defined by:

$$\ddot{\phi} = \frac{ROLLTORQ}{I_X} \quad (3.12)$$

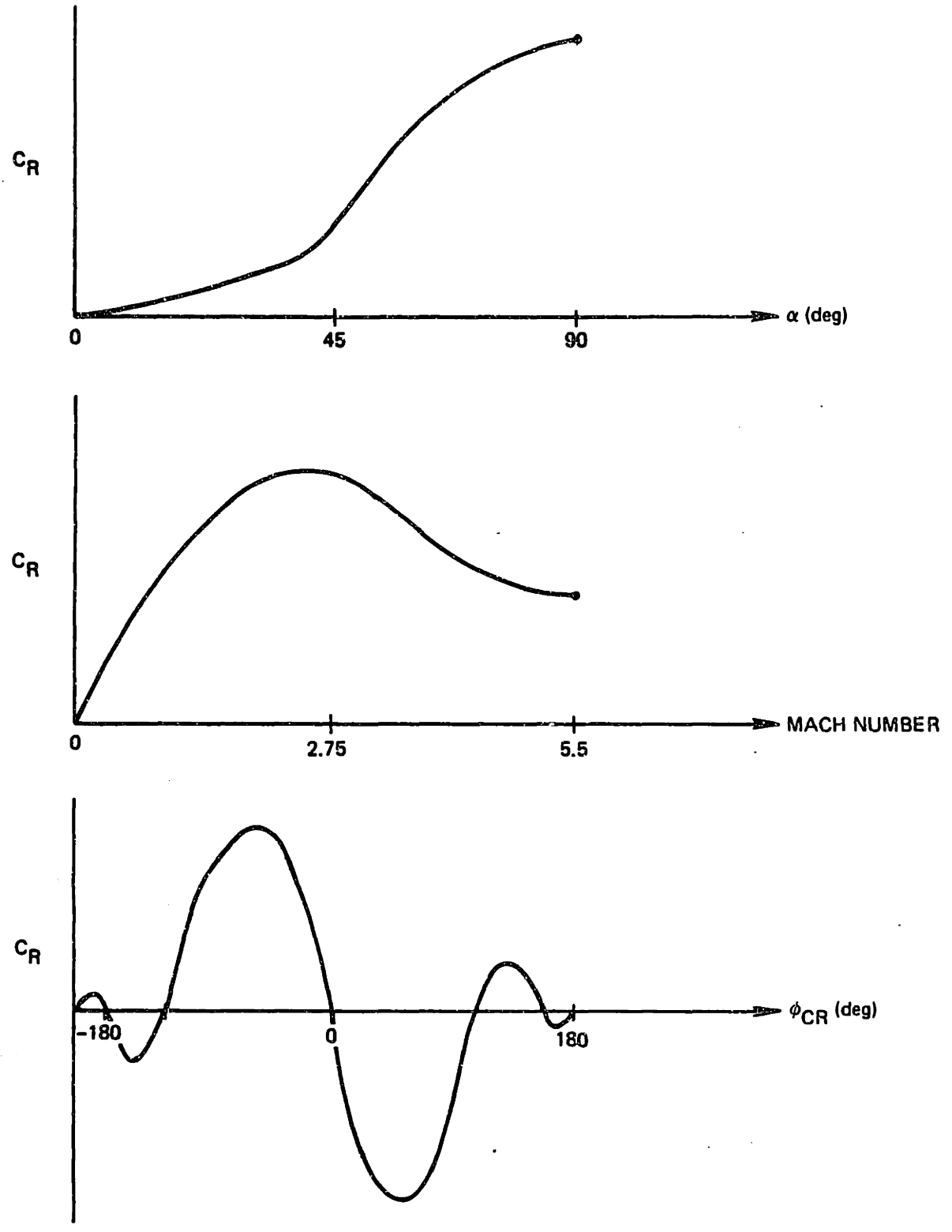

Figure 3-4. Qualitative graphs of C_R vs Mach, α, and ϕ_{CR}.

where I_X is the moment of inertia about the X_B (roll) axis. This definition implies that positive roll torque produces a positive angular acceleration.

3.2.3 Worst-Case Manufactured Booster Configuration

For the given models of the center of gravity and engine hinge point offsets, it is possible to specify the manufactured booster configuration which results in the largest applied roll torque. Since the magnitude of the applied roll torque is directly related to the magnitude of the vectors $\bar{R}_{CP}$ and $\bar{R}_{HNG}$, the largest roll torques will be caused by the largest offsets of the engine hinge point and center of gravity. Although it is highly improbable that 3σ offsets of both the hinge point and the cg would exist in the same boost vehicle, use of this combination provides a clear definition of the worst-case configuration. Assigning the cg offset its 3σ value of 0.20 inches, the worst-case magnitude of $\bar{R}_{CP}$ is 0.20 inches. Assigning the hinge point offset its 3σ value of 0.16 inches, and placing it on the opposite side of the vehicle center line from the cg, the worst-case magnitude of $\bar{R}_{HNG}$ is 0.36 inches.

It is also possible to specify the worse-case orientation of the cg and hinge point offsets relative to the vehicle raceway. To specify this orientation, it is important to realize that the autopilot commands the engine deflection to counter the aerodynamic normal force, balancing the moments on the vehicle. Therefore, in a steady state flight configuration, the thrust component in the Y_B-Z_B plane will be in the same direction as the aerodynamic normal force. If these forces, acting at the engine hinge point and the center of pressure, produce reinforcing roll torques in the same direction as the raceway roll torque, all three roll torque components will be "in phase", supplying the largest magnitude roll torque to the vehicle.

The worst-case manufactured vehicle configuration is shown in Figure 3-5. The vehicle model fixes the raceway on the $-Z_B$ axis. The worst-case location of the engine hinge point is then also on the

$-Z_B$ axis, so that both the hinge point and the raceway are at a maximum offset distance from the cg location. Note that in this configuration, the three components of the total roll torque ($ROLLTORQ_{ENG}$, $ROLLTORQ_{AERO}$, and $ROLLTORQ_{RCWY}$) are all of the same polarity.

3.3 Effect of Flight Conditions on Boost Vehicle Roll Dynamics

For a vehicle with given manufactured offsets, the applied roll torque at any given time during its flight is strongly related to two flight conditions:

(1) The roll orientation of the vehicle relative to the direction of the aerodynamic normal force

(2) The magnitude of the angle of attack

The roll orientation of the vehicle is not controlled during flight. The angle of attack is influenced by the first stage load relief system, and can by limited by constraining the trajectory plane steering during the second stage flight phase. It is important to understand the effects of both these flight conditions on the roll dynamics of the vehicle.

3.3.1 Angle of Attack

Referring to Section 3.2.2, all three components of the applied roll torque are produced by forces that are related to the angle of attack. When the vehicle develops an angle of attack, an aerodynamic normal force acts at the center of pressure. The magnitude of the aerodynamic normal force is directly related to the angle of attack:

$$FAERO_{NORM} \cong S\ Q\ CN_{\alpha}\alpha \qquad (3.13)$$

In order to balance the moments on the vehicle, the magnitude of the lateral engine force must equal the magnitude of the aerodynamic normal force times the ratio of their acting moment arms:

$$\left|\bar{F}_{ENG}\right| \cong \left|\bar{FAERO}\right| \frac{L_{CP}}{L_{CG}} \qquad (3.14)$$

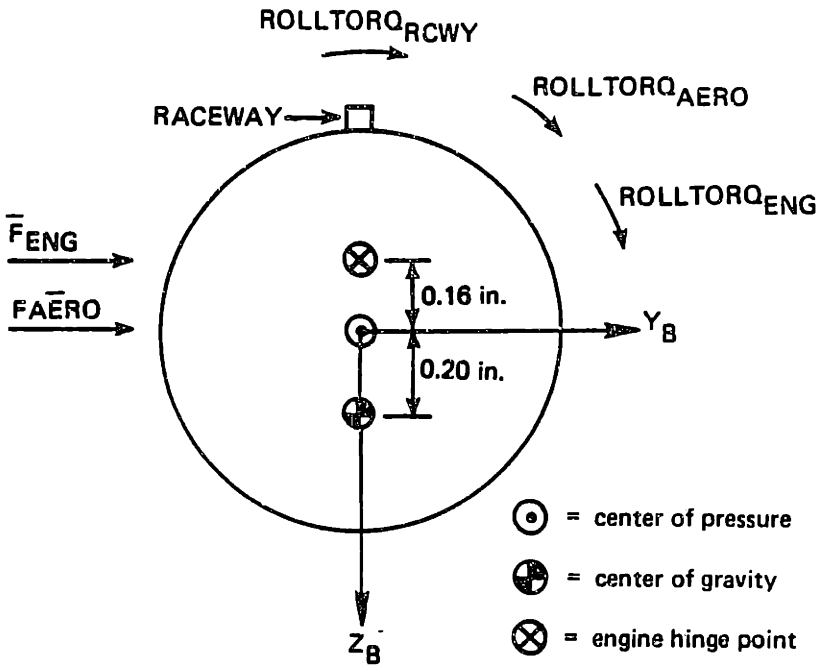

Figure 3-5. Worst-case manufactured vehicle configuration.

Thus, in the steady state, the magnitude of the lateral engine force is also proportional to the angle of attack.

Referring to Figure 3-4, notice that the magnitude of the raceway rolling moment coefficient, C_R, is also a function of the angle of attack. For a given Mach number and ϕ_{CR}, the magnitude of C_R increases with the angle of attack.

3.3.2 Roll Orientation

The forces applied to the vehicle in a non-zero angle of attack flight condition may or may not produce large roll torques, depending on the roll orientation of the vehicle. As developed in Section 3.2.2.4, the roll torque components ROLLTORQ$_{ENG}$ and ROLLTORQ$_{AERO}$ are produced by the cross-product of the applied forces and the offset distance between their points of application and the cg. For a given normal force direction, the magnitude of its cross-product with the vectors $\bar{R}_{HNG}$ and $\bar{R}_{CP}$ is dependent on the roll angle of the vehicle. Furthermore, the

raceway rolling moment coefficient, C_R, is a function of the angle between the raceway and the direction of the aerodynamic normal force, ϕ_{CR}.

As a demonstration of the effect of roll orientation on the applied roll torque, Figure 3-6 shows the boost vehicle subjected to a normal aerodynamic force and a compensating lateral engine force at a specified point along its trajectory. In Figure 3-6(a), the vehicle roll angle, ϕ, is 180 degrees, and the normal forces act along the vehicle $-Y_B$ axis. This roll orientation results in a large roll acceleration produced by all three roll torque components. Note, however, that the polarity of the roll acceleration is now opposite the roll acceleration produced by the same forces shown in Figure 3-5. In Figure 3-6(b), the vehicle roll angle is 90 degrees, and the normal forces act along the $-Z_B$ axis. In this roll orientation, the applied forces are parallel to the offset vectors $\bar{R}_{CP}$ and $\bar{R}_{HNG}$, the cross product of the forces with the offset vectors is zero, and so $ROLLTORQ_{ENG}$ and $ROLLTORQ_{AERO}$ are equal to zero. Furthermore, the raceway is "hidden" from the aerodynamic normal force by the vehicle body, so that no roll torque is produced by flow of air past the raceway.

3.4 Single-Degree-of-Freedom Roll Simulation

The roll motion of the vehicle in each flight phase is a function of its roll conditions at the beginning of that flight phase. For a given set of initial conditions, an initial roll torque will cause a change in the vehicle roll angle and roll rate, which will then, in turn, effect a change in the applied roll torque. Small changes in the initial roll conditions of the vehicle can yield large differences in the roll motion of the vehicle. As an example of this phenomenon, Figure 3-7 shows how the vehicle roll rate and roll angle at I/II stage separation are affected by the roll angle at the beginning of the first stage flight phase, assuming an initial roll rate of 10 deg/sec. In each of 36 successive simulations, the vehicle flew the same trajectory, but the

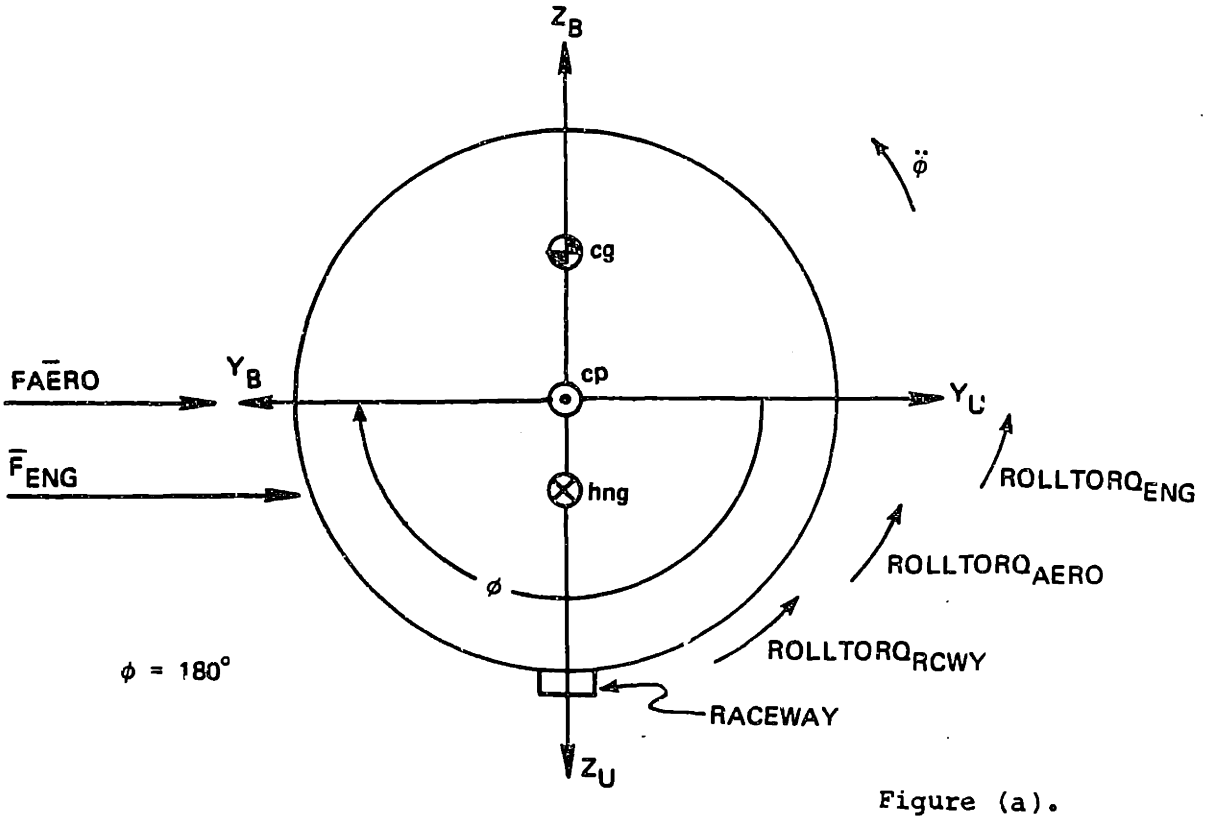

Figure (a).

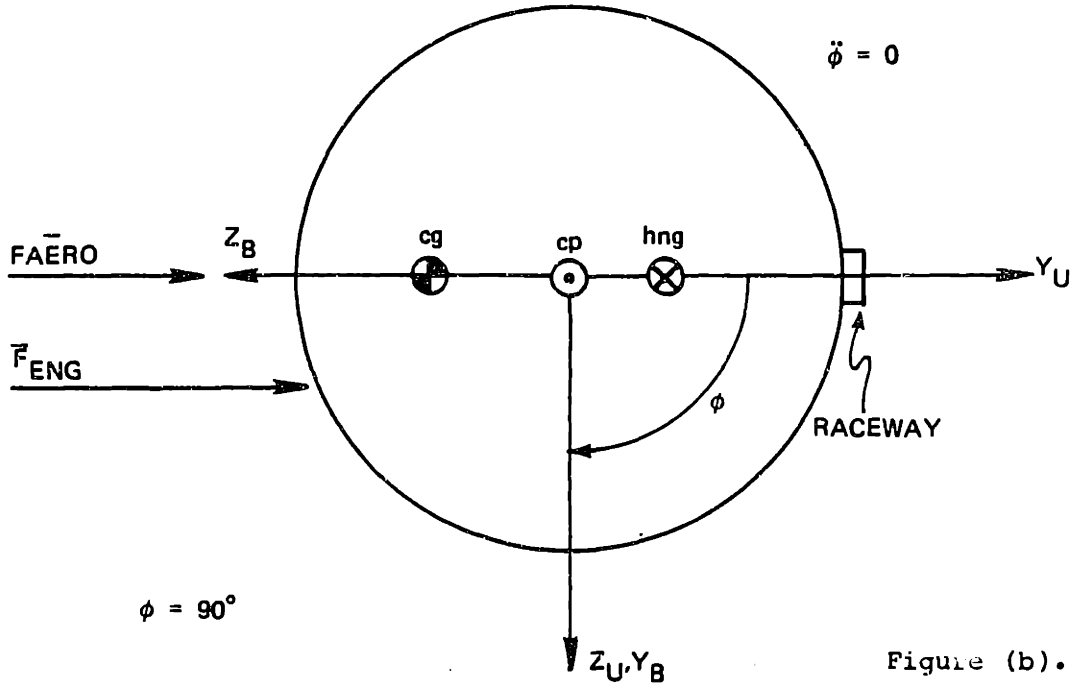

Figure (b).

Figure 3-6. Effect of roll angle on the applied roll torque.

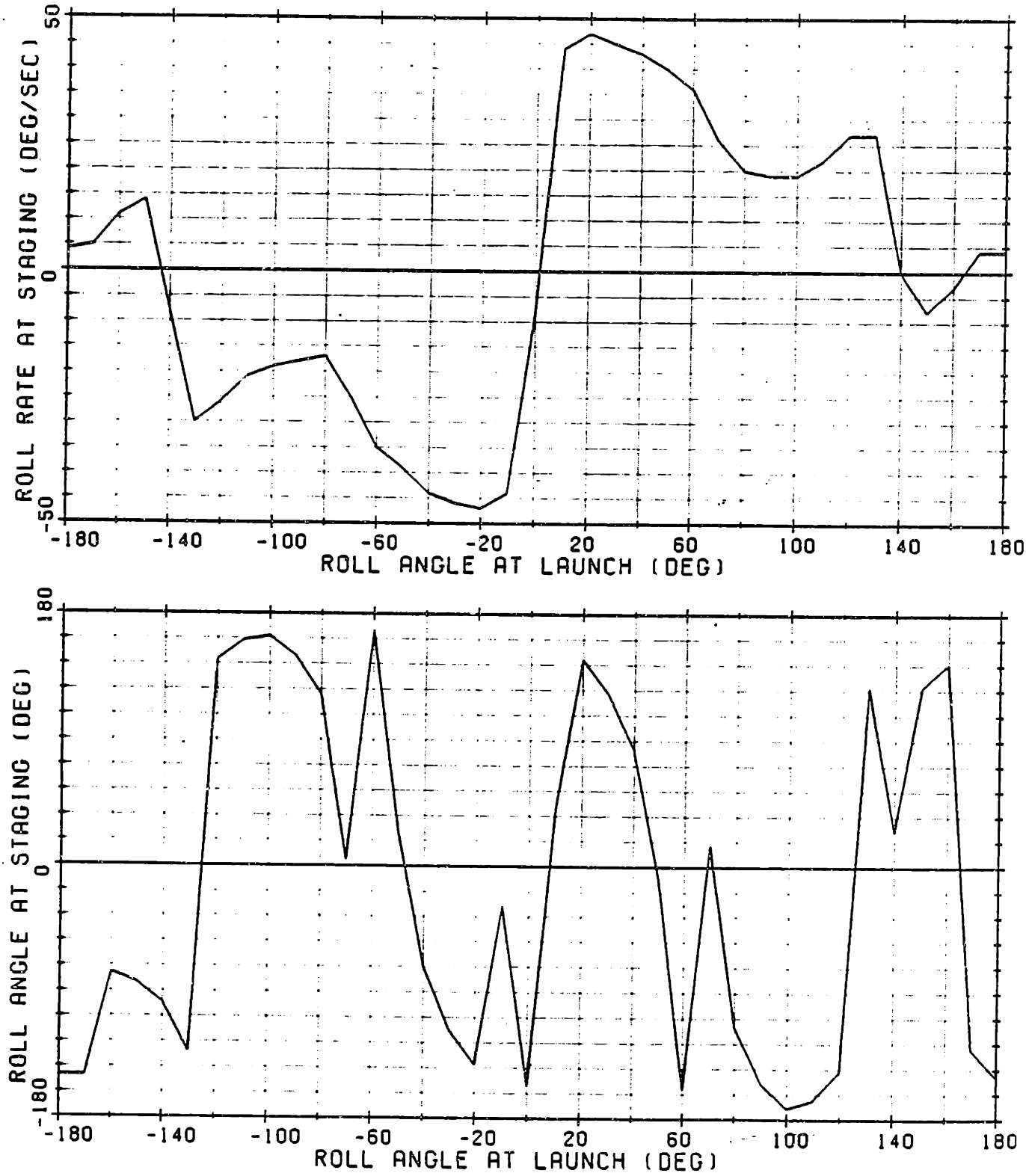

Figure 3-7. Roll angle and roll rate at I/II staging vs initial roll angle.

initial roll angle was changed by 10 degrees. Note that a small change in the initial roll angle from 0 to 10 degrees produced a large change in the staging roll rate, from -10 to 40 degrees/sec.

Generating the data required for Figure 3-7 is very time consuming and very costly if a six-degree-of-freedom simulation is used. To permit more efficient analysis of the roll dynamics of the boost vehicle, a single-degree-of-freedom roll simulation has been developed. This simulation, developed by J. F. Dailey at CSDL, can be used to perform a set of roll simulations under a variety of initial conditions. Instead of repeatedly simulating the translational motion of the vehicle along the same trajectory, the simulation saves the unrolled coordinate frame time histories of the applied forces that affect the vehicle roll rate. These time histories can then be applied along the rotating body axes generated by the roll simulation. For more information on this simulation, consult Dailey [4]. The roll simulation allows the programmer to specify ranges of values for the following four input parameters:

(1) Initial Roll Angle
(2) Initial Roll Rate
(3) Center of Gravity Offset
(4) Engine Hinge Point Offset

In this thesis, the single-degree-of-freedom roll simulation is used to find conditions that produce large roll rates in both the first and second stage flight phases.

3.5 Simulation Results

3.5.1 Six-Degree-of-Freedom Reference Trajectories

The three trajectories shown in Figure 3-8 were generated using the complete vehicle model and six-DOF simulation described in Chapter 2. These three trajectories will be referenced often as points of comparison for roll rate studies and trajectory shaping results in later

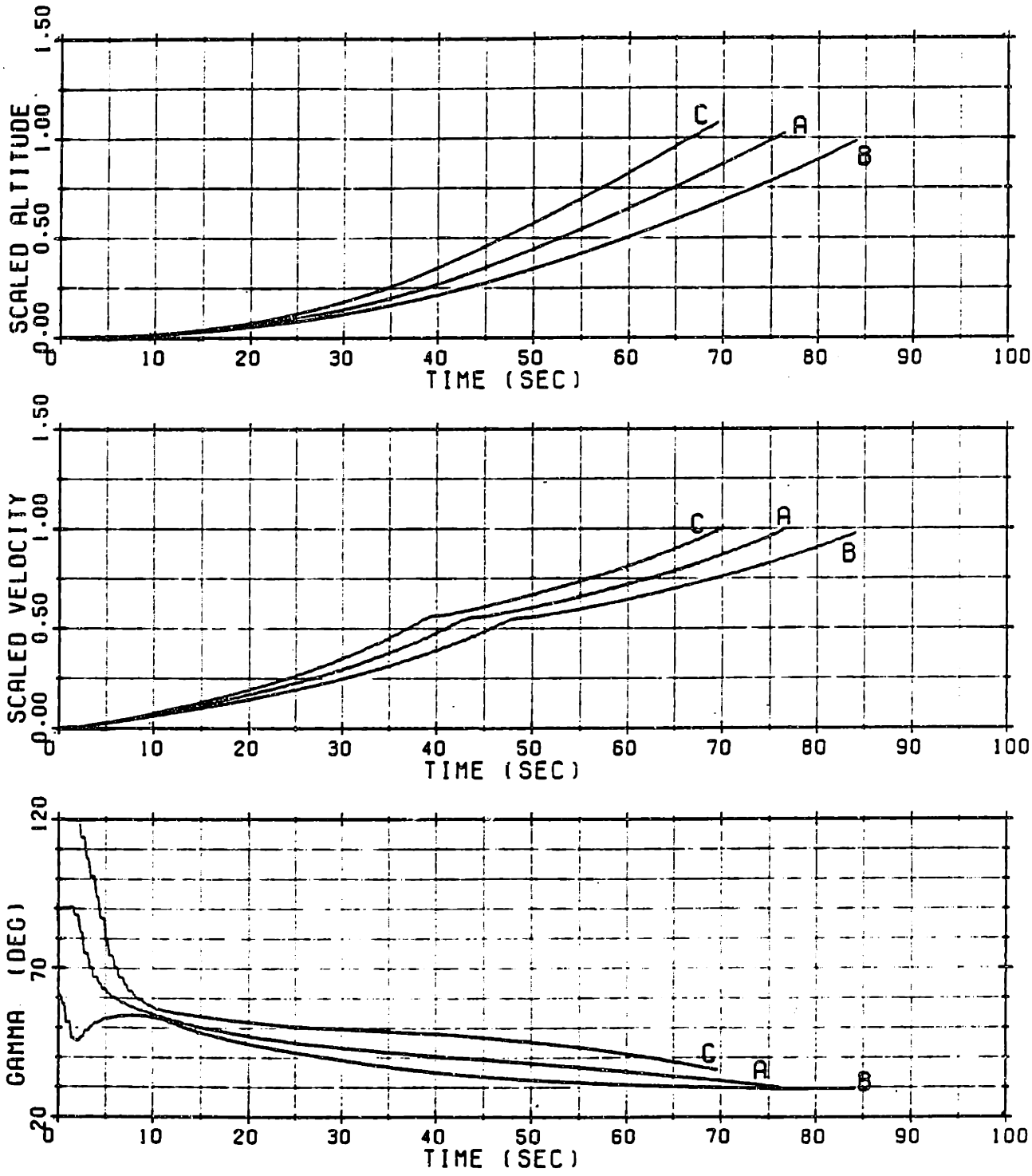

Figure 3-8. Profiles of altitude, velocity, and flight path angle along three reference trajectories.

chapters of this thesis. The first trajectory was chosen to represent the nominal boost trajectory under ideal conditions. The other two trajectories, based on high and low thrust values with corresponding worst-case winds and launch angles, were chosen to illustrate the bounds within which all other off-nominal trajectories would be encompassed. All three trajectories were commanded by the steering algorithms discussed in Chapter 2, under the assumption that these algorithms had received a perfect estimate of the thrust level.

Trajectory A in Figure 3-8 was generated with a launch angle of 90 degrees, the nominal thrust level ($\lambda = 1.0$), and no winds. Note that altitude and velocity are plotted as normalized variables, with 1.0 being the altitude and velocity along Trajectory A at the end of the second stage flight phase.

Trajectory B in Figure 3-8 was generated with a launch angle of 61 degrees, a low thrust level ($\lambda = 0.9$), and a 99% headwind spike in the region of maximum dynamic pressure. This trajectory was selected to illustrate the lowest, or most depressed, trajectory the vehicle could follow. Because the low thrust rocket has a longer burn time, the steering algorithms command the vehicle along a more shallow flight path angle history to reach the desired dynamic pressure at I/II staging. In addition, the headwind spike forces the vehicle to rotate into the wind, depressing the trajectory even further.

Trajectory C in Figure 3-8 was generated with a launch angle of 119 degrees, a high thrust level ($\lambda = 1.10$), and a 99% tailwind spike in the region of maximum dynamic pressure. This trajectory was selected to illustrate the highest, or most lofty, trajectory that the vehicle could follow. Because the high thrust rocket has a shorter burn time, the steering algorithms command the vehicle to fly a more inclined flight path angle history to reach the higher atmosphere and the desired dynamic pressure at I/II staging. In addition, the tailwind spike forces the vehicle to rotate toward the wind, lofting the trajectory even further.

Figures 3-9, 3-10, and 3-11 show the time histories of the dynamic pressure, the pitch angle of attack, and the aerodynamic loading factor

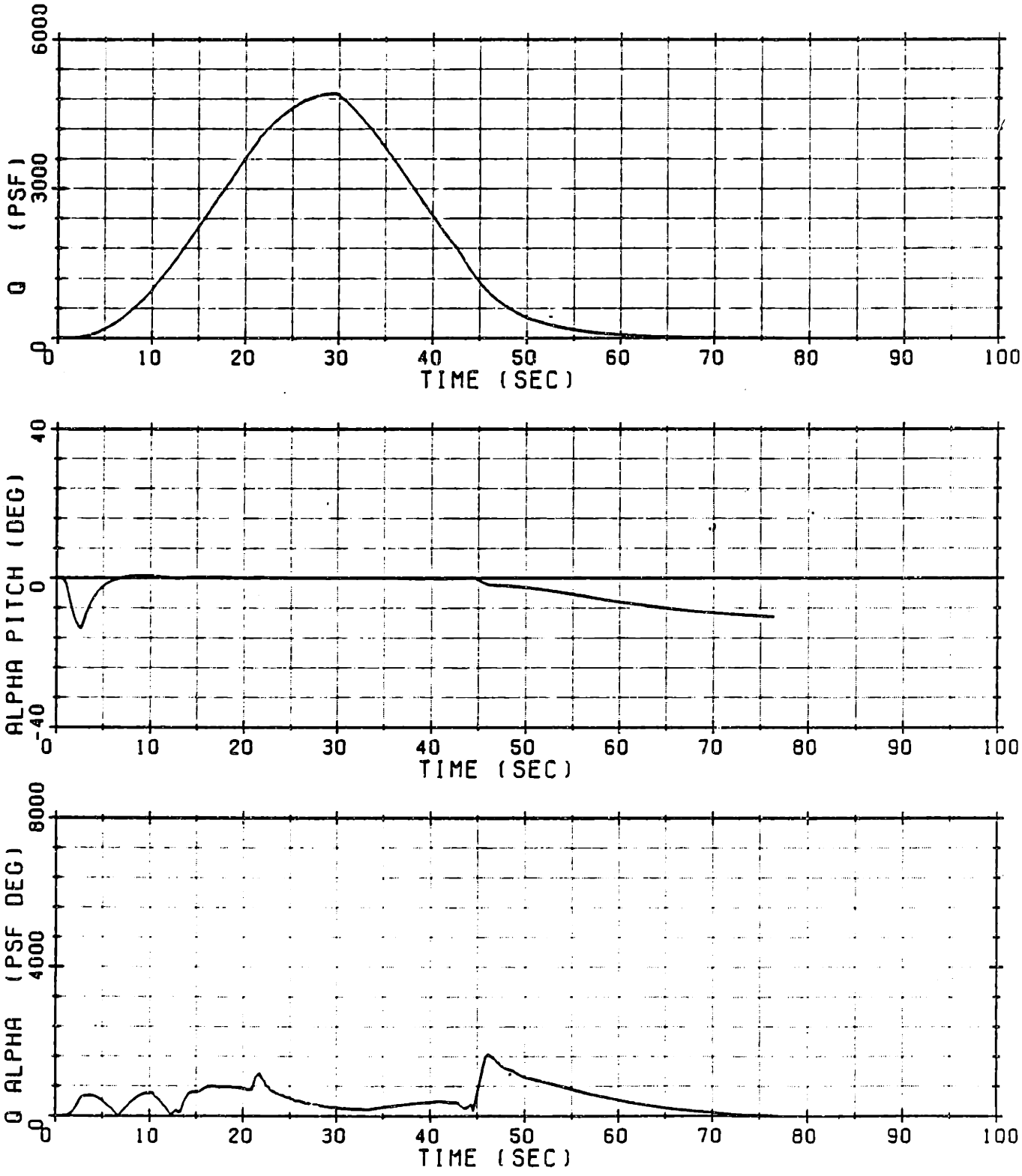

Figure 3-9. Profiles of Q, α, and $Q\alpha$ for Trajectory A.

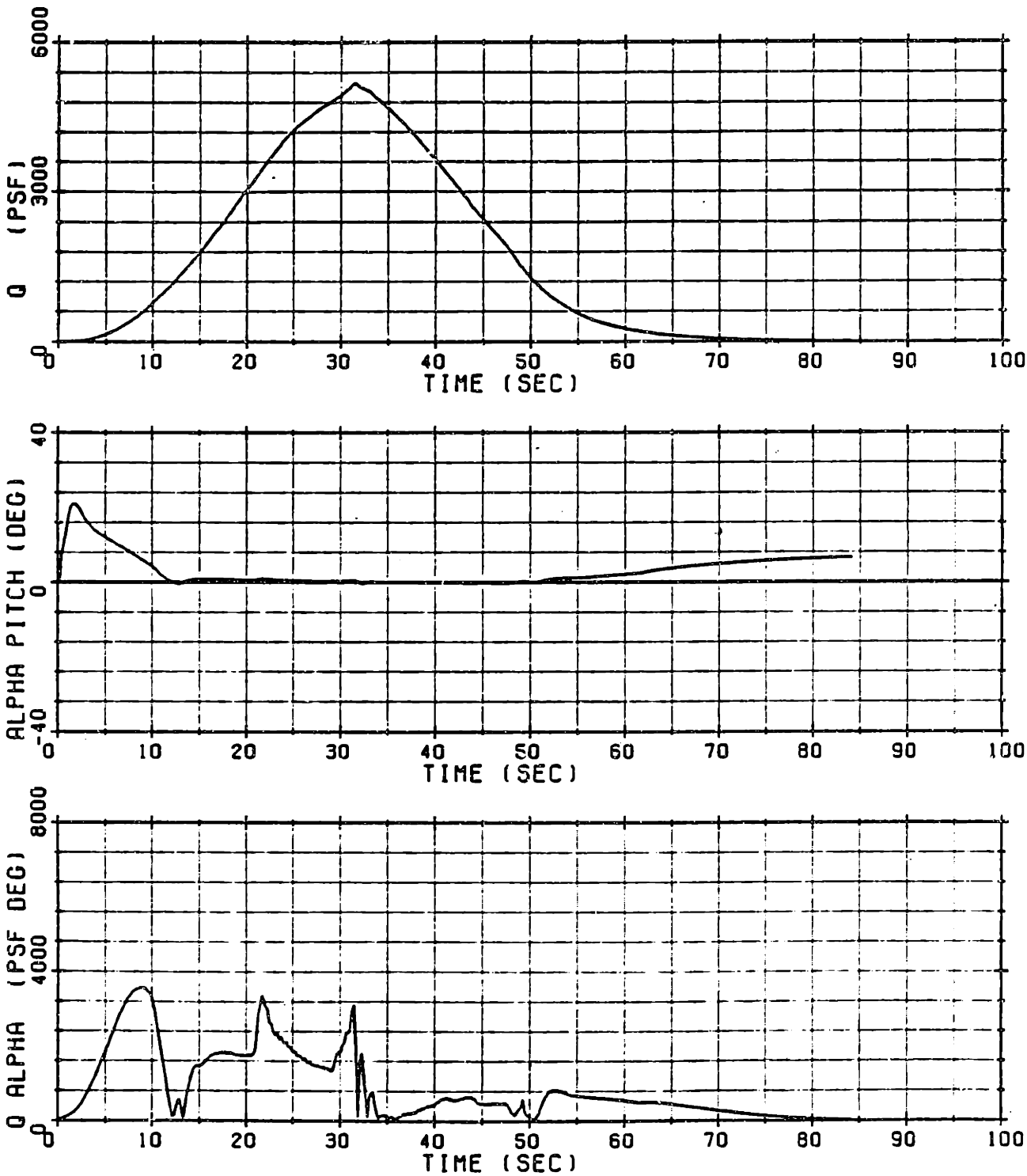

Figure 3-10. Profiles of Q, α, and $Q\alpha$ for Trajectory B.

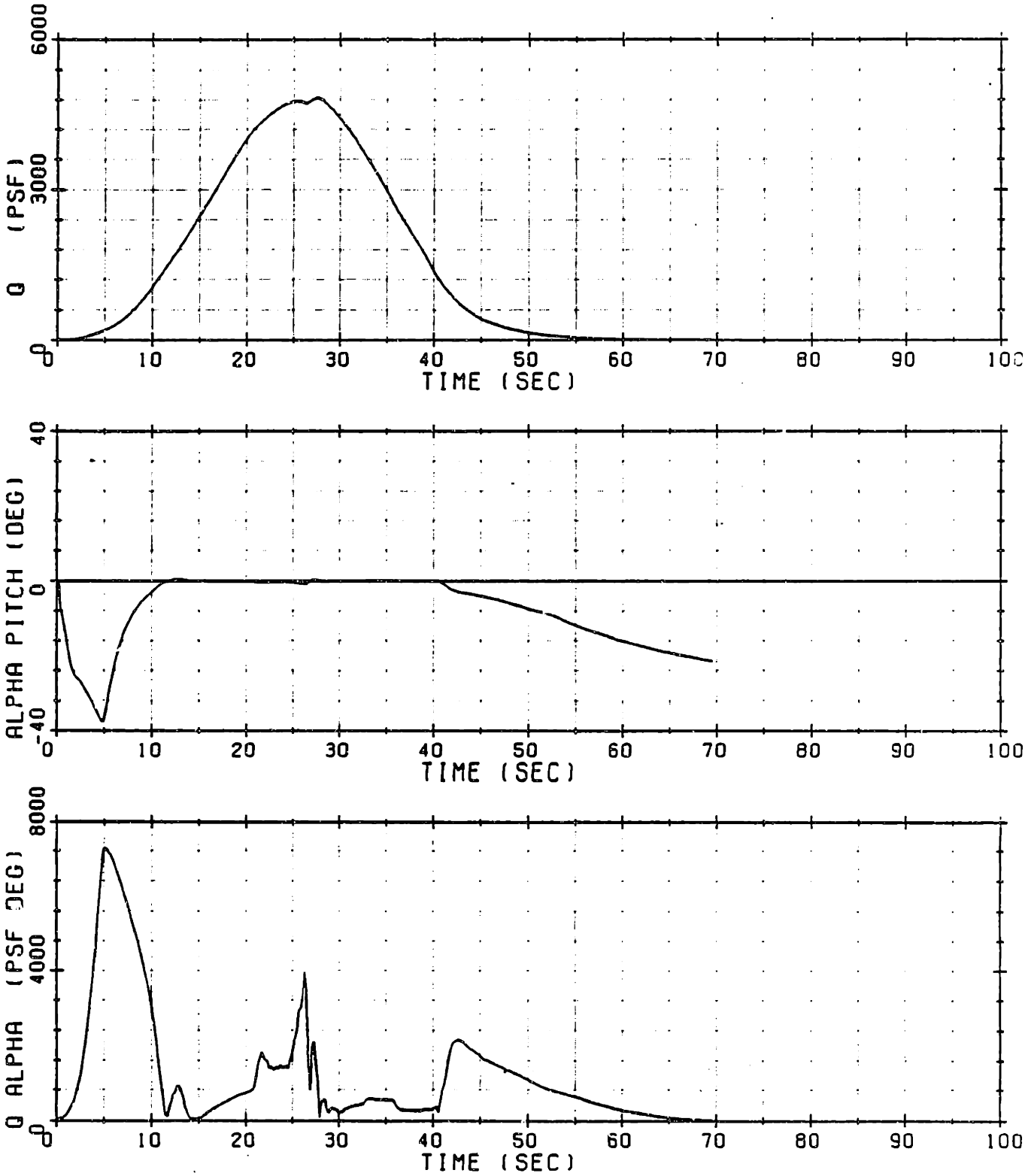

Figure 3-11. Profiles of Q, α, and Qα for Trajectory C.

$Q\alpha$ along the three reference trajectories. Note that the high thrust trajectory has the largest angle of attack during the kick maneuver, since it requires the largest rotation between the launch angle and the commanded kick angle. This large angle of attack also causes the high thrust trajectory to produce the largest $Q\alpha$ product of any of the trajectories. The high thrust trajectory also produces the largest angle of attack during the second stage flight phase, because the vehicle must develop a negative angle of attack to apply more thrust in the horizontal (downrange) direction.

The low thrust trajectory develops a positive angle of attack during the second stage flight phase. Following the depressed first stage trajectory, the vehicle must apply more thrust in the vertical direction to reach the desired II/III staging altitude.

Table 3-1 presents a summary of the pertinent flight data along the three reference trajectories. It is interesting to note that the nominal thrust profile produces a slightly larger velocity magnitude at the end of the second stage flight phase than either of the other trajectories. This is due to the fact that the high thrust profile wastes some ΔV capability maneuvering in the second stage, and the low thrust profile loses more velocity to gravity and drag forces over its longer burn time.

3.5.2 Roll Simulation Results for Reference Trajectories

For the three reference trajectories, the time histories of the forces on the vehicle were stored in unrolled axes, and a study was performed using the roll simulation procedure. The roll simulation searched for initial conditions which yield the highest roll rates during the first and second stage flight phases.

First, a roll rate study was performed to verify the worst-case vehicle offset configuration discussed in Section 3.2.3. Along the high thrust trajectory (Trajectory C), the roll simulation was performed for a variety of cg and engine hinge point offsets. The roll simulation was repeated for all possible initial roll angles until the highest Stage I

Table 3-1. Trajectory data for 3 reference trajectories.

Trajectory		t (sec)	$\bar{h}$ (nd)	$\bar{v}$ (nd)	γ (deg)	Q (psf)
LAUNCH						
	A	0	0	0.007	90	0
	B	0	0	0.007	61	0
	C	0	0	0.007	119	0
I/II STAGING						
	A	44.24	0.335	0.561	39.84	1342
	B	49.11	0.324	0.560	32.78	1506
	C	40.26	0.336	0.553	47.62	1323
II/III STAGING						
	A	76.52	1.000	1.000	30.26	0
	B	84.70	0.966	0.991	29.56	0
	C	69.79	1.040	0.987	34.97	0

roll rate was found for the given cg and engine hinge point offsets. Figure 3-12 shows the worst-case roll rate as a function of the cg offset magnitude, with the engine hinge point equal to zero. Note that for a given cg offset magnitude, higher roll rates are produced if that offset is along the Z_B axis, as was predicted in Section 3.2.2. Figure 3-13 shows the worst-case roll rate as a function of the cg and hinge point offsets along the Z_B axis, with CG_Y and HNG_Y equal to zero. For a given value of CG_Z, higher roll rates are produced if the engine hinge point offset is equal to its maximum value of 0.16 inches.

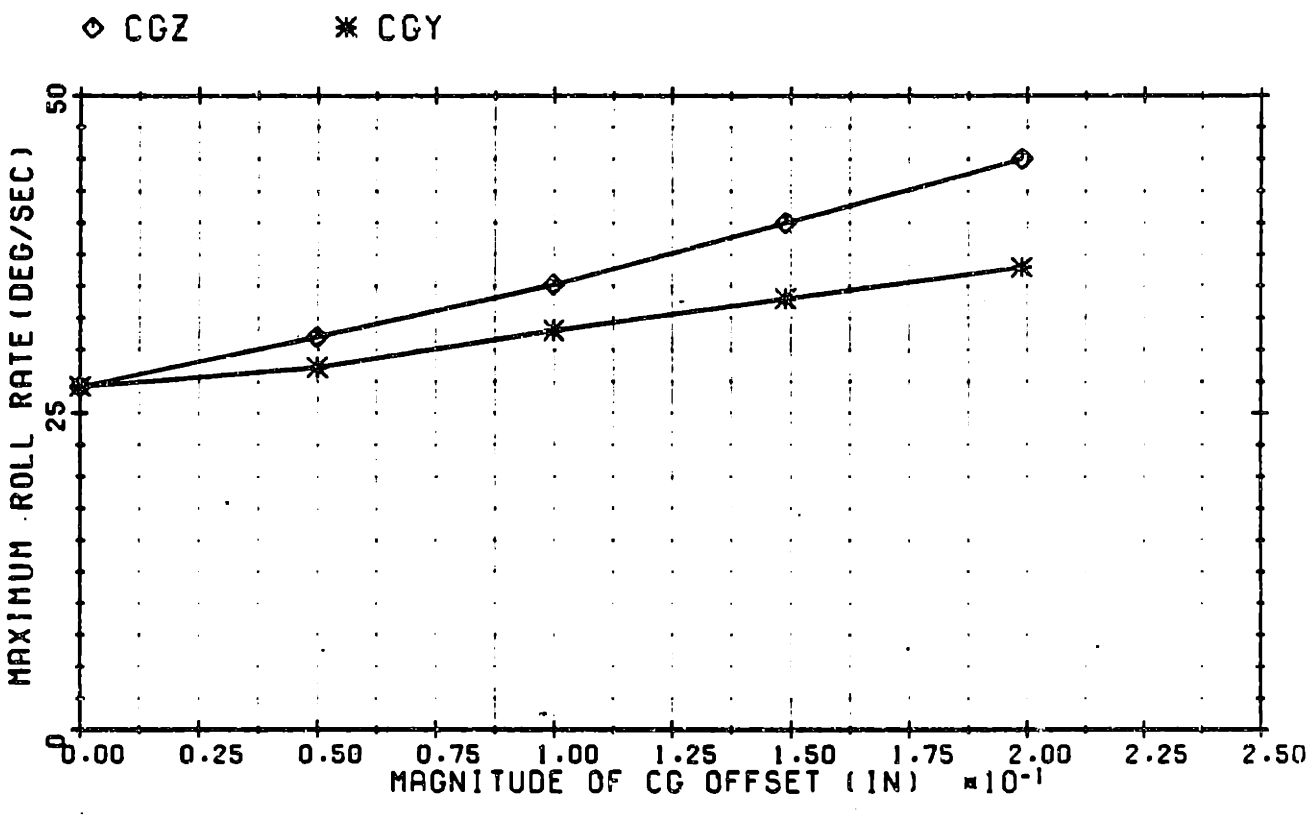

Figure 3-12. First stage worst-case maximum roll rate vs Y_B- and Z_B-axis cg offsets.

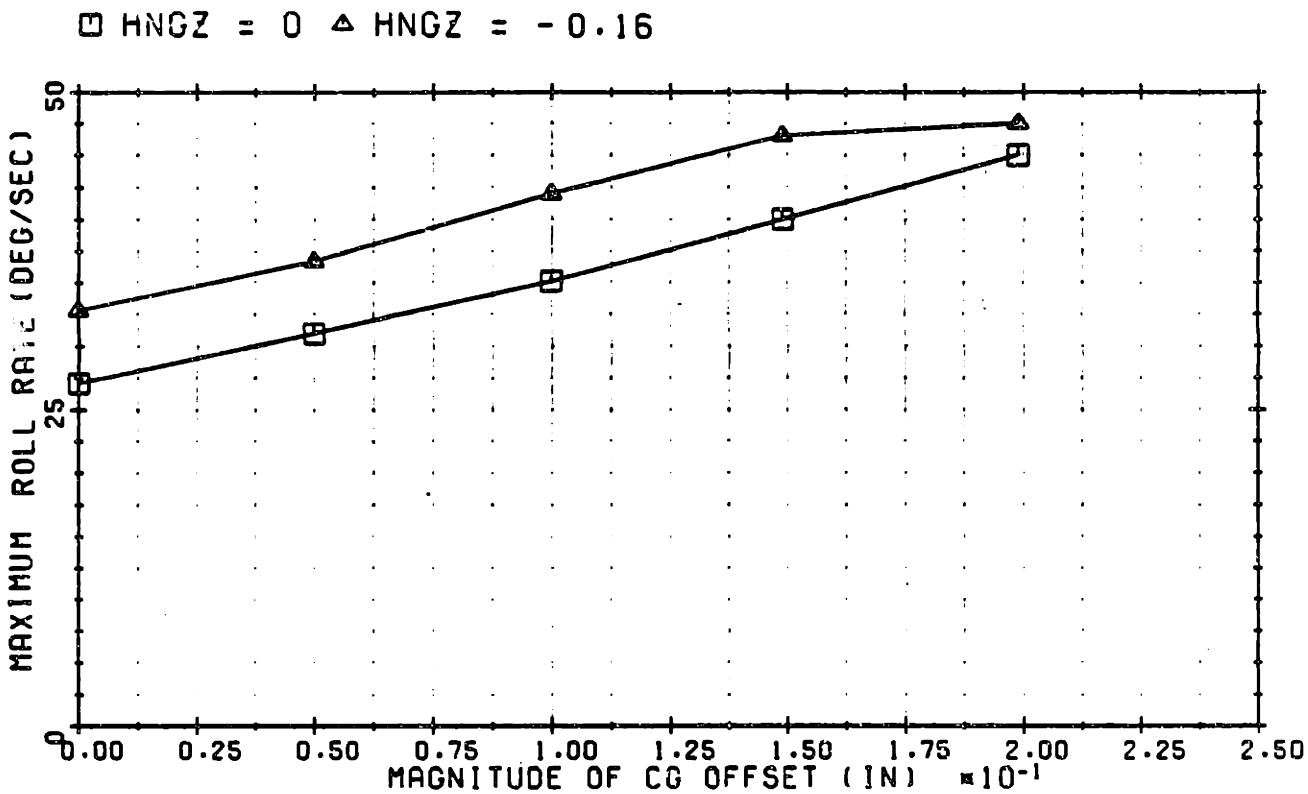

Figure 3-13. First stage worst-case maximum roll rate vs Z_B-axis cg and hinge point offsets.

Examination of both Figures 3-12 and 3-13 shows that even if the boost vehicle has no lateral offsets of the cg and hinge point relative to the vehicle centerline, it is possible to achieve a roll rate of almost deg/sec in the first stage. If the cg and engine hinge point are perfectly centered, then $ROLLTORQ_{ENG}$ and $ROLLTORQ_{AERO}$ are equal to zero, and this roll rate increase is due solely to aerodynamic forces acting on the raceway.

Next, a study was performed to determine the largest first stage roll rate as a function of the initial roll rate. This study assumed the previously described worst-case vehicle offsets (CG_Z = 0.20", HNG_Z = -0.16"), and varied the initial roll rate from zero to the maximum specified value of 10 deg/sec. Figure 3-14 shows the results of this study. For all three trajectories, high initial roll rates produce high maximum roll rates during flight. Note that the highest first stage roll rates are produced by Trajectory C. For this trajectory, an initial roll rate of 10 deg/sec can result in the maximum allowable roll rate of 50 deg/sec in the first stage.

Finally, a study was performed to find the maximum second stage roll rates as a function of the roll rate at I/II stage separation. Figure 3-15 shows the results of this study along all three trajectories. Once again, higher roll rates at the beginning of the flight phase yield higher maximum roll rates during the flight phase. The highest maximum roll rates are again found along the high thrust trajectory. The interesting fact to notice in this study is that the larger the roll rate at stage separation, the shorter the time until the maximum roll rate occurs following staging. For Trajectory C, an initial roll rate of 50 deg/sec can lead to a maximum roll rate of 64 deg/sec only 4.2 seconds after stage separation.

To allow further insight into the previous studies, Figures 3-16, 3-17, and 3-18 show typical roll rate profiles for a boost vehicle with worst-case offsets along each of the three reference trajectories. The second group of plots in each figure shows the three roll torque components, as well as their sum, the net roll torque. Since the vehicl

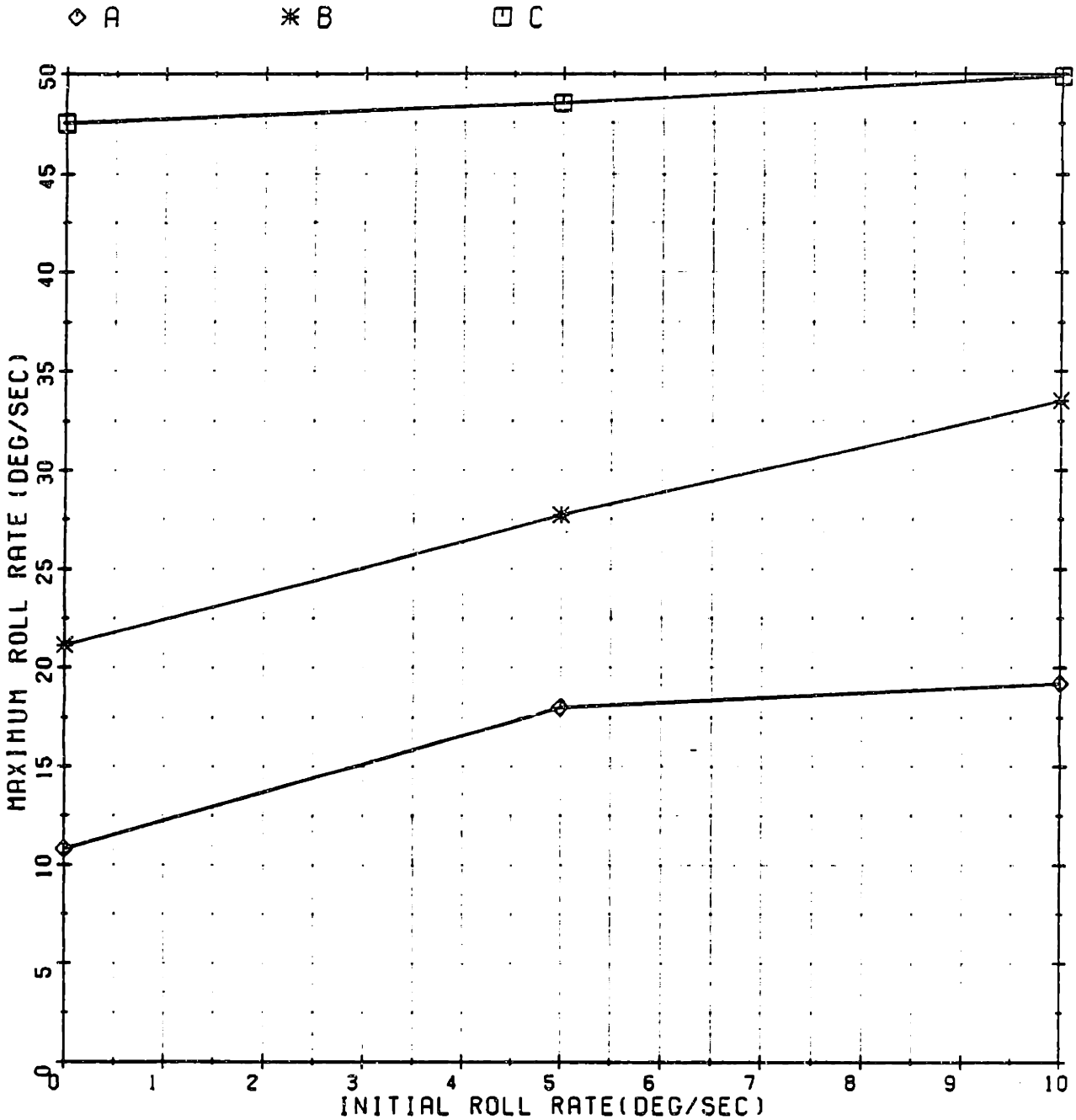

Figure 3-14. First stage worst-case maximum roll rate vs initial roll rate.

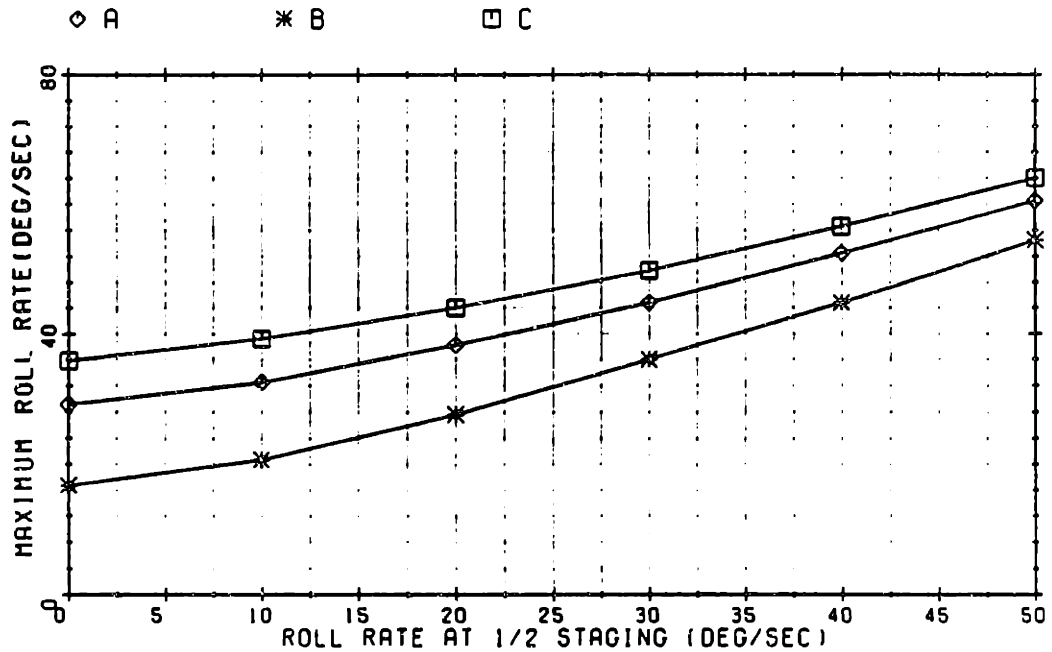

ROLL RATE STUDY

TIME TO MAX STAGE 2 ROLL RATE. 3 TRAJECTORIES

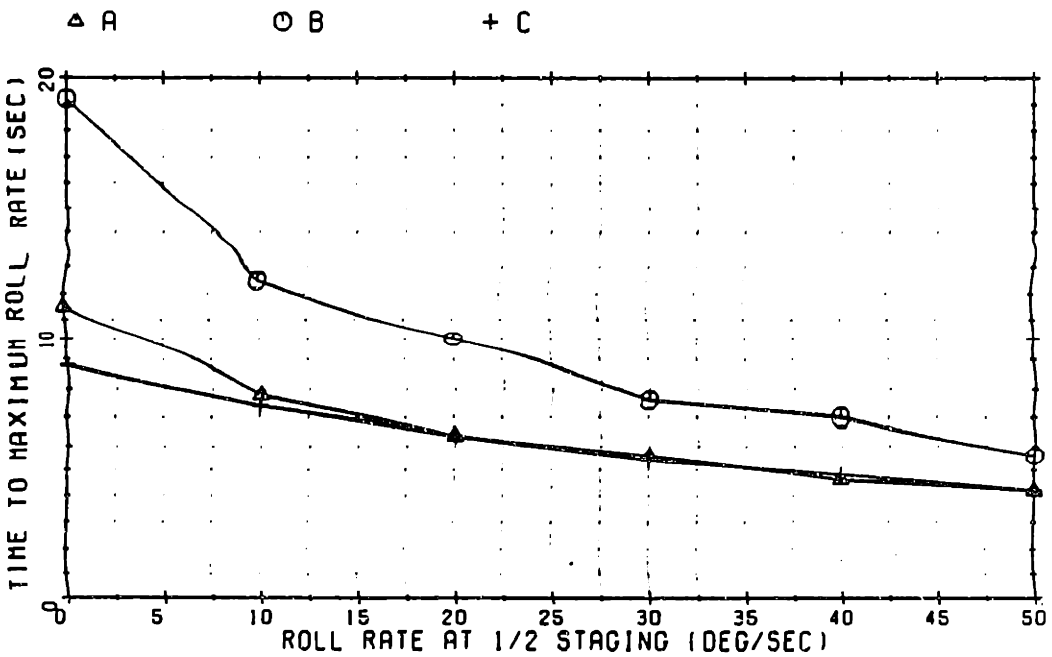

Figure 3-15. Second stage worst-case maximum roll rate vs I/II staging roll rate.

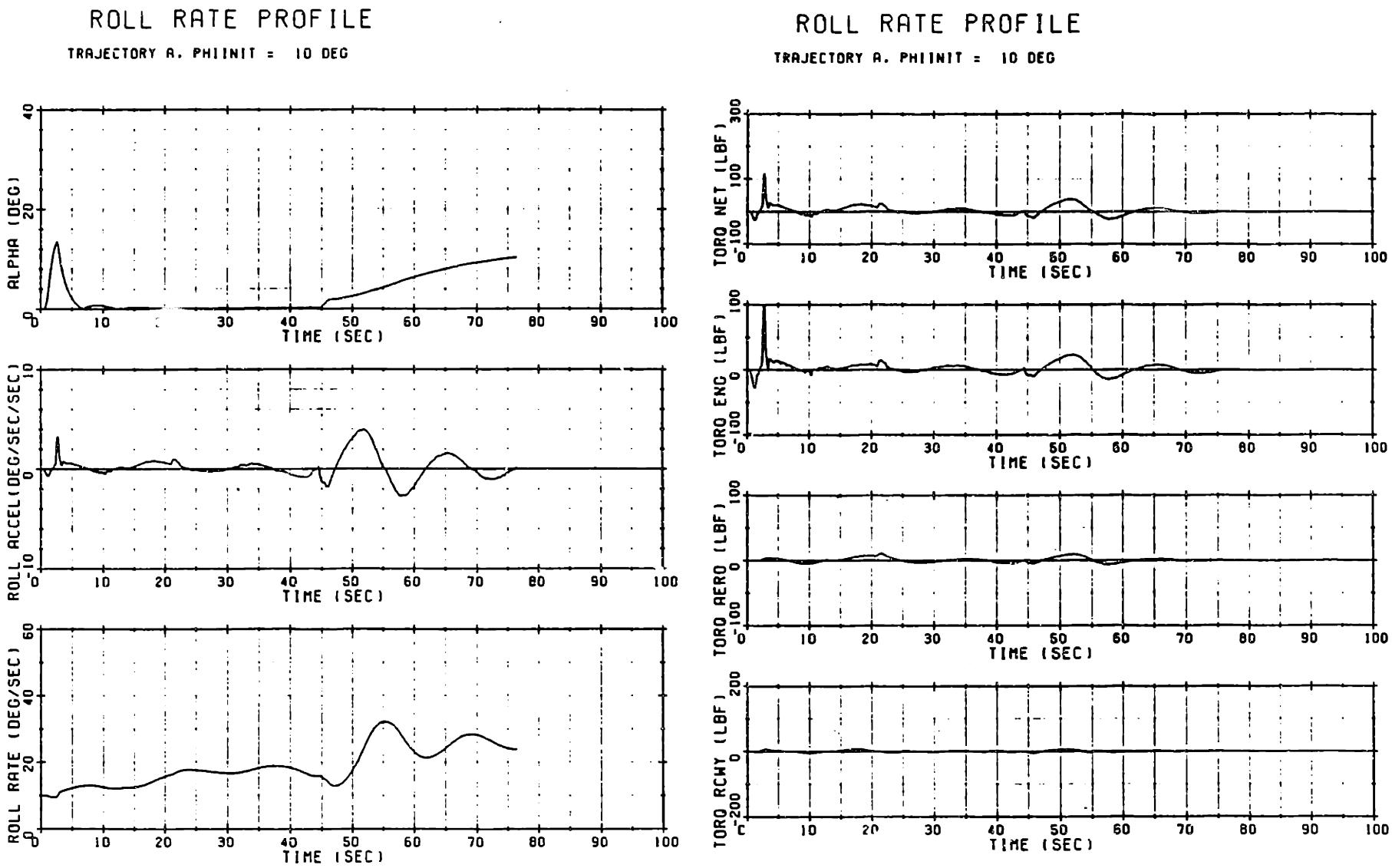

Figure 3-16. Roll rate profile, Trajectory A.

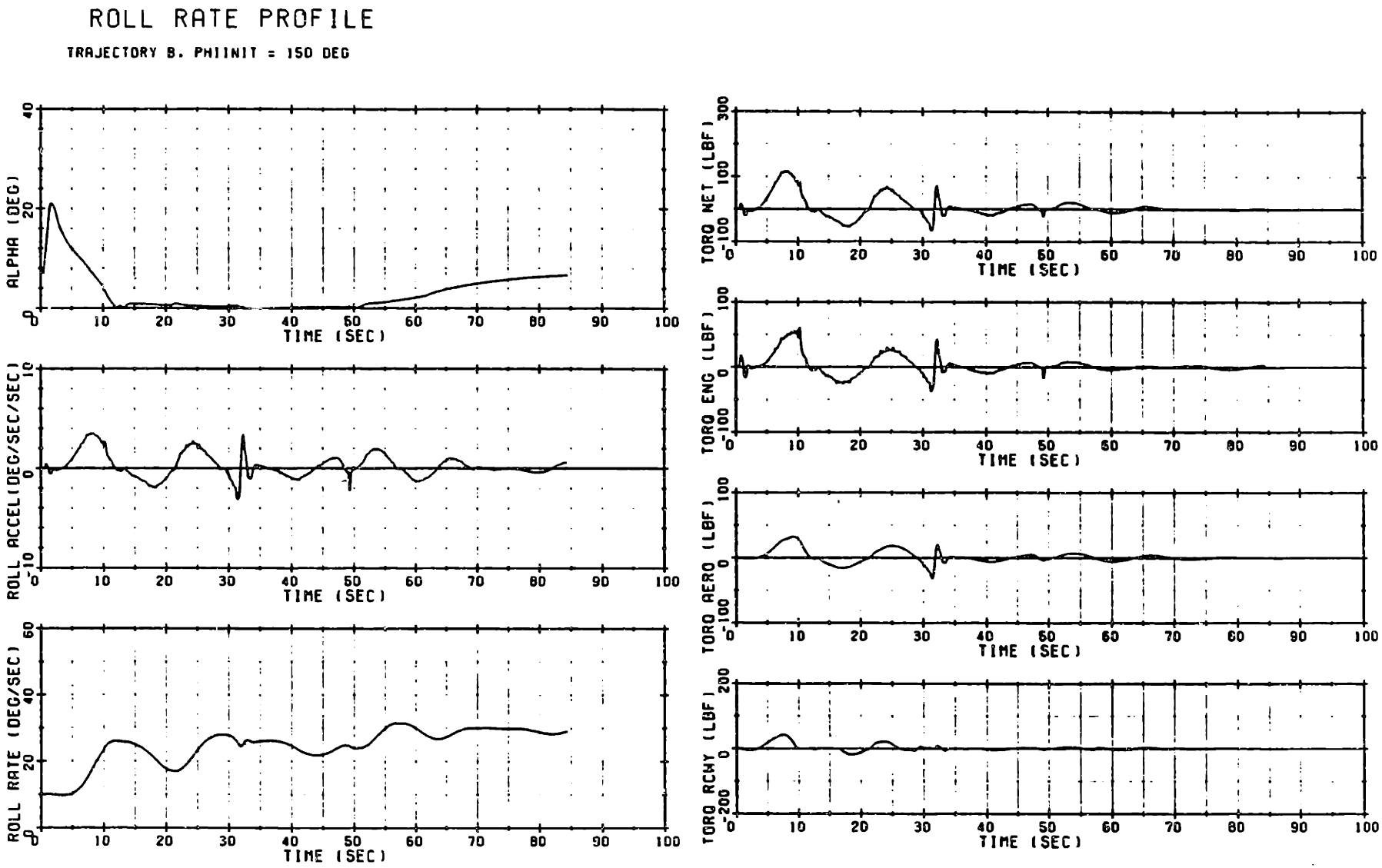

Figure 3-17. Roll rate profile, Trajectory B.

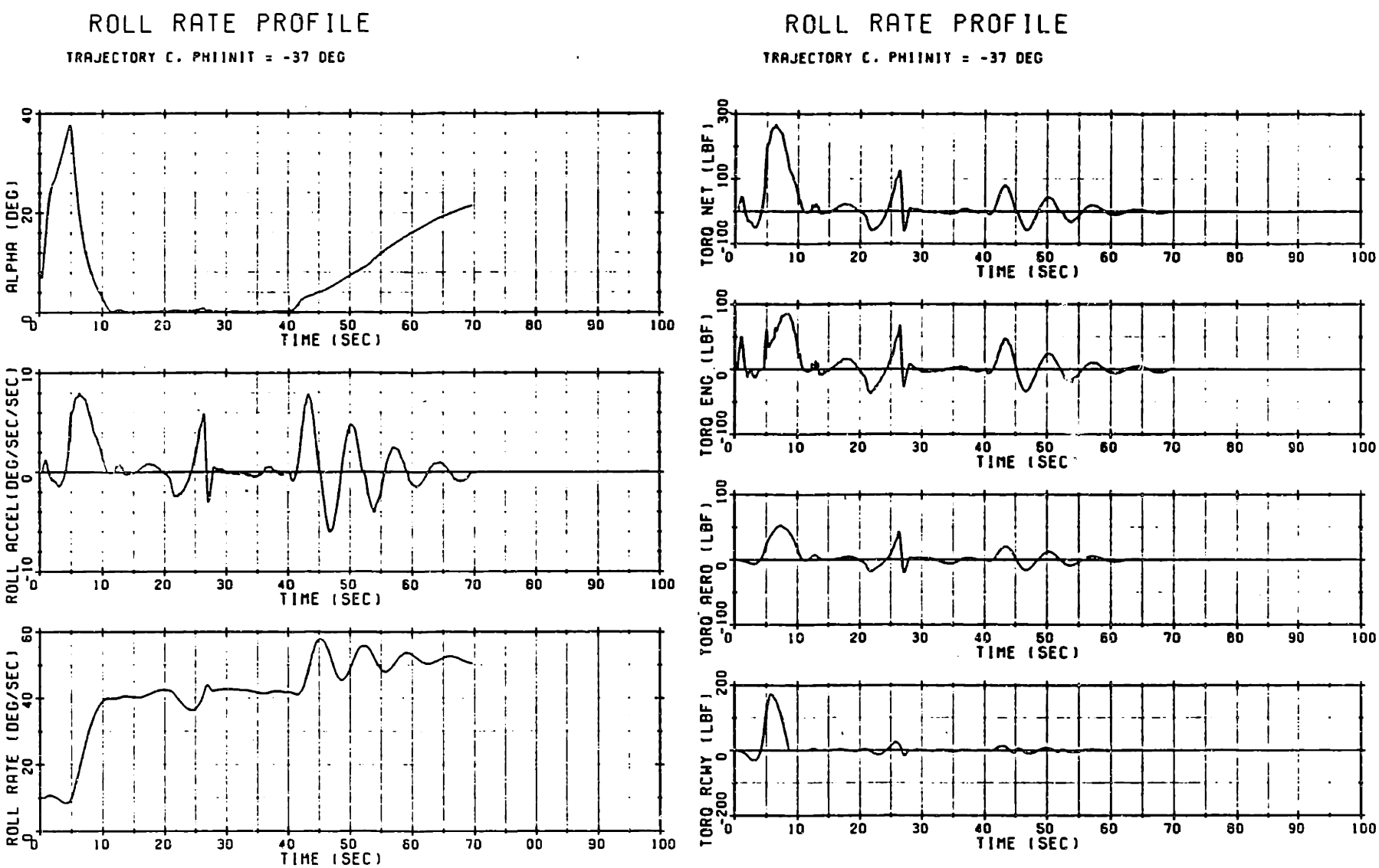

Figure 3-18. Roll rate profile, Trajectory C.

has its cg and hinge point offsets on the $\pm Z_B$ axis along with the raceway, the roll torque components act in phase, as predicted in Section 3.2.3. It is interesting to note that the largest roll torques in all three trajectories are produced by the following flight conditions:

- The angle of attack excursion during the launch maneuver.
- The occurrence of the wind spike in the region of maximum dynamic pressure. (For Trajectory B, the wind spike occurs approximately 32 seconds after launch. For Trajectory C, the wind spike occurs approximately 26 seconds after launch.)
- The angle of attack commanded early in the second stage flight phase. (Although the angle of attack continues to grow in the second stage flight phase, the normal forces acting on the vehicle decrease as the vehicle leaves the atmosphere, and the magnitude of the roll acceleration decreases towards zero.)

Since the high thrust boost trajectory produces the largest angles of attack during both the kick maneuver and the second stage flight phase, it is not surprising that the largest roll rates are produced along this trajectory. Among the roll rate profiles shown, the roll rate exceeds the 50 deg/sec specification only along Trajectory C.

CHAPTER 4

STAGING RECOVERY ISSUES

4.1 Introduction

When a boost vehicle stages at a significantly high dynamic pressure, great care must be taken to guarantee that the commanded staging sequence results in a safe and stable transfer of thrust vector control from the lower to the upper stage. Because very low thrust levels are supplied by the two involved stages prior to and just following stage separation, aerodynamic forces are the dominant forces acting on the vehicle during this period.

In this chapter, a staging sequence is presented for thrust transition from the first to the second stage of the boost vehicle. The staging sequence allows the vehicle to stage safely within a limited angle of attack versus angle of attack rate performance boundary. This performance boundary will be developed theoretically, then tested through simulation in the presence of disturbance inputs. Since the staging process allows angle of attack excursions to occur, this chapter will also explore the effect of these angle of attack excursions on the vehicle's roll rate. It will also be shown that the second stage roll rate can be reduced when angle of attack feedback control is employed following stage separation.

4.2 Staging Sequence

For the analysis performed in this chapter, a staging sequence has been programmed into the digital flight computer model. The flight

computer initiates the sequence according to two conditions on the measurement of the axial sensed velocity increment, ΔV_X, supplied by the IMU. Following initiation of the command sequence, the events in the sequence are executed as a function of time. The events in the staging sequence are shown in Figure 4-1, superimposed on a graph of thrust versus time. The events that occur at the indicated times are described subsequently.

Event (-1)

The event denoted as (-1) in Figure 4.1 occurs when the flight computer detects that the first stage thrust level is falling, or "tailing off". At this point a command is issued to add a minor cycle integral load relief signal to the load relief feedback path. As described in Section 2.4.3, the purpose of the minor cycle integral load relief signal is to drive the angle of attack as close to zero as possible in the presence of the steering commands.

The flight computer interprets the beginning of thrust tailoff through measurement of the axial sensed velocity increment, ΔV_X. ΔV_X is related to the thrust level T by:

$$\Delta V_X = \frac{T - FAERO_{AXIAL}}{M} T_{DAP} \qquad (4.1)$$

where M is the vehicle mass, and $FAERO_{AXIAL}$ is the axial component of the aerodynamic force on the vehicle. Near the end of the first stage flight phase, $FAERO_{AXIAL}$ is a decreasing function of time, since the vehicle has already flown through the region of maximum dynamic pressure. The vehicle mass, M, is also a monotonically decreasing function of time. If T is constant, the measured ΔV_X at the IMU will be a monotonically increasing function of time. The thrust tailoff is therefore

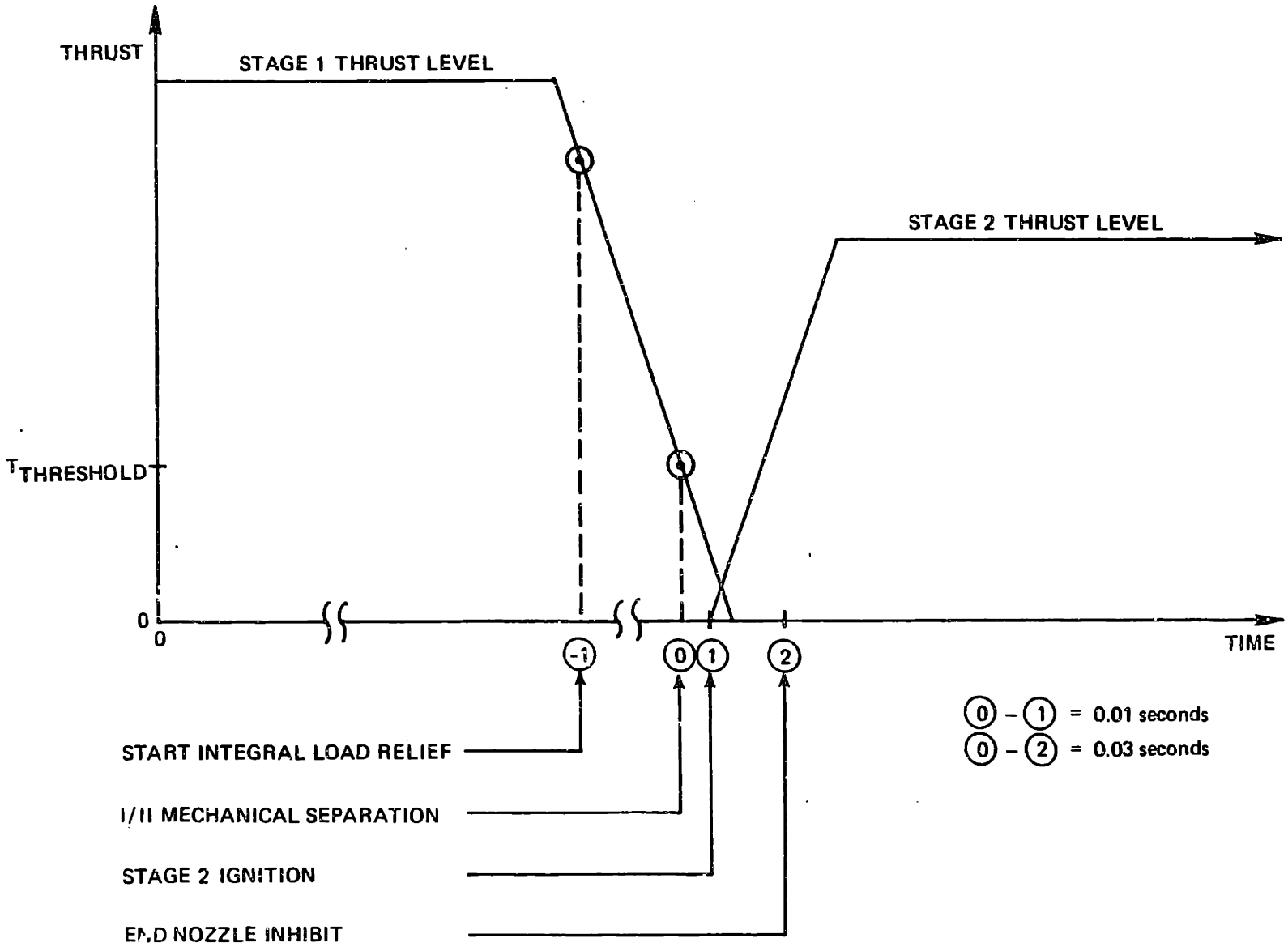

Figure 4-1. I/II staging sequence event profile.

indicated by decreasing values of ΔV_X. To prevent a thrust perturbation or noisy measurement from giving a false indication of thrust tailoff, Event (-1) is not initiated until ΔV_X drops below 90% of its maximum value:

$$\Delta V_{X,TAILOFF} = (0.9)\ \Delta V_{X,MAX} \tag{4.2}$$

where $\Delta V_{X,MAX}$ is the maximum value of ΔV_X recorded after the vehicle has passed through the region of maximum dynamic pressure.

Event (0)

The flight computer initiates Event (0) when it detects that the thrust level of the first stage has fallen below a threshold value. At Event (0), The flight computer issues the ignition command to detonate the explosive bolts in the interstage. The ignition command is assumed to be instantaneously executed. Therefore, following execution of Event (0), the second stage is effectively separated from the first stage. Event (0) is so designated because initiation of Event (0) defines the zero reference time for the second stage flight phase.

A threshold value of the sensed velocity increment ΔV_X is used to initiate Event (0). In this case the ΔV_X is a predetermined constant, chosen to indicate a threshold value of thrust, $T_{THRESHOLD}$. The relationship between the ΔV_X threshold and $T_{THRESHOLD}$ is:

$$\Delta V_{X,THRESHOLD} = \frac{T_{THRESHOLD} - FAERO_{AXIAL}}{M} T_{DAP} \tag{4.3}$$

where

$$FAERO_{AXIAL} = S\ Q\ CA \tag{4.4}$$

S, Q, CA, and M are all known either precisely or approximately at staging, so that $\Delta V_{X,THRESHOLD}$ can be selected prior to flight to cause stage separation to occur at $T_{THRESHOLD}$. The selection of $T_{THRESHOLD}$ may be influenced by a number of factors, including the desire to maximize the ΔV capability of the first stage, the need to limit adverse staging transients, and the need to limit the period of time during which the thrust vector controls are inactive.

Event (1)

Event (1) is initiated by the computer at a fixed time step, 0.01 seconds, after Event (0). At Event (1), the computer sends the ignition command to the second stage engine. This command is assumed to be instantaneously executed.

Event (2)

This event is initiated by the flight computer at a fixed time step, 0.02 seconds, after Event (1). Prior to Event (2), the second stage engine nozzle is not allowed to deflect. This constraint is imposed so that the nozzle will not collide with the surrounding interstage fairing. At Event (2), the engine nozzle is assumed to have exited the interstage, and the flight computer removes the inhibiting signals from the engine nozzle actuators. Following Event (2), the actuators are then allowed to deflect the engine nozzle to the position commanded by the autopilot.

4.3 The Staging Recovery Boundary

During the staging sequence, a short period of time exists in which aerodynamic forces are the primary forces acting on the vehicle. In order to keep the aerodynamic forces from rising to an uncontrollable level, the angle of attack, α, as well as its rate of change, $\dot{\alpha}$, must be tightly controlled prior to staging. If the angle of attack or the angle of attack rate lies outside a certain boundary at staging, the thrust

control capability of the second stage engine will not be able to "recover," or stabilize the vehicle. In this section, a theoretical development of the staging recovery boundary is presented. This theoretical boundary is then compared with results obtained from computer simulations of the staging sequence.

4.3.1 Theoretical Development

In order that the vehicle remain statically stable following stage separation, the engine moment must be able to balance the aerodynamic moment, so that the angular acceleration of the vehicle in the angle of attack plane may be controlled:

$$\left| T\ L_{CG}\ \delta_{MAX} \right| \geq \left| S\ Q\ CN_{\alpha}\ L_{CP}\ \alpha \right| \tag{4.5}$$

where all symbols are as defined in Figure 4-2. Rearranging Equation (4.5), the static stability criterion may be stated as a limit on the magnitude of the angle of attack:

$$\left| \alpha \right| \leq \frac{T\ L_{CG}}{S\ Q\ CN_{\alpha}\ L_{CP}} \left| \delta_{MAX} \right| \tag{4.6}$$

where δ_{MAX} is the maximum permissible engine deflection. Examining Equation (4.6), the tightest bound on the angle of attack at stage separation is specified by the smallest possible value of T and the largest possible value of Q. For the vehicle specifications in this thesis, the largest value of Q at I/II staging is 1600 psf. The lowest possible thrust level is 90% of the nominal thrust level. Solving Equation (4.6) using the vehicle mass and aerodynamic parameters at a staging dynamic pressure of 1600 psf, the low thrust level, and the maximum second stage engine deflection of five degrees, it is possible to compute the maximum magnitude of α for which the vehicle can be stabilized following stage separation. This value will be designated $\alpha_{STABLEBND}$.

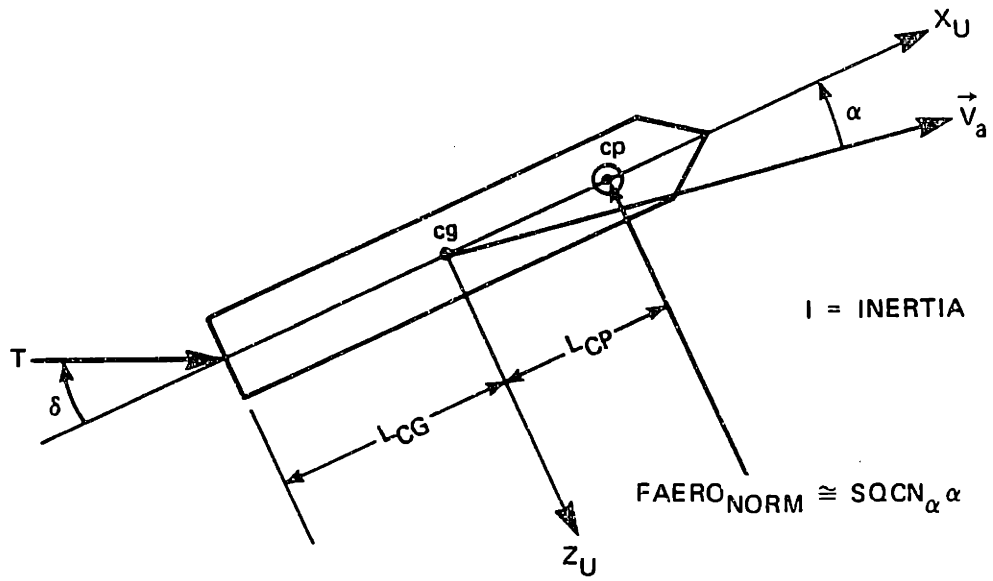

cp	CENTER OF PRESSURE
cg	CENTER OF GRAVITY
L_{CG}	DISTANCE BETWEEN NOZZLE HINGE POINT AND cg
L_{CP}	DISTANCE BETWEEN cg AND cp
T	THRUST
δ	NOZZLE DEFLECTION
$\bar{V}_a$	AIR-RELATIVE VELOCITY VECTOR
α	ANGLE OF ATTACK
S	AERODYNAMIC REFERENCE AREA
Q	DYNAMIC PRESSURE
CN_α	NORMAL FORCE STABILITY DERIVATIVE

Figure 4-2. Applied forces in the angle of attack plane.

At stage separation, the nozzle deflection is inhibited until the nozzle exits the surrounding interstage. During this time period, the engine is unable to provide any control moment. Furthermore, the dynamic response of the actuators causes the nozzle position to lag the nozzle deflection command after the nozzle inhibit is removed. For the purposes of this analysis, the response of the engine nozzle to the initial deflection command is modelled as a pure time delay of 0.2 seconds.

Because of the delay in the response of the engine nozzle actuators following stage separation, it is necessary to examine the dynamics of α in the absence of any control moment. If the angular acceleration of the flight path angle is small relative to the angular acceleration of the vehicle, then the approximate equation of motion for the vehicle in the angle of attack plane is given by:

$$I\,\ddot{\alpha} = FAERO_{NORM}\,L_{CP} \tag{4.7}$$

where all quantities are as defined in Figure 4-2. Relating $FAERO_{NORM}$ to α and rearranging:

$$\ddot{\alpha} - \xi^2 \alpha = 0 \tag{4.8}$$

where

$$\xi^2 = \frac{S\,Q\,CN_{\alpha}\,L_{CP}}{I} \tag{4.9}$$

At stage separation, the numerical value of ξ is:

$$\xi = 6.854\ sec^{-1} \tag{4.10}$$

Recognizing Equation (4.8) as a homogeneous differential equation in α, the solution is easily obtained:

$$\alpha(t) = D1\ e^{\xi t} + D2\ e^{-\xi t} \tag{4.11}$$

where D1 and D2 are constants of integration. Note that $\alpha(t)$ does contain an unstable component. Defining the initial conditions at stage separation:

$$t = t_0, \quad \alpha(t_0) = \alpha_0, \quad \dot{\alpha}(t_0) = \dot{\alpha}_0 \tag{4.12}$$

These initial conditions can be used to solve for the constants of integration:

$$D1 = 1/2\ (\alpha_0 + \dot{\alpha}_0/\xi)$$

$$D2 = 1/2\ (\alpha_0 - \dot{\alpha}_0/\xi) \tag{4.13}$$

Assuming the engine is not able to exert a control moment until 0.2 seconds after stage separation, constraints on the initial angle of attack conditions may then be determined by evaluating Equation (4.11) at t = 0.2 seconds, using the final condition constraint that α at 0.2 seconds must be less than $\alpha_{STABLEBND}$. Analytical solutions for Equation (4.11) are obtainable for the following two extremal cases:

Case 1 ($\dot{\alpha}_0 = 0$)

then

$$\alpha(t = 0.2) = \frac{\alpha_0\ e^{.2\xi}}{2} + \frac{\alpha_0\ e^{-.2\xi}}{2} \leq \alpha_{STABLEBND} \tag{4.14}$$

$$\Longrightarrow \quad \left|\alpha_0\right|_{MAX} = (0.477)\ \alpha_{STABLEBND} \tag{4.15}$$

Case 2 ($\alpha_0 = 0$)

then

$$\alpha(t = 0.2) = \frac{\dot{\alpha}_0\, e^{.2\xi}}{2\xi} + \frac{\dot{\alpha}_0\, e^{-.2\xi}}{2\xi} \leq \alpha_{STABLEBND} \tag{4.16}$$

$$\Longrightarrow \quad \left|\dot{\alpha}_0\right|_{MAX} = (3.720\ \text{sec}^{-1})\ \alpha_{STABLEBND} \tag{4.17}$$

These extreme cases determine the corner points of the staging recovery boundary. This boundary represents the worst combinations of angle of attack, α_0, and angle of attack rate, $\dot{\alpha}_0$, at stage separation from which the second stage can successfully recover. A graph of the theoretical staging recovery boundary, normalized in terms of $\left|\alpha_0\right|_{MAX}$ and $\left|\dot{\alpha}_0\right|_{MAX}$, is shown in Figure 4-3.

4.3.2 Simulation Results

In order to verify the staging recovery boundary, a single-degree-of-freedom simulation was used to simulate the rotational motion of the boost vehicle in the angle of attack plane at I/II staging. The simulation assumed the nominal mass and aerodynamic properties of the vehicle at a staging dynamic pressure of 1600 psf, and a low thrust profile. The commanded staging sequence described in Section 4.2 was included in the simulation, as well as the second order engine actuator model. The effects of wind disturbances and staging side forces were neglected in this simulation.

The simulation was repeated over many combinations of the initial conditions α_0 and $\dot{\alpha}_0$. Results of the computer simulations determined the staging recovery boundary shown in Figure 4-3. The recovery boundary obtained through computer simulation does agree closely with the theoretical staging recovery boundary.

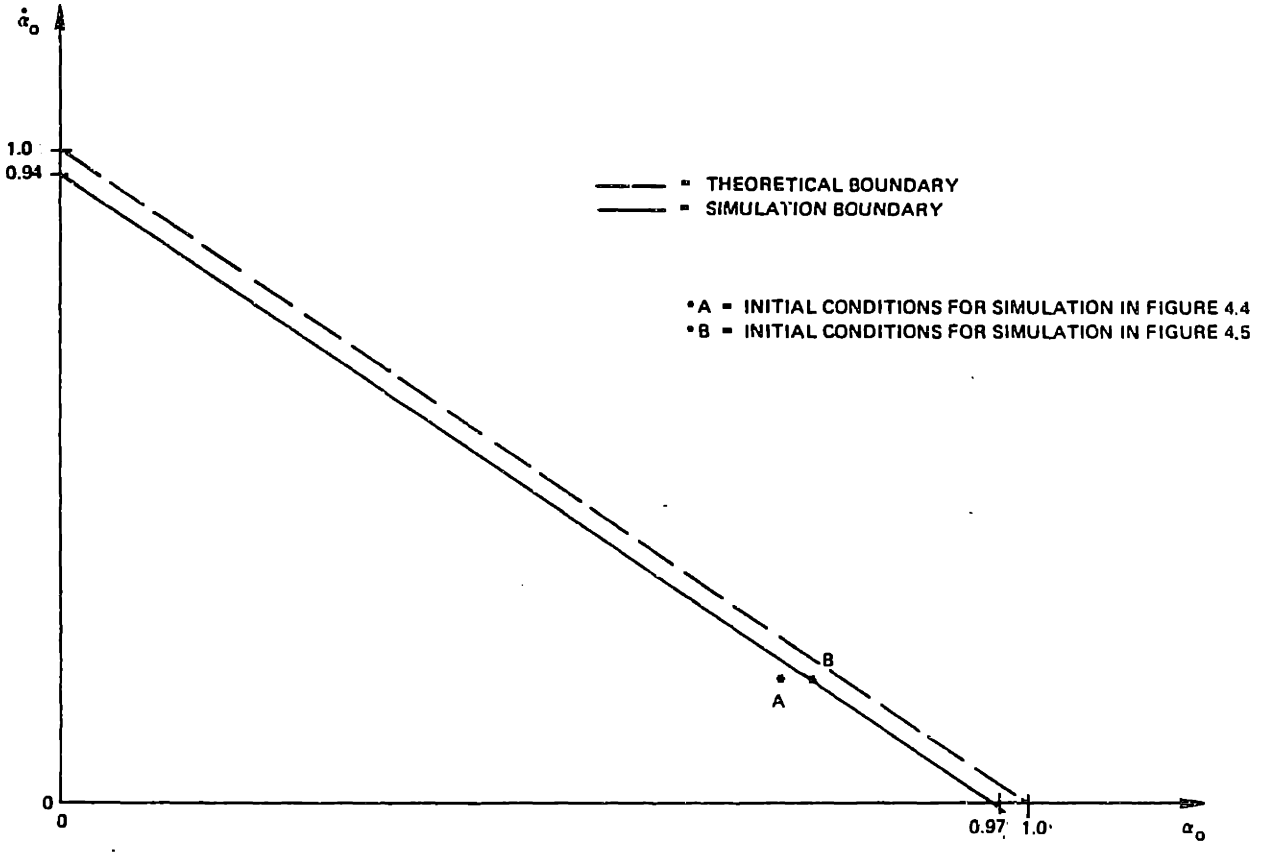

Figure 4-3. Staging recovery boundary.

The plots in Figures 4-4 and 4-5 show the simulated time responses of the vehicle motion for the initial condition sets marked A and B in Figure 4-3. In these plots, the zero time reference is the time of mechanical stage separation (Event ⓪). Just a small change in the angle of attack at staging leads to a markedly different vehicle response. Figure 4-4 shows a successful recovery. The engine deflects towards its maximum angular position as soon as its inhibit is removed at 0.03 seconds. The angle of attack is reduced before the aerodynamic loading limit of $Q\alpha$ = 6000 psf deg is exceeded. In Figure 4-5, the

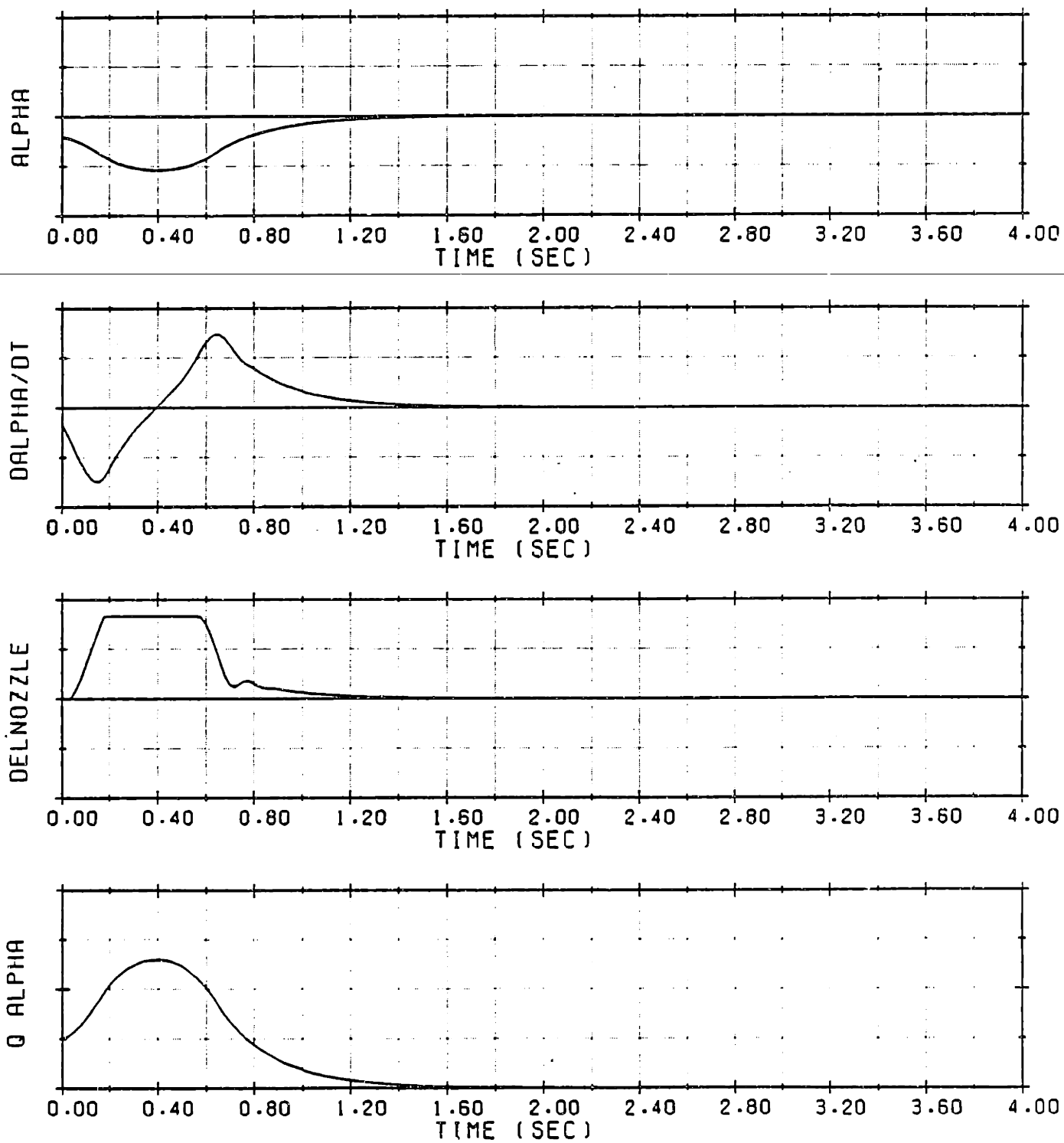

Figure 4-4. Simulated vehicle response from initial condition set A in Figure 4-3.

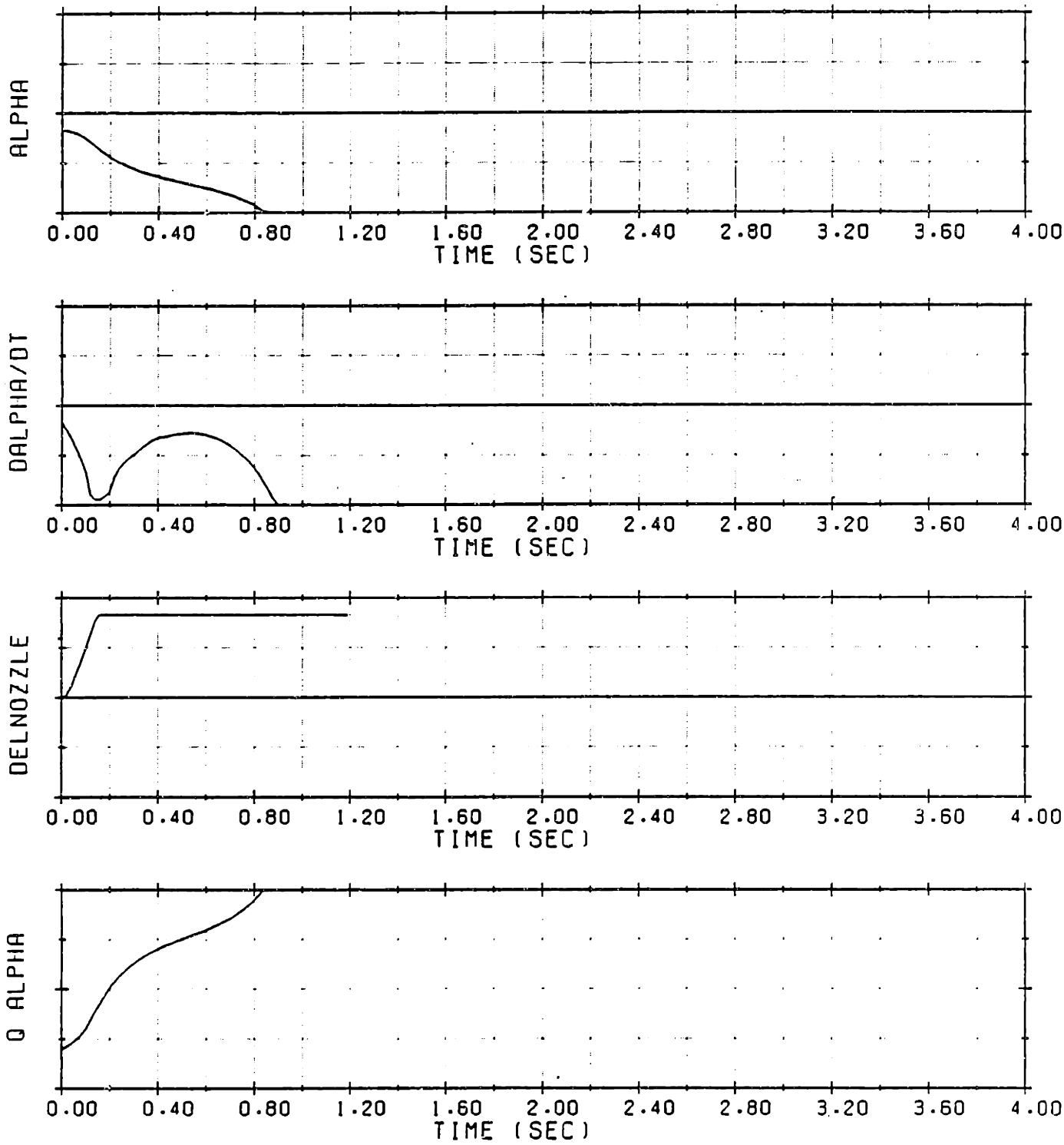

Figure 4-5. Simulated vehicle response from initial condition set B in Figure 4-3.

vehicle is unable to recover, and tumbles wildly. Notice that even at the edge of the recovery boundary, if the vehicle is able to recover at all, it does so within the first two seconds following stage separation.

4.3.3 Effect of Disturbances

There are two disturbance inputs which may adversely affect the boost vehicle's ability to recover from stage separation. These disturbances, which are discussed subsequently, are:

(1) Staging Side Forces

(2) A Wind Spike

Staging Side Forces

When a boost vehicle stages in the atmosphere, transient forces act in the vicinity of the upper stage engine nozzle. Since the engine nozzle is located quite far from the center of gravity, any force applied there can produce a large rotational torque. Thus the cause and effects of these transient forces must be carefully understood. Staging side forces are attributable to two primary factors:

(1) A pressure differential exists between the air within the interstage, which is at sea level pressure, and the air surrounding the vehicle, which is at a much lower local pressure. If the interstage separates asymmetrically, a side force may be created by the non-uniform flow of air between the two pressure regions.

(2) Following mechanical stage separation (Event ⓪), there is a finite time interval during which the deflected engine plume interacts with the interstage fairing to produce a side force.

The forces caused by these two factors have been modelled as two independent components, which are then summed to produce the total staging side force. Since the direction of the interstage separation asymmetry and its resultant pressure wave is unknown, the first component of

the staging side force is applied in a time-invariant random direction. This random direction is assigned according to a random number generated within the IBM simulation computer. The second component of the staging side force is defined to act in the direction opposite the deflection of the second stage engine nozzle.

The magnitude vs time profiles of the two staging side force components are derived from a limited sample of existing experimental data. Graphs of the actual magnitude vs time profiles used in this thesis are shown in Figure 4-6. The randomly directed component of the staging side force is denoted SF_{RAND}. The deterministic component, due to the backlash of the engine plume, is termed $SF_{BACKLASH}$. Note that the total duration of the two applied forces is quite short. Although SF_{RAND} acts for a shorter time than $SF_{BACKLASH}$, SF_{RAND} supplies approximately 60 percent of the total side force impulse.

Wind Spike

If a wind spike occurs near the staging altitude, the wind speed changes rapidly with altitude, as outlined in Section 2.6. A change in the wind speed causes a change in the direction and magnitude of the vehicle's air-relative velocity vector. Since the angle of attack is defined as the angle between the vehicle's longitudinal axis and the air-relative velocity vector, a change in the wind speed will cause a change in the angle of attack.

In the simulations presented in this section, a wind spike has been placed 1000 feet above the staging altitude. Since the wind shear is greatest in the region of the wind spike altitude $\pm$1000 feet, this placement of the wind spike will provide the largest wind disturbance during the staging recovery.

Staging Recovery Boundary with Worst-Case Disturbances

The most severe combination of staging recovery disturbances occurs when all disturbances act to increase the magnitude of the

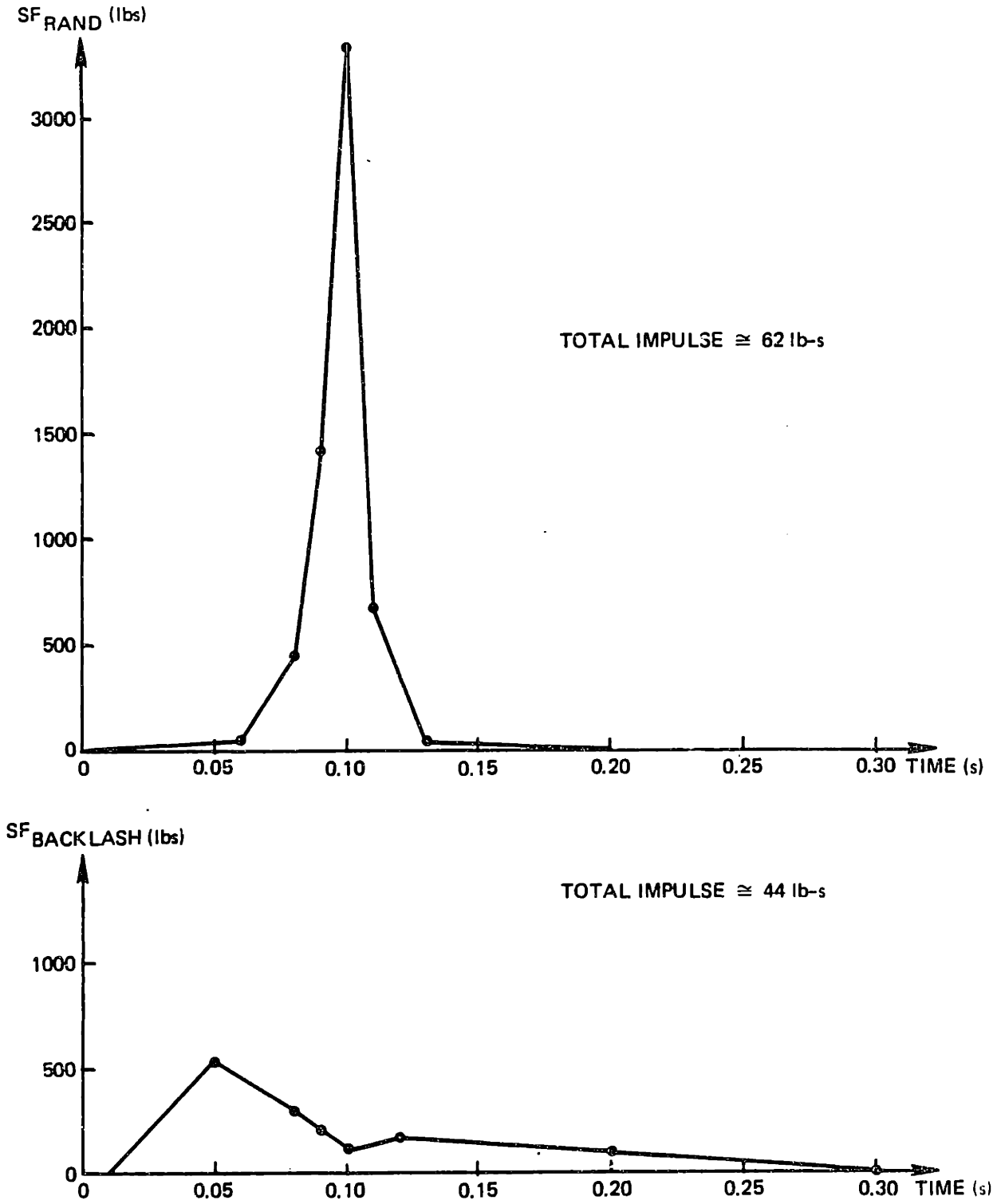

Figure 4-6. Magnitude vs time profiles for staging side force components.

vehicle's angle of attack. Figure 4-7 shows the worst combination of disturbance inputs for a vehicle with a negative angle of attack at stage separation. If both components of the staging side force are aligned and act in the $-Z_U$ direction, this will produce an angular acceleration of the vehicle in the negative angle of attack direction. A tailwind spike just above the staging altitude will cause a decrease in the downrange component of the vehicle's air-relative velocity vector, $\bar{V}_A$, resulting in an increase in the magnitude of the angle of attack.

The above-mentioned disturbance inputs were introduced into the six-degree-of-freedom vehicle simulation. As in the previous section, this simulation assumed a vehicle with a low thrust profile, staging at the highest allowable dynamic pressure, 1600 psf. An iterative study was again performed to determine the effects of the disturbance inputs on the staging recovery boundary. The results of this study are shown in Figure 4-8. This figure shows the normalized staging recovery boundary in the presence of disturbance inputs, plotted along with the staging recovery boundary that was obtained without disturbance inputs in Section 4.3.2. Although the worst-case disturbances are not totally destabilizing, they do further constrain the permissible conditions on α_0 and $\dot{\alpha}_0$.

Figures 4-9 and 4-10 show time profiles of the vehicle motion for the sets of initial conditions denoted by the letters C and D in Figure 4-8. Once again, these points were chosen to illustrate the limits of the recovery boundary. Figure 4-9 shows a successful staging recovery. Notice that once the vehicle has recovered from its initial angle of attack transient, it then begins to develop a steady-state angle of attack due to the attitude commands produced by the exponential steering algorithm. In Figure 4-10, the vehicle is unable to recover from the given initial conditions.

4.4 The Staging Roll Rate Boundary

As shown in the preceding sections of this chapter, the limitations of the control system allow angle of attack excursions to occur

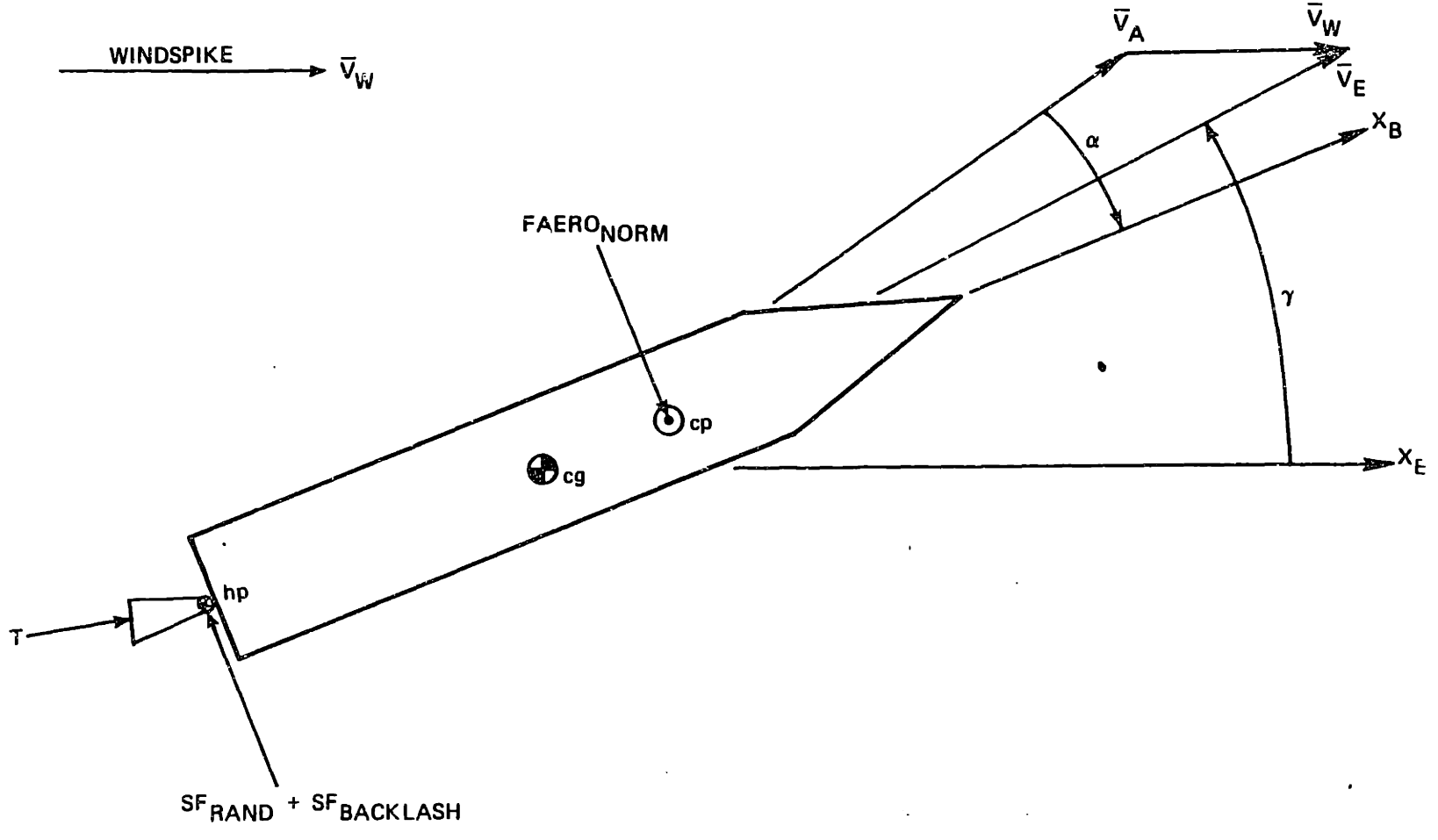

Figure 4-7. Worst-case staging disturbances.

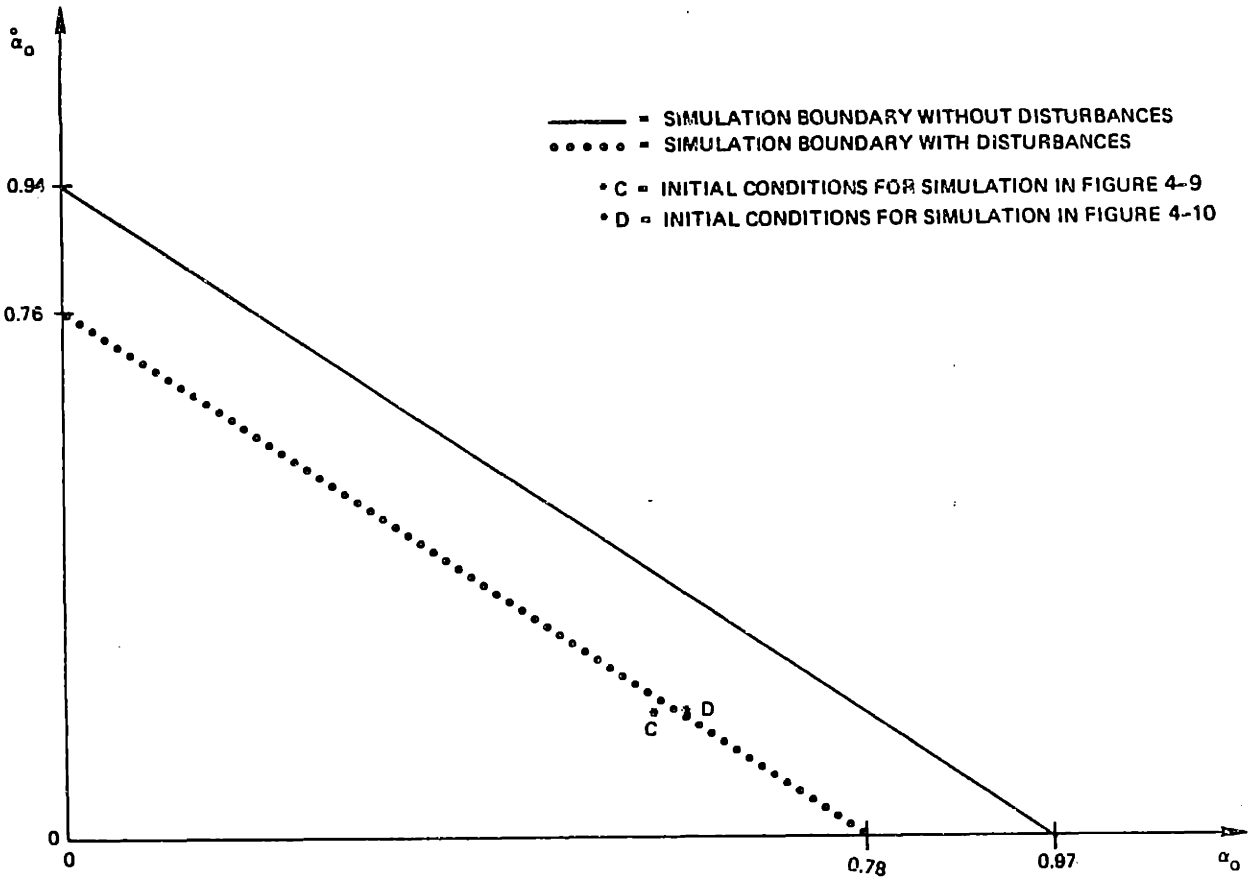

Figure 4-8. Staging recovery boundary in the presence of disturbance inputs.

following stage separation. During staging recovery, the aerodynamic and engine forces acting on the vehicle produce roll torques, which may lead to an increase in the vehicle roll rate. Following staging recovery, the second stage steering commands may cause the vehicle to develop an angle of attack. This angle of attack could also lead to an increase in the vehicle roll rate.

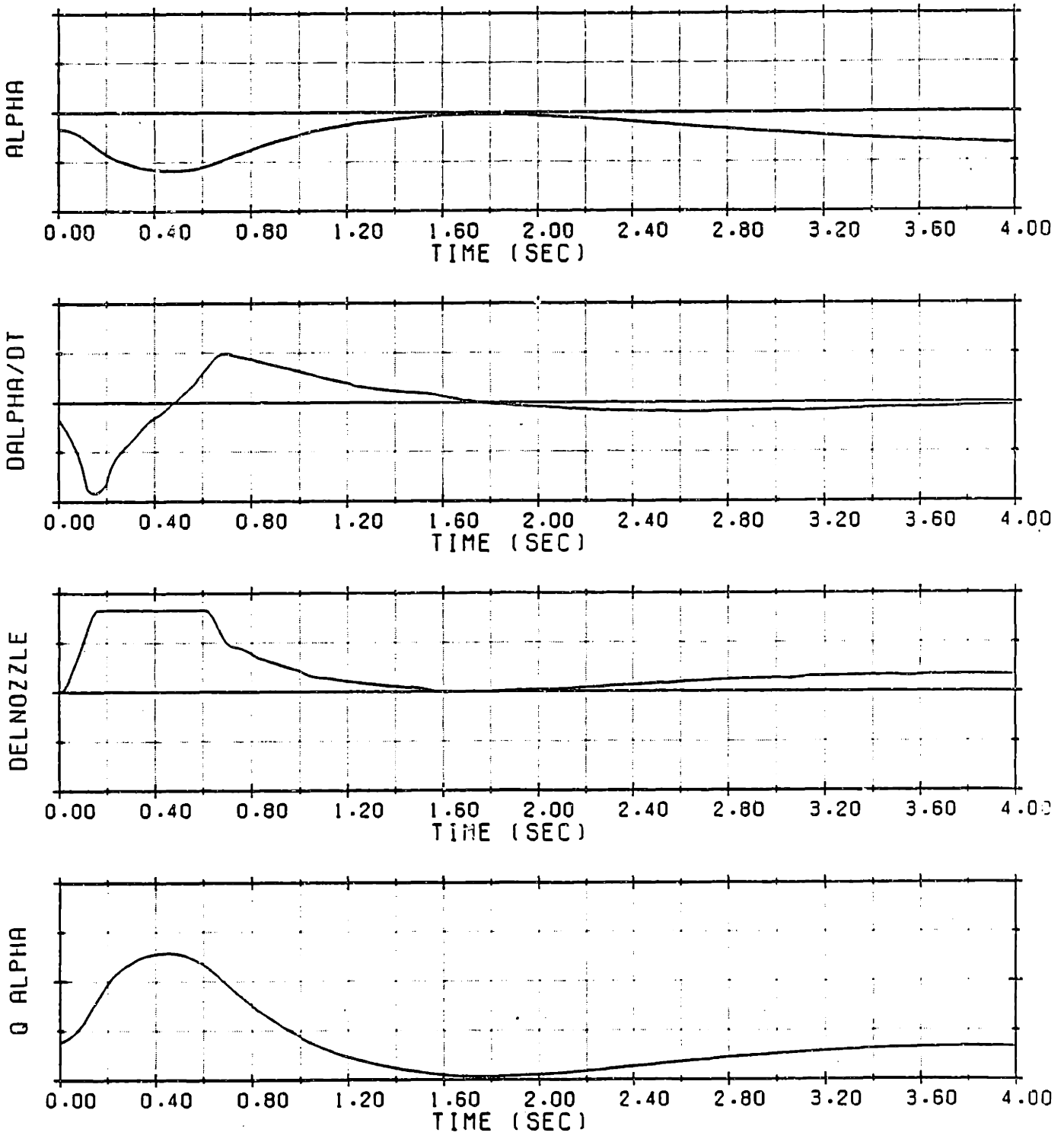

Figure 4-9. Simulated vehicle response from initial condition set C in Figure 4-8.

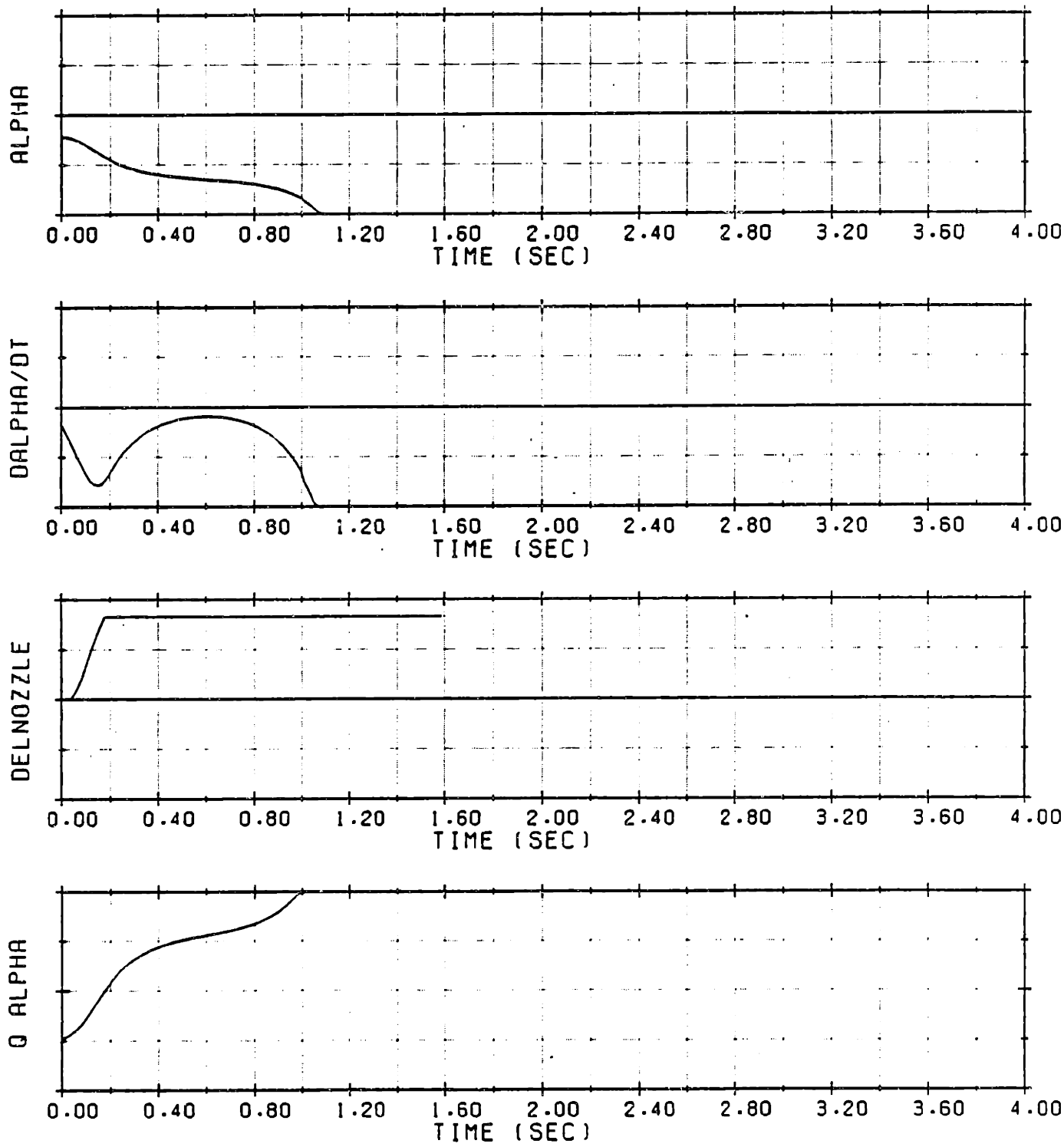

Figure 4-10. Simulated vehicle response from initial condition set D in Figure 4-8.

In a roll rate control algorithm proposed by Dailey [4], an attempt is made to first estimate the combined effect of the cg and engine hinge point offsets, and then use this knowledge to command an angle of attack that results in applied roll torques of the desired polarity. Immediately following stage separation, however, it is not possible to explicitly control the roll rate using Dailey's method, because new cg and engine hinge point offsets are established when the vehicle stages. Preliminary studies have shown that at least four seconds are required to obtain an estimate of the new offsets following stage separation. Therefore, it is important to analyze the uncontrolled roll motion of the vehicle during this short time interval.

In this section, the single-degree-of-freedom roll simulation was employed to determine the largest potential roll rate increase in the first four seconds following stage separation. In order to limit the number of variables in this analysis, the roll simulation only examined the roll motion of the vehicle along the high thrust reference trajectory (Trajectory C) from Chapter 3. This trajectory was chosen because it achieves the largest values of angle of attack during the first four seconds of the second stage flight phase. The roll simulation searched for the maximum roll rate produced during the first four seconds of the second stage flight phase as a function of:

- The angle of attack conditions at stage separation
- The vehicle roll rate at stage separation

Since the boost vehicle had already encountered a wind spike along Trajectory C in the region of maximum dynamic pressure, no wind spike was placed at the staging altitude. However, staging side forces were included in the force histories passed to the roll simulation. All roll simulations assumed the worst-case vehicle offsets (CG_Z = 0.20 inches, HNG_Z = -0.16 inches).

The roll simulation results are summarized in Table 4-1. For four different initial roll rates (0, 15, 30, and 45 degrees/sec), the worst-case maximum second stage roll rate is listed as a function of the angle of attack conditions at stage separation. As in Chapter 3, the term

"worst-case" is used to describe the largest roll rate produced from all the possible initial roll angles of the vehicle. In Table 4-1(A), the maximum roll rate is given as a function of the initial angle of attack, with an initial angle of attack rate of zero. In Table 4-1(B), the maximum roll rate is given as a function of the initial angle of attack rate, with the initial angle of attack equal to zero. These tables show that if the vehicle roll rate at stage separation is zero, then the vehicle roll rate will not exceed the 50 deg/sec specification for any set of initial angle of attack conditions within the staging recovery boundary. However, for even moderate roll rates at stage separation, it is possible to exceed the roll rate limit in the first four seconds following stage separation. If the vehicle enters the second stage flight phase with a roll rate of 45 deg/sec, the roll rate can surpass the specified limit regardless of the initial angle of attack conditions.

The results presented in Tables 4-1(A) and 4-1(B) permit the construction of new α_0 vs $\dot{\alpha}_0$ boundaries, representing staging conditions that result in the specified maximum roll rate during the first four seconds of the second stage flight phase under worst-case conditions. These boundaries, which have been found to be approximately linear, are termed the "staging roll rate boundaries". Assuming that these boundaries are exactly linear, they have been plotted in Figure 4-11 by interpolating α_0 and $\dot{\alpha}_0$ intercepts from Tables 4-1(A) and 4-1(B), then connecting these intercepts with a straight line. The particular staging roll rate boundary of interest depends on the roll rate at stage separation. If the roll rate at stage separation is greater than seven degrees per second, notice that the staging roll rate boundary places tighter constraints on the initial angle of attack conditions than the staging recovery boundary.

4.5 Introduction of Angle of Attack Feedback Control Following Stage Separation

The preceding section showed that there is potential for a large roll rate increase in the first four seconds following stage separation.

Table 4-1(A). Maximum roll rates following staging recovery ($\dot{\alpha}_0 = 0$).

$\dot{\phi}_0$ (deg/sec) \ α_0*	$\dot{\phi}_{MAX}$ (deg/sec)					
	0.00	0.12	0.24	0.36	0.48	0.60
0	40.24	39.67	38.82	38.44	37.79	41.51
15	40.81	39.95	39.92	42.12	45.05	50.39
30	44.94	47.72	49.69	54.36	59.67	64.64
45	56.20	59.63	62.86	67.75	75.85	78.23

* α_0 is normalized relative to $|\alpha_0|_{MAX}$

Table 4-1(B). Maximum roll rates following staging recovery ($\dot{\alpha}_0 = 0$).

$\dot{\phi}_0$ (deg/sec) \ $\dot{\alpha}_0$**	$\dot{\phi}_{MAX}$ (deg/sec)			
	0.00	0.18	0.44	0.76
0	40.24	39.67	38.99	46.91
15	40.81	39.35	42.37	57.73
30	44.94	48.32	56.80	70.08
45	56.20	60.43	75.64	81.64

** $\dot{\alpha}_0$ is normalized relative to $|\dot{\alpha}_0|_{MAX}$

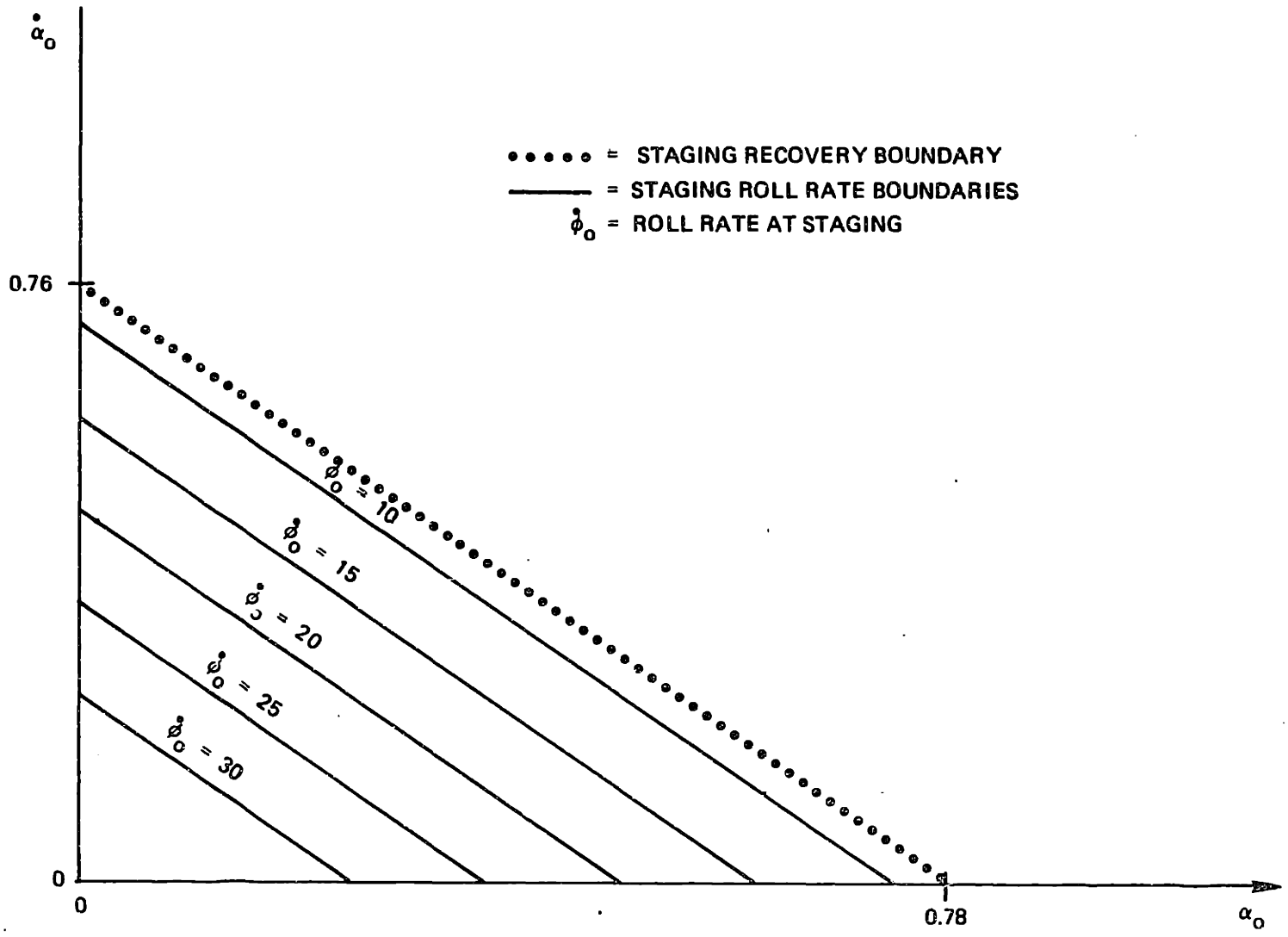

Figure 4-11. Staging roll rate boundaries.

This roll rate increase is attributable to two effects:

(1) An angle of attack transient produced during stage separation.

(2) A commanded angle of attack produced by the second stage steering algorithm.

Clearly, nothing can be done to reduce the roll rate attributed to the staging recovery. For any nonzero angle of attack conditions at stage separation, roll torques will be applied during the recovery process. However, it is possible to reduce the roll torques applied after the staging recovery, by limiting the vehicle's subsequent angle of attack. In this section, an alternative control system is introduced which uses angle of attack feedback to steer the vehicle to a zero angle of attack ("zero-alpha") flight condition. The roll simulation is then used to find the worst-case roll rates when this zero-alpha steering system is used for the first four seconds of the second stage flight phase.

4.5.1 Angle of Attack Estimation

The zero-alpha steering system must utilize an angle of attack feedback control system. An angle of attack control system requires accurate angle of attack estimates. In Chapter 2, a steady-state angle of attack estimator was presented in connection with the load relief system. This estimator is accurate at low frequencies. In an angle of attack feedback control system, however, it is necessary to obtain an angle of attack estimate which is accurate at both low and high frequencies.

The angle of attack control system used for zero-alpha steering employs an estimation algorithm developed by Gilbert Stubbs at CSDL to form estimates of both high and low frequency angle of attack components in the body-fixed coordinate frame. The high frequency angle of attack estimates are computed from body angle increments supplied by the IMU. The low frequency estimates are then calculated as a function of both the IMU ΔV measurements and the measured engine nozzle deflection. The high and low frequency estimates are processed by a complementary filter,

similar to the filter used to process the high and low frequency angular rate estimates. A block diagram of this angle of attack estimator is shown in Figure 4-12. For more information on this estimator, consult Reference [1].

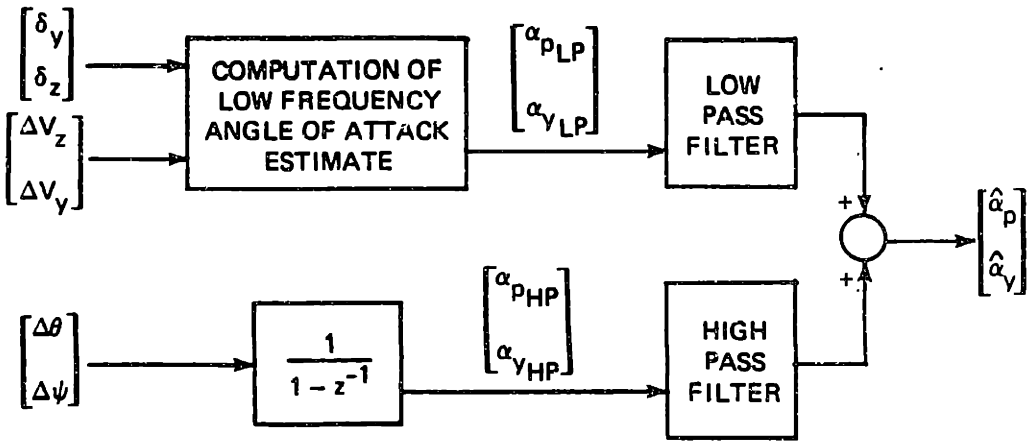

Figure 4-12. Angle of attack estimator block diagram.

4.5.2 Angle of Attack Autopilot

The angle of attack control system used for zero-alpha steering is described by the pitch channel block diagram in Figure 4-13. (This control system will also be used in conjunction with another steering approach in Chapter 6.) This autopilot is almost identical to the baseline autopilot pictured in Figure 2-8. Instead of forming a pitch attitude error signal at the autopilot input, however, this autopilot computes an angle of attack error from the difference between the commanded

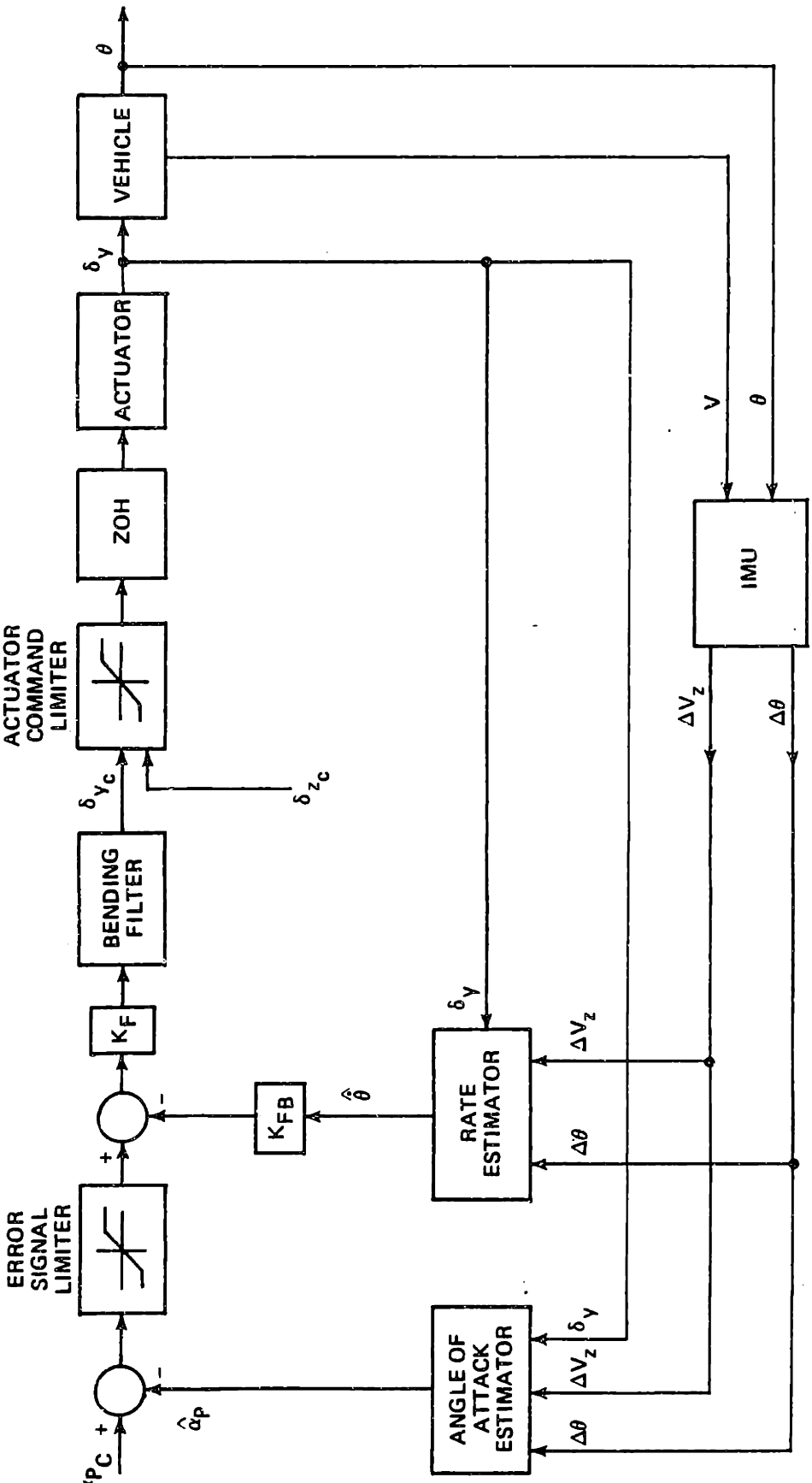

Figure 4-13. Angle of attack autopilot pitch channel block diagram.

angle of attack, α_{p_c} (for zero-alpha steering, α_{p_c} is zero), and the estimated angle of attack in the pitch plane, $\hat{\alpha}_p$. Note that attitude rate feedback is still necessary to stabilize the system. Since this autopilot explicitly limits the angle of attack, no load relief is necessary when this autopilot is used.

4.5.3 Roll Simulation Results

Force histories on the vehicle were saved for the first four seconds of the second stage flight phase, using the six-degree-of-freedom simulation and the zero-alpha steering system. The six-degree-of-freedom simulation generated these histories from the same set of staging conditions and vehicle parameters used to obtain the results of Section 4.4; that is, a high thrust profile, with a staging dynamic pressure of 1600 psf. The roll simulation was then used to find the worst-case roll rates produced using the zero-alpha steering system. The results of this analysis are summarized in Table 4-2. For each of the four initial second stage roll rates considered in Section 4.4, the maximum roll rate during the first four seconds of the second stage flight is listed as a function of the initial angle of attack. In all these trials, the initial angle of attack rate was zero. Table 4-2 shows how the maximum roll rate obtained previously with exponential steering is decreased through the use of zero-alpha steering. This decrease is expressed as a percentage of the corresponding maximum roll rates from Table 4-1(A) in Section 4.4. As Table 4-2 shows, however, the capability of the new steering system to reduce the second stage roll rate diminishes as the initial angle of attack increases. This is due to the fact that a larger initial angle of attack results in larger applied roll torques during the staging recovery itself, so that the maximum roll rate becomes less dependent on the subsequent second stage steering commands.

Table 4-2. Maximum roll rates following staging recovery, zero-alpha steering ($\dot{\alpha}_0 = 0$).

$\dot{\phi}_0$ (deg/sec) \ α_0*	$\dot{\phi}_{MAX}$ (deg/sec)			% Reduction in $\dot{\phi}_{MAX}$†		
	0.00	0.12	0.24	0.36	0.48	0.60
0	40.24	39.67	38.82	38.44	37.79	41.51
15	40.81	39.95	39.92	42.12	45.05	50.39
30	44.94	47.72	49.69	54.36	59.67	64.64
45	56.20	59.63	62.86	67.75	75.85	78.23

* α_0 is normalized relative to $|\alpha_0|_{MAX}$

† this represents the percentage reduction of the maximum roll rate from Table 4.1(A).

The capability of the zero-alpha steering system to reduce the maximum roll rate is highly dependent on staging conditions, as illustrated by the comparisons provided in Figures 4-14 and 4-15. Each figure contains two sets of plots obtained for second stage trajectories from the same staging conditions. The first set of plots in each figure was obtained using exponential steering, the second set with zero-alpha steering.

In Figure 4-14(A), the vehicle stages with zero angle of attack, an initial roll rate of 30 deg/sec, and an initial roll angle of 90 degrees. The roll rate changes minimally during staging recovery, but then increases when the second stage exponential steering commands cause the vehicle to develop an angle of attack. Note that the roll torques attributable to the engine force, the aerodynamic force, and the raceway all oscillate as the vehicle rotates. In Figure 4-14(B), the vehicle inherits the same staging conditions, but the zero-alpha steering system

limits the angle of attack following stage separation, and the roll rate remains relatively unchanged. In the case of Figure 4-14, use of the zero-alpha steering system has effectively limited the roll rate.

In Figure 4-15(A), the vehicle stages with an angle of attack of -0.4 degrees, an initial roll rate of 30 deg/sec, and an initial roll angle of 0 degrees. The roll rate increases sharply during the staging recovery, then increases slightly when the exponential steering commands cause the vehicle to develop an angle of attack. In Figure 4-15(B), the vehicle inherits the same staging conditions, and the roll rate again increases sharply during staging recovery. Although the zero-alpha steering system does prevent any further increase in the roll rate in the second stage flight phase, it is unable to reduce the roll rate from a dangerously high 46.5 deg/sec. Thus, in Figure 4-15, the zero-alpha steering system has certainly done no worse than the exponential steering in limiting the roll rate, but it is still not able to compensate for the increase in roll rate caused by staging recovery.

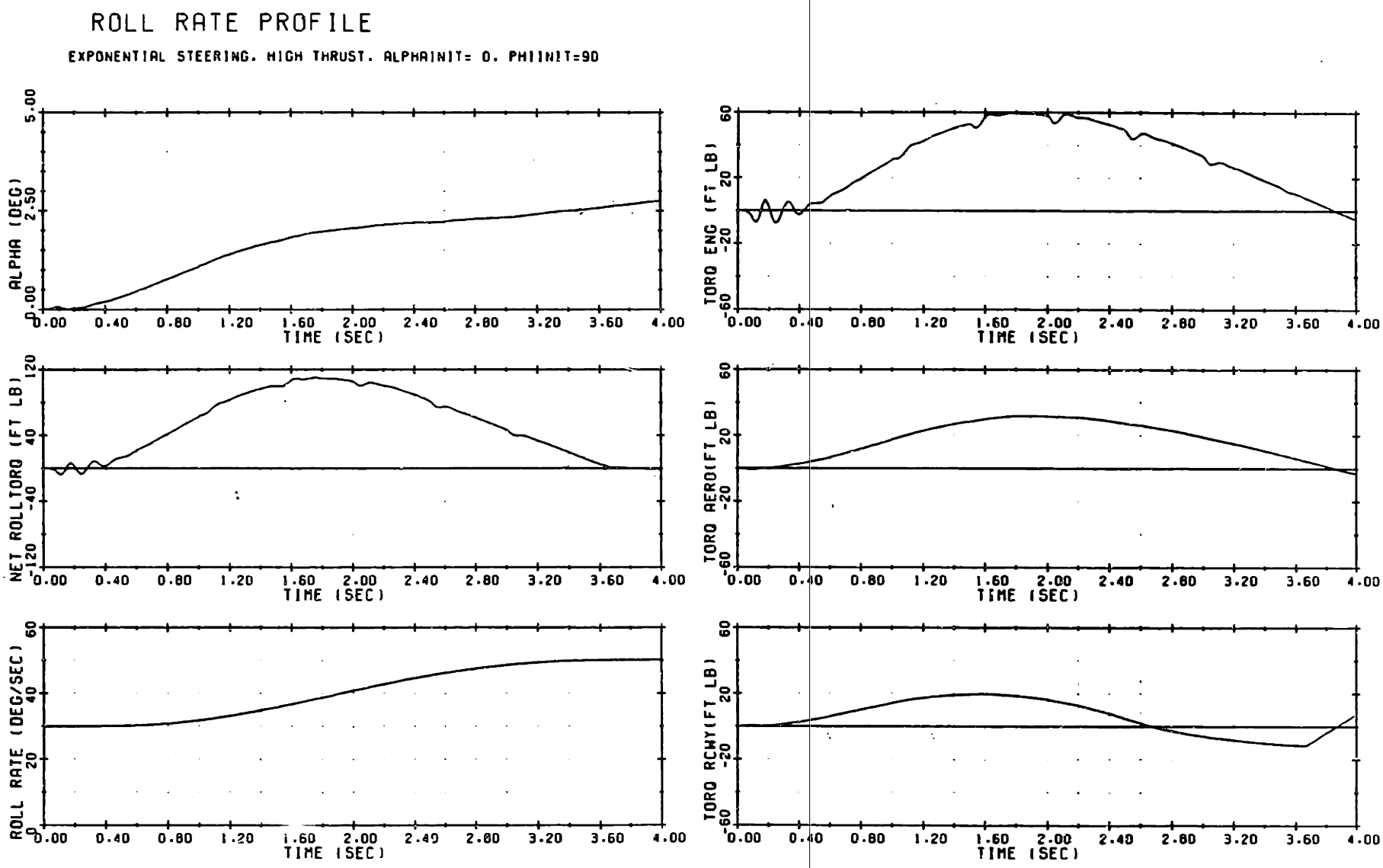

Figure 4-14(A). Roll rate profile for $\alpha_0 = 0$, exponential steering.

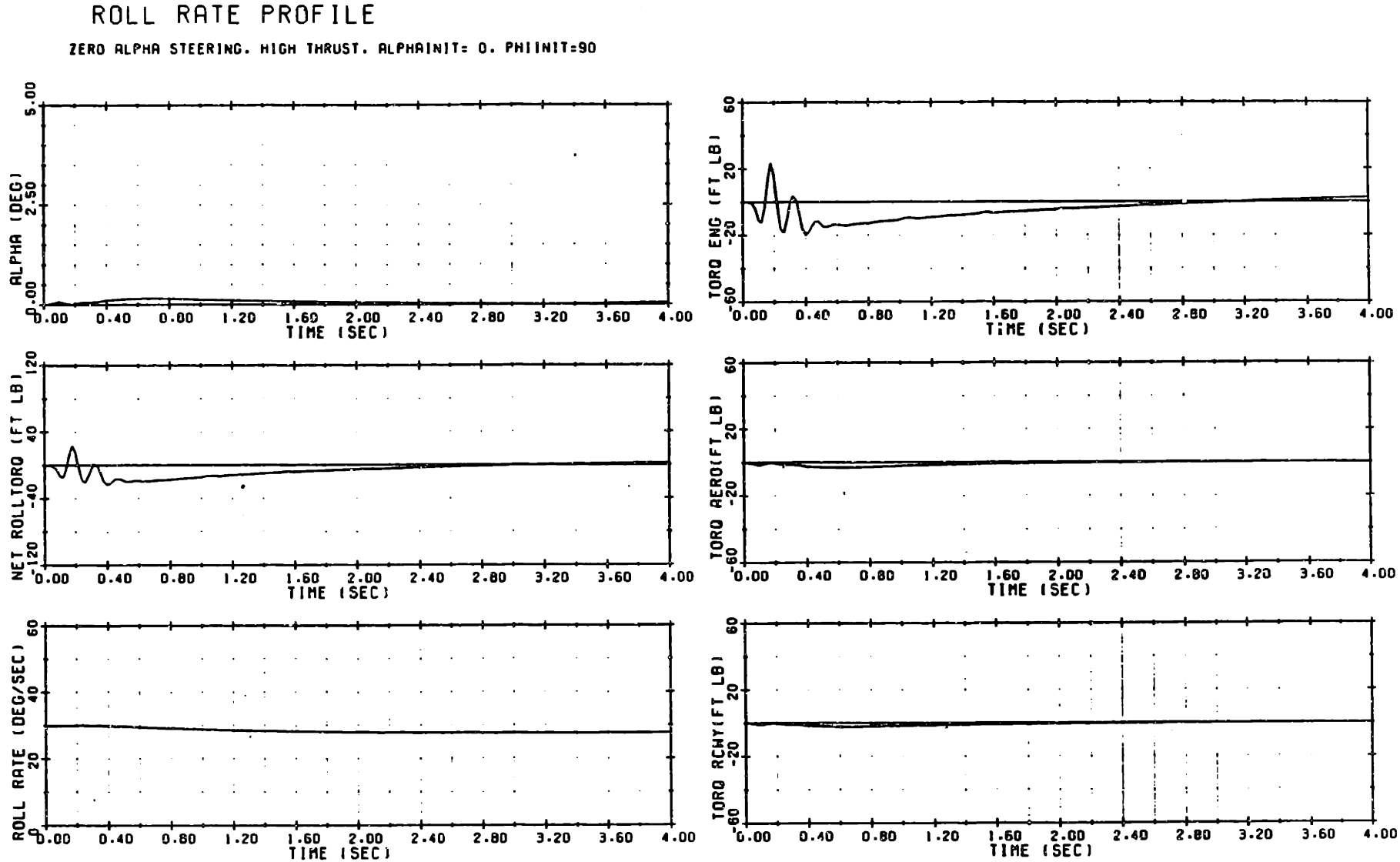

Figure 4-14(B). Roll rate profile for $\alpha_0 = 0$, zero-alpha steering.

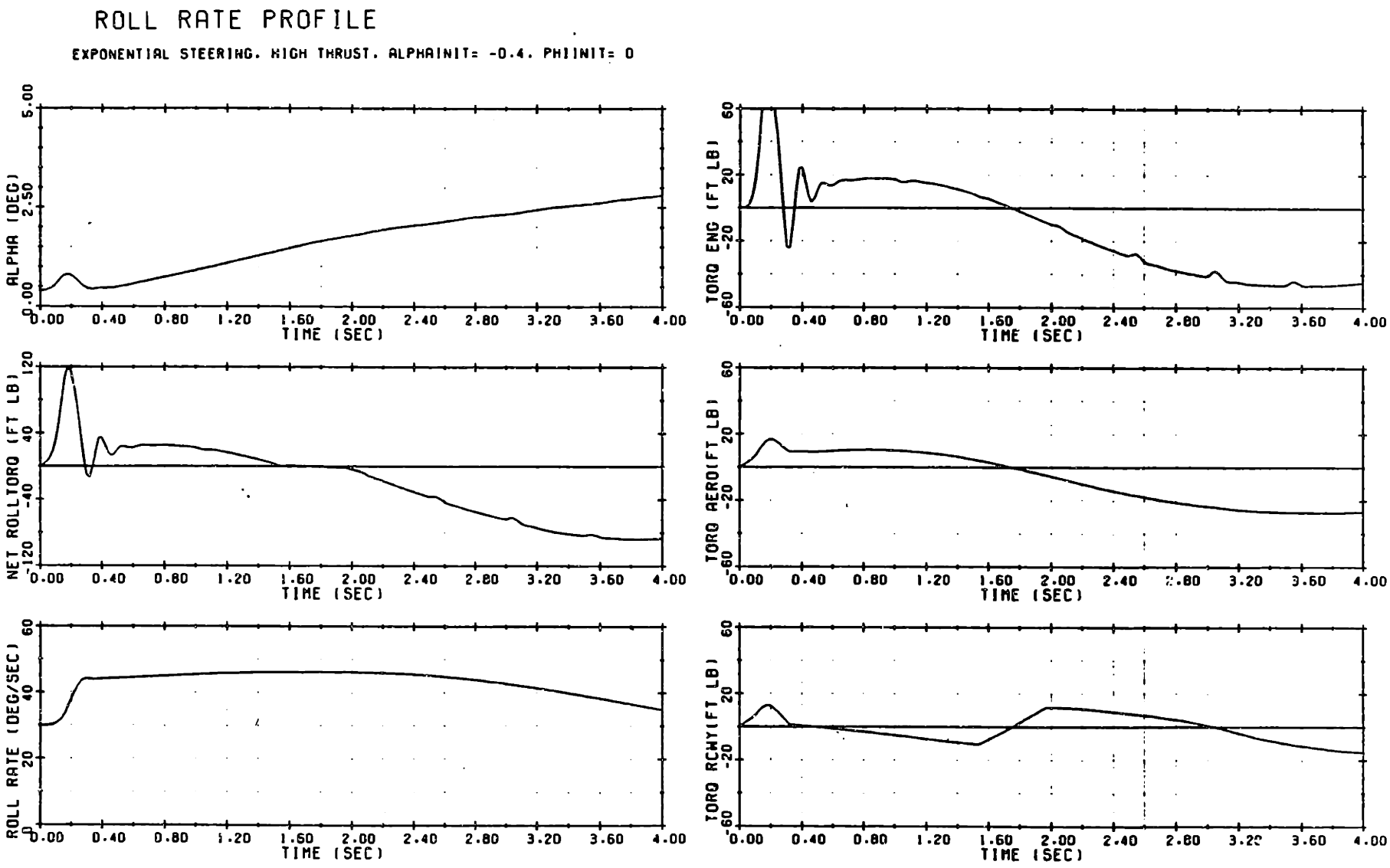

Figure 4-15(A). Roll rate profile for $\alpha_0 = -0.4$, exponential steering.

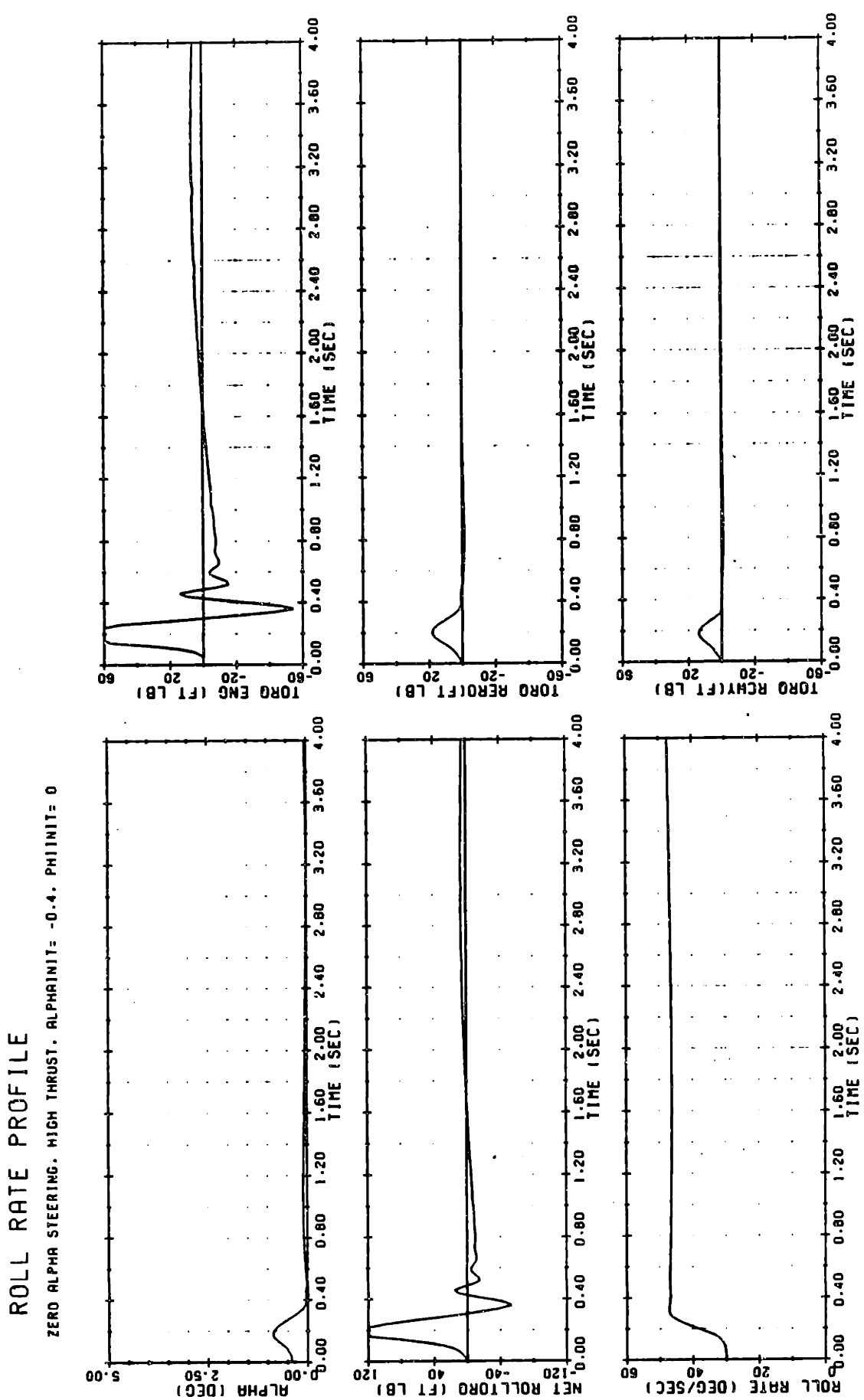

Figure 4-15(B). Roll rate profile for $\alpha_0 = -0.4$, zero-alpha steering.

CHAPTER 5

SECOND STAGE TRAJECTORY OPTIMIZATION SUBJECT TO AN AERODYNAMIC LOADING CONSTRAINT

5.1 Introduction

This chapter examines different steering methods in the second stage flight phase, in an attempt to optimize the second stage trajectory. The stated second stage trajectory goals are to boost the vehicle to a specified staging altitude, and to minimize the velocity to be gained through thrust application in the third stage. Chapter 3 showed that an exponential steering law can be used to command a thrust direction history that carries the vehicle to a desired staging altitude from a variety of staging conditions. Chapter 3, however, did not discuss the ability of the exponential steering law to minimize the velocity to be gained. In this chapter, an iterative numerical algorithm will be developed to find second stage thrust direction histories which minimize the third stage velocity to be gained for a variety of initial staging conditions and desired final altitudes. An aerodynamic loading constraint will be imposed upon this optimization. The performance of the exponential steering law will then be compared to the performance of this numerical optimization algorithm, as well as to a more easily implemented optimal steering algorithm, the linear tangent steering law.

In order to clearly analyze the differences between the steering methods, the simulation used in this chapter assumes perfect IMU measurements, and limits the motion of the vehicle to translation and rotation in the commanded trajectory plane; therefore, the effect of a roll rate constraint on the second stage trajectory will not be considered at this time.

5.2 Optimal Control Formulation for the Second Stage Trajectory

In this section, necessary conditions will be developed for a second stage trajectory which carries the boost vehicle to the desired staging altitude while minimizing the third stage velocity to be gained through thrust application. Referring to Appendix A, the necessary conditions for the optimal control history $\beta(t)$ are:

$$\dot{\bar{x}}(t) = \frac{\partial H}{\partial \bar{p}}(t) \tag{5.1a}$$

$$\dot{\bar{p}}(t) = -\frac{\partial H}{\partial \bar{x}}(t) \tag{5.1b}$$

$$0 = \frac{\partial H}{\partial \beta}(t) \tag{5.1c}$$

subject to the boundary conditions:

$$\bar{x}(t_0) = \bar{x}_0 \tag{5.1d}$$

$$\bar{p}(t_f) = \frac{\partial f}{\partial \bar{x}}(\bar{x}(t_f), t_f) \tag{5.1e}$$

where

$\bar{x}$ is the (nx1) state vector

$\bar{p}$ is the (nx1) costate vector

β is the angle between the commanded thrust vector and the horizon

H is the Hamiltonian for the optimization problem

t_f is the "terminal time" (time of second stage burnout)

$f(\bar{x}(t_f), t_f)$ is the terminal penalty function

The task at hand is then to construct an optimization state model, introduce appropriate performance constraints, and develop a suitable performance measure, so that necessary conditions can be determined in the form of Equations (5.1a-e).

5.2.1 Optimization State Model

The optimization state model is based on the vehicle's equations of motion. Assuming no deflection of the engine nozzle, the equations of motion in the velocity coordinate frame are:

$$M \begin{bmatrix} \dot{V} \\ 0 \\ V\dot{\gamma} \end{bmatrix} = \begin{bmatrix} T\cos\alpha - S\,Q\,CN_\alpha\,\alpha\sin\alpha - S\,Q\,CA\cos\alpha - Mg\sin\gamma \\ 0 \\ T\sin\alpha + S\,Q\,CN_\alpha\,\alpha\cos\alpha - S\,Q\,CA\sin\alpha - Mg\cos\gamma \end{bmatrix} \tag{5.2}$$

where all variables are as defined in Figure 5-1. Since the aerodynamic parameters CA and CN_α are slowly varying at the high mach number of the second stage atmospheric flight phase, they are modelled as constants in this analysis.

For small values of α, $\sin\alpha$ is approximately equal to α. Assuming that α is small during the atmospheric portion of the second stage flight phase, the equation for $\dot{V}$ contains a second order term in α that can be ignored. Equation 5.2 can then be simplified:

$$M \begin{bmatrix} \dot{V} \\ 0 \\ V\dot{\gamma} \end{bmatrix} = \begin{bmatrix} (T - S\,Q\,CA)\cos\alpha - Mg\sin\gamma \\ 0 \\ (T - S\,Q\,CA)\sin\alpha + S\,Q\,CN_\alpha\,\alpha\cos\alpha - Mg\cos\gamma \end{bmatrix} \tag{5.3}$$

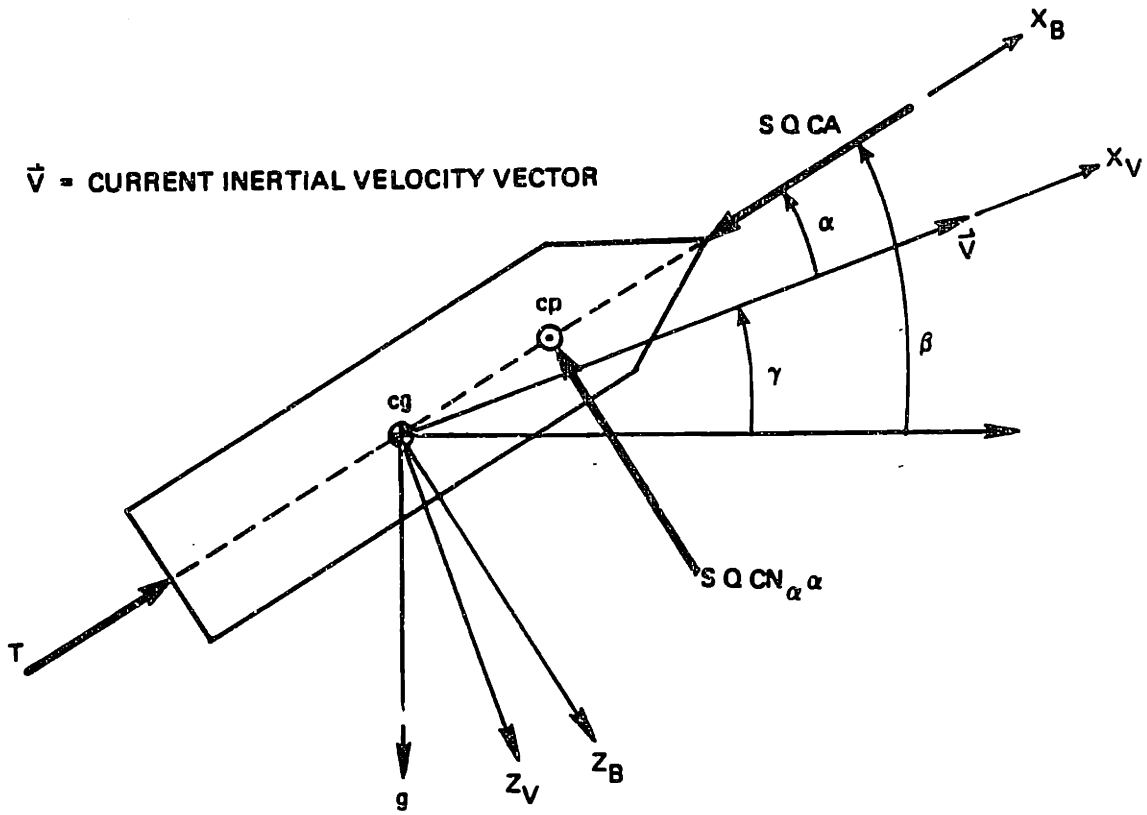

X_B, Z_B	=	BODY-FIXED COORDINATE AXES
X_V, Z_V	=	VELOCITY COORDINATE AXES
T	=	THRUST
SQCA	=	AERODYNAMIC AXIAL FORCE
$SQCN_\alpha\alpha$	=	AERODYNAMIC NORMAL FORCE
β	=	COMMANDED THRUST ANGLE
γ	=	FLIGHT PATH ANGLE
α	=	ANGLE OF ATTACK
g	=	GRAVITATIONAL ACCELERATION VECTOR

Figure 5-1. Applied forces relative to the velocity coordinate frame.

Assuming the thrust vector lies close to the vehicle's longitudinal axis and the effects of winds are small:

$$\alpha \approx \beta - \gamma \tag{5.4}$$

Substituting the above approximation into the equations of motion:

$$M \begin{bmatrix} \dot{V} \\ 0 \\ V\dot{\gamma} \end{bmatrix} = \begin{bmatrix} (T - S\,\varrho\,CA)\cos(\beta-\gamma) - Mg\sin\gamma \\ 0 \\ (T - S\,Q\,CA)\sin(\beta-\gamma) + S\,\varrho\,CN_{\alpha}\,(\beta-\gamma)\cos(\beta-\gamma) - Mg\cos\gamma \end{bmatrix} \tag{5.5}$$

Since the staging altitude is a variable of interest, altitude must be included in the optimization state model. The altitude rate may be defined in terms of V and γ:

$$\dot{h} = V\sin\gamma \tag{5.6}$$

The dynamic pressure ϱ affects the rate of change of both the magnitude and direction of the vehicle's velocity vector. Therefore, ϱ should be included as a state in the optimization model. Simulations have shown that following I/II stage separation, Q falls sharply as the atmospheric density decreases with altitude. A crude equation for the rate of change of ϱ may then be formed from the existing state variables:

$$\dot{\varrho} = K_{\varrho}\,\dot{h} = K_{\varrho}\,V\sin\gamma \tag{5.7}$$

where K_{ϱ} represents the rate of change of ϱ with height in the vicinity of the I/II staging altitude.

Combining all equations developed so far, the trajectory may be optimized using a model with four state variables and one control variable:

$x_1 = h$ = altitude (ft)

$x_2 = V$ = magnitude of the inertial velocity vector (ft/sec)

$x_3 = \gamma$ = flight path angle (deg)

$x_4 = Q$ = dynamic pressure (psf)

$u = \beta$ = commanded thrust angle in the trajectory plane (deg)

The state equations are:

$$\dot{h} = V \sin\gamma \tag{5.8a}$$

$$\dot{V} = \frac{(T - S\,Q\,CA)\cos(\beta-\gamma)}{M} - g\sin\gamma \tag{5.8b}$$

$$\dot{\gamma} = \frac{(T - S\,Q\,CA)\sin(\beta-\gamma) + S\,Q\,CN_\alpha\,(\beta-\gamma)\cos(\beta-\gamma)}{MV} - \frac{g\cos\gamma}{V} \tag{5.8c}$$

$$\dot{Q} = K_Q\,V\sin\gamma \tag{5.8d}$$

It is important to note that although M, the mass of the boost vehicle, is certainly time variant, it is not necessary to define M in the optimization state model. In this boost vehicle, the mass flow is not controllable; therefore, the mass flow rate cannot be optimized. It is only necessary to include M in the differential equations, without defining M itself as an optimization state.

5.2.2 Performance Measure

One of the goals of the second stage trajectory is to minimize the magnitude of the velocity to be gained through thrust application in the third stage. For a known third stage burn duration t_3, $\bar{V}_{GO}$ at the end of the second stage flight phase is given by:

$$\bar{V}_{GO} = \bar{V}_{REQ} - \bar{g}\, t_3 - \bar{V}_2 \tag{5.10}$$

where $\bar{V}_{REQ}$ is the total required velocity and $\bar{V}_2$ is the inertial velocity at the end of the second stage burn. Defining:

$$\bar{V}_{DES} = \bar{V}_{REQ} - \bar{g}\, t_3 \tag{5.11}$$

$\bar{V}_{GO}$ may then be expressed as:

$$\bar{V}_{GO} = \bar{V}_{DES} - \bar{V}_2 \tag{5.12}$$

The magnitude of $\bar{V}_{GO}$ may be minimized by minimizing the sum of the squares of its components. Assuming the component of $\bar{V}_{GO}$ out of the trajectory plane to be insignificant, the scalar function to be minimized is :

$$f_1(\bar{x}(t_f)) = \left\{(V_{DES,X} - V(t_f)\cos\gamma(t_f))^2 + (V_{DES,Z} - V(t_f)\sin\gamma(t_f))^2\right\}/2 \tag{5.13}$$

A second goal of the second stage trajectory is to carry the boost vehicle to the desired staging altitude, h_{DES}. It is possible to define a penalty function that assumes large values for even small differences between the actual and desired staging altitude:

$$f_2(\bar{x}(t_f)) = \left\{h_{PENALTY}\,(h(t_f) - h_{DES})^2\right\}/2 \tag{5.14}$$

where $h_{PENALTY}$ is a large positive constant.

The terminal penalty function for the second stage trajectory optimization problem may now be formed as the sum of the individual penalty functions f_1 and f_2:

$$f(\bar{x}(t_f)) = \{h_{PENALTY}\,(h(t_f) - h_{DES})^2 \qquad (5.15)$$

$$+ \; (V_{DES,X} - V(t_f)\cos\gamma(t_f))^2$$

$$+ \; (V_{DES,Z} - V(t_f)\sin\gamma(t_f))^2\}/2$$

The second stage trajectory optimization goals may be stated solely in terms of the states at the terminal time, t_f. Therefore, the performance measure J for this problem is equal to the terminal penalty function; J contains no integral term of the form discussed in Appendix A. Defining the performance measure as a function of β:

$$J(\beta) = \{h_{PENALTY}\,(h(t_f) - h_{DES})^2 \qquad (5.16)$$

$$+ \; (V_{DES,X} - V(t_f)\cos\gamma(t_f))^2$$

$$+ \; (V_{DES,Z} - V(t_f)\sin\gamma(t_f))^2\}/2$$

Note that although β does not appear explicitly in the performance measure, J is an implicit function of β, because $h(t_f)$, $V(t_f)$, and $\gamma(t_f)$ are dependent on the control history $\beta(t)$.

5.2.3 Performance Constraints

A single performance constraint will be imposed on this trajectory optimization problem. The aerodynamic loading factor $Q\alpha$ must be limited to a value smaller than the specified second stage limit of 6000 psf deg. Assuming the thrust vector lies close to the vehicle's longitudinal axis and the effects of winds are small, the $Q\alpha$ constraint may be stated using the existing state variables:

$$Q\,|\beta - \gamma| \leq 6000 \qquad (5.17)$$

Expressing this constraint in the standard form $c(\bar{x},\beta,t) \geq 0$:

$$6000 - Q|\beta - \gamma| \geq 0 \tag{5.18}$$

5.2.4 Hamiltonian

Now that the state model, the performance measure, and the performance constraint have been defined, it is possible to form the Hamiltonian for the optimization problem. Referring to the form of the Hamiltonian constructed in Appendix A, and noting that this optimization problem has no integral term in the performance measure:

$$H = \bar{p}^T(t)\ \bar{a}(\bar{x},\beta,t) + s(t)\ c(\bar{x},\beta,t) \tag{5.19}$$

where s is a "slack variable" associated with the performance constraint. The slack variable behaves like a Lagrange multiplier when the trajectory lies on the performance boundary, but assumes a value of zero when the boundary is not constraining upon the optimization. Expanding the terms in H:

$$\begin{aligned} H = {} & p_1\ V \sin\gamma \\ & + p_2 \left[\frac{(T - S\ Q\ CA)\ \cos(\beta-\gamma)}{M}\right] - g \sin\gamma \\ & + p_3 \left[\frac{(T - S\ Q\ CA)\ \sin(\beta-\gamma) + S\ Q\ CN_\alpha\ (\beta-\gamma)\ \cos(\beta-\gamma)}{M\ V} - \frac{g\ \cos\gamma}{V}\right] \\ & + p_4\ K_Q\ V \sin\gamma \\ & + s\ [6000 - Q(\beta - \gamma)] \end{aligned} \tag{5.20}$$

5.2.5 Necessary Conditions

Applying Equations (5.1a) through (5.1e) to the Hamiltonian, the necessary conditions to be satisfied by the optimal second stage

trajectory are:

STATE EQUATIONS

$$\dot{h} = V \sin\gamma \tag{5.21a}$$

$$\dot{V} = \frac{(T - S\,Q\,CA)\cos(\beta-\gamma)}{M} - g\sin\gamma \tag{5.21b}$$

$$\dot{\gamma} = \frac{(T - S\,Q\,CA)\sin(\beta-\gamma) + S\,Q\,CN_{\alpha}\,(\beta-\gamma)\cos(\beta-\gamma)}{M\,V} - \frac{g\cos\gamma}{V} \tag{5.21c}$$

$$\dot{Q} = K_{Q}\,V\sin\gamma \tag{5.21d}$$

COSTATE EQUATIONS

$$\dot{p}_1 = 0 \tag{5.22a}$$

$$\dot{p}_2 = -p_1\sin\gamma \tag{5.22b}$$

$$+ p_3\left[\frac{(T - S\,Q\,CA)\sin(\beta-\gamma) + S\,Q\,CN_{\alpha}\,(\beta-\gamma)\cos(\beta-\gamma)}{M\,V^2} - \frac{g\cos\gamma}{V^2}\right]$$

$$- p_4\,K_{Q}\sin\gamma$$

$$\dot{p}_3 = -p_1\,V\cos\gamma + p_2\,g\cos\gamma \tag{5.22c}$$

$$+ p_3\left[\frac{(T - S\,Q\,CA + S\,Q\,CN_{\alpha})\cos(\beta-\gamma)}{M\,V} - \frac{g\sin\gamma}{V}\right]$$

$$- p_4\,K_{Q}\,V\cos\gamma - s\,Q$$

$$\dot{p}_4 = p_2 \frac{(S\ CA \cos(\beta-\gamma))}{M} + p_3 \frac{S\ CA \sin(\beta-\gamma) - S\ CN_\alpha\ (\beta-\gamma) \cos(\beta-\gamma)}{M\ V} + s\ (\beta-\gamma) \tag{5.22d}$$

CONTROL EQUATION

$$0 = p_3 \frac{(T - S\ Q\ CA + S\ Q\ CN_\alpha) \cos(\beta-\gamma)}{M\ V} - p_2 \frac{(T - S\ Q\ CA) \sin(\beta-\gamma)}{M} - s\ Q \tag{5.23}$$

INITIAL CONDITIONS

$$h(t_0) = h_{STG} \tag{5.24a}$$

$$V(t_0) = V_{STG} \tag{5.24b}$$

$$\gamma(t_0) = \gamma_{STG} \tag{5.24c}$$

$$Q(t_0) = Q_{STG} \tag{5.24d}$$

FINAL CONDITIONS

$$p_1(t_f) = h_{PENALTY}(h(t_f) - h_{DES}) \tag{5.25a}$$

$$p_2(t_f) = V(t_f) - V_{DES,X} \sin\gamma(t_f) - V_{DES,Z} \cos\gamma(t_f) \tag{5.25b}$$

$$p_3(t_f) = V(t_f) \left[V_{DES,X} \sin\gamma(t_f) - V_{DES,Z} \cos\gamma(t_f)\right] \tag{5.25c}$$

$$p_4(t_f) = 0 \tag{5.25d}$$

The subscript STG refers to the value of the specified variable at I/II stage separation.

When the performance boundary is not constraining upon the optimization, the current states and costates are calculated using Equations (5.21) and (5.22) with the slack variable s equal to zero, and the optimal control β is determined by the control equation, Equation (5.23). When the trajectory becomes constrained by the performance boundary, β is calculated according to the constraint condition, Equation (5.18), and a value for s may then be determined using the control equation. This value of s is then used to calculate the current states and costates.

5.3 Numerical Solution of the Second Stage Trajectory Optimization Problem Using a Steepest Descent Algorithm

The problem defined by Equations (5.21) through (5.25) in the preceding section is termed a two-point boundary value problem, because the given boundary conditions are split between the initial and final times. It is not generally possible to solve two-point boundary value problems using purely analytical methods. Therefore, an algorithm has been developed that iterates Equations (5.21) through (5.25) to determine the optimal control history, $\beta(t)$. This numerical technique, termed the steepest descent algorithm by Denham and Bryson in Reference [3], is described subsequently.

The concept behind the steepest descent algorithm springs from an analogous calculus problem. In order to find the minimum of a function in differential calculus, one must evaluate the slope, or gradient, of the function at the current point, and then move in the direction of the gradient. When the magnitude of the gradient is zero, a local minimum has been found. In the second stage trajectory optimization problem, we wish to find the minimum of the augmented functional J_A. The first variation of J_A, δJ_A, may be defined using the Hamiltonian:

$$\delta J_A = \left[\frac{\partial f}{\partial \bar{x}}(\bar{x}(t_f),t_f) - \bar{p}(t_f)\right]^T \delta\bar{x}(t_f) \qquad (5.26)$$

$$+ \int_{t_o}^{t_f} \left\{\left[\dot{\bar{p}}(t) + \frac{\partial H}{\partial \bar{x}}(t)\right] \delta\bar{x}(t) + \frac{\partial H}{\partial \beta}(t)\, \delta\beta(t)\right.$$

$$\left. + \left[\bar{a}(\bar{x},\beta,t) - \dot{\bar{x}}(t)\right]^T \delta\bar{p}(t)\right\} dt$$

Suppose that some nominal control history can be used to solve the state and costate equations (Equations (5.21) and (5.22)) subject to the specified boundary conditions. All the terms in Equation (5.26) will then equal zero, except for the term multiplying the variation in the control, $\delta\beta(t)$. δJ_A is then given by:

$$\delta J_A = \int_{t_o}^{t_f} \frac{\partial H}{\partial \beta}(t)\, \delta\beta(t)\, dt \qquad (5.27)$$

Since our goal is to minimize J_A, we wish to choose a subsequent control history which will cause a decrease ΔJ_A in the value of J_A. In Reference [7], Kirk states that for minor perturbations in the control history $\delta\beta(t)$, the sign of ΔJ_A is equal to the sign of the variation δJ_A. Thus we wish to make δJ_A negative. If the control history is "varied" as follows:

$$\delta\beta(t) = \beta_{NEW}(t) - \beta_{LAST}(t) = -\tau \frac{\partial H}{\partial \beta}(t) \qquad (5.28)$$

then the resulting variation in J_A is:

$$\delta J_A = -\tau \int_{t_o}^{t_f} \left[\frac{\partial H}{\partial \beta}(t)\right]^2 dt \qquad (5.29)$$

If τ is restricted to positive values, then δJ_A should remain negative, and should approach zero only as the integral of $\frac{\partial H}{\partial \beta}(t)$ approaches zero. When the integral of $\frac{\partial H}{\partial \beta}(t)$ is equal to zero, J_A has reached a relative minimum.

Proper adjustment of the control history according to Equation (5.28) should guarantee that each new value of the performance measure J_A will be at least as small as the value of J_A obtained with the preceding control history. However, adjustment of the control history is dependent on the value of τ. Note that τ itself is not a function of time. A single variable search may then be conducted to find the value of τ that causes the largest decrease in J_A for a given control history This is the theoretical basis of the steepest descent algorithm.

A complete flowchart of the steepest descent optimization algorithm is shown in Figure 5-2. The following steps outline the logic of this algorithm:

(1) A nominally suitable control history $\beta(t)$ is chosen, and stored as a piecewise-constant function in the memory of a digital computer.

(2) Using this nominal control history and given initial conditions, the state equations are integrated from t_0 to t_f, and the resulting state trajectory is stored as a set of piecewise-constant values.

(3) The final values of the costates, $\bar{p}(t_f)$, are computed by substituting the final values of the states and controls into Equation (5.25).

(4) Using the values of $\bar{p}(t_f)$ obtained in Step 3, the costate equations are integrated backward in time from t_f to t_0, using the piecewise-constant values of the states along the trajectory. $\frac{\partial H}{\partial \beta}(t)$ is evaluated along the costate trajectory, and stored as a set of piecewise-constant values.

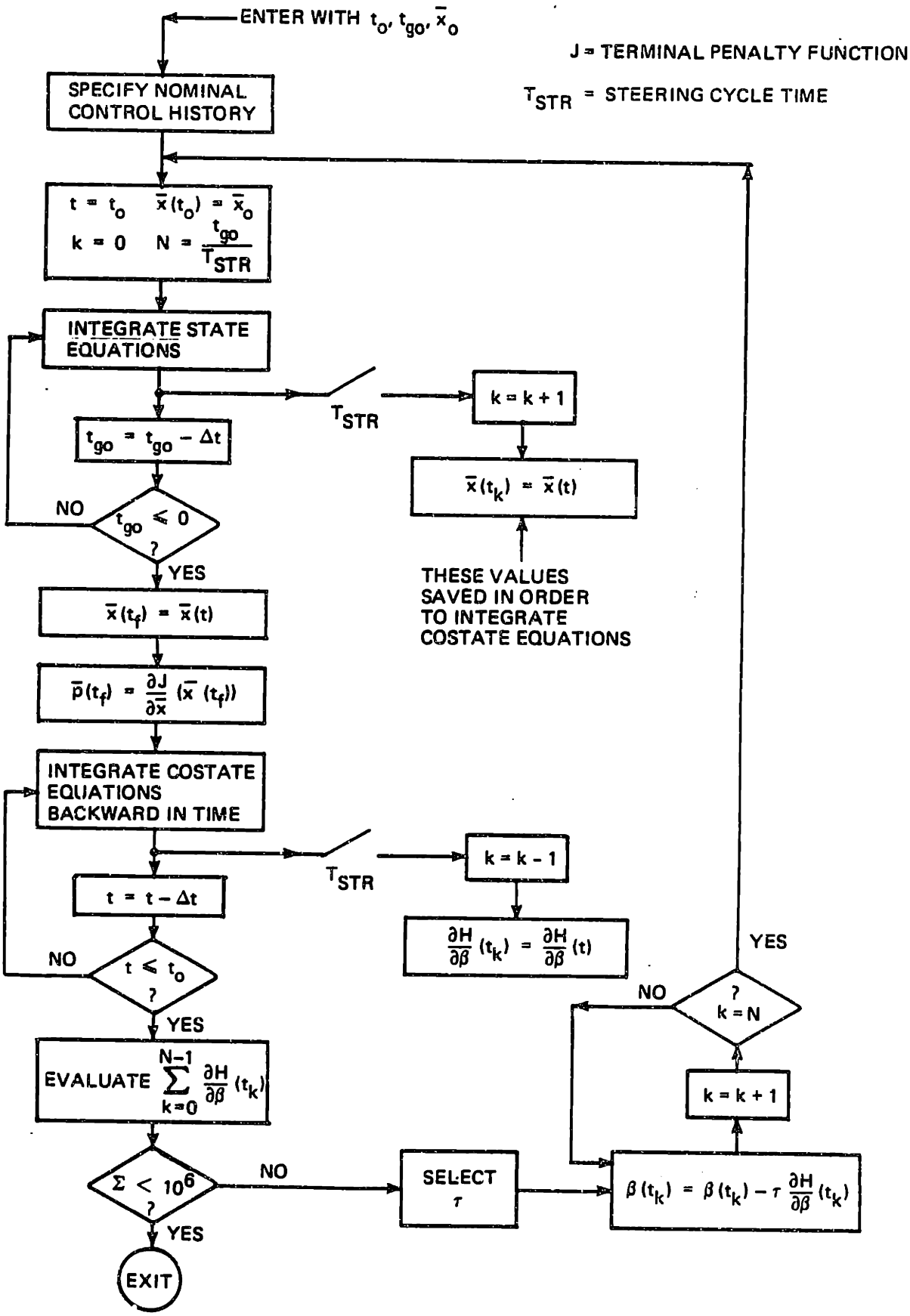

Figure 5-2. Flowchart of the steepest descent optimization algorithm.

(5) If the integral of $\frac{\partial H}{\partial \beta}(t)$ is small enough to indicate that the algorithm has converged upon the optimal trajectory, then the optimal control has been determined and the iterative procedure may be halted. If the stopping criterion is not satisfied, the optimal control history is adjusted according to Equation (5.28):

$$\beta_{NEW}(t_K) = \beta_{LAST}(t_K) - \tau \frac{\partial H}{\partial \beta}(t_K) \qquad (5.30)$$

Using this new trial control history, the algorithm returns to Step 2.

Selection of τ

The convergence properties of the steepest descent algorithm depend on the program's ability to select a proper value of the adjustment gain τ. As mentioned previously, a single variable search may be used to find the value of τ that causes the largest decrease in J_A from a given prior control history. This search, however, can be expensive in terms of computer time and money. Rather than search through a wide range of possible values for the "best" τ, it is usually better to develop a subroutine which quickly guesses a reasonable value for τ. One method for choosing a suitable τ may be formulated by approximating the variation δJ_A as equal to the change in J_A. The percentage change in the value of J_A from one iteration of the algorithm to the next is then approximately:

$$\% \text{ change} = \frac{\delta J_A}{J_A} \times 100 \qquad (5.31)$$

Making use of the relation between τ and δJ_A given in Equation (5.29), a change of P percent in the value of J_A may be achieved by selecting τ as:

$$\tau = \frac{P}{100} \frac{|J_A|}{\int_{t_o}^{t_f} \left[\frac{\partial H}{\partial \beta}(t)\right]^2 dt} \tag{5.32}$$

This method for choosing τ works well when J_A is not in the neighborhood of its minimum value. However, as J_A approaches a minimum, the integral of $\frac{\partial H}{\partial \beta}(t)$ becomes small, and choosing τ according to Equation (5.32) may result in a severe adjustment of the control history. Therefore, allowance must be made for redefining τ if there has been an overshoot of the minimum value of J_A. Using the same trial control history, this method keeps selecting different values of τ and evaluates J_A. When a τ is found which decreases the value of J_A, the trial control history is updated and the process is repeated.

Figure 5-3 shows the actual subroutine used to select τ for the optimization problem addressed in this thesis. Initially, the algorithm chooses τ to theoretically reduce J_A by 30% during each trial. When the actual decrease in J_A from one trial to the next becomes less than 5%, J_A is assumed to be approaching its minimum value, and a "steady state" flag (SSFLAG, see Figure 5-3) is set. Once the SSFLAG is set, τ is adjusted using a pair of fixed gains. This pair of gains was empirically chosen to avoid repetitious cycling in the final adjustments of τ. As long as J_A keeps decreasing, τ is doubled between trials. Once this doubling of τ causes an increase in J_A, τ is reduced by a factor of ten. Using the selection subroutine shown in Figure 5-3, the steepest descent algorithm typically converged towards the minimum solution after twenty iterations.

5.4 The Linear Tangent Steering Law

As outlined so far in this chapter, it is theoretically possible to find the commanded thrust direction history that minimizes the third stage velocity to be gained subject to given constraints. However, determination of this "optimal" control history is not an easy task: the steepest descent algorithm must integrate the state and costate equations

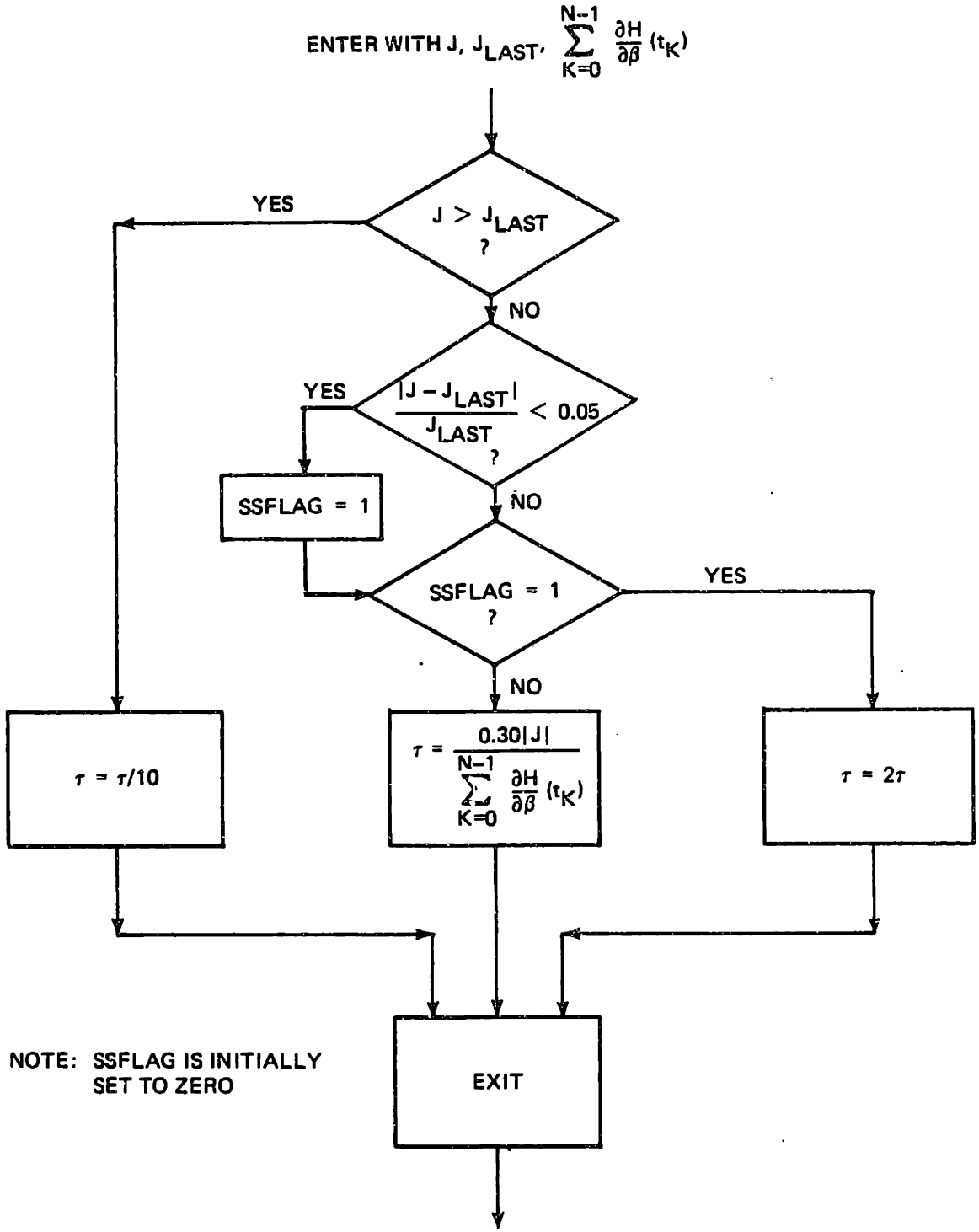

Figure 5-3. Selection of τ.

repeatedly over the entire duration of the second stage burn. Generally, the computer time and memory needed to employ the steepest descent algorithm are not available in the actual flight computer. Therefore, a more efficient means must be found to generate optimal steering commands. In this section, a more easily mechanized algorithm, the linear tangent steering law, is presented and discussed. The performance of the linear tangent steering law, which has already been utilized during Space Shuttle ascent phases, can then be compared with the exponential steering law and the theoretically optimal thrust program in the second stage flight phase of this boost vehicle.

5.4.1 Background and Theory

In Reference [9], Lawden used the calculus of variations to show that the minimum fuel solution for an exoatmospheric ascent trajectory with position and velocity end constraints is achieved when the tangent of the thrust attitude angle varies linearly with time. This result encouraged the development of a family of steering algorithms in which the commanded thrust vector is calculated in the following form:

$$\bar{\beta}(t) = \bar{\beta}_{VGO} + (t - t_{\beta})\,\dot{\bar{\beta}} \tag{5.33}$$

A graphical description of this control history is given in Figure 5-4. $\bar{\beta}_{VGO}$ is a unit vector in the direction of the velocity to be gained through thrust application, and $\dot{\bar{\beta}}$ is a constant vector that determines the angular rotation of the commanded thrust vector, $\bar{\beta}$. Since the magnitude of the vector $(t - t_{\beta})\,\dot{\bar{\beta}}$ changes linearly with time, and the magnitude of $\bar{\beta}_{VGO}$ is unity by definition, the commanded thrust angle β can be determined from:

$$\tan(\beta(t) - \beta_{VGO}) = (t - t_{\beta})\left|\dot{\bar{\beta}}\right| \tag{5.34}$$

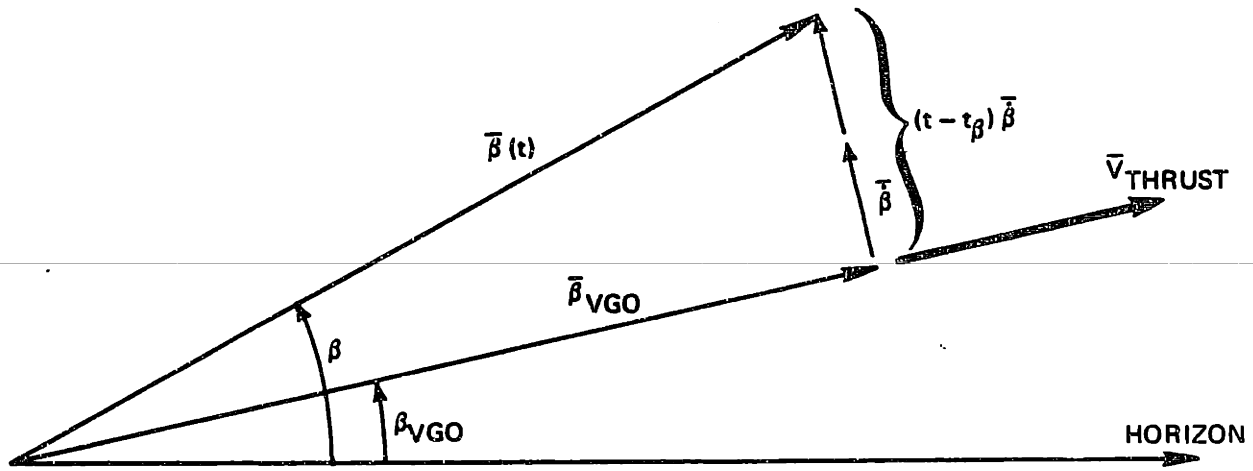

$\bar{\beta}_{VGO}$ = UNIT VECTOR IN THE DIRECTION OF $\bar{V}_{THRUST}$

$\bar{\bar{\beta}}$ = CONSTANT VECTOR PERPENDICULAR TO $\bar{\beta}_{VGO}$

$\bar{\beta}$ = COMMANDED THRUST VECTOR

t_β = TIME AT WHICH $\bar{\beta}$ IS COLINEAR WITH $\bar{\beta}_{VGO}$

Figure 5-4. Vector construction of the linear tangent steering law.

where β_{VGO} is the angle between $\bar{\beta}_{VGO}$ and the horizon. For small angles β and β_{VGO}, the tangent of their difference is approximately equal to the difference of their tangents. Rearranging Equation (5.34) using this approximation:

$$\tan(\beta(t)) = \tan(\beta_{VGO}) + (t - t_\beta)\left|\dot{\bar{\beta}}\right| \qquad (5.35)$$

Thus a steering algorithm employing Equation (5.33) will produce a commanded thrust angle whose tangent varies linearly with time.

In initializing a linear tangent steering law, the task is to choose a set of linear tangent steering parameters β_{VGO}, $\dot{\bar{\beta}}$, and t_β that will guide the vehicle to the desired end conditions. In Reference [11], McHenry and Brand outline a predictor-corrector sequence which may be used to adjust the linear tangent steering parameters during flight in order to guide the vehicle to precise position and velocity end conditions.

5.4.2 Implementation in the Second Stage Flight Phase

The optimality of the linear tangent steering law in the second stage flight phase of this boost vehicle will be somewhat compromised, for two different reasons:

(1) The second stage trajectory is not entirely exoatmospheric.

(2) The second stage steering command $\beta(t)$ may vary over a wide range of angles, violating the small angle approximation used by Equation (5.35).

Nevertheless, implementation of a linear tangent steering law will still provide useful results. For the second stage trajectory optimization problem considered in this chapter, a desired end condition on position is specified (the II/III staging altitude), but there is no explicit velocity requirement. Instead, the second stage trajectory goal is to minimize the velocity to be gained through thrust application in the third stage. Appendix B outlines an algorithm which calculates a set of linear tangent steering parameters that will guide the vehicle to a specified altitude while supplying a total velocity change due to thrust, $\bar{V}_{THRUST}$, which is in a specified direction. This algorithm does not attempt to optimize the magnitude of $\bar{V}_{THRUST}$ when selecting the steering parameters. However, once a set of linear tangent steering parameters has been selected, the magnitude of the velocity which will be gained through thrust application in the second stage can be predicted using Equation (B.13) from Appendix B:

$$\bar{V}_{THRUST} = \bar{\beta}_{VGO}\left[I_1 - \frac{1}{2}\left|\dot{\bar{\beta}}\right|^2(I_3 - 2\,t_\beta\,I_2 + t_\beta{}^2\,I_1)\right] + \dot{\bar{\beta}}(I_2 - t_\beta\,I_1) \tag{5.36}$$

where I_1, I_2, and I_3 are first integrals of the vehicle's acceleration. These integrals differ slightly from those defined in Appendix B, because they include the acceleration due to drag along the nominal thrust second stage trajectory. Using the value of $\bar{V}_{THRUST}$ calculated in Equation (5.36), it is then possible to estimate the third stage velocity to be gained through thrust application, $\bar{V}_{3GO}$. Assuming $\bar{V}_{THRUST}$ is actually achieved by thrust application in the second stage:

$$\bar{V}_{3GO} = \bar{V}_{REQ} - (\bar{V}_{THRUST} + \bar{g}\,(t_{GO} + t_3)) \tag{5.37}$$

where $\bar{V}$ is the current inertial velocity, t_{GO} is the remaining second stage burn time, and t_3 is the third stage burn time.

Using the algorithm outlined in Appendix B to select a set of linear tangent steering parameters for a given direction of $\bar{V}_{THRUST}$, an outer search algorithm can then be constructed to find the best direction of $\bar{V}_{THRUST}$. Referring to Figure 5-4, the angle between the specified $\bar{V}_{THRUST}$ and the horizon is β_{VGO}. Thus the outer search algorithm can specify an angle β_{VGO}, call the selection routine, then estimate the $\bar{V}_{3GO}$ which would result if these steering parameters were actually used in the second stage flight phase. Since every set of selected steering parameters will satisfy the staging altitude constraint, the outer algorithm need only concern itself with finding the angle β_{VGO} which minimizes its estimate of $\bar{V}_{3GO}$.

A flowchart of the outer search algorithm used to find the "best" set of linear tangent steering parameters for the second stage trajectory is shown in Figure 5-5. Since it is only necessary to solve for the parameters at the beginning of a linear tangent steering phase, this algorithm will be referred to as the linear tangent steering initialization algorithm. The outer search algorithm is itself initialized by solving Equation (5.37) for $\bar{V}_{3GO}$ with $\bar{V}_{THRUST}$ equal to zero, and then

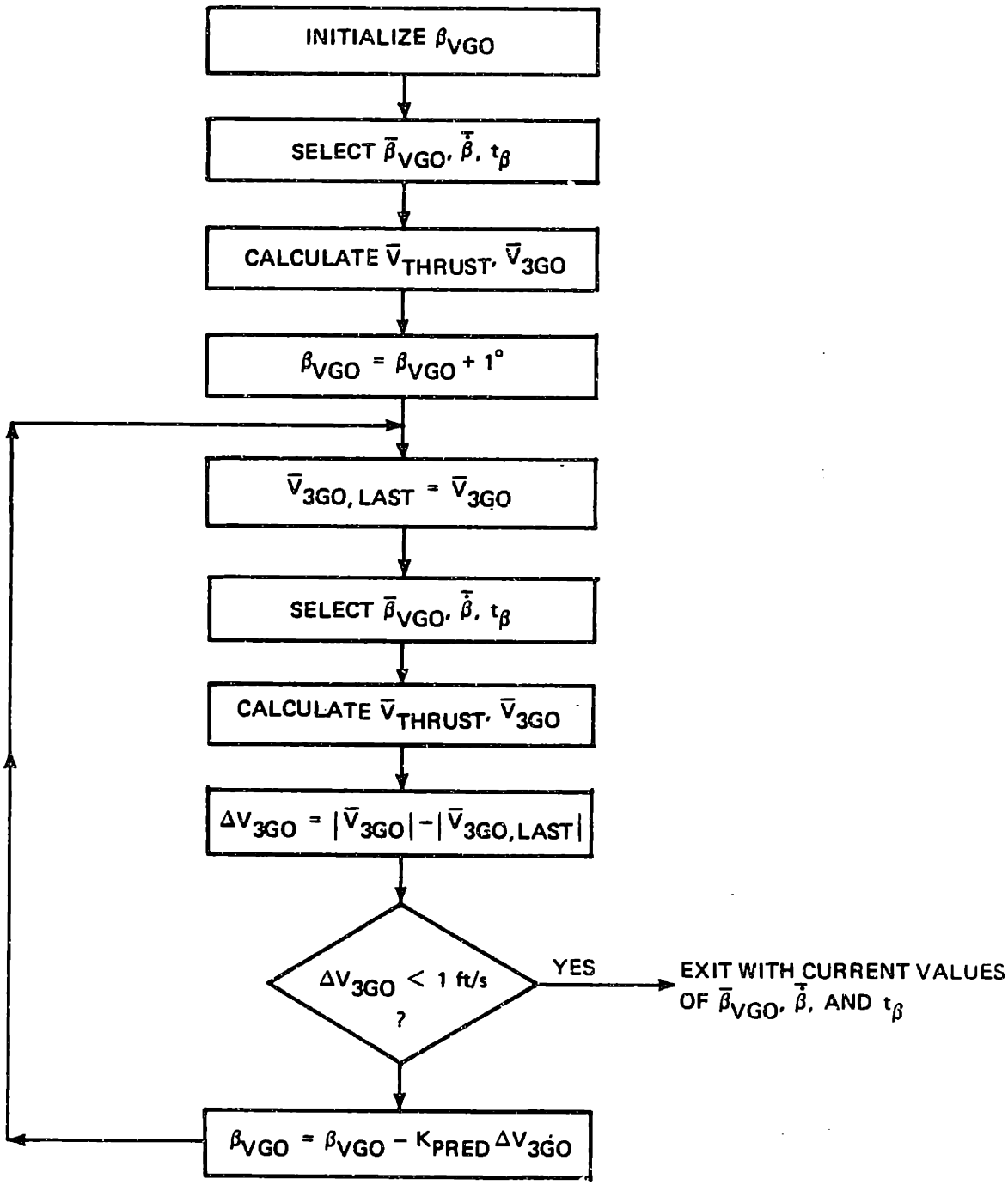

Figure 5-5. Linear tangent steering initialization algorithm.

choosing β_{VGO} equal to the angle between $\bar{V}_{3GO}$ and the horizontal:

$$[\beta_{VGO}]_{INIT} = TAN^{-1} [\frac{V_{3GO,Z}}{V_{3GO,X}}] \quad (5.38)$$

A set of steering parameters is selected, the resulting magnitude of $\bar{V}_{THRUST}$ is calculated using Equation (5.36), and $\bar{V}_{3GO}$ is recalculated and stored as $\bar{V}_{3GO,LAST}$. β_{VGO} is then incremented by one degree, steering parameters are reselected, and $\bar{V}_{3GO}$ is calculated again. The difference in the magnitude of $\bar{V}_{3GO}$ predicted by this one degree rotation of the direction of $\bar{V}_{THRUST}$ is given by:

$$\Delta V_{3GO} = |\bar{V}_{3GO}| - |\bar{V}_{3GO,LAST}| \quad (5.39)$$

β_{VGO} may then be adjusted for the next trial according to:

$$\beta_{VGO} = \beta_{VGO} - K_{PRED} \Delta V_{3GO} \quad (5.40)$$

where K_{PRED} is an appropriately chosen adjustment gain. This process of adjusting β_{VGO} continues until $|\bar{V}_{3GO}|$ converges towards a minimum:

$$\Delta V_{3GO} \leq 1 \text{ ft/sec} \quad (5.41)$$

At this point, the iterative procedure terminates, and the "optimal" set of steering parameters is then saved for use in the linear tangent steering law.

In this thesis, an empirically determined value of 1.15 deg/ft/sec is used for K_{PRED}. Using this value of K_{PRED}, the initialization algorithm typically converges to the best set of linear tangent steering parameters in five to eight iterations.

5.4.3 Mechanization of the Aerodynamic Loading Limit

The implementation of a linear tangent steering law according to Equation (5.33) in no way constrains $\beta(t)$ with respect to the vehicle's

$Q\alpha$ limit during the atmospheric portion of the second stage flight phase. It is therefore necessary to apply an external limit to the steering commands. In this thesis, an approximate $Q\alpha$ limit is imposed on the linear tangent steering law by monitoring the difference between the steering command β and the flight path angle γ (γ is accurately determined by the navigation system during flight). If the quantity $Q|\beta - \gamma|$ is greater than the limit of 6000 psf deg, then β is recalculated according to:

$$\beta = \left(\frac{6000}{Q} + \gamma\right) \text{sign}(\beta - \gamma) \qquad (5.42)$$

The linear tangent steering parameters are calculated under the assumption that the thrust commands will not become constrained. If $\beta(t)$ becomes constrained following calculation of the linear tangent steering parameters, this will cause an error in the II/III staging altitude. Fortunately, since Appendix B shows that the linear tangent steering parameters are calculated as a function of t_{GO}, the linear tangent steering law can be reinitialized at any time during the second stage flight phase. Thus when β becomes constrained according to Equation (5.42), the linear tangent steering law is reinitialized at the next steering cycle, and new steering parameters are selected using the current value of t_{GO}.

5.5 Simulation Results

In order to clearly analyze the differences between the optimization methods, the simulation used to generate the results of this section limits the motion of the second stage vehicle to translation and rotation in the commanded trajectory plane. This so-called pitch plane simulation assumes perfect IMU measurements and a perfect autopilot, so that the actual thrust angle is always equal to the commanded thrust angle. Wind disturbances are not included in the flight environment of any of the second stage trajectories presented in this chapter.

I/II staging conditions produced by the first stage reference trajectories in Chapter 3 are used as initial conditions for the second stage trajectories in the following sections. Thus, there are three

possible sets of I/II staging conditions: those produced by a vehicle with a nominal thrust level, a low thrust level, and a high thrust level. These three sets of staging conditions are listed in Table 5-1.

Table 5-1. I/II staging conditions for second stage trajectory studies.

Thrust Level	$\bar{h}$ (nd)	$\bar{V}$ (nd)	γ (deg)	Q (psf)
Nominal (λ = 1.0)	0.335	0.561	39.84	1342
Low (λ = 0.9)	0.324	0.560	32.78	1506
High (λ = 1.1)	0.336	0.553	47.62	1323

NOTE: λ = Ratio of actual thrust to nominal thrust
$\bar{h}$ = Normalized altitude
$\bar{V}$ = Normalized velocity

5.5.1 Effect of Constraints on the Optimal Thrust Angle History

In order to get a perspective on the abilities of the second stage steepest descent optimization algorithm, this section will briefly illustrate the effects of a staging altitude requirement and the aerodynamic loading constraint on the algorithm's determination of the optimal thrust angle history. In this particular set of studies, the second stage trajectory assumes the nominal second stage thrust level, and originates from the nominal thrust I/II staging conditions shown in Table 5-1.

To establish a baseline for comparison, the steepest descent algorithm first determined the optimal thrust program in the absence of any constraints. $h_{PENALTY}$ was zeroed in the performance measure, so that an error in the II/III staging altitude would not be penalized. The logic of the algorithm was also adjusted to ignore the $Q\alpha$ limit. With no constraints upon the optimization, the optimization algorithm output the thrust angle history $\beta(t)$ shown in Figure 5-6, which resulted in the

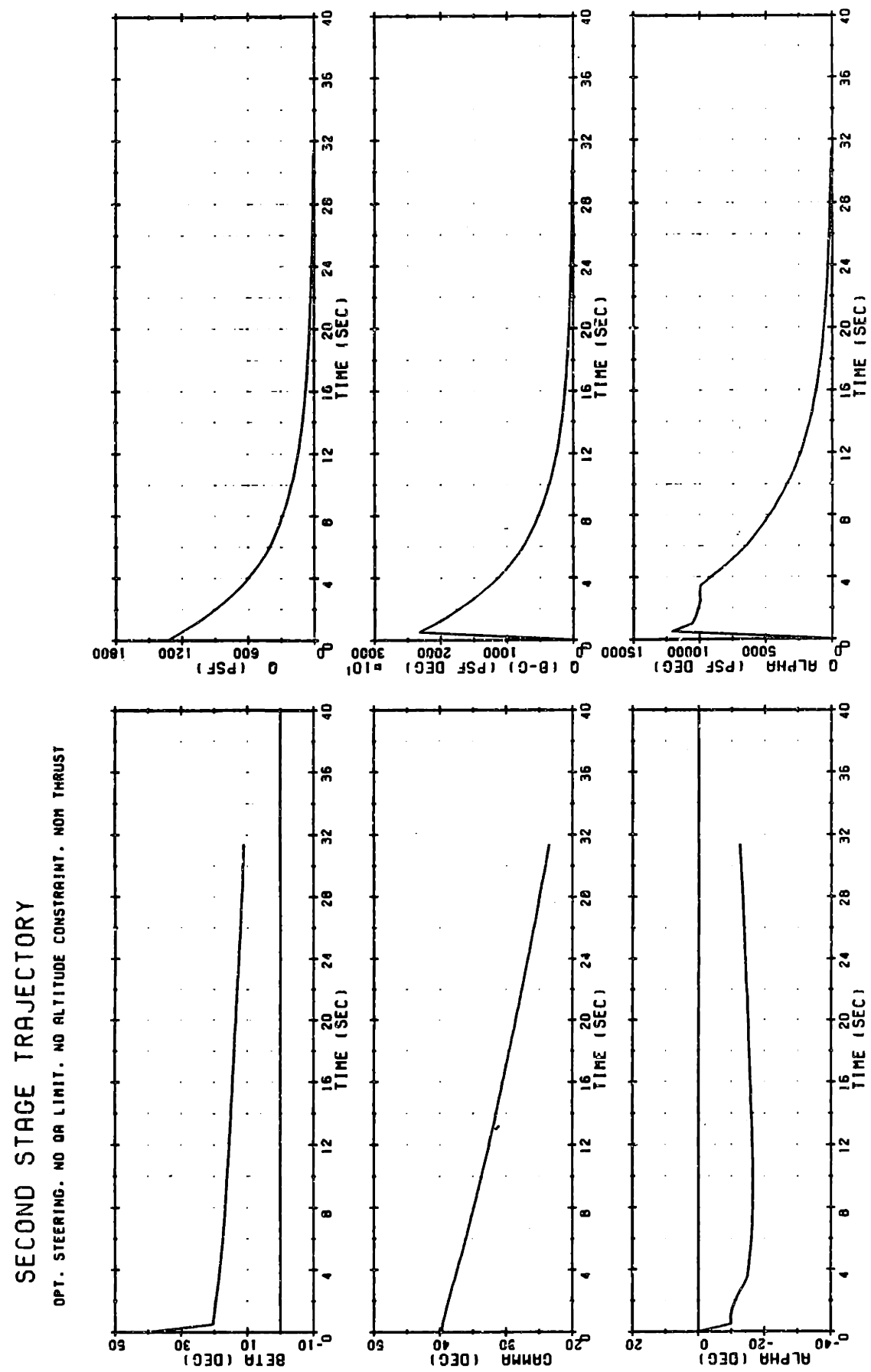

Figure 5-6. Optimal second stage trajectory with no constraints, nominal thrust.

second stage trajectory indicated by the other graphs in that figure. The optimal thrust direction lies well below the velocity vector during the entire flight phase, forcing the vehicle to develop a large negative angle of attack.

Figure 5-7 shows the optimal $\beta(t)$ when the $Q\alpha$ performance constraint is considered by the optimization algorithm. Since the optimization constrains the quantity $Q(\beta-\gamma)$, the vehicle does not actually travel along the $Q\alpha$ boundary. However, $Q\alpha$ is always less than $Q(\beta-\gamma)$, since the engine nozzle deflects to balance the aerodynamic moment created by the angle of attack. For this particular trajectory, consideration of the $Q\alpha$ limit constrained $\beta(t)$ for approximately eight seconds.

Figure 5-8 shows the optimal $\beta(t)$ when a staging altitude requirement is enforced in the algorithm with an appropriately large $h_{PENALTY}$. The optimal $\beta(t)$ is now more inclined with respect to the horizon, because the vehicle must gain more vertical velocity in order to reach the desired altitude.

Table 5-2 illustrates the trade-offs which the optimization algorithm makes in determining the optimal thrust angle history. It is convenient (and more demonstrative) to relate the values of $|\bar{V}_{3GO}|$ to the particular value of $|\bar{V}_{3GO}|$ obtained for the nominal trajectory with optimal steering and both constraints employed. Therefore, values of $|\bar{V}_{3GO}|$ in this and subsequent tables are given in terms of the relative quantity:

$$|\bar{V}_{3GO}|_{REL} = |\bar{V}_{3GO}| - |\bar{V}_{3GO}|_{\substack{\text{Nominal thrust,}\\ \text{optimal steering}\\ \text{with constraints}}} \tag{5.43}$$

For the sake of brevity, the symbol $|\bar{V}_{3GO}|$ will continue to be used in the text, even when referring to values that are tabulated in terms of $|\bar{V}_{3GO}|_{REL}$. Table 5-2 also lists the staging altitude error, h_{ERR} (which is the difference between the actual and desired altitude at II/III staging), and the maximum value of $Q\alpha$ for the three trajectories

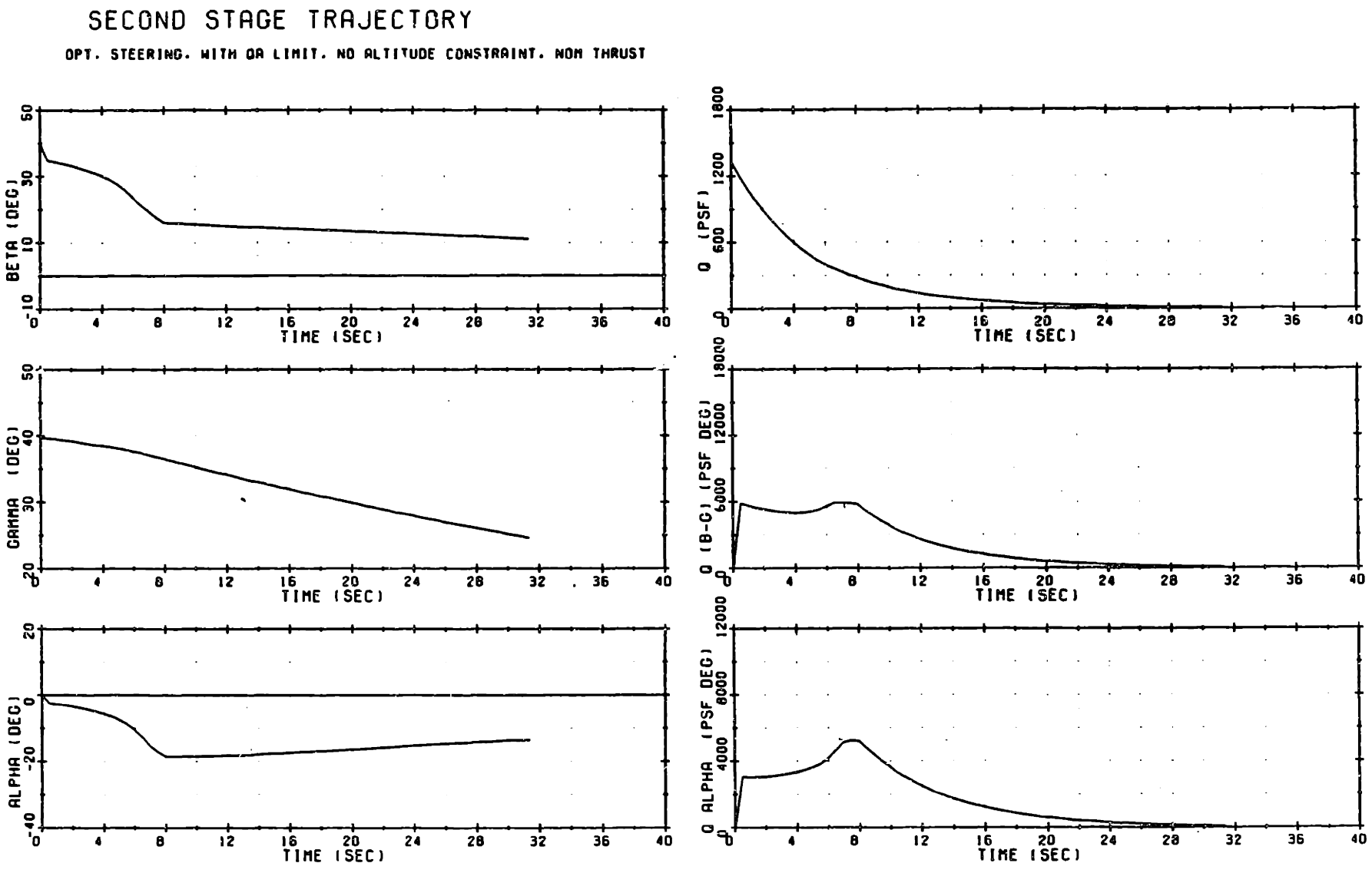

Figure 5-7. Optimal second stage trajectory with Qα constraint, nominal thrust.

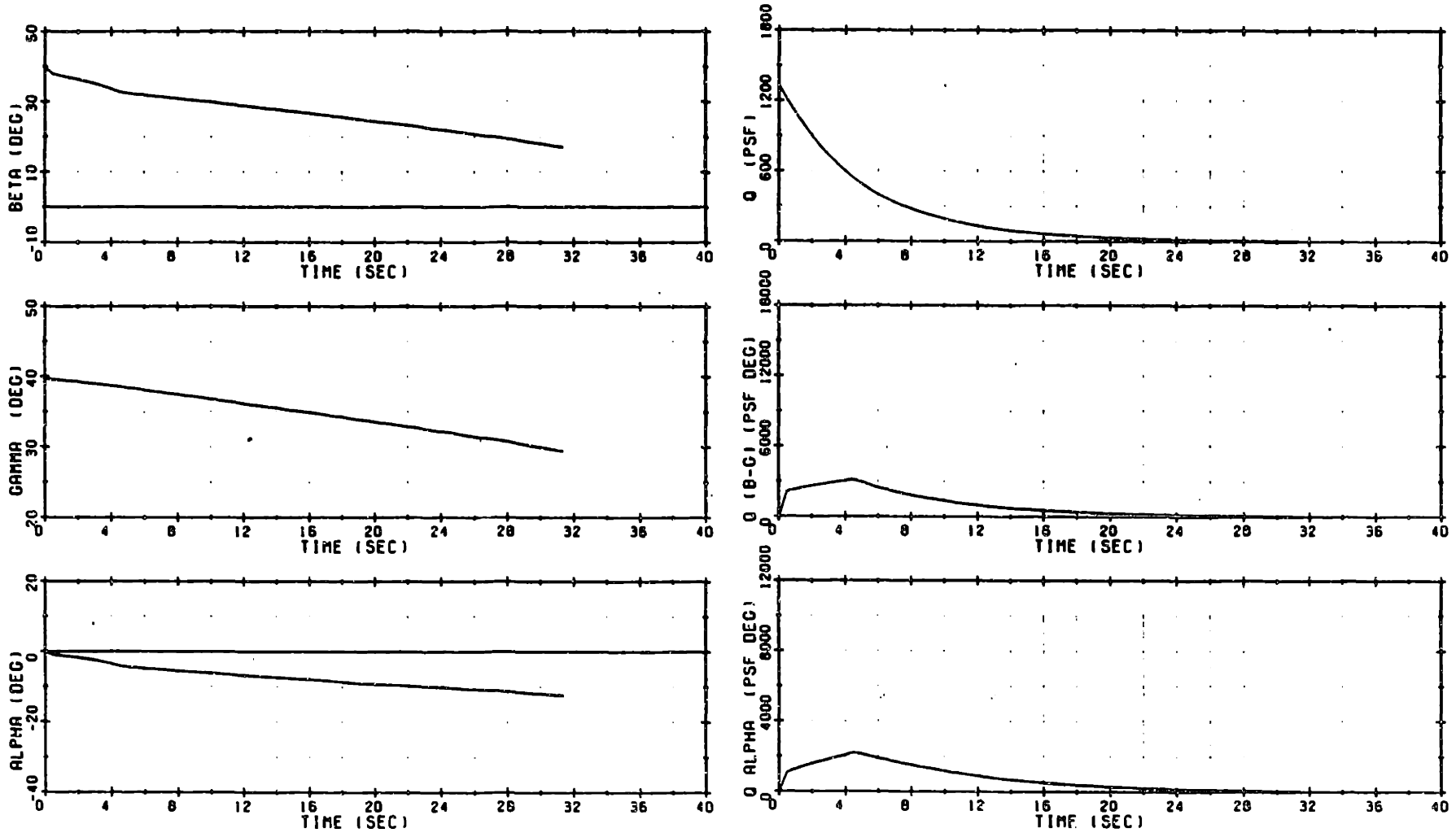

Figure 5-8. Optimal second stage trajectory with Qα constraint and staging altitude requirement, nominal thrust.

Table 5-2. Nominal thrust second stage trajectory data with and without constraints.

Constraints	h_{ERR} (ft)	$Q\alpha_{max}$ (psf deg)	$\left\|\bar{V}_{3GO}\right\|_{REL}$ (ft/sec)
None	-21,466	12,116	-193
$Q\alpha$ Constraint	-15,056	5,255	-151
$Q\alpha$ Constraint and Staging Altitude Requirement	-195	2,208	0

shown in Figures 5-6 through 5-8. When no constraints are imposed on the second stage trajectory, the optimal thrust history causes the vehicle to experience a maximum $Q\alpha$ that is more than double the specified limit of 6000 psf deg. The unconstrained trajectory also leaves the vehicle more than 20,000 feet short of the nominally desired staging altitude. Introduction of the $Q\alpha$ constraint causes an undesirable increase in $\left|\bar{V}_{3GO}\right|$. When the optimization algorithm must consider the staging altitude requirement in its determination of $\beta(t)$, this causes a further increase in $\left|\bar{V}_{3GO}\right|$ of approximately 150 ft/sec.

5.5.2 Comparison of Steering Methods for Three Thrust Levels

The three steering methods were used to command the thrust angle during the second stage flight phase. Starting from each of the three sets of I/II staging conditions shown in Table 5-1, the relevant end conditions achieved by the three steering methods are shown in Table 5-3. At first glance, Table 5-3 appears to show that compared to the exponential steering law, both the optimal thrust program and the linear tangent steering law trade large increases in the staging altitude error for

Table 5-3. Comparison of steering methods for different thrust levels.

Thrust Level	Steering Method	h_{ERR} (ft)	$Q\alpha_{max}$ (psf deg)	$\left\|\bar{V}_{3GO}\right\|_{REL}$ (ft/sec)
Nominal Thrust	Optimal	-195	2,208	0
	Exponential	+170	1,423	56
	Linear Tangent	-741	2,904	32
Low Thrust	Optimal	-655	3,706	119
	Exponential	+199	1,296	352
	Linear Tangent	-444	5,222	165
High Thrust	Optimal	-324	5,354	459
	Exponential	+151	3,663	478
	Linear Tangent	-318	4,295	480

small decreases in $\left|\bar{V}_{3GO}\right|$. In actuality, it is unfair to compare percentage changes in these quantities. For the high velocity of the vehicle at II/III staging, the listed values of h_{ERR} represent timing errors in reaching the desired staging altitude that are on the order of a fraction of a second. In fact, this thesis will consider staging altitude errors of less than 3000 feet to be acceptable. Changes in $\left|\bar{V}_{3GO}\right|$ however, represent additional velocity which must be gained through a longer period of thrust application in the third stage. Therefore, savings of 50 ft/sec in $\left|\bar{V}_{3GO}\right|$ are meaningful.

Compared to the exponential steering law, the optimization algorithm effected the largest reduction in $\left|\bar{V}_{3GO}\right|$ for the low thrust staging conditions. Almost no reduction in $\left|\bar{V}_{3GO}\right|$ could be obtained from the staging conditions produced by the high thrust vehicle. Because

the flight path angle at I/II staging for the low thrust vehicle is very shallow, more vertical velocity must be added during the second stage flight phase to reach the desired staging altitude. The optimal thrust history appears to add the necessary vertical velocity more efficiently than the exponential steering law. For the high thrust first stage trajectory, the velocity vector is much more inclined at I/II staging. Since the vehicle already has a larger vertically velocity component, there is little need for additional vertical velocity to be supplied in the second stage. In this case, the optimal application of thrust is in the direction of $\bar{V}_{GO}$. However, it is not possible to thrust at the low inclination of $\bar{V}_{GO}$ early in the second stage flight phase because of the $Q\alpha$ constraint, as shown by the plots in Figure 5-9.

The linear tangent steering law performs comparably with the exponential steering law for both the nominal thrust and high thrust staging conditions. Although its performance is similar, the thrust history commanded by the linear tangent steering law is markedly different from that of the exponential steering law. This difference is illustrated by Figures 5-10 and 5-11. Figure 5-10 shows the thrust angle history $\beta(t)$ using the exponential steering law for nominal thrust I/II staging conditions; Figure 5-11 shows the thrust angle history commanded by the linear tangent steering law for these same staging conditions. Notice that the linear tangent steering commands cause the vehicle to develop a positive angle of attack early in the second stage flight phase. The linear tangent steering law tends to rotate the thrust command through a wider angle during the second stage flight phase, resulting in a larger maximum value of $Q\alpha$. This maximum value is still well within the specification of 6000 psf deg., however.

For the second stage trajectory from low thrust I/II staging conditions, the linear tangent steering law achieves a large reduction in $|\bar{V}_{3GO}|$ compared to the exponential steering law, similar to the reduction in $|\bar{V}_{3GO}|$ achieved with the optimal thrust angle history. In fact, for all three sets of staging conditions examined, the difference in $|\bar{V}_{3GO}|$ between the linear tangent steering law and the optimal thrust angle history is less than 50 ft/sec.

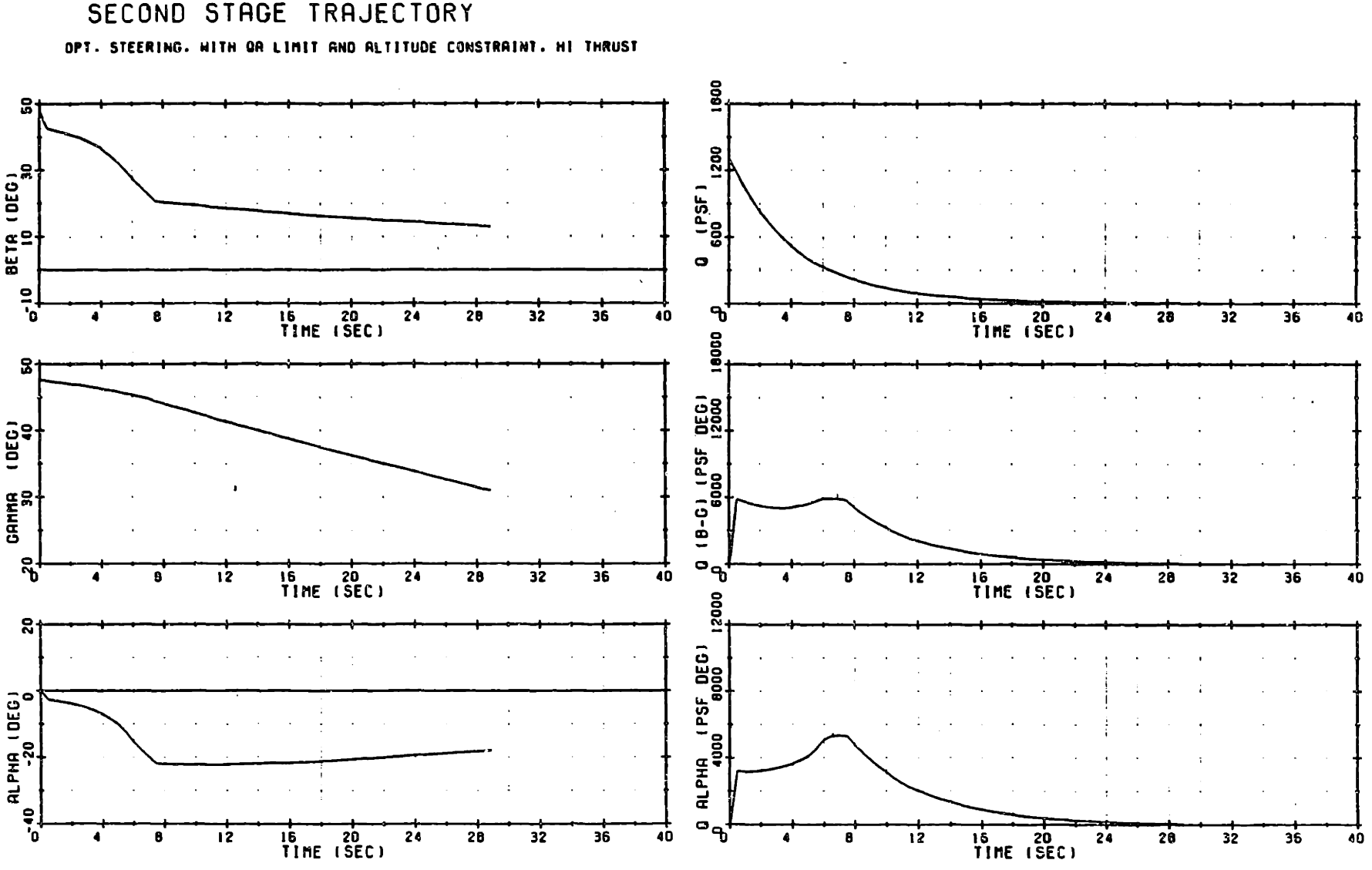

Figure 5-9. Optimal second stage trajectory with Qα constraint and staging altitude requirement, high thrust.

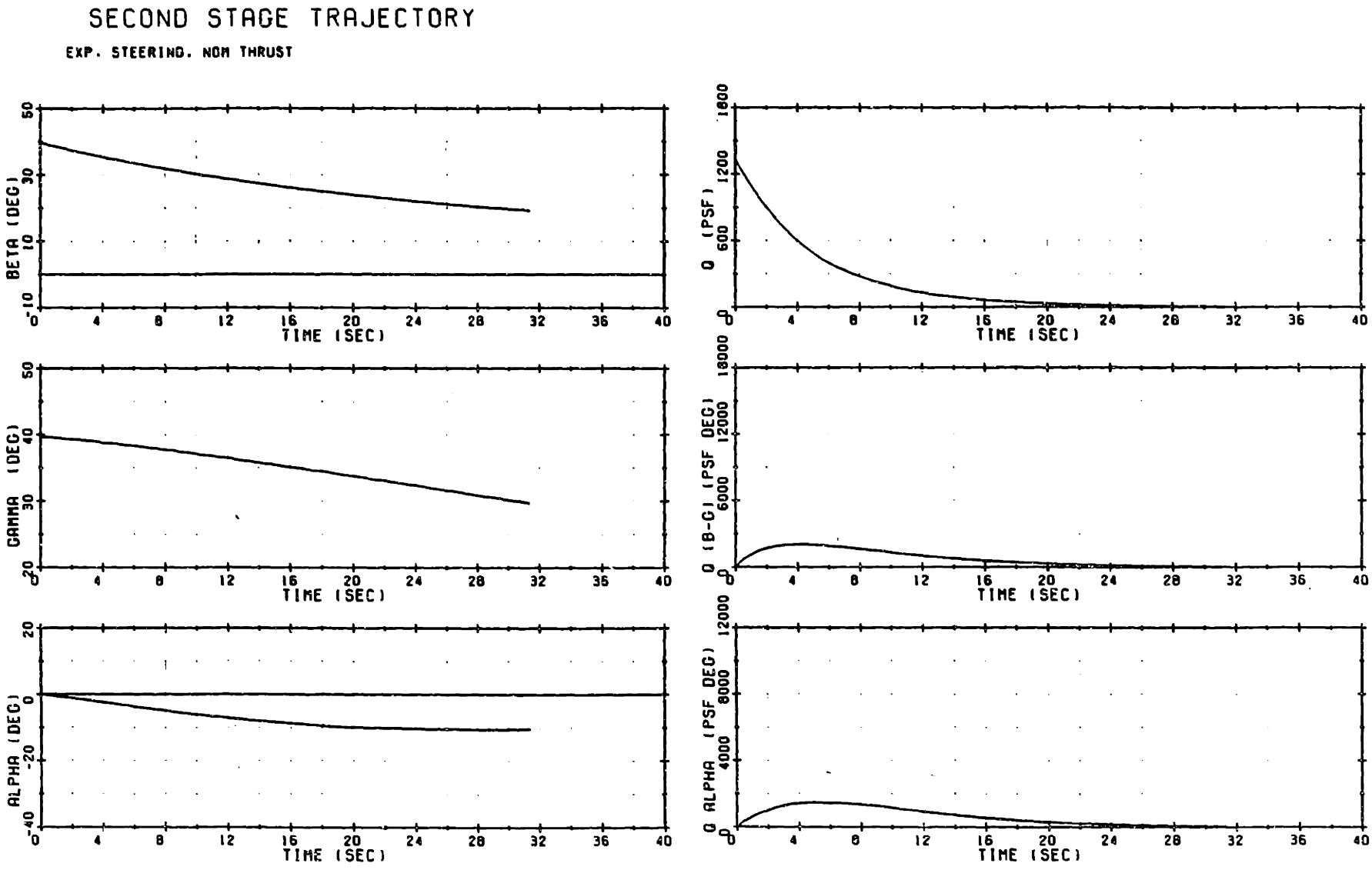

Figure 5-10. Second stage trajectory with exponential steering, nominal thrust.

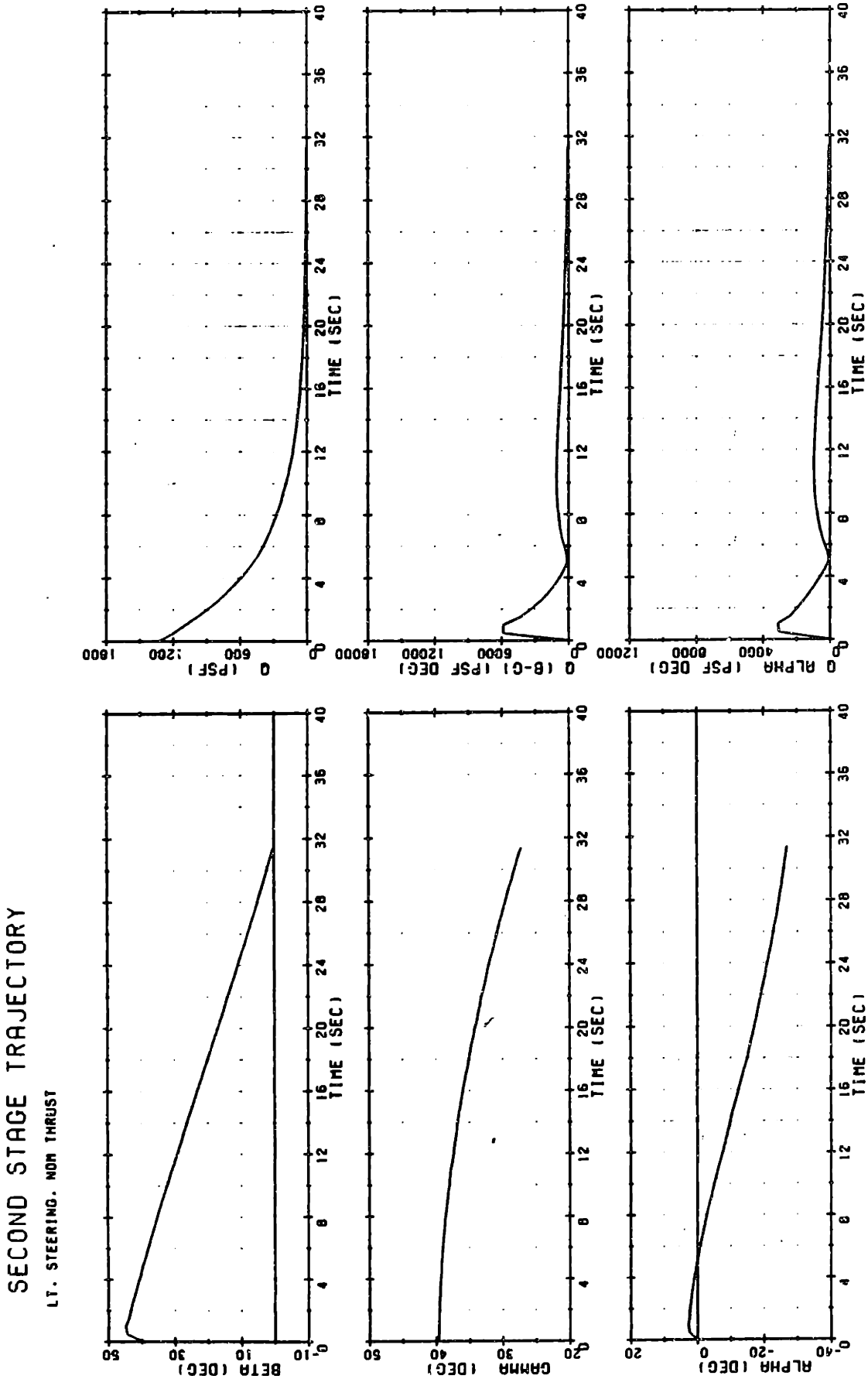

Figure 5-11. Second stage trajectory with linear tangent steering, nominal thrust.

5.5.3 Comparison of Steering Methods for Different II/III Staging Altitudes

In this study, the three steering methods were used to command second stage trajectories which carried the vehicle to a variety of altitudes at II/III staging. All trajectories in this study originate from the nominal thrust I/II staging conditions. The performance of the steering methods is compared in Table 5-4, as a function of the desired staging altitude. Δh_{DES} is the difference between the staging altitude actually specified in these simulations and the nominally specified I/II staging altitude. Table 5-4 illustrates further the trade-off between the desired altitude and the third stage velocity to be gained, $|\bar{V}_{3GO}|$. By increasing the staging altitude requirement from Δh_{DES} = -20,000 to Δh_{DES} = +20,000, $|\bar{V}_{3GO}|$ is increased by 452 ft/sec, even when the optimal thrust history is used.

Table 5-4. Comparison of steering methods for different II/III staging altitudes.

Δh_{DES} (ft)	Steering Method	h_{ERR} (ft)	$Q\alpha_{max}$ (psf deg)	$\|\bar{V}_{3GO}\|_{REL}$ (ft/sec)
-20,000	Optimal	-108	5,449	-141
-20,000	Exponential	+163	3,616	-4
-20,000	Linear Tangent	-97	5,488	-139
-10,000	Optimal	+57	3,566	-128
-10,000	Exponential	+270	2,617	-107
-10,000	Linear Tangent	+120	5,307	-119
0	Optimal	-195	2,208	0
0	Exponential	+170	1,423	56
0	Linear Tangent	-741	2,904	32
+10,000	Optimal	-655	2,910	284
+10,000	Exponential	-159	319	490
+10,000	Linear Tangent	-212	4,014	310
+20,000	Optimal	+11	2,931	311
+20,000	Exponential	-150	1,078	1,303
+20,000	Linear Tangent	+189	4,051	322

Table 5-4 shows that the "optimality" of the exponential steering law depends on the desired II/III staging altitude. For desired staging altitudes in the range of the nominal staging altitude minus 10,000 feet, the performance of the exponential steering law closely resembles the performance of the optimal thrust program. The comparative performance of the exponential steering law diminishes greatly for higher required staging altitudes, however. For Δh_{DES} = +20,000 feet, the other two steering methods are able to achieve a reduction in $|\bar{V}_{3GO}|$ of almost 1000 ft/sec relative to the value of $|\bar{V}_{3GO}|$ when the exponential steering law is used.

The performance of the linear tangent steering law remains nearly optimal for the entire range of II/III staging altitudes. For the required staging altitudes considered in this study, the largest difference found in $|\bar{V}_{3GO}|$ between the linear tangent steering law and the optimal thrust history was 26 ft/sec.

5.5.4 Comparison of Steering Methods Following Zero-Alpha Steering Periods

As discussed in the preceding chapter on staging concerns, there is potential for a large roll rate rate increase following stage separation, in part due to the angle of attack commanded by the second stage steering. As shown in that chapter, it may be desirable to introduce angle of attack feedback and thrust along the velocity vector following stage separation, in order to limit the increase in roll rate. Chapter 4 did not discuss the effects of maintaining a zero angle of attack ("zero-alpha") flight condition on the end conditions of the second stage trajectory. Those effects will be addressed in this section.

Using the pitch plane simulation, the thrust vector was directed along the the vehicle velocity vector for a specified length of time following staging recovery, resulting in a zero-alpha flight condition. Once the specified zero-alpha steering time was reached, the simulation generated the thrust angle command with one of the three available steering algorithms.

Table 5-5 shows the performance of the three steering methods following zero-alpha steering periods of various lengths. This study restricted the I/II staging conditions to those produced by the nominal thrust first stage trajectory. As would be expected, flying in a zero-alpha flight configuration for any period of time reduces the amount of thrust which can be applied to better shape the trajectory, resulting in a loss in ΔV capability. Even when a subsequent optimal thrust angle history is used, the time spent thrusting at zero-alpha leads to an increase in $\left|\bar{V}_{3GO}\right|$. However, the linear tangent steering law does outperform the exponential steering law for increased periods of zero-alpha steering. This result may be explained by the fact that the mechanization of the linear tangent algorithm allows the steering parameters to be recalculated as a function of t_{GO}. In the exponential steering system, the final reference command direction β_{FINAL} is calculated as a function of the thrust estimate made during the launch maneuver, and is not recalculated in the second stage. Therefore, even small periods of zero-alpha steering can severely affect the performance of the exponential steering algorithm.

In Table 5-6, the performance of the various steering modes is compared following second stage zero-alpha flight periods from the I/II staging conditions produced by the high and low thrust first stage trajectories. Once again, the performance of the linear tangent steering law more closely resembles the performance of the theoretically optimal control history. Because the linear tangent steering system can reinitialize itself, with this system it is possible to remain in a zero angle of attack flight configuration for up to four seconds without significantly increasing $\left|\bar{V}_{3GO}\right|$.

Table 5-5. Comparison of steering methods following zero-alpha steering periods, nominal staging conditions.

t_{ZA} (sec)	Steering Method	h_{ERR} (ft)	$Q\alpha_{max}$ (psf deg)	$\lvert\bar{V}_{3GO}\rvert_{REL}$ (ft/sec)
0	Optimal	-195	2,208	0
0	Exponential	+170	1,423	56
0	Linear Tangent	-741	2,904	32
2.0	Optimal	-607	3,027	22
2.0	Exponential	+1,548	1,238	89
2.0	Linear Tangent	-174	2,810	55
4.0	Optimal	+20	982	24
4.0	Exponential	+3,227	920	134
4.0	Linear Tangent	-95	1,838	62
6.0	Optimal	+129	1,602	27
6.0	Exponential	+4,717	652	178
6.0	Linear Tangent	-9	959	68
8.0	Optimal	+379	1,166	33
8.0	Exponential	+6,031	473	222
8.0	Linear Tangent	+70	665	71

Table 5-6. Comparison of steering methods following zero-alpha steering periods, off-nominal staging conditions.

t_{ZA} (sec)	Steering Method	h_{ERR} (ft)	$Q\alpha_{max}$ (psf deg)	$\lvert\bar{V}_{3GO}\rvert_{REL}$ (ft/sec)
Low Thrust Staging Conditions				
0	Optimal	-655	3,706	119
	Exponential	+199	1,296	352
	Linear Tangent	-444	5,222	165
4.0	Optimal	-99	4,858	168
	Exponential	-1,975	893	299
	Linear Tangent	-563	5,316	190
8.0	Optimal	-189	5,307	233
	Exponential	-4,151	560	218
	Linear Tangent	+228	5,437	294
High Thrust Staging Conditions				
0	Optimal	-324	5,354	459
	Exponential	+151	3,663	478
	Linear Tangent	-318	4,295	480
4.0	Optimal	-205	5,408	483
	Exponential	+7,878	2,008	633
	Linear Tangent	+211	5,184	509
8.0	Optimal	-504	5,538	575
	Exponential	+14,844	911	846
	Linear Tangent	-174	5,539	573

CHAPTER 6

SECOND STAGE TRAJECTORY OPTIMIZATION SUBJECT TO A ROLL RATE CONSTRAINT

6.1 Introduction

Chapters 3 and 4 showed that angle of attack excursions earlier in the boost mission can cause the vehicle to develop a high roll rate prior to the second stage flight phase. This chapter addresses the problem of roll rate control during the second stage flight phase, assuming that the second stage inherits a roll rate which is below the specified limit of 50 deg/sec. The second stage roll rate need not be actively controlled or even reduced; it must simply be constrained to remain below this limit.

In this chapter, a theoretical relationship is developed between the current roll rate and the maximum subsequent roll rate attributable to quasi-steady state forces on the vehicle. The ability of this theory to predict a future worst-case roll rate will be discussed, and then compared with roll simulations of the second stage vehicle. It will be shown that the roll rate can be limited by imposing a limit on the aerodynamic normal force. This roll rate imposed aerodynamic normal force limit will generally be smaller than the limit associated with the aerodynamic loading constraint.

In a flight control system, an aerodynamic normal force limit may be imposed by employing feedback control to limit the vehicle's angle of attack. Using the angle of attack feedback system introduced in Chapter 4, a hybrid autopilot will be implemented to mix and/or replace steering attitude errors with angle of attack error signals as the vehicle nears a predetermined angle of attack limit. The effect of the roll rate

constraint on the angle of attack limit and its subsequent effects on the "optimal" second stage trajectories will then be discussed.

6.2 Worst-Case Maximum Roll Rate Prediction

This section analyzes the roll torques applied to the vehicle during the second stage flight phase, in an attempt to predict the maximum roll rate increase attributable to an aerodynamic normal force of constant magnitude and inertial orientation. A worst-case maximum roll rate predictor will be developed theoretically, and then tested through roll simulations of the second stage vehicle.

6.2.1 Theoretical Prediction of the Worst-Case Maximum Roll Rate

As shown in Chapter 3, the instantaneous roll acceleration of the vehicle is the result of the separate contributions of three roll torque components:

$$\ddot{\phi} = \frac{\text{ROLLTORQ}_{ENG} + \text{ROLLTORQ}_{AERO} + \text{ROLLTORQ}_{RCWY}}{I_X} \qquad (6.1)$$

Neglecting the component of the applied roll torque produced by the raceway, which is relatively small at the high mach number of the second stage flight phase, the applied roll torque is approximately equal to the summed cross products of the thrust and aerodynamic normal forces and their corresponding offset vectors. Expressing the cross products in scalar form, the resulting equation for $\ddot{\phi}$ is:

$$\ddot{\phi} = \frac{\left|\bar{R}_{HNG}\right| \left|\bar{F}_{ENG}\right| \sin\phi_T + \left|\bar{R}_{CP}\right| \left|\bar{FAERO}\right| \sin\phi_A}{I_X} \qquad (6.2)$$

where all symbols are as defined in Figure 6-1. For given flight conditions, the largest roll torques are applied when the magnitudes of the offset vectors $\bar{R}_{HNG}$ and $\bar{R}_{CP}$ are equal to the maximum values specified

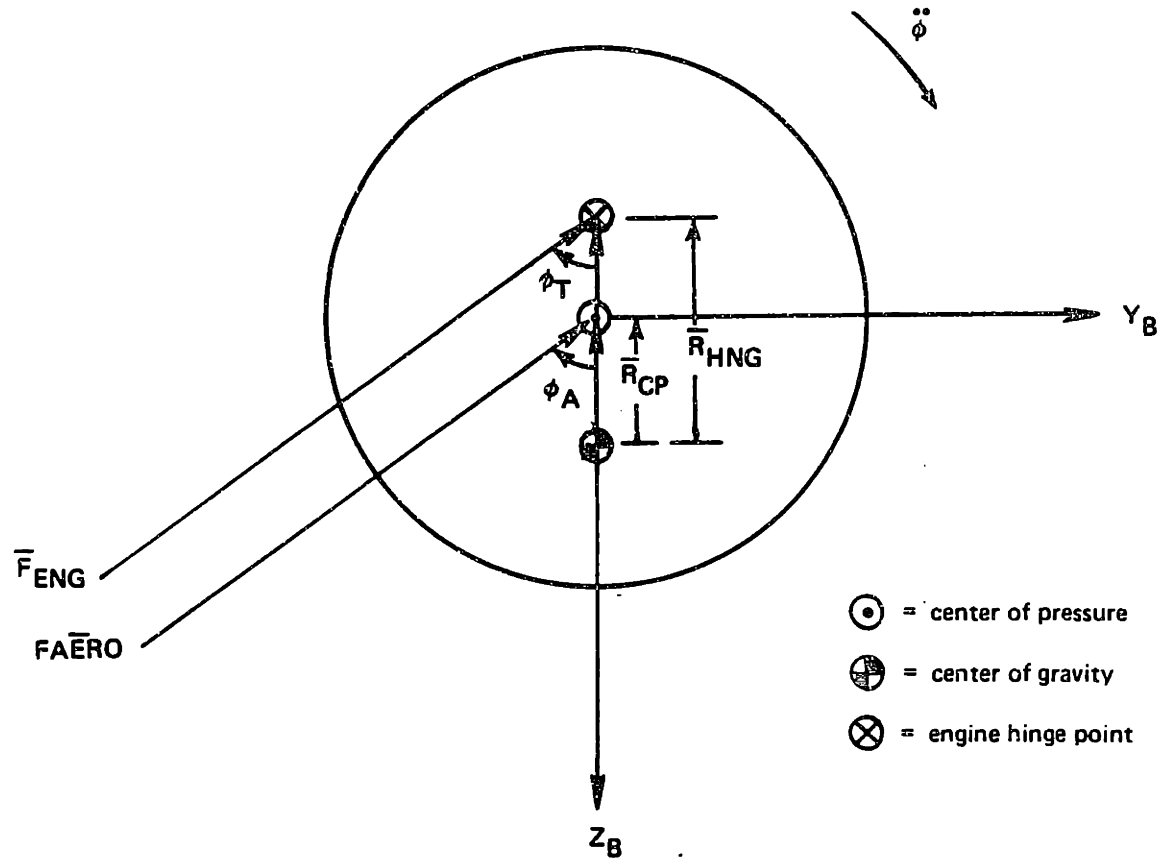

Figure 6-1. Aerodynamic and engine forces acting on worst-case manufactured booster.

by the worst-case cg and hinge point offsets (See Section 3.2.3). These maximum values are:

$$r_{HNG} = \left|\bar{R}_{HNG}\right|_{MAX} = 0.36 \text{ inches} \qquad (6.3a)$$

$$r_{CP} = \left|\bar{R}_{CP}\right|_{MAX} = 0.20 \text{ inches} \qquad (6.3b)$$

Referring to Figure 6-1, $\bar{R}_{HNG}$ is parallel to $\bar{R}_{CP}$ in the worst-case booster configuration. Also, for a steady state flight condition, $\bar{F}_{ENG}$ must be approximately parallel to $\bar{FAERO}$ in order to balance the aerodynamic and engine moments about the vehicle's pitch and yaw axes. Therefore, for a vehicle with worst-case cg and hinge point offsets under steady state flight conditions, $\phi_T = \phi_A$. Defining the magnitudes of the aerodynamic normal force and the compensating lateral engine thrust:

$$FAERO_{NORM} = \left|\bar{FAERO}\right| \tag{6.4a}$$

$$T_{NORM} = \left|\bar{F}_{ENG}\right| \tag{6.4b}$$

the maximum roll angular acceleration of the vehicle under steady state flight conditions may then be found by substituting the maximum values of $\left|\bar{R}_{HNG}\right|$ and $\left|\bar{R}_{CP}\right|$ (r_{HNG} and r_{CP}) into Equation (6.2) and assuming $\phi_T = \phi_A$. Equation (6.2) may then be rewritten:

$$\phi = \frac{(T_{NORM}\, r_{HNG} + FAERO_{NORM}\, r_{CP})}{I_X} \sin\phi_A \tag{6.5}$$

Equating the steady state aerodynamic and engine moments on the vehicle:

$$FAERO_{NORM}\, L_{CP} = T_{NORM}\, L_{CG} \tag{6.6}$$

then substituting for T_{NORM} in Equation (6.5):

$$\phi = \frac{FAERO_{NORM}\, (r_{CP} + K_L\, r_{HNG})}{I_X} \sin\phi_A \tag{6.7}$$

where:

$$K_L = \frac{L_{CP}}{L_{CG}} \tag{6.8}$$

If the direction and magnitude of $\bar{FAERO}$ remains constant with respect to the unrolled body axes, the angular roll acceleration will vary with ϕ_A as the body rotates. Assuming the current roll rate $\dot{\phi}_0$ is known, the roll rate at some future time can then be predicted by integrating Equation (6.7):

$$\dot{\phi}(t) = \dot{\phi}_0 + \frac{FAERO_{NORM}\ (r_{CP} + K_L\ r_{HNG})}{I_X} \int_0^t \sin\phi_A(t)\ dt \tag{6.9}$$

Making a change of variable in the above integral:

$$\dot{\phi}(t) = \dot{\phi}_0 + \frac{FAERO_{NORM}\ (r_{CP} + K_L\ r_{HNG})}{I_X} \int_0^{\phi_A} \frac{\sin\phi_A(t)\ d\phi_A}{\dot{\phi}_A(t)} \tag{6.10}$$

It might be possible to evaluate the integral in Equation (6.10) using an iterative numerical technique; however, since the eventual goal of this development is to implement a real-time control law based on the relationship between $\dot{\phi}(t)$ and $FAERO_{NORM}$, a simple analytical solution is desired. An approximate solution to Equation (6.10) can be obtained by assuming that the denominator function in the integral, $\dot{\phi}_A(t)$, can be replaced by a constant value of the roll rate. If the initial roll rate $\dot{\phi}_0$ is much greater than the change in roll rate over the time interval of interest, then:

$$\dot{\phi}_A(t) \cong \dot{\phi}_0 \tag{6.11}$$

in which case, Equation (6.10) becomes:

$$\dot{\phi}(t) = \dot{\phi}_0 + \frac{FAERO_{NORM}\,(r_{CP} + K_L\, r_{HNG})}{I_X\,\dot{\phi}_0} \int_0^{\phi_A} \sin\phi_A(t)\, d\phi_A \qquad (6.12)$$

By removing $\dot{\phi}_A(t)$ from the integral, the change in roll rate over the time period of interest is, in effect, obtained by integrating the roll torque applied to the vehicle as it rotates at a constant initial roll rate. Evaluating the integral on the right hand side of Equation (6.12):

$$\dot{\phi}(t) = \dot{\phi}_0 + \frac{FAERO_{NORM}\,(r_{CP} + K_L\, r_{HNG})\,(1 - \cos\phi_A)}{I_X\,\dot{\phi}_0} \qquad (6.13)$$

Equation (6.13) assumes its maximum value when $\phi_A = \pi$ radians. Therefore, the predicted worst-case maximum roll rate is the sum of the current roll rate and the change in roll rate caused by applied roll torques during a half revolution of the body:

$$\dot{\phi}_{MAX} = \dot{\phi}_0 + \frac{2\,FAERO_{NORM}\,(r_{CP} + K_L\, r_{HNG})}{I_X\,\dot{\phi}_0} \qquad (6.14)$$

6.2.2 Simulation Results

The accuracy of Equation (6.14) as a predictor of the worst-case maximum roll rate was tested using a roll simulation of the second stage vehicle. In the first step of the roll simulation process, the six-degree-of-freedom (6 DOF) simulation was used to store the mass and aerodynamic parameters of the vehicle during the first ten seconds of the second stage flight phase. However, the roll simulation did not employ the actual aerodynamic and engine forces generated in the 6 DOF run. Instead, the roll simulation assumed a constant aerodynamic normal force

in unrolled body axes, then used the vehicle parameters obtained in the 6 DOF simulation to assign a lateral engine force according to Equation (6.6). The application of quasi-steady state force histories in this manner allowed the roll simulation to search for the worst-case maximum second stage roll rate attributable to a constant aerodynamic normal force.

Roll simulations were performed for three constant magnitudes of the aerodynamic normal force. In the first simulation, the vehicle was subjected to an aerodynamic normal force of 500 pounds. Substituting this value into Equation (6.14), and using a nominal value of $K_L = 1.02$ at stage separation, the worst-case maximum roll rate predicted by Equation (6.14) is:

$$\dot{\phi}_{MAX} = \dot{\phi}_0 \text{ (deg/sec)} + \frac{248.5 \text{ (deg/sec)}^2}{\dot{\phi}_0 \text{ (deg/sec)}} \qquad (6.15)$$

where $\dot{\phi}_0$ is the roll rate at stage separation. (In this simulation, the angle of attack at stage separation is assumed to be small enough that large roll torques are not produced by the transient forces associated with staging recovery). Figure 6-2(a) shows the predicted value of the worst-case maximum roll rate as a function of $\dot{\phi}_0$, along with the actual maximum roll rates found using the roll simulation. Figures 6-2(b) and 6-2(c) present plots of the predicted and actual worst-case maximum roll rates produced when the second stage vehicle is subjected to constant aerodynamic normal forces of 1000 and 1500 pounds, respectively.

In order to properly assess the results shown in Figures 6-2(a), (b), and (c), it is important to understand the two primary sources of error in the worst-case maximum roll rate predicted by Equation (6.14):

(1) Equation (6.14) assumes that $\dot{\phi}_0 >> \Delta\dot{\phi}$. As the figures show, this assumption causes a large error in the predicted maximum roll rate for smaller values of $\dot{\phi}_0$. For $\dot{\phi}_0$ less than 25 deg/sec, however, this error is always on the

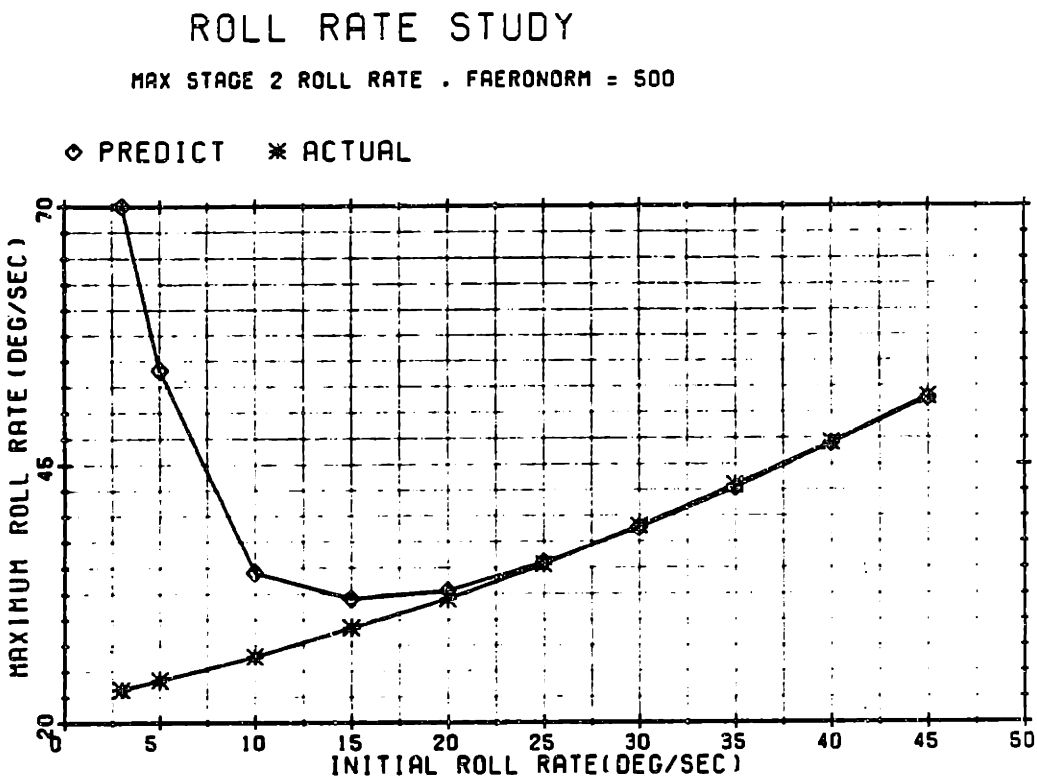

Figure 6-2(a). Predicted and actual worst-case maximum roll rates produced by an aerodynamic normal force of 500 lbs.

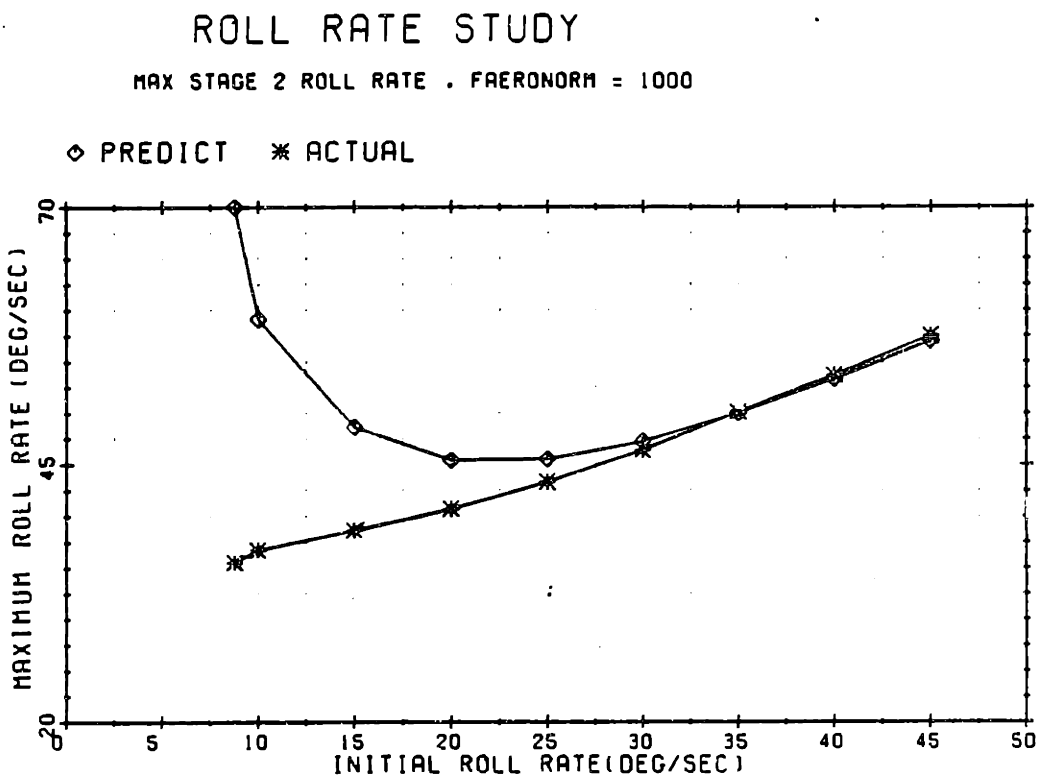

Figure 6-2(b). Predicted and actual worst-case maximum roll rates produced by an aerodynamic normal force of 1000 lbs.

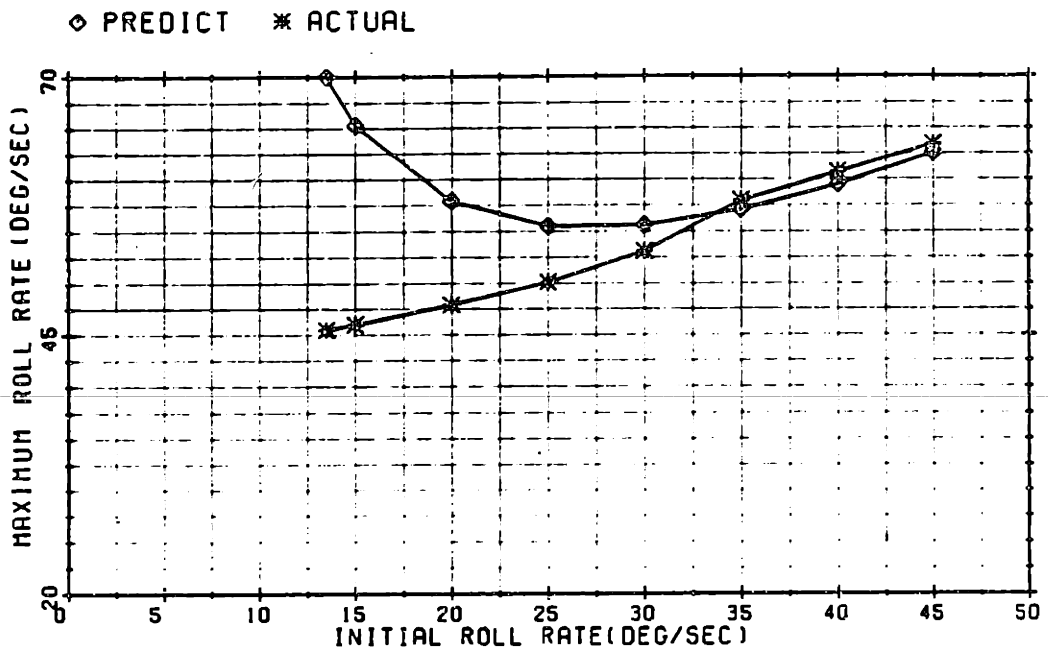

Figure 6-2(c). Predicted and actual worst-case maximum roll rates produced by an aerodynamic normal force of 1500 lbs.

conservative side; that is, the predicted roll rate is always greater than the actual rate found through simulation.

(2) The worst-case maximum roll rate predicted by Equation (6.14) does not include the effect of the applied raceway torque on the roll acceleration of the vehicle. Thus, there are some sets of initial conditions for which the actual maximum roll rate can exceed the predicted maximum roll rate, as shown in Figure 6-2(c).

Despite the two sources of error described above, Equation (6.14) does predict the future worst-case maximum roll rate within ±10% accuracy for current roll rates in the range $25 < \dot{\phi} < 45$ deg/sec. For this range of roll rates (which is just below the roll rate limit of 50 deg/sec), it is appropriate to use Equation (6.14) to predict whether or not current flight conditions could possibly result in a future roll rate that exceeds the specified limit. As the preceding figures showed, the predictor is not accurate below roll rates of 25 deg/sec; fortunately, it is

not necessary to employ the predictor at these low roll rates. Because the roll rate varies slowly compared to the cycle times of the flight control software, it is acceptable to wait until the roll rate exceeds 25 deg/sec before attempting to predict a future worst-case maximum roll rate.

6.3 Roll Rate Limiting Control System

The previous section demonstrated that a relationship can be derived between a constant aerodynamic normal force and the resultant worst-case maximum roll rate at some future time. This relationship can be reversed to establish the basis for a roll rate limiting control system in the second stage flight phase. This system will indirectly limit the roll rate by limiting the aerodynamic normal force on the vehicle. Because the aerodynamic normal force is approximately proportional to the angle of attack, an angle of attack control system can be used to impose this limit. The roll rate limiting control system contains four software routines which are not included in the baseline flight control system:

(1) Hybrid Autopilot

(2) Angle of Attack Command Limiter

(3) Roll Rate Estimator

(4) Autopilot Mode Selector

These routines are discussed in the following subsections.

6.3.1 Hybrid Autopilot

In Chapter 2, a baseline autopilot was introduced to control the attitude of the boost vehicle. Chapter 4 presented an alternative autopilot which uses angle of attack feedback to control the angle of attack of the vehicle. Referring to Figures 2-8 and 4-13, the two autopilots are almost identical in form; they differ primarily in their calculation of the initial error signal. A general purpose "hybrid" autopilot may be formed which combines the error signals from the respective autopilots.

For example, the total error signal at the input to the pitch channel of the hybrid autopilot may be defined in the following form:

$$\theta_E = K_E(\alpha_{p_C} - \hat{\alpha}_p) + (1 - K_E)(\theta_C - \theta) \tag{6.16}$$

where all symbols are as defined in Figure 6-3. In the hybrid autopilot, the angle of attack command α_p may assume non-zero values. Note that with K_E equal to zero, the hybrid autopilot is equivalent to the baseline autopilot, acting only on the attitude error with respect to the steering command. Alternatively, with K_E set to unity, the hybrid autopilot ignores the steering command, and acts to correct the angle of attack error.

6.3.2 Angle of Attack Command Limiter

The angle of attack loop in the hybrid autopilot is used to impose an angle of attack limit, corresponding to a computed limit on the aerodynamic normal force. Using the results of Section 6.2, the angle of attack limit required to satisfy the roll rate constraint can be determined by predicting the worst-case maximum roll rate that could result from the current aerodynamic normal force. For an estimated value of the present roll rate, Equation (6.14) can be used to predict the maximum roll rate that could occur during the next half revolution of the body, if the vehicle were at its worst-case roll orientation with worst-case cg and hinge point offsets. Expressed in terms of the current estimated roll rate, $\hat{\dot{\phi}}$, Equation (6.14) becomes:

$$\dot{\phi}_{MAX} = \hat{\dot{\phi}} + \frac{2\ FAERO_{NORM}\ (r_{CP} + K_L\ r_{HNG})}{\dot{I}_X\ \hat{\dot{\phi}}} \tag{6.17}$$

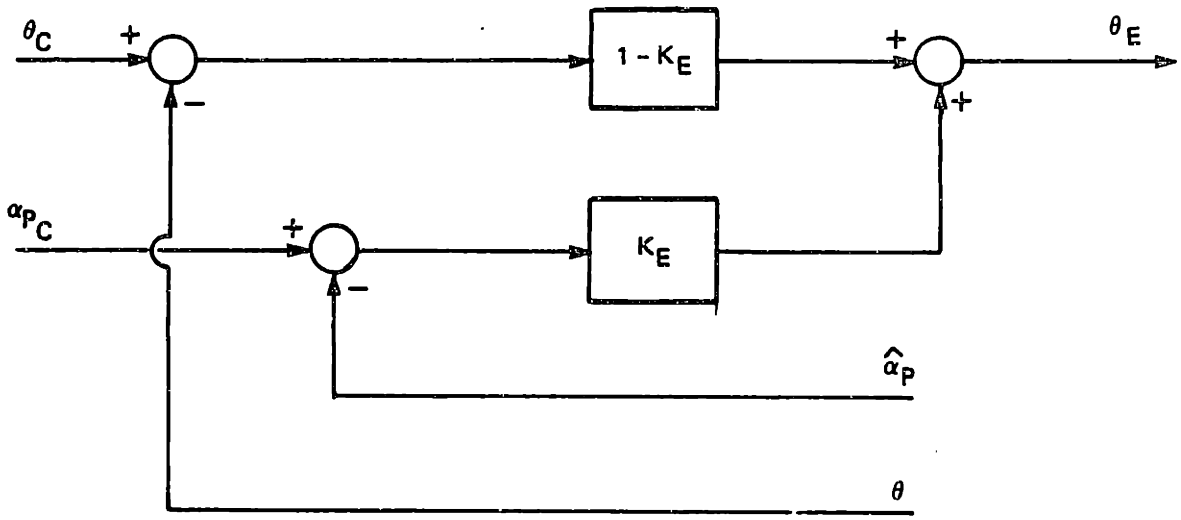

Figure 6-3. Input to pitch channel of hybrid autopilot.

If the roll rate limiting control system must limit $\dot{\phi}_{MAX}$ below a specified value $\dot{\phi}_{LIM}$, the above equation can be rearranged to specify a corresponding limit on the magnitude of the aerodynamic normal force:

$$FAERO_{NORM} \leq \frac{(\dot{\phi}_{LIM} - \hat{\dot{\phi}})\ I_X\ \hat{\dot{\phi}}}{2(r_{CP} + K_L\ r_{HNG})} \tag{6.18}$$

Since $FAERO_{NORM}$ is approximately proportional to α:

$$FAERO_{NORM} = S\ Q\ CN_\alpha\ \alpha \tag{6.19}$$

the corresponding limit on α specified by Equation (6.18) is:

$$\alpha_{LIM} = \frac{(\dot{\phi}_{LIM} - \hat{\dot{\phi}})\, I_X\, \hat{\dot{\phi}}}{2\, S\, Q\, CN_\alpha (r_{CP} + K_L\, r_{HNG})} \tag{6.20}$$

To recapitulate, α_{LIM} represents the maximum steady state angle of attack which the vehicle can maintain while assuring that its roll rate remains less than $\dot{\phi}_{LIM}$.

6.3.3 Roll Rate Estimator

A current estimate of the vehicle roll rate is required to calculate α_{LIM} according to Equation (6.20). Since the autopilot requires only pitch and yaw rate estimates for control purposes, a separate roll rate estimate must be obtained. Because the angle of attack command is calculated at the steering cycle, a new roll rate estimate is only necessary every steering cycle. In this thesis, a sufficiently accurate roll rate estimate is obtained by simply summing the IMU-measured body angle increments over the steering cycle and dividing by the steering cycle time, T_{STR}:

$$\hat{\dot{\phi}} = \frac{\sum \Delta\phi}{T_{STR}} \tag{6.21}$$

6.3.4 Autopilot Mode Selector

The hybrid autopilot may be used to drive the vehicle to a commanded angle of attack (alpha), a commanded attitude, or some combination of the two, depending on the value of the gain K_E. In this thesis, the hybrid autopilot is designed to produce a smooth transition between a commanded attitude mode and a commanded alpha mode. For notational convenience, these modes will be designated as modes 1 and 0, corresponding to the value of K_E in that mode:

Autopilot Mode 0 = (K_E = 0)

Autopilot Mode 1 = (K_E = 1)

The gain K_E is linearly ramped over a steering cycle when switching between the two modes, in order to avoid step changes in the autopilot error signal.

To follow the steering commands as closely as possible, it is usually desirable to operate the autopilot in Mode 0. If the vehicle develops an angle of attack which is too large with respect to the current roll rate, the roll rate limiting control system must "override" the steering commands by switching the hybrid autopilot to Mode 1 and commanding a reduction in the angle of attack. The task of the autopilot mode selector is to determine which autopilot mode should be used over the next steering cycle.

A block diagram of the autopilot mode selector is shown in Figure 6-4. The initial autopilot mode following stage separation is Mode 0. At the beginning of each steering cycle (500 msec), estimates are made of the current roll rate and angle of attack components. The angle of attack limit associated with the roll rate constraint is then calculated using Equation (6.20). The in-plane angle of attack command is set equal to the angle of attack limit; the out-of-plane command is always zero. The estimated total angle of attack is then compared to the angle of attack limit. If the estimated total angle of attack is less than the angle of attack limit, the autopilot remains in Mode 0. If the estimated angle of attack is greater than the specified limit, the autopilot is commanded to change to Mode 1. The autopilot then remains in Mode 1, commanding the vehicle to fly at the angle of attack limit, and does not return to Mode 0 until the difference between the commanded thrust angle, β, and the flight path angle, γ, is less than the estimated total angle of attack. This process of monitoring α, β, and γ continues until the vehicle exits the atmosphere (in this thesis, the edge of the atmosphere is defined by a dynamic pressure of 100 psf). Because the relationship

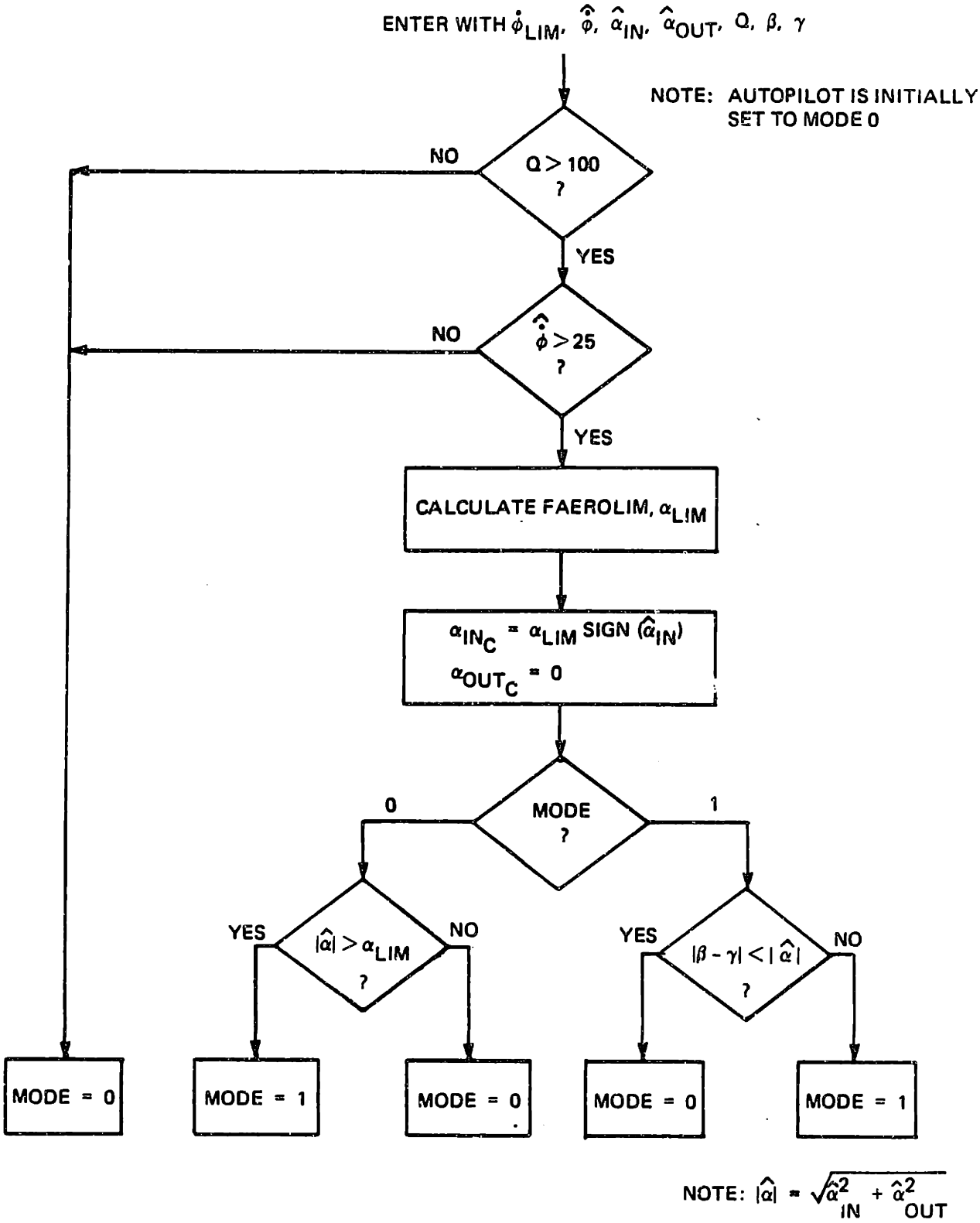

Figure 6-4. Autopilot mode selector block diagram.

between the aerodynamic normal force and the worst-case maximum roll rate predicted by Equation (6.14) is overly conservative for low roll rates, the a pilot is automatically reset to Mode 0 if the estimated roll rate drops below 25 deg/sec.

6.4 Simulation Results

The roll rate limiting control system was incorporated into the second stage flight control software. The entire system was then tested using the six-degree-of-freedom simulation. In the simulations presented in this section, the angle of attack limit calculated by the roll rate limiting control system was based on a roll rate limit, $\dot{\phi}_{LIM}$, of 45 deg/sec. This slightly conservative limit was chosen because the relationship between aerodynamic normal force and worst-case maximum roll rate developed in Section 6.2 does not consider the angular acceleration produced by aerodynamic normal forces acting on the raceway. If the estimated vehicle roll rate exceeds 45 deg/sec at any time during the flight, the angle of attack limit calculated by Equation (6.20) is automatically set to zero.

The performance of the roll rate limiting control system, as well as the system's interaction with the exponential and linear tangent steering systems, was investigated with two sets of six-degree-of-freedom simulation runs. The first set of runs, summarized in Tables 6-1, 6-3, and 6-5, employed the roll rate limiting control system in conjuction with exponential steering. These three tables present second stage trajectory data for nominal, low, and high thrust levels in the first and second stages, where the second stage trajectory originates from the I/II staging conditions associated with these thrust levels. For a summary of the nominal thrust, low thrust, and high thrust I/II staging conditions, see Table 5-1. The second set of runs, summarized in Tables 6-2, 6-4, and 6-6, used these same sets of staging conditions and thrust levels, but employed the roll rate limiting control system in conjunction with linear tangent steering.

In Chapter 5, the sets of trajectory data obtained with the various steering systems were always comparable, because all steering calculations were based on the same desired II/III staging altitude. In this chapter, unfortunately, the performance of the exponential and linear tangent steering systems cannot be directly compared for nominal and low thrust conditions. For these two cases, the functionalizations of the exponential steering law, which were used in the reference trajectories in Chapter 3, produced II/III staging altitudes that were roughly 3,000 feet and 5,000 feet above the nominally desired staging altitude. The performance of the steering systems for high thrust conditions, however, is directly comparable. For this case, the linear tangent and exponential functionalizations were both calculated for the same desired II/III staging altitude. Since Chapter 3 showed that the high thrust second stage trajectory yielded the most severe roll rates, direct comparison of the results for this case (shown in Tables and 6-5 and 6-6)) should be the most insightful.

To better focus presentation of the results shown in Tables 6-1 through 6-6, subsequent discussion will be divided into two categories:

(1) Roll rate limiting control system performance.

(2) Effect of the roll rate constraint on the second stage trajectory.

6.4.1 Roll Rate Limiting Control System Performance

The roll rate limit of 50 deg/sec was exceeded in 8 out of the 18 simulation runs which were made without roll rate limiting control in Tables 6-1 to 6-6. When the roll rate limiting control system was employed, however, the roll rate did not exceed the limit in any of the simulations performed. Comparing the runs made with and without the roll rate limiting control system, it is seen that more roll rate limiting control is generally required for high initial roll rates than for low rates, and for the high thrust trajectory than the nominal or low thrust trajectories.

Table 6-1. Nominal thrust exponential steering second stage trajectories, with and without roll rate limiting control system.

Run #	Roll Rate Limiting Control	$\dot{\phi}_o$ (deg/sec)	ϕ_o (deg)	Second Stage Winds	# of Steering Cycles in Autopilot Mode 1	$\dot{\phi}_{MAX}$ (deg/sec)	h_{ERR} (ft)	Qa_{MAX} (psf deg)	$\lvert\bar{V}_{3GO}\rvert_{REL}$ (ft/sec)
1	No	20	180	None	0	30.57	3,954	1,283	137
2	Yes	20	0	None	0	20.12	4,740	1,291	157
3	Yes	20	180	None	0	30.57	3,954	1,283	137
4	No	30	180	None	0	37.48	3,859	1,436	136
5	Yes	30	0	None	0	30.16	4,079	1,320	140
6	Yes	30	180	None	12	37.89	4,098	1,436	141
7	Yes	30	180	Tail	16	39.15	4,412	1,741	147
8	Yes	30	180	Head	13	37.53	3,558	1,299	127
9	No	40	180	None	0	45.38	3,750	1,659	134
10	Yes	40	0	None	25	40.25	4,671	1,393	154
11	Yes	40	180	None	25	43.47	6,407	1,178	198

Table 6-2. Nominal thrust linear tangent steering second stage trajectories, with and without roll rate limiting control system.

Run #	Roll Rate Limiting Control	ϕ_o (deg/sec)	$\dot{\phi}_o$ (deg)	Second Stage Winds	# of Steering Cycles in Autopilot Mode 1	$\dot{\phi}_{MAX}$ (deg/sec)	h_{ERR} (ft)	$Q\alpha_{MAX}$ (psf deg)	$\lvert\bar{V}_{3GO}\rvert_{REL}$ (ft/sec)
12	No	20	0	None	0	40.14	702	5,478	61
13	Yes	20	0	None	13	39.54	818	4,207	60
14	Yes	20	180	None	0	20.02	526	4,173	53
15	No	30	0	None	0	50.13	789	5,596	65
16	Yes	30	0	None	17	41.37	1,643	2,879	74
17	Yes	30	180	None	5	30.01	643	2,891	52
18	Yes	30	0	Tail	18	43.76	1,815	2,629	79
19	Yes	30	0	Head	16	41.17	1,476	3,460	71
20	No	40	0	None	0	57.55	804	5,715	66
21	Yes	40	0	None	19	44.95	1,071	3,021	109
22	Yes	40	180	None	7	40.02	875	2,424	73

Table 6-3. Low thrust exponential steering second stage trajectories, with and without roll rate limiting control system.

Run #	Roll Rate Limiting Control	$\dot{\phi}_o$ (deg/sec)	ϕ_o (deg)	Second Stage Winds	# of Steering Cycles in Autopilot Mode 1	$\dot{\phi}_{MAX}$ (deg/sec)	h_{ERR} (ft)	$Q\alpha_{MAX}$ (psf deg)	$\lvert\bar{V}_{3GO}\rvert_{REL}$ (ft/sec)
23	No	20	0	None	0	28.04	-3,888	1,019	198
24	Yes	20	0	None	0	28.04	-3,888	1,019	198
25	No	30	0	None	0	35.63	-3,734	1,118	201
26	Yes	30	0	None	0	35.63	-3,734	1,118	201
27	No	40	0	None	0	43.89	-3,692	1,214	203
28	Yes	40	0	None	30	43.51	-5,149	1,056	173

Table 6-4. Low thrust linear tangent steering second stage trajectories, with and without roll rate limiting control system.

Run #	Roll Rate Limiting Control	$\dot{\phi}_o$ (deg/sec)	ϕ_o (deg)	Second Stage Winds	# of Steering Cycles in Autopilot Mode 1	$\dot{\phi}_{MAX}$ (deg/sec)	h_{ERR} (ft)	$Q\alpha_{MAX}$ (psf deg)	$\lvert\bar{V}_{3GO}\rvert_{REL}$ (ft/sec)
29	No	20	0	None	0	46.72	-987	5,292	101
30	Yes	20	0	None	30	41.25	-1,794	4,792	209
31	No	30	0	None	0	53.10	-1,284	5,519	92
32	Yes	30	0	None	32	48.91	-1,607	4,086	255
33	No	40	0	None	0	63.02	-617	5,989	119
34	Yes	40	0	None	33	49.86	-2,025	2,663	301

Table 6-5. High thrust exponential steering second stage trajectories, with and without roll rate limiting control system.

Run #	Roll Rate Limiting Control	$\dot{\phi}_o$ (deg/sec)	ϕ_o (deg)	Second Stage Winds	# of Steering Cycles in Autopilot Mode 1	$\dot{\phi}_{MAX}$ (deg/sec)	h_{ERR} (ft)	$Q\alpha_{MAX}$ (psf deg)	$\lvert\bar{V}_{3GO}\rvert_{REL}$ (ft/sec)
35	No	20	180	None	0	35.67	15,430	1,892	847
36	Yes	20	180	None	16	34.16	16,241	1,851	877
37	No	30	180	None	0	41.44	15,348	1,987	855
38	Yes	30	180	None	21	38.50	17,287	1,545	916
39	No	40	180	None	0	50.02	15,254	2,065	855
40	Yes	40	180	None	22	42.67	22,498	1,306	1,163

Table 6-6. High thrust linear tangent steering second stage trajectories, with and without roll rate limiting control system.

Run #	Roll Rate Limiting Control	$\dot{\phi}_o$ (deg/sec)	ϕ_o (deg)	Second Stage Winds	# of Steering Cycles in Autopilot Mode 1	$\dot{\phi}_{MAX}$ (deg/sec)	h_{ERR} (ft)	$Q\alpha_{MAX}$ (psf deg)	$\lvert\bar{V}_{3GO}\rvert_{REL}$ (ft/sec)
41	No	20	180	None	0	54.46	786	5,514	491
42	Yes	20	180	None	20	41.19	780	4,886	780
43	No	30	180	None	0	58.67	576	5,647	489
44	Yes	30	180	None	21	41.72	1,168	3,163	781
45	No	40	180	None	0	64.31	478	5,749	490
46	Yes	40	180	None	22	43.74	1,001	3,124	966

The effectiveness of the roll rate limiting control system is best illustrated by the simulations performed with the linear tangent steering system. The linear tangent steering commands generally cause the vehicle to develop larger angles of attack, and therefore tend to require more limitation of the angle of attack when the roll rate limiting control system is employed. However, the more severe angle of attack limitation does not necessarily mean that the linear tangent steering is outperformed by the exponential steering method. Since the linear tangent steering parameters can be readjusted during flight to adapt to the constraining action of the roll rate limiting control system, it is still possible for the linear tangent steering system to achieve better II/III staging conditions than the exponential steering.

A good demonstration of the control action of the roll rate limiting control system is provided by Runs #15 and #16 in Table 6-2. Run #15, which did not use the roll rate limiting control system, produced an increase in the roll rate from 30 deg/sec to 50.13 deg/sec in the first 2.4 seconds following stage separation, as shown in Figure 6-5. This increase in roll rate is directly attributable to the angle of attack which the vehicle develops to follow the linear tangent steering commands. When the roll rate limiting control system was employed for the same set of staging conditions in Run #16, the resulting maximum roll rate was only 41.37 deg/sec. This lower roll rate results from the angle of attack of attack limit imposed by the hybrid autopilot when the autopilot operates in Mode 1. The plots presented in Figure 6-6 show that when the roll rate increases in Run #16, the roll rate limiting control system calculates a lower value for the aerodynamic normal force limit, then translates this limit into an angle of attack command. Notice in Figure 6-6 how the aerodynamic normal force limit varies inversely with the estimated roll rate. Since the dynamic pressure Q decreases following stage separation, however, the angle of attack command limit remains almost constant during the first six seconds. As discussed previously in Section 6-3, the angle of attack command limit is used only

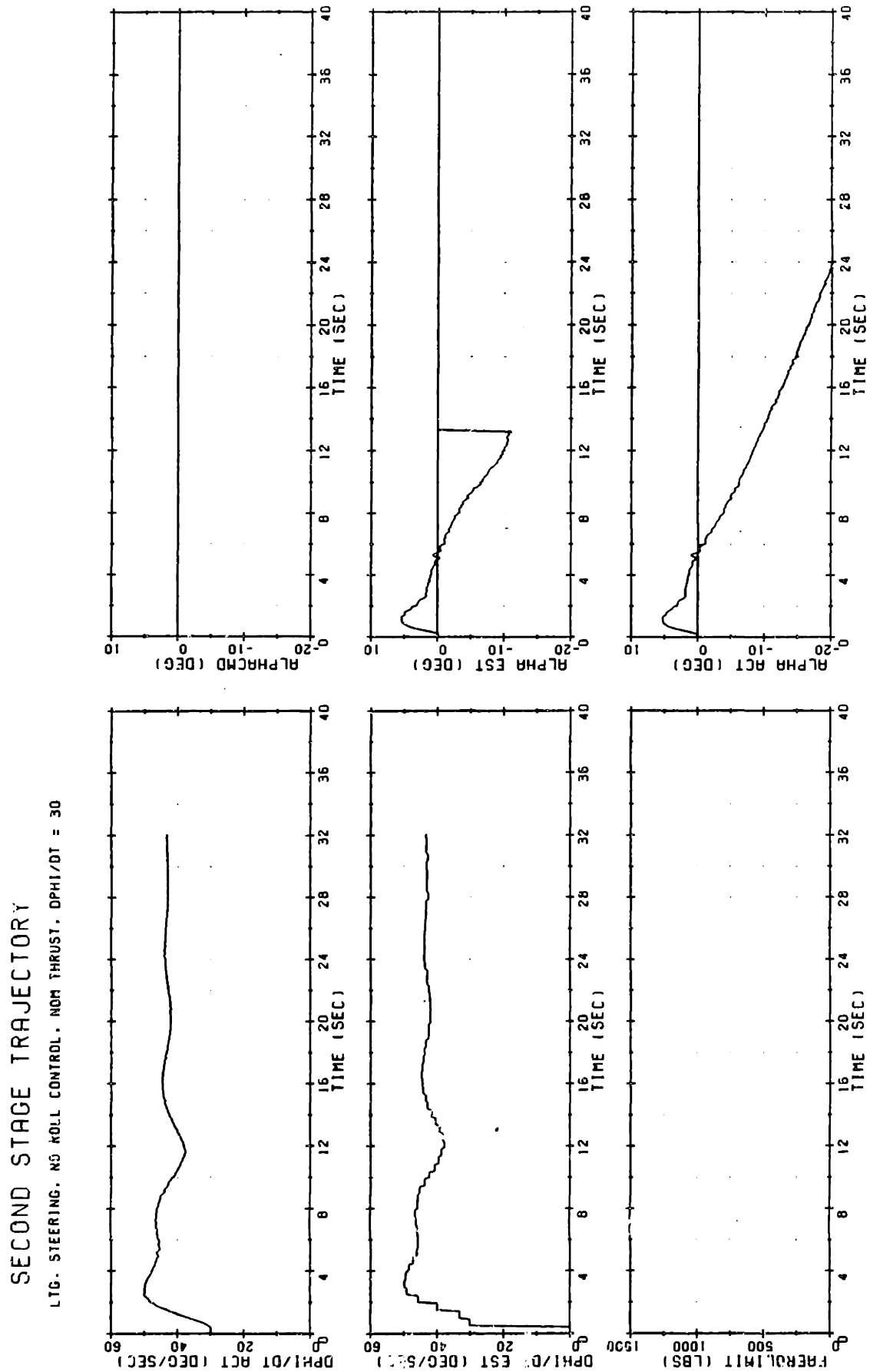

Figure 6-5. Simulation Run #15 (page 1 of 2).

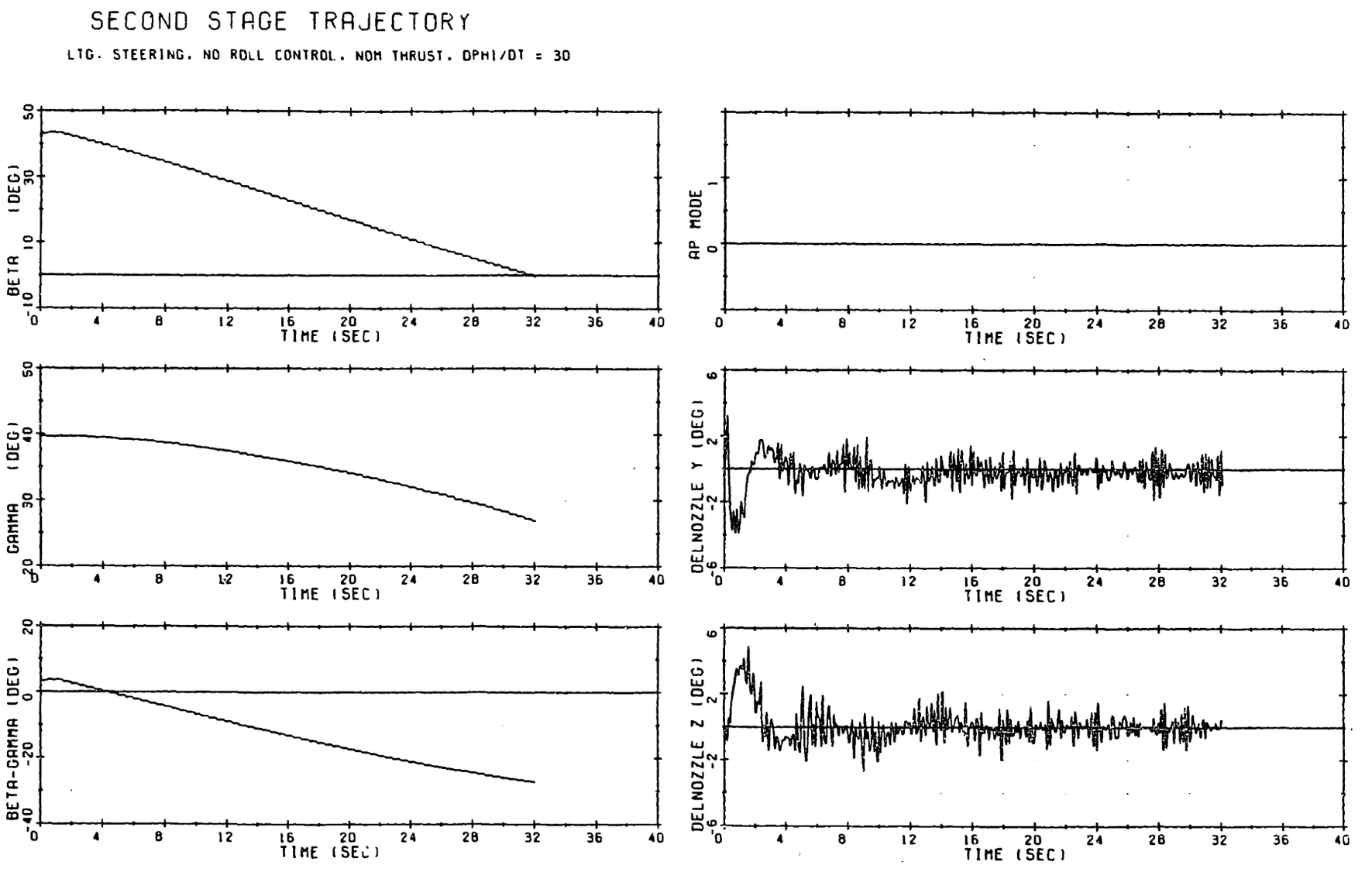

Figure 6-5. Simulation Run #15 (page 2 of 2).

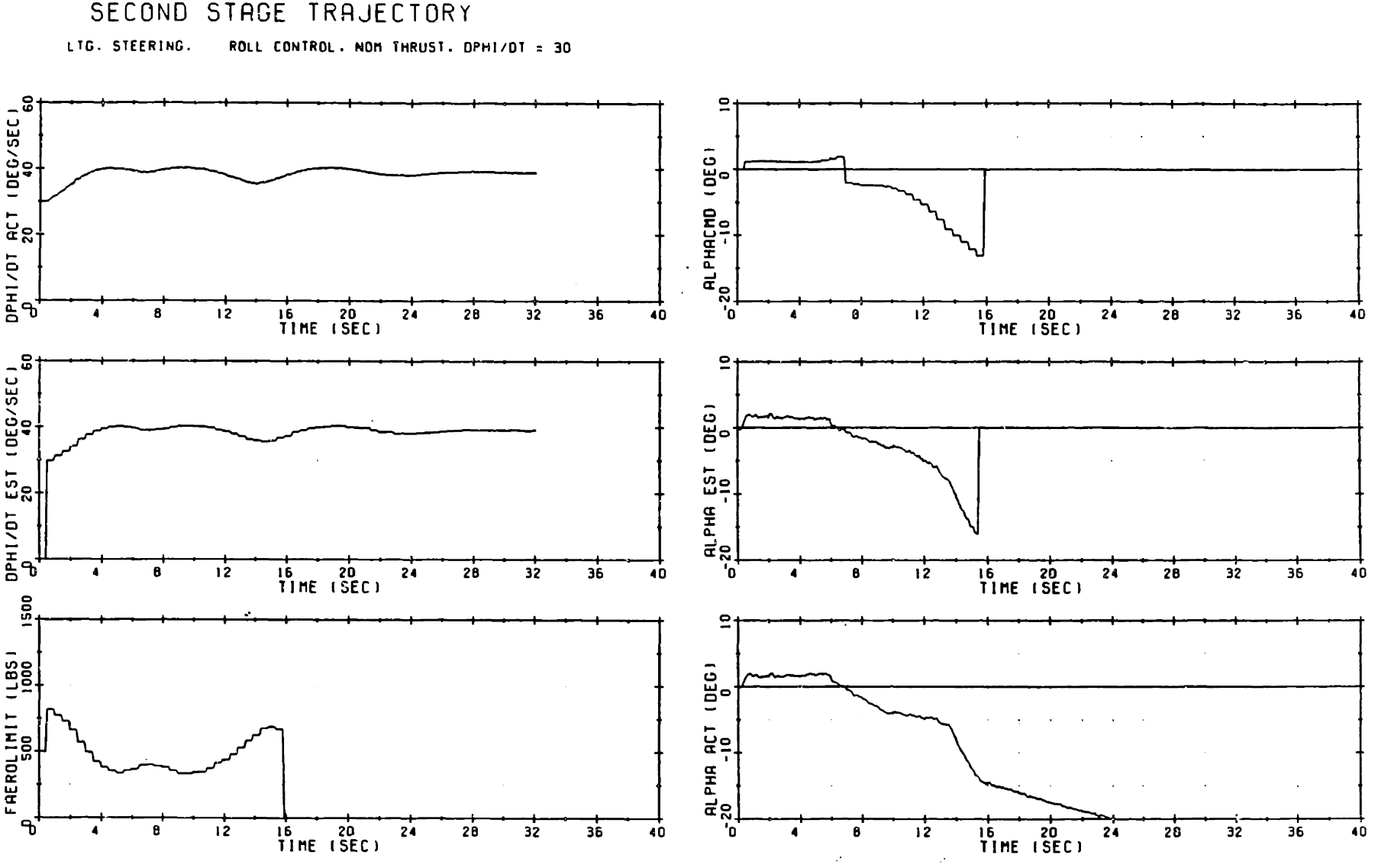

Figure 6-6. Simulation Run #16 (page 1 of 2).

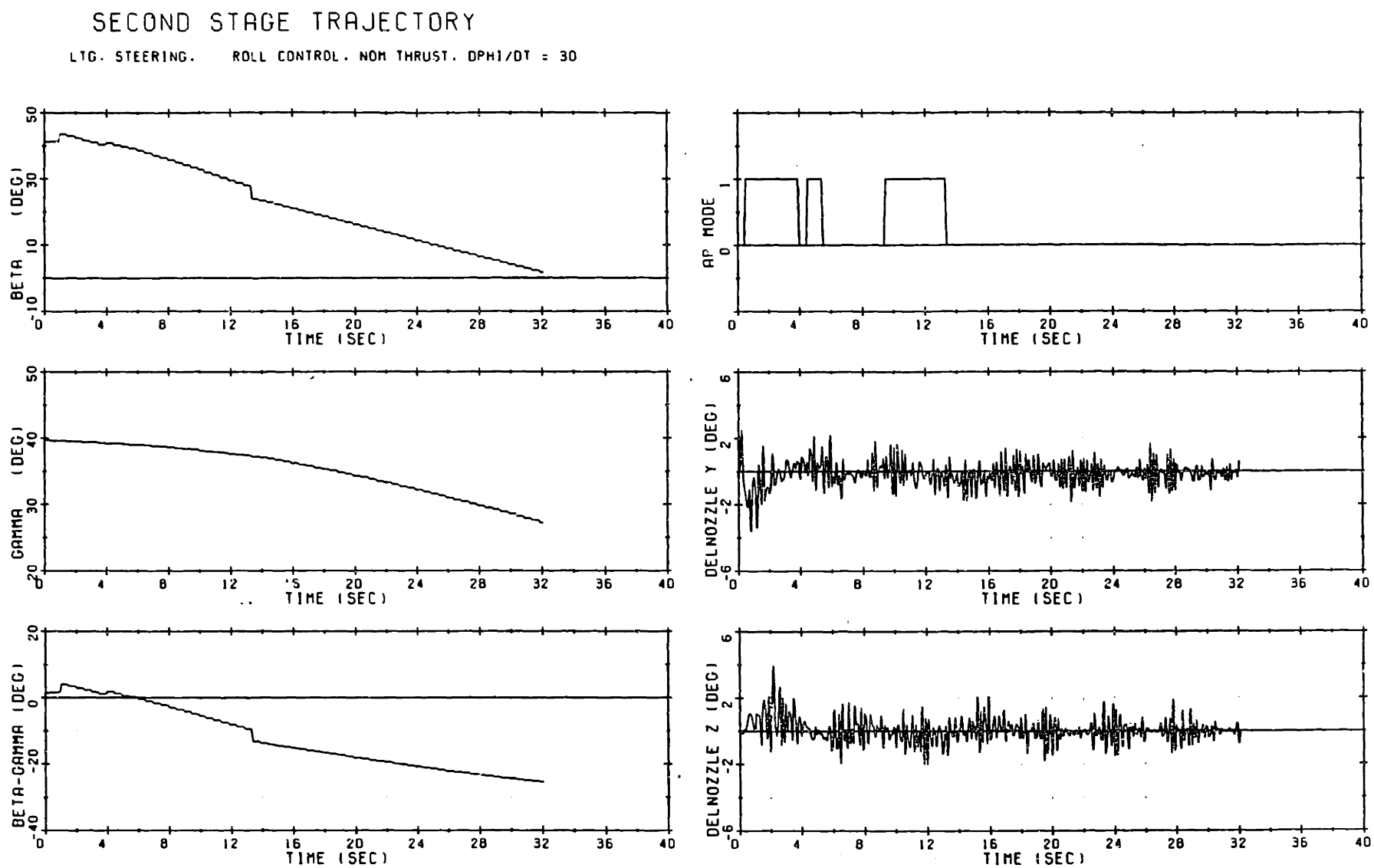

Figure 6-6. Simulation Run #16 (page 2 of 2).

when the hybrid autopilot is in Mode 1. Figure 6-6 shows that in Run #16, the autopilot transferred between modes three times, operating in Mode 1 for a total of 17 steering cycles. In this figure, note also how the linear tangent steering law recalculates the commanded thrust angle history, $\beta(t)$, each time the autopilot leaves Mode 1. This recalculation of $\beta(t)$ can cause a large discontinuity in β, such as the step shown at 13.5 seconds. Howev ce the steering command is flared in at the input to the autopi the resulting attitude error is flared in by the ramping of K_E, this discontinuity in β does not produce any large transient nozzle deflections. Also, notice that the angle of attack estimation, the calculation of FAEROLIMIT and ALPHACMD, and Mode 1 autopilot operation are halted after the vehicle leaves the atmosphere.

The control action required of the roll rate limiting control system depends on the staging roll angle as well as the staging roll rate. Notice that for Run #17 in Table 6-2, the staging conditions are the same as those listed for Run #16, except that the roll angle at staging has been shifted 180 degrees. For this initial roll angle, the angle of attack during the first few seconds of the second stage flight phase causes the roll rate to decrease, as shown in Figure 6-7. This lower roll rate does not require severe restriction of the aerodynamic force, so the autopilot only operates in Mode 1 for five steering cycles.

The roll rate limiting control system is designed to calculate the angle of attack limit under the pessimistic assumption that the roll rate is about to increase. This assumption unnecessarily constrains the angle of attack under some conditions. For example, Figure 6-7 shows that in the first four seconds of Run #17, the roll rate is decreasing, yet the roll rate limiting control system still imposes a limit on the angle of attack. If the angle of attack had not been limited, the roll rate would have actually decreased further. The point to be made is that this roll rate control system considers only the current value of the estimated roll rate when it calculates the angle of attack limit; no consideration is given to the change in the roll rate from one cycle to the next. A possible modification that might alleviate this performance problem will be discussed in the final chapter.

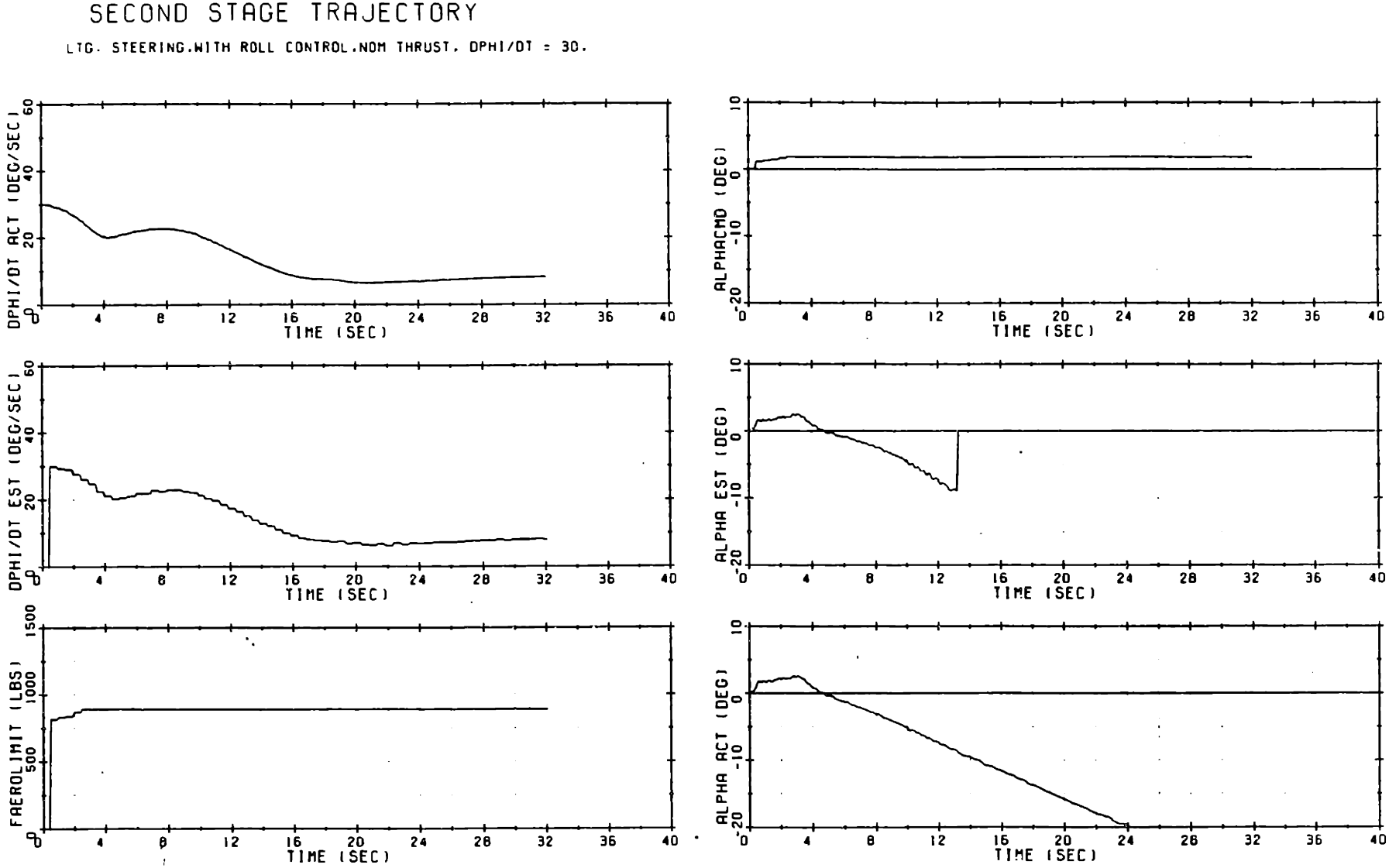

Figure 6-7. Simulation Run #17 (page 1 of 2).

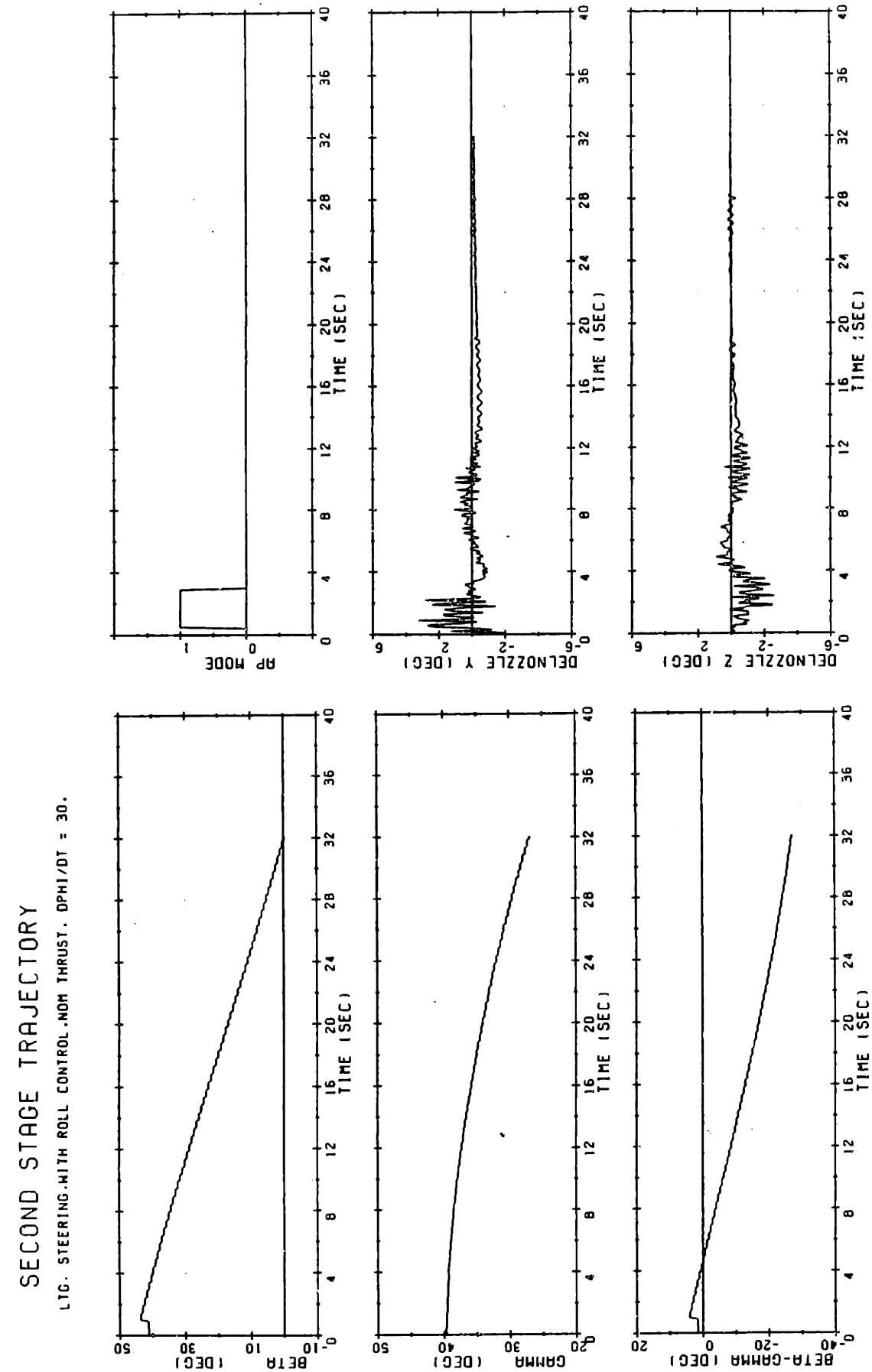

Figure 6-7. Simulation Run #17 (page 2 of 2).

The roll rate limiting control system works well with either the exponential or the linear tangent steering system. For Run #6 in Table 6-1, all staging conditions are the same as in Run #17. During Run #6, however, steering commands were calculated using the exponential steering law. The performance of the roll rate limiting control system in this run is shown in Figure 6-8. Comparing Figure 6-8 with Figure 6-7, notice that for these particular staging conditions, the angle of attack caused by the exponential steering commands in Run #6 acts to increase the roll rate, whereas the initial angle of attack excursion caused by linear tangent steering commands in Run #17 yields a decrease in roll rate. In fact, in Run #6 the second stage roll rate never exceeds the initial second stage roll rate of 30 deg/sec. As a result, the maximum roll rate in Run #6 is greater than the maximum roll rate in Run #17, even though the roll rate limiting control system constrains the angle of attack for a longer period of time in Run #6.

The performance of the roll rate limiting control system was tested in the presence of wind disturbances with both steering methods for nominal thrust conditions. The wind model used in this analysis produced a wind spike which the vehicle encountered approximately six seconds following stage separation. The results of the wind runs are included in Tables 6-1 and 6-2. For Run #18 in Table 6-2, which employed linear tangent steering, a tailwind spike was specified. A tailwind causes a positive rotation of the vehicle's air-relative velocity vector, decreasing the angle of attack of the vehicle following stage separation. The graphs presented in Figure 6-9 show that in this particular case, the tailwind did not appreciably change the roll rate profile from the profile obtained along the no wind trajectory (Run #16, see Figure 6-6).

For Run #19 in Table 6-2, a headwind spike was specified. A headwind causes a negative rotation of the vehicle's air-relative velocity vector, increasing the angle of attack of the vehicle following stage separation. As shown in Figure 6-10, this increase in angle of attack causes the roll rate to increase much more rapidly than the no wind case

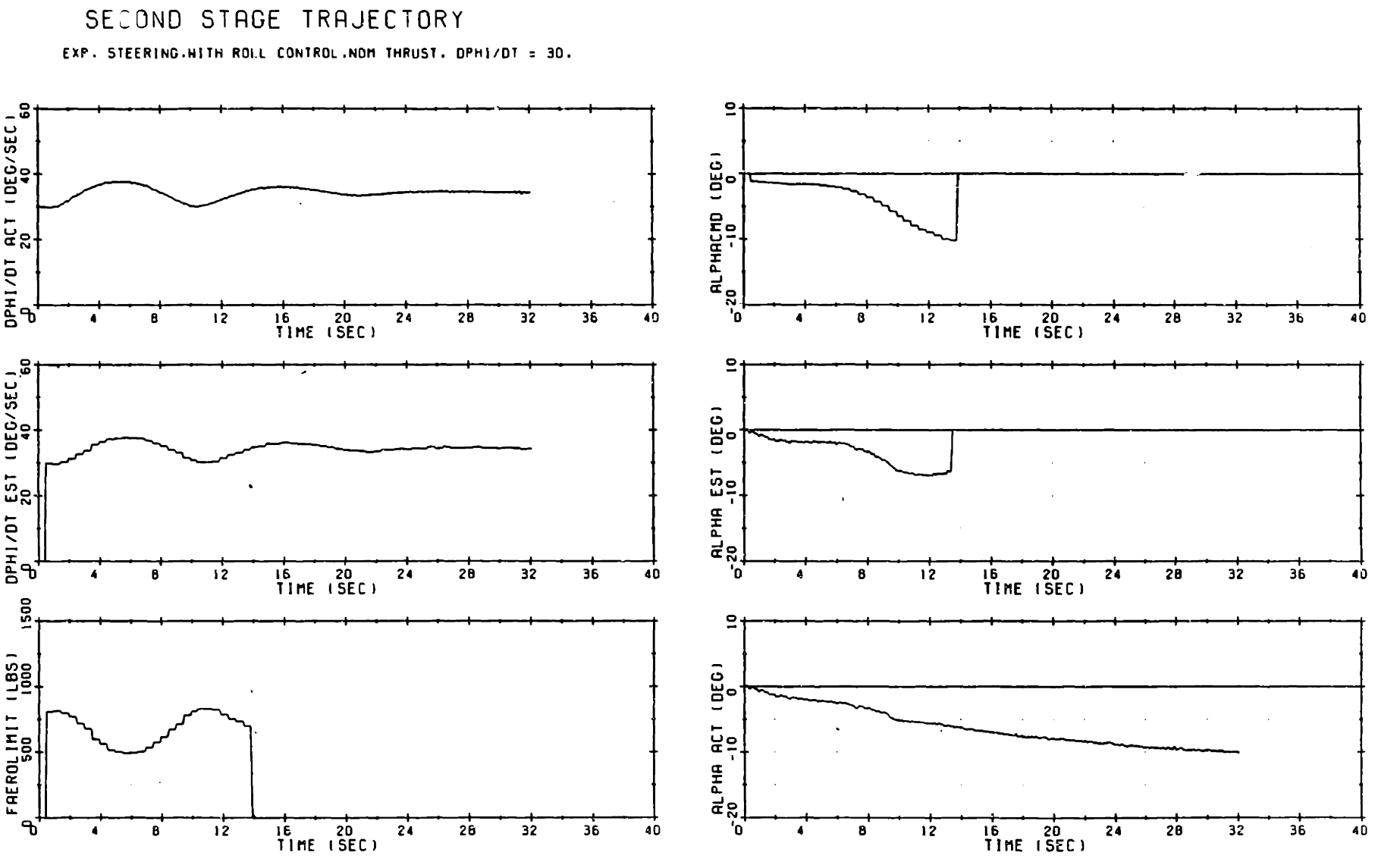

Figure 6-8. Simulation Run #6 (page 1 of 2).

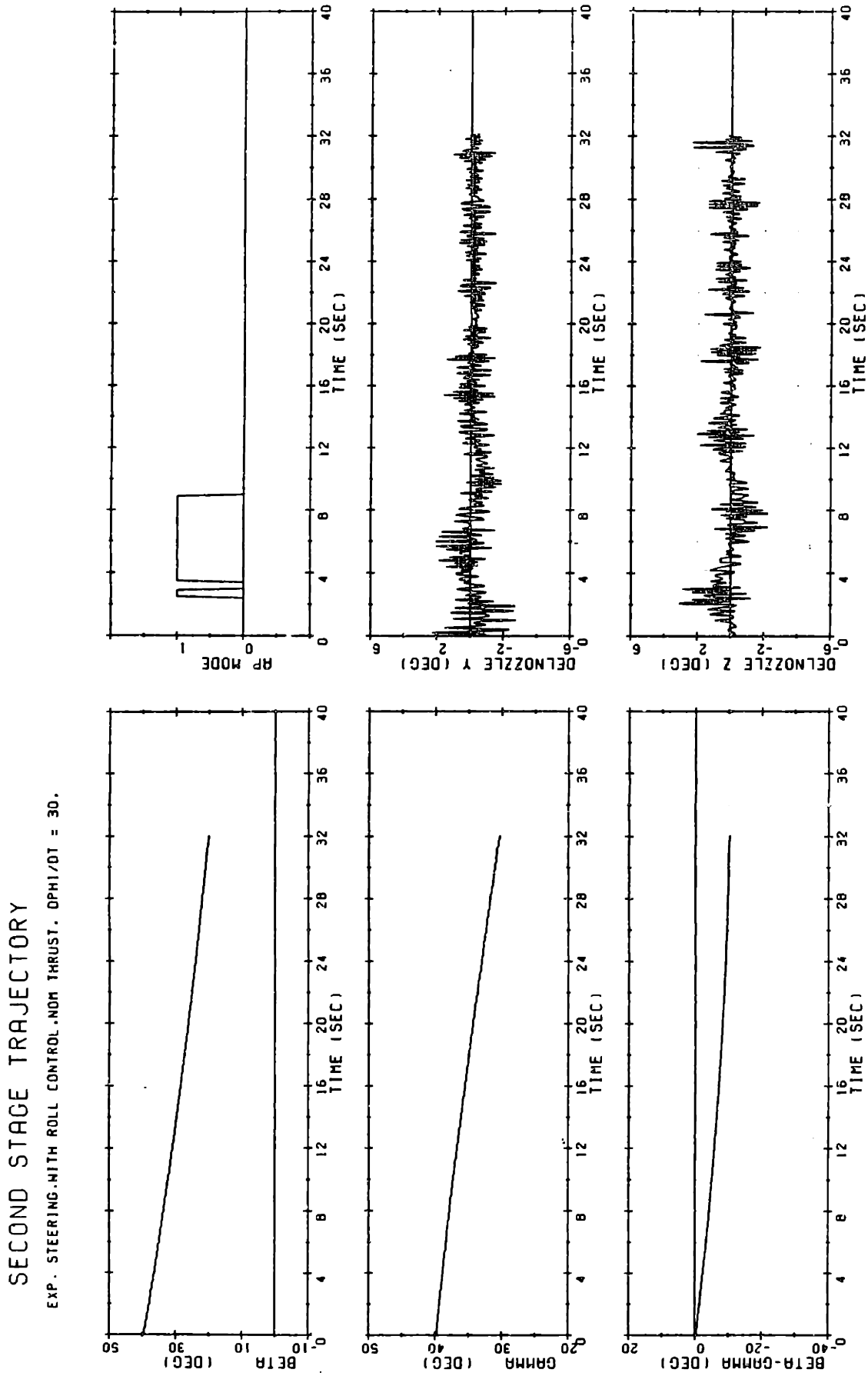

Figure 6-8. Simulation Run #6 (page 2 of 2).

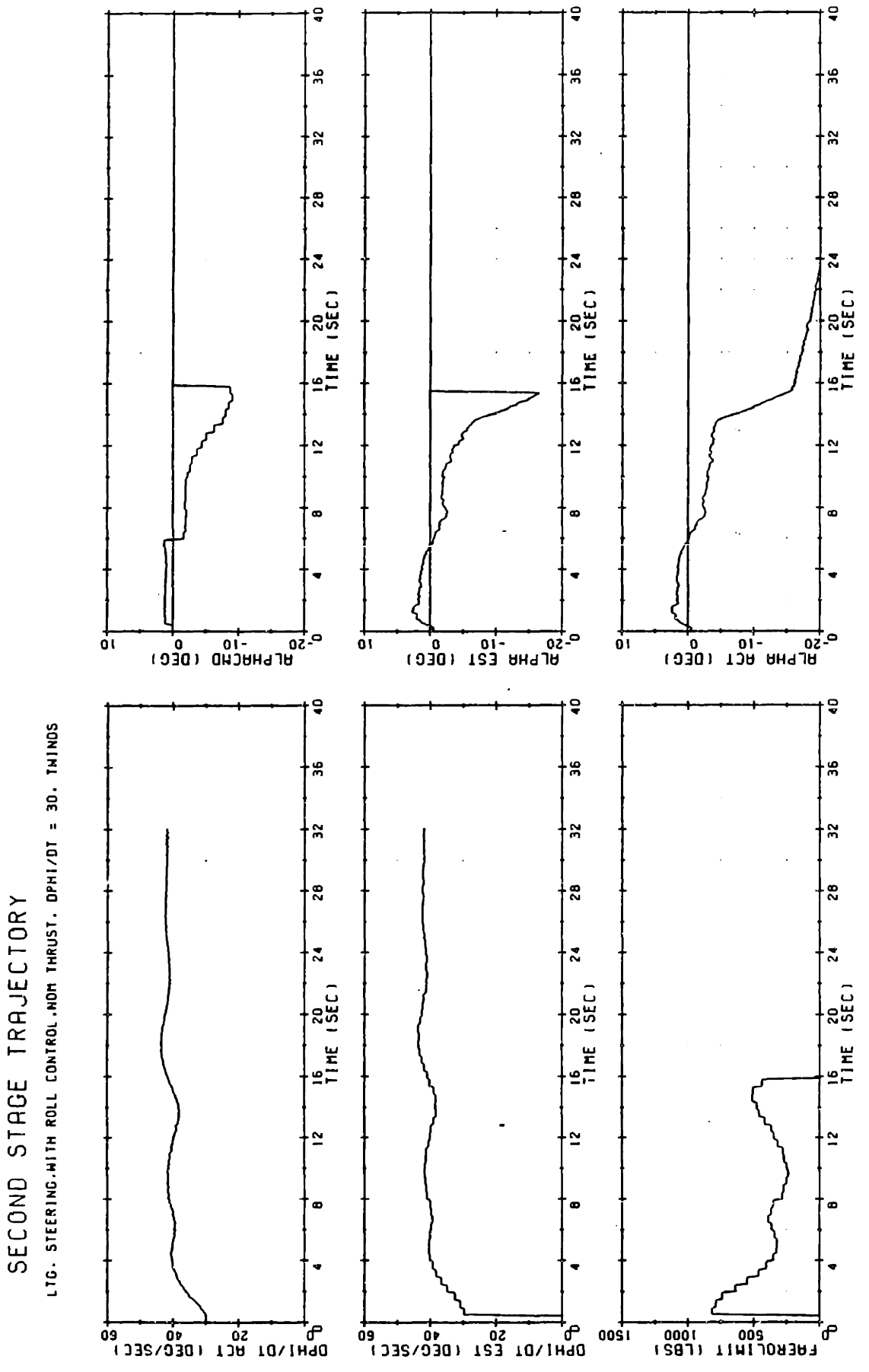

Figure 6-9. Simulation Run #18 (page 1 of 2).

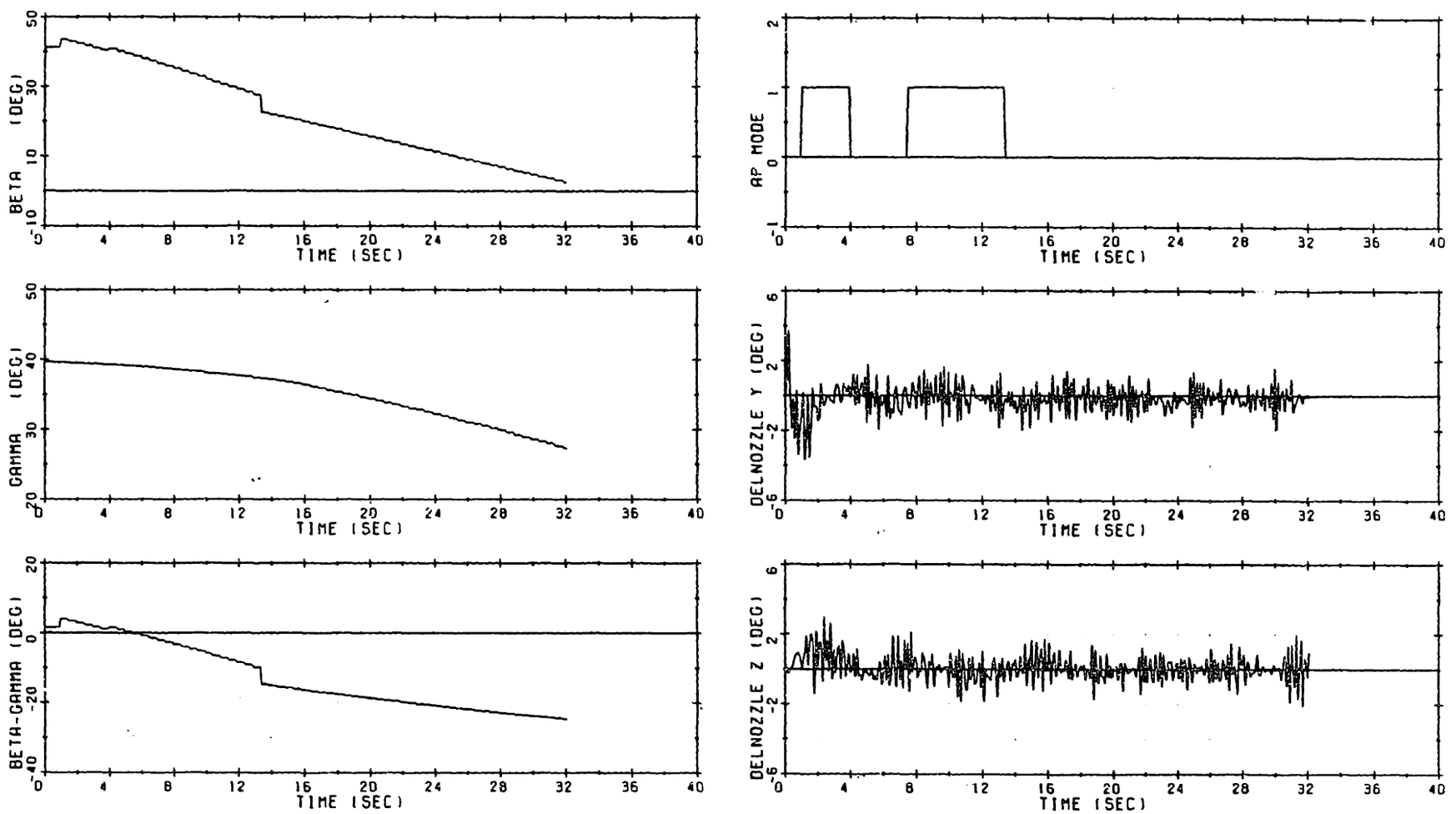

Figure 6-9. Simulation Run #18 (page 2 of 2).

of Run #16 (see Figure 6-6). Because the roll rate is higher, the angle of attack must be more tightly constrained by the roll rate limiting control system. In fact, it can be seen that the commanded angle of attack is forced to zero when the estimated roll rate climbs higher than the 45 deg/sec roll rate limit conservatively employed by the roll rate limiting control system. Figure 6-10 shows that in this run, the autopilot was forced to operate in Mode 1 for a total of 24 steering cycles, but was successful in keeping the roll rate below 50 deg/sec.

Tables 6-3 and 6-4 illustrate the performance of the roll rate limiting control system for low thrust second stage trajectories. In all these simulations, the staging roll orientation of the vehicle was chosen to produce an increase in the roll rate following stage separation. Notice that for both steering methods, higher roll rates at stage separation result in higher maximum roll rates during the trajectory. Using the roll rate limiting control system, however, the maximum roll rate never exceeds 50 deg/sec. As mentioned previously, the thrust angle history commanded by the linear tangent steering law causes the vehicle to develop a higher angle of attack than the exponential steering law. Therefore, when the linear tangent steering system is used, the roll rate imposed constraint on the angle of attack forces the autopilot to ignore the steering commands and operate in Mode 1 a larger portion of the time.

Tables 6-5 and 6-6 illustrate the performance of the roll rate limiting control system for high thrust second stage trajectories. For the high thrust conditions, both the linear tangent and the exponential steering laws cause the vehicle to develop a large angle of attack, so the roll rate constraint affects their performance similarly. For both steering systems, the roll rate limiting control system commands the autopilot to operate in Mode 1 during the majority of the time the vehicle is in the atmosphere.

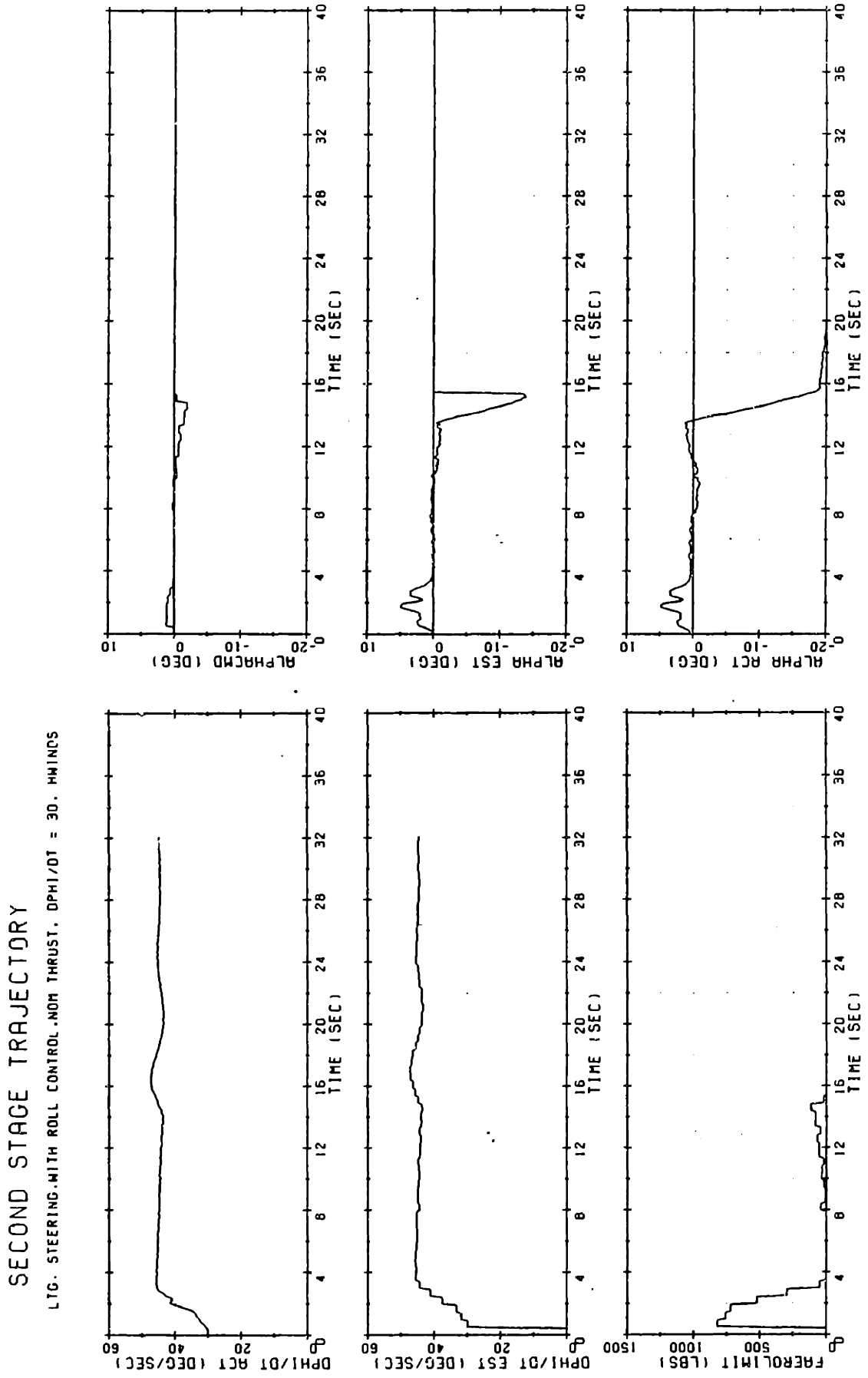

Figure 6-10. Simulation Run #19 (page 1 of 2).

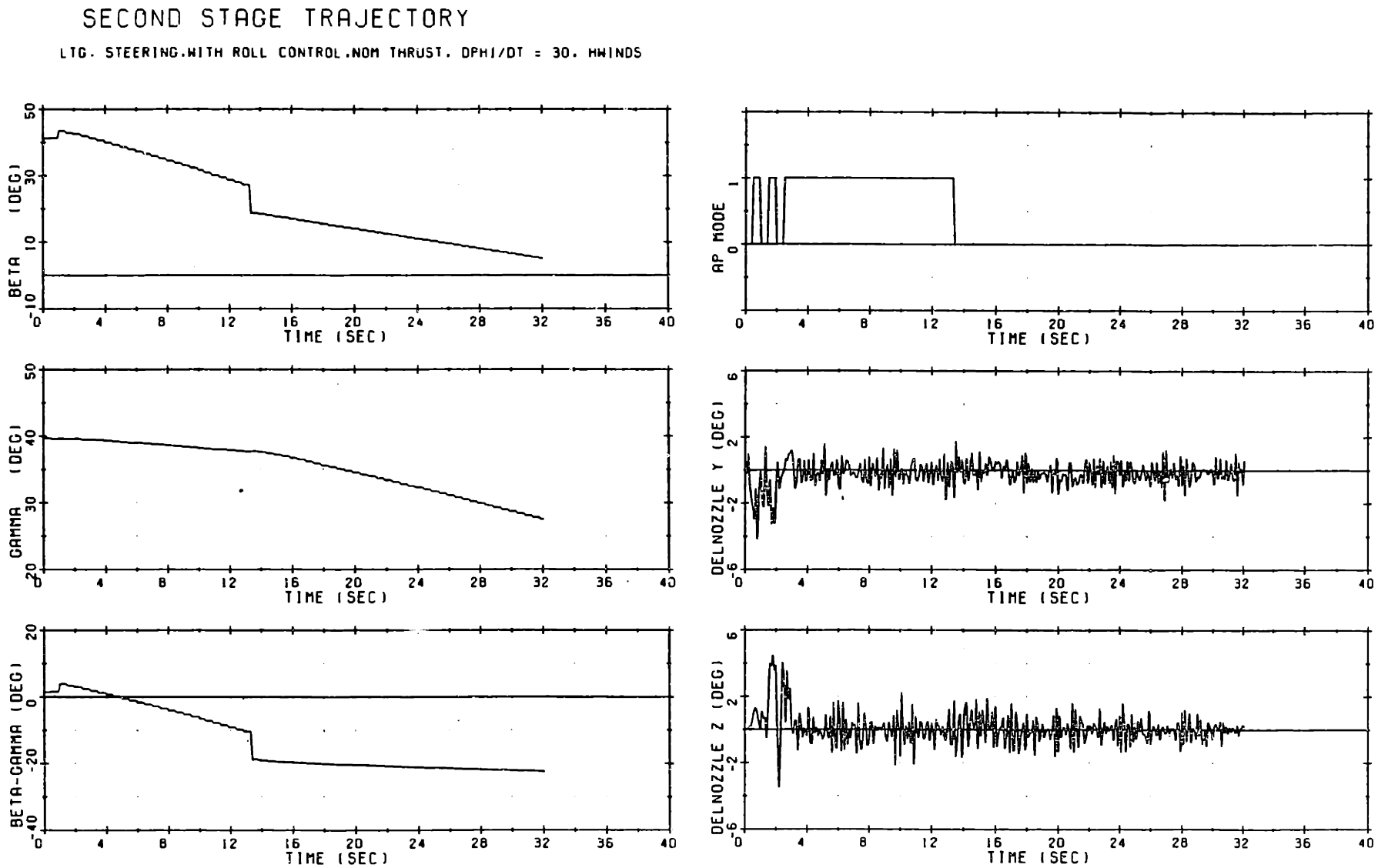

Figure 6-10. Simulation Run #19 (page 2 of 2).

6.4.2 Effect of the Roll Rate Constraint on the Second Stage Trajectory

The previous section demonstrated how the roll rate limiting control system limits the second stage roll rate by constraining the vehicle's angle of attack. For roll rates in the neighborhood of the specified roll rate limit, the roll rate imposed angle of attack limit is smaller than the angle of attack limit associated with the aerodynamic loading constraint; thus the roll rate limit becomes the dominant constraint on the second stage trajectory. The effect that this roll rate imposed angle of attack limit has on the second stage trajectory depends on the steering method used in the second stage flight phase. This section analyzes separately the effect of the roll rate limiting control action on second stage trajectories commanded by the exponential and linear tangent steering methods.

6.4.2.1 Exponential Steering

The last three columns in Tables 6-1, 6-3, and 6-5 summarize the performance of the second stage exponential steering algorithm for the roll rate control simulations discussed in the preceding section. $Q\alpha_{MAX}$ is the largest value of the product $Q\alpha$ during the second stage flight phase, and h_{ERR} is the error between the actual and the nominally desired altitude at II/III staging. $\left|\bar{V}_{3GO}\right|_{REL}$ is the magnitude of the velocity to be gained through thrust application in the third stage, relative to the value obtained in Chapter 5 for the optimal nominal thrust second stage trajectory subject to the aerodynamic loading constraint (see Table 5-2).

Table 6-1 shows that when exponential steering is used for nominal thrust conditions, the action of the roll rate limiting control system has little effect on the second stage trajectory. In fact, this table shows that for the nominal thrust second stage trajectory, the control action of the roll rate limiting control system would not even be required for initial roll rates of 20 deg/sec up to 40 deg/sec. The largest maximum roll rate found without use of the roll rate limiting

control system was 45.38 deg/sec. This maximum rate occurred for the highest initial roll rate examined (40 deg/sec, see Run #9). When the roll rate limiting control system was employed, in three of the runs the angle of attack never exceeded the roll rate imposed limit, and the hybrid autopilot remained in Mode 0 for the entire second stage flight phase. In the other runs, the angle of attack only slightly exceeded the roll rate imposed limit, so that the action of the roll rate limiting control system only slightly altered the second stage trajectory.

For the nominal thrust runs, the largest changes in maximum roll rate, $Q\alpha_{MAX}$, and trajectory end conditions occurred when roll rate limiting control was employed for an initial second stage roll rate of 40 deg/sec. Comparison of Runs #9 and #11 in Table 6-1 shows that use of the roll rate limiting control system decreased the maximum second stage roll rate from 45.38 deg/sec to 43.37 deg/sec. An extended period of angle of attack limiting (25 steering cycles in Mode 1) was required to achieve this small decrease in the maximum roll rate. In this case, however, autopilot operation in Mode 1 did not severely constrain the trajectory, because the angle of attack commanded in Mode 1 was only slightly smaller than the angle of attack which the vehicle would have developed anyway to follow the steering commands. The fact that the second stage trajectory was not severely constrained is evident from the relatively small decrease in $Q\alpha_{MAX}$ (from 1659 psf deg in Run #9 to 1178 psf deg in Run #11). The increase in $\left|\bar{V}_{3GO}\right|_{REL}$ caused by the action of the roll rate limiting control system was 64 ft/sec (from 134 ft/sec in Run #9 to 198 ft/sec in Run #11).

Table 6-3 shows how the action of the roll rate limiting control system affects the second stage exponential steering performance for low thrust conditions. Runs #27 and #28 demonstrate the effects of the roll rate imposed angle of attack limit for the same initial roll rate of 40 deg/sec examined previously for nominal thrust conditions. In Run #28, it is seen that the presence of the roll rate constraint causes the system to limit its angle of attack by operating in Mode 1 for a total of 30

steering cycles during the second stage flight phase. This angle of attack limit prevents the vehicle from rotating to the attitude necessary to follow the exponential steering commands. Because the vehicle is not allowed to apply its thrust in the direction commanded by the exponential steering, the staging altitude error h_{ERR} changes by 1,457 feet (from -3,692 feet in Run #27 to -5,149 feet in Run #28). In this case, because the vehicle has achieved a lower altitude at staging, $\left|\bar{V}_{3GO}\right|_{REL}$ in Run #28 is slightly lower than the $\left|\bar{V}_{3GO}\right|_{REL}$ achieved in Run #27

Table 6-5 shows the effect of the roll rate limiting control action on the second stage exponential steering performance for high thrust conditions. Notice that when the roll rate limiting control system is not used, the commanded high thrust second stage trajectory can cause large roll rates to develop from a wide range of initial roll rates. This result reinforces the results of Chapter 3, which showed that for a given initial roll rate, the worst-case maximum second stage roll rate is largest along the high thrust trajectory. When the roll rate limiting control system is employed, the simulations listed in Table 6-5 show a correlation between the number of steering cycles spent in autopilot Mode 1 and the resultant increases in h_{ERR} and $\left|\bar{V}_{3GO}\right|_{REL}$. For the largest initial roll rate of 40 deg/sec, the changes in h_{ERR} and $\left|\bar{V}_{3GO}\right|_{REL}$ for the high thrust second stage trajectory far exceed those produced for the nominal and low thrust levels. Comparing Runs #39 and #40, it is seen that the roll rate imposed angle of attack limit in Run #40 results in large increases in both h_{ERR} (from 15,254 feet to 22,498 feet) and $\left|\bar{V}_{3GO}\right|_{REL}$ (from 855 ft/sec to 1,163 ft/sec).

6.4.2.2 Linear Tangent Steering

When linear tangent steering is employed, the control action of the roll rate limiting control system has a somewhat different effect on the second stage trajectory. Table 6-2 shows differences in nominal

thrust second stage trajectories using linear tangent steering with and without the roll rate limiting control system, as a function of the initial second stage roll rate. In Run #20 from this table, the roll rate limiting control system is not employed, and the resulting maximum $Q\alpha$ for the trajectory is just below the aerodynamic loading limit of 6000 psf deg. In Run #21, the roll rate limiting control system constrains α, resulting in a much smaller $Q\alpha$ maximum (3,021 psf deg). Comparing Run #21 to Run #20, constraining the trajectory to limit the roll rate causes an increase of 43 ft/sec in $\left|\bar{V}_{3GO}\right|_{REL}$. In this case, even though the presence of the roll rate constraint severely limits the angle of attack early in the second stage flight phase, the linear tangent steering system is able to reinitialize itself following the constrained flight period, effectively reoptimizing the trajectory over the remaining burn time t_{GO}. As a result, the change in h_{ERR} between Runs #20 and #21 is limited to 267 feet. In fact, examining the values of h_{ERR} listed in Table 6-2, the largest change in the staging altitude error caused by action of the roll rate limiting control system in the nominal thrust second stage trajectory is less than 1,000 feet.

Table 6-4 shows how the action of the roll rate limiting control system affects the second stage linear tangent steering performance for low thrust conditions. In order to limit the roll rate, the control system severely limits the maximum value of $Q\alpha$ for only higher values of the initial second stage roll rate. Constraining the low thrust second stage trajectory in this manner causes significant increases in $\left|\bar{V}_{3GO}\right|_{REL}$. For example, comparing Runs #33 and #34 for an initial roll rate of 40 deg/sec, the roll rate imposed angle of attack limit in Run #34 results in an increase of 182 ft/sec in $\left|\bar{V}_{3GO}\right|_{REL}$.

Table 6-6 shows how the action of the roll rate limiting control system affects the second stage linear tangent steering performance for high thrust conditions. Comparing Runs #45 and #46 in Table 6-6, it can be seen that the limit imposed on the angle of attack in Run #46 resulted in an increase of 476 ft/sec in $\left|\bar{V}_{3GO}\right|_{REL}$.

6.4.2.3 Comparison of Exponential and Linear Tangent Steering for the High Thrust Second Stage Trajectory

As mentioned previously at the beginning of this section, the performance of the second stage exponential and linear tangent steering systems can only be compared for the high thrust trajectory, because this is the only thrust level for which the exponential steering parameters were actually functionalized for the desired II/III staging altitude. Examining Tables 6-5 and 6-6, it can be seen that the second stage end conditions achieved with exponential steering, both with and without roll rate limiting control, are markedly different from the end conditions achieved with linear tangent steering. The most obvious difference in the performance of the two steering methods is in the II/III staging altitude error. For the three runs in Table 6-5 for which exponential steering was employed without the roll rate limiting system, the smallest value of h_{ERR} is15,254 feet. When linear tangent steering was used without roll rate limiting control, the maximum value of h_{ERR} shown in Table 6-6 is 786 feet. As has been emphasized previously, the linear tangent steering parameters are originally selected at the beginning of the second stage flight phase, and may be adjusted during the second stage burn to more accurately reach the staging altitude. The exponential parameters, on the other hand, are chosen as a fixed functionalization of the thrust estimate obtained during the launch maneuver. This functionalization of the exponential steering parameters is based on no wind assumptions. Table 6-5 shows that in this case, even though no winds were present at the second stage altitudes, the wind spike during the first stage flight phase (see Chapter 3) was severe enough to cause a large staging altitude error.

Chapter 5 showed that the second stage vehicle must generally sacrifice some of its ΔV capability in order to achieve a higher staging altitude. Since the "misfitted" second stage exponential steering commands carry the vehicle to a much higher staging altitude, it is not surprising that the values of $\left|\bar{V}_{3GO}\right|_{REL}$ in Table 6-5 are consistently higher than the values obtained for the linear tangent steering trajectories with similar initial conditions in Table 6-6.

When the roll rate limiting control system is employed in the second stage flight phase, its limitation of the angle of attack more severely affects the performance of the linear tangent steering system. In carrying the vehicle to a higher staging altitude, the exponential steering commands do not cause the vehicle to develop a large negative angle of attack flight condition. Therefore, the values of $Q\alpha_{MAX}$ for the high thrust exponential steering trajectory are relatively small, as shown in Table 6-5. When the roll rate limiting control system is employed, it is not necessary for the system to severely constrain the angle of attack. In Table 6-5 the largest decrease in $Q\alpha_{MAX}$ caused by the control action of the roll rate limiting control system occurred for the highest initial roll rate of 40 deg/sec. By decreasing $Q\alpha_{MAX}$ from 2,065 psf deg to 1,306 psf deg, use of the roll rate limiting control system caused an increase in the staging altitude error of 7,244 feet (from 15,254 feet to 22,498 feet), and an increase in $\left|\bar{V}_{3GO}\right|_{REL}$ of 308 ft/sec.

From Tables 6-5 and 6-6, it can be seen that the use of roll rate limiting control has a greater effect on the value of $\left|V_{3GO}\right|_{REL}$ for linear tangent steering than for exponential steering. This is a result of the action of roll rate limiting on the higher angle of attack produced by linear tangent steering for the high thrust case. It should be noted, however, that the values of $\left|V_{3GO}\right|_{REL}$ are still smaller for linear tangent steering than for exponential steering. When roll rate limiting is used for the extreme case of a 40 deg/s initial roll rate, the value of $\left|\bar{V}_{3GO}\right|_{REL}$ for linear tangent steering is approximately 200 ft/s less than the value for exponential steering.

CHAPTER 7

SUMMARY, CONCLUSIONS, AND RECOMMENDATIONS

7.1 Summary and Conclusions

This thesis has shown that when a boost vehicle with even small asymmetries develops an angle of attack, the forces that act on the vehicle can cause it to develop a high roll rate. This thesis has also shown that by modifying the flight control software, the roll rate can be limited without severely affecting the trajectory. Specifically, it has been shown that the roll rate in the second stage of a boost vehicle can be limited below a specified value through the use of an angle of attack feedback control system. The angle of attack system overrides the normal steering and controls when necessary to limit the angle of attack. This thesis has shown that it is possible to make smooth transitions between normal steering and control and the angle of attack override control system when the estimated angle of attack rises above or drops below a specified limit. The current angle of attack limit can be computed as a function of the current estimated roll rate and dynamic pressure. This analytically-derived function, which is based on conservative assumptions, reduces the angle of attack limit as the estimated roll rate increases.

This thesis presented two second stage steering methods that command the orientation of the thrust vector with respect to inertial space:

(1) A steering system that varies the thrust angle in the trajectory plane as an exponential function of time. The constants used in this exponential steering law are

functionalized in terms of the estimated first stage thrust level.

(2) A steering system that varies the tangent of the thrust angle as a linear function of time. The constants used in the linear tangent steering law can be adjusted during flight to achieve a specified altitude at the end of the second stage flight phase.

The performance of both these steering methods (that is, their ability to achieve the desired staging altitude while minimizing the third stage velocity to be gained through thrust application) was examined both with and without the roll rate limited control system. It was shown that both the linear tangent and exponential steering laws provide near-optimal second stage performance for nominal and high thrust levels in the absence of winds and the roll rate limiting control system. However, for low thrust levels the linear tangent steering law yields a significant reduction in the third stage velocity to be gained through thrust application. Moreover, when winds are introduced and the constraining action of the roll rate limiting control system is considered, the linear tangent steering law allows for better control of the second stage end conditions. For these off-nominal conditions, the linear tangent steering method yields better performance because it adapts its steering commands to changing flight conditions as a function of the remaining burn time. The exponential steering method, on the other hand, relies on a fixed functionalization of the trajectory, assuming no winds and no overriding control action of the roll rate limiting control system.

It has been shown that among the three thrust levels considered, the steering commands for the high thrust second stage trajectory cause the vehicle to develop the largest angle of attack and, subsequently, the highest roll rate. Therefore, the high thrust trajectory requires the most severe angle of attack limitation during the second stage flight phase. When the roll rate limiting control system is employed, its limiting action for the high thrust trajectory causes the largest

increase in the third stage velocity to be gained through thrust application. For this case, however, use of the linear tangent steering method shows a substantial improvement over the exponential steering, both in its control of the II/III staging altitude and in its minimization of the velocity to be gained.

7.2 Recommendations

This thesis provided an analysis of steering-related problems in the second stage flight phase. The analysis particularly highlighted alternative trajectory shaping methods and control concepts that would allow the second stage to satisfy altitude and velocity goals while effectively constraining the aerodynamic loading and the roll rate. If the design concepts described in this thesis were to be applied to a specific boost vehicle, the following refinements in analysis and implementation might be considered:

(1) Rather than using worst-case analyses to develop and evaluate steering and control concepts, Monte Carlo simulations might be employed to obtain more realistic (and less conservative) results. These Monte Carlo simulations could be applied to the first stage vehicle to better define "typical" I/II staging conditions. Second stage Monte Carlo simulations could then be used to more realistically assess the performance of the second stage steering and control methods.

(2) It may be possible to reduce the vehicle's angle of attack and angular rate at I/II staging by modifying the steering and controls during the first stage thrust tailoff period. Specifically, during thrust tailoff, the baseline steering, control, and load relief systems could be replaced by the angle of attack control system developed in this thesis. During tailoff, this angle of attack system could explicitly command a zero angle of attack.

(3) If recommendation (2) achieves better control of the vehicle's angle of attack and angular rate during thrust tailoff, it might be possible to stage at a higher dynamic pressure. For a higher permissible staging dynamic pressure, the first stage trajectory could be targeted to reach a lower altitude, allowing the first stage to thrust closer to the velocity to be gained direction.

(4) Design modifications might be considered in the angle of attack control system. For example, an integral signal could be added in the forward loop to help reduce steady-state angle of attack errors.

(5) The performance of the linear tangent and exponential steering laws might be fully evaluated for a wider range of error sources, including:

(a) Errors in the estimated thrust level

(b) Errors in the predicted second stage burn time

(c) Errors in the vehicle mass and aerodynamic parameters

(6) To allow a fairer performance comparison between exponential steering and linear tangent steering, it would be useful to investigate possibilities for modifying the exponential steering parameters β_{FINAL} and K_{EXP} during flight in accordance with predictive in-flight simulations. (First stage steering concepts based on predictive simulations are described by Ozaki [13].)

(7) Appendix B shows that each calculation of the linear tangent parameters neglects second order terms that could have been considered to more accurately achieve the targeted altitude. It might be possible to reduce the final staging altitude error caused by omission of these terms, by re-selecting a set of parameters later in the second stage flight phase - perhaps after the boost vehicle has left the atmosphere.

(8) The performance of the roll rate limiting control system might be fully evaluated for a wider range of error sources, including:

   (a) Errors in the estimated angle of attack components

   (b) Errors in the estimated dynamic pressure

(9) The logic used to calculate the roll rate imposed angle of attack limit could be made less conservative by implementing the following improvements in the roll rate limiting control system:

   (a) The current roll rate limiting control logic assumes a vehicle with worst-case cg and hinge point offsets. If these offsets could be even roughly estimated during flight, this information could be used to relax the roll rate imposed angle of attack limit.

   (b) If the second stage cg and engine hinge point offsets could be estimated with sufficient accuracy, it might be desirable to implement an active roll rate control algorithm, such as the algorithm employed by Dailey [4]. Dailey's method selectively overrides the normal steering to command both the magnitude and direction of the angle of attack relative to the current roll orientation of the vehicle.

   (c) The current roll rate limiting control logic pessimistically assumes that the current roll rate is always about to increase. Since this thesis has shown that the second stage roll rate actually tends to oscillate with the roll orientation of the vehicle, perhaps the derivative of the roll rate could be incorporated into the calculation of the angle of attack limit. A derivative of the roll rate could be obtained by simply back-differencing previous roll rate estimates, or by directly estimating the roll angular acceleration of the vehicle.

APPENDIX A

NECESSARY CONDITIONS FOR AN OPTIMAL CONTROL HISTORY

Assume the dynamics of a given system are described by the set of equations:

$$\dot{\bar{x}} = \bar{a}(\bar{x},\bar{u},t) \tag{A.1}$$

where $\bar{x}$ is the (nx1) state vector, and $\bar{u}$ is the (mx1) vector of control inputs. The generalized optimal control problem is to find an admissible control history $\bar{u}(t)$ which causes the system to follow a state trajectory $\bar{x}(t)$ which is in some sense "optimal". The criterion used to judge the optimality of the solution is termed the performance measure. The performance measure may be written as a functional in Bolza form:

$$J(\bar{u}) = f(\bar{x}(t_f),t_f) + \int_{t_o}^{t_f} w(\bar{x},\bar{u},t)\, dt \tag{A.2}$$

The integral term in Equation (A.2) represents a quantity (e.g., fuel consumption, state excursions) that is to be minimized along the trajectory. The term $f(\bar{x}(t_f),t_f)$, known as the terminal penalty function, represents a quantity that is to be minimized at the final time, t_f.

Assuming that f is a differentiable function,

$$f(\bar{x}(t_f),t_f) = f(\bar{x}(t_0),t_0) + \int_{t_o}^{t_f} \frac{d}{dt}\,[f(\bar{x},t)]\, dt \tag{A.3}$$

For the problems considered in this thesis, $\bar{x}(t_0)$ and t_0 will be considered fixed, so that their values do not affect the minimization of the performance measure. The performance measure to be minimized may then be expressed as:

$$J(\bar{u}) = \int_{t_o}^{t_f} \{w(\bar{x},\bar{u},t) + \frac{d}{dt}[f(\bar{x},t)]\}\, dt \qquad (A.4)$$

Applying the chain rule of differentiation:

$$J(\bar{u}) = \int_{t_o}^{t_f} \{w(\bar{x},\bar{u},t) + [\frac{\partial f}{\partial \bar{x}}(\bar{x},t)]^T \dot{\bar{x}}(t) + \frac{\partial f}{\partial t}(\bar{x},t)\}\, dt \qquad (A.5)$$

The optimization is constrained by the dynamics of the system, defined in Equation (A.1). System constraints may be added to the performance measure to define an augmented performance measure, J_A:

$$J_A(\bar{u}) = \int_{t_o}^{t_f} \{w(\bar{x},\bar{u},t) + [\frac{\partial f}{\partial \bar{x}}(\bar{x},t)]^T \dot{\bar{x}}(t) + \frac{\partial f}{\partial t}(\bar{x},t) + \bar{p}^T(t)[\bar{a}(\bar{x},\bar{u},t) - \dot{\bar{x}}(t)]\}\, dt \qquad (A.6)$$

where the p_i are the Lagrange multipliers, or costates, related to the state variables. For a discussion on the significance of Lagrange multipliers, see Reference [7]. Note that the numerical value of J_A is equal to the value of the original performance measure J, because all the constraint terms in J_A are equal to zero.

For notational convenience, an augmented weighting function is introduced to include the system constraints. This augmented weighting function, w_A, is defined as:

$$w_A = w(\bar{x},\bar{u},t) + \bar{p}^T(t)[\bar{a}(\bar{x},\bar{u},t) - \dot{\bar{x}}(t)] \qquad (A.7)$$

Notice that the explicit dependence of w_A on $\bar{x}$, $\dot{\bar{x}}$, $\bar{u}$, $\bar{p}$, and t has been dropped from the notation.

The calculus of variations shows that the minimum of the augmented performance measure J_A will be achieved when the first variation of J_A, δJ_A, is equal to zero. Defining δJ_A in terms of the individual variations in $\delta\bar{x}$, $\delta\dot{\bar{x}}$, $\delta\bar{u}$, and $\delta\bar{p}$:

$$\delta J_A(\bar{u}) = \int_{t_o}^{t_f}\{[\frac{\partial w_A}{\partial \bar{x}}]^T + \frac{\partial}{\partial \bar{x}}[[\frac{\partial f}{\partial \bar{x}}(\bar{x},t)]^T \dot{\bar{x}}(t) + \frac{\partial f}{\partial t}(\bar{x},t)]\}\,\delta\bar{x}(t)\,dt$$

$$+ \int_{t_o}^{t_f}\{[\frac{\partial w_A}{\partial \dot{\bar{x}}}]^T + [\frac{\partial f}{\partial \bar{x}}(\bar{x},t)]^T\}\,\delta\dot{\bar{x}}(t)\,dt$$

$$+ \int_{t_o}^{t_f}[\frac{\partial w_A}{\partial \bar{u}}]^T \delta\bar{u}(t)\,dt + \int_{t_o}^{t_f}[\frac{\partial w_A}{\partial \bar{p}}]^T \delta\bar{p}(t)\,dt \qquad (A.8)$$

The above expression may be modified by replacing $\delta\dot{\bar{x}}(t)$ with $\frac{d}{dt}[\delta\bar{x}(t)]$ and integrating the terms in $\delta\bar{x}(t)$ by parts:

$$\delta J_A(\bar{u}) = \{[\frac{\partial w_A}{\partial \dot{\bar{x}}}]^T + [\frac{\partial f}{\partial \bar{x}}(\bar{x},t_f)]^T\}\,\delta\bar{x}(t_f)$$

$$- \{[\frac{\partial w_A}{\partial \dot{\bar{x}}}]^T + [\frac{\partial f}{\partial \bar{x}}(\bar{x},t_o)]^T\}\,\delta\bar{x}(t_o)$$

$$+ \int_{t_o}^{t_f}\{[\frac{\partial w_A}{\partial \bar{x}}]^T + \frac{\partial}{\partial \bar{x}}[[\frac{\partial f}{\partial \bar{x}}(\bar{x},t)]^T \dot{\bar{x}}(t) + \frac{\partial f}{\partial t}(\bar{x},t)]$$

$$- \frac{d}{dt}[\frac{\partial w_A}{\partial \dot{\bar{x}}}]^T - \frac{d}{dt}[\frac{\partial f}{\partial \bar{x}}(\bar{x},t)]^T\}\,\delta\bar{x}(t)\,dt$$

$$+ \int_{t_o}^{t_f}[\frac{\partial w_A}{\partial \bar{u}}]^T \delta\bar{u}(t)\,dt + \int_{t_o}^{t_f}[\frac{\partial w_A}{\partial \bar{p}}]^T \delta\bar{p}(t)\,dt \qquad (A.9)$$

$\bar{x}(t_0)$ is considered to be fixed, so $\delta\bar{x}(t_0)$ is equal to zero. Applying the chain rule of differentiation to the terms in $f(\bar{x},t)$ and evaluating the indicated partial derivatives:

$$\delta J_A(\bar{u}) = \{[\frac{\partial w_A}{\partial \dot{\bar{x}}}]^T + [\frac{\partial f}{\partial \bar{x}}(\bar{x},t_f)]^T\}\,\delta\bar{x}(t_f)\,dt$$

$$+ \int_{t_o}^{t_f}[\frac{\partial w_A}{\partial \bar{u}}]^T + [\frac{\partial^2}{\partial \bar{x}^2} f(\bar{x},t)]^T \dot{\bar{x}}(t) + [\frac{\partial^2}{\partial \bar{x}\partial t} f(\bar{x},t)]^T$$

$$- \frac{d}{dt}[\frac{\partial w_A}{\partial \dot{\bar{x}}}]^T - [\frac{\partial^2}{\partial \bar{x}^2} f(\bar{x},t)]^T \dot{\bar{x}}(t) - [\frac{\partial^2}{\partial \bar{x}\partial t} f(\bar{x},t)]^T\}\,\delta\bar{x}(t)\,dt$$

$$+ \int_{t_o}^{t_f}[\frac{\partial w_A}{\partial \bar{u}}]^T \delta\bar{u}(t)\,dt + \int_{t_o}^{t_f}[\frac{\partial w_A}{\partial \bar{p}}]^T \delta\bar{p}(t)\,dt \qquad (A.10)$$

In the $\delta\bar{x}$ term, notice that all the second partial derivatives sum to zero. The simplified expression for δJ_A is now:

$$\delta J_A(\bar{u}) = \{[\frac{\partial w_A}{\partial \dot{\bar{x}}}]^T + [\frac{\partial f}{\partial \bar{x}}(\bar{x},t_f)]^T\}\,\delta\bar{x}(t_f)\,dt$$

$$+ \int_{t_o}^{t_f}\{[\frac{\partial w_A}{\partial \bar{u}}]^T - \frac{d}{dt}[\frac{\partial w_A}{\partial \dot{\bar{x}}}]^T\}\,\delta\bar{x}(t)\,dt$$

$$+ \int_{t_o}^{t_f}[\frac{\partial w_A}{\partial \bar{u}}]^T \delta\bar{u}(t)\,dt + \int_{t_o}^{t_f}[\frac{\partial w_A}{\partial \bar{p}}]^T \delta\bar{p}(t)\,dt \qquad (A.11)$$

Since the variations $\delta\bar{x}$, $\delta\bar{p}$, and $\delta\bar{u}$ are considered to be independent, δJ_A is equal to zero unconditionally only if each term in Equation (A.11) is equal to zero. Analysis of each term in Equation (A.11) provides the necessary conditions which must be satisfied by an optimal control:

- $\delta\bar{p}$ term:

$$\frac{\partial w_A}{\partial \bar{p}} = \bar{0} \tag{A.12}$$

Resubstituting for w_A using Equation (A.7):

$$\dot{\bar{x}}(t) - \bar{a}(\bar{x},\bar{u},t) = \bar{0} \tag{A.13}$$

These are the previously defined state equations.

- $\delta\bar{x}$ term:

$$\frac{\partial w_A}{\partial \bar{x}} - \frac{d}{dt}\left[\frac{\partial w_A}{\partial \dot{\bar{x}}}\right] = \bar{0} \tag{A.14}$$

Resubstituting for w_A using Equation (A.7), it is possible to solve Equation (A.14) for the derivatives of the costates:

$$\dot{\bar{p}}(t) = -\frac{\partial w}{\partial \bar{x}}(\bar{x},\bar{u},t) - \left[\frac{\partial \bar{a}}{\partial \bar{x}}(\bar{x},\bar{u},t)\right]^T \bar{p}(t) \tag{A.15}$$

- $\delta\bar{u}$ term:

$$\frac{\partial w_A}{\partial \bar{u}} = \bar{0} \tag{A.16}$$

Resubstituting for w_A using Equation (A.7):

$$\frac{\partial w}{\partial \bar{u}}(\bar{x},\bar{u},t) + \left[\frac{\partial \bar{a}}{\partial \bar{u}}(\bar{x},\bar{u},t)\right]^T \bar{p}(t) = \bar{0} \qquad \text{(A.17)}$$

- $\delta\bar{x}(t_f)$ term:

$$\frac{\partial w_A}{\partial \dot{\bar{x}}} + \frac{\partial f}{\partial \bar{x}}(x,t_f) = \bar{0} \qquad \text{(A.18)}$$

Resubstituting for w_A, it is possible to solve for the boundary conditions on the costates at t_f:

$$\bar{p}(t_f) = \frac{\partial f}{\partial \bar{x}}(\bar{x},t_f) \qquad \text{(A.19)}$$

The above statements of the necessary conditions for optimality are rather unwieldy. To permit a more compact statement of the optimality conditions, a new function, called the Hamiltonian, is introduced. The Hamiltonian for this problem is:

$$H = w(\bar{x},\bar{u},t) + \bar{p}^T(t)[\bar{a}(\bar{x},\bar{u},t)] \qquad \text{(A.20)}$$

The necessary conditions given by Equations (A.12) through (A.19) can now be simply stated using the Hamiltonian:

$$\dot{\bar{x}}(t) = \frac{\partial H}{\partial \bar{p}} \qquad \text{(A.21a)}$$

$$\dot{\bar{p}}(t) = -\frac{\partial H}{\partial \bar{x}} \qquad \text{(A.21b)}$$

$$\bar{0} = \frac{\partial H}{\partial \bar{u}} \qquad \text{(A.21c)}$$

subject to the boundary conditions:

$$\bar{x}(t_0) = \bar{x}_0 \qquad \text{(A.21d)}$$

$$\bar{p}(t_f) = \frac{\partial f}{\partial \bar{x}}(\bar{x}, t_f) \qquad \text{(A.21e)}$$

APPENDIX B

SELECTION OF THE LINEAR TANGENT STEERING PARAMETERS

The linear tangent steering law commands the thrust vector $\bar{\beta}$ to vary with time according to the following equation:

$$\bar{\beta}(t) = \bar{\beta}_{VGO} + (t - t_\beta)\,\dot{\bar{\beta}} \qquad (B.1)$$

where

$\bar{\beta}_{VGO}$ is a unit vector in the direction of the velocity to be gained through thrust application

$\dot{\bar{\beta}}$ is a vector normal to $\bar{\beta}_{VGO}$, representing the rate of change of $\bar{\beta}$

t_β is a reference time, chosen such that the total velocity change produced by thrust during the maneuver is colinear with $\bar{\beta}_{VGO}$

The entire control history during the thrusting phase is then determined by the three linear tangent steering parameters $\bar{\beta}_{VGO}$, $\dot{\bar{\beta}}$, and t_β. In order to choose these parameters correctly, it is necessary to examine the equation of motion for the vehicle, given by:

$$\ddot{\bar{r}}(t) = a_T(t)\,\bar{u}_\beta(t) + \bar{g} \qquad (B.2)$$

where a_T is the magnitude of the vehicle's acceleration due to thrust, and $\bar{g}$ is the gravitational acceleration vector. $\bar{u}_\beta$ is the unit vector in the direction of the applied thrust, which may be defined in terms of the linear tangent steering parameters:

$$\bar{u}_\beta(t) = \frac{\bar{\beta}_{VGO} + (t - t_\beta)\,\dot{\bar{\beta}}}{\sqrt{1 + (t - t_\beta)^2 \left|\dot{\bar{\beta}}\right|^2}} \tag{B.3}$$

where $\left|\dot{\bar{\beta}}\right|$ is the magnitude of $\dot{\bar{\beta}}$

For $(t - t_\beta)\left|\dot{\bar{\beta}}\right| << 1$, the square root term in the denominator of Equation (B.3) can be approximated by the truncated series:

$$\frac{1}{\sqrt{1 + (t - t_\beta)^2 \left|\dot{\bar{\beta}}\right|^2}} = 1 - \frac{1}{2}(t - t_\beta)^2 \left|\dot{\bar{\beta}}\right|^2 \tag{B.4}$$

Substituting the approximate expression for $\bar{u}_\beta$ into Equation (B.2) and dropping terms above second order:

$$\ddot{\bar{r}}(t) = a_T(t)\,\bar{\beta}_{VGO}\left[1 - \frac{1}{2}(t - t_\beta)^2 \left|\dot{\bar{\beta}}\right|^2\right] + a_T(t)\,(t - t_\beta)\,\dot{\bar{\beta}} + \bar{g} \tag{B.5}$$

Taking the first integral of Equation (B.5):

$$\bar{V}_f - \bar{V}_0 = \bar{V}_{THRUST} + \bar{V}_{GRAV} \tag{B.6}$$

where:

$$\bar{V}_{THRUST} = \bar{\beta}_{VGO}\left[\int_0^{t_{GO}} a_T(t)dt - \frac{1}{2}\left|\dot{\bar{\beta}}\right|\left(\int_0^{t_{GO}} a_T(t)t^2dt - 2t_\beta \int_0^{t_{GO}} a_T(t)t\,dt\right.\right.$$

$$\left.\left. + t_\beta^2 \int_0^{t_{GO}} a_T(t)dt\right)\right] + \dot{\bar{\beta}}\left[\int_0^{t_{GO}} a_T(t)t\,dt - t_\beta \int_0^{t_{GO}} a_T(t)dt\right] \qquad (B.7)$$

$$\bar{V}_{GRAV} = \int_0^{t_{GO}} \bar{g}\,dt \qquad (B.8)$$

and t_{GO} is the remaining burn time.

Taking the second integral of Equation (B.5):

$$\bar{r}_f - \bar{r}_0 - \bar{V}_0 t_{GO} = \bar{r}_{THRUST} + \bar{r}_{GRAV} \qquad (B.9)$$

where:

$$\bar{r}_{THRUST} = \bar{\beta}_{VGO}\left[\int_0^{t_{GO}}\int_0^{t} a_T(t)dt - \frac{1}{2}\left|\dot{\bar{\beta}}\right|\left(\int_0^{t_{GO}}\int_0^{t} a_T(t)t^2dt - 2t_\beta \int_0^{t_{GO}}\int_0^{t} a_T(t)t\,dt\right.\right.$$

$$\left.\left. + t_\beta^2 \int_0^{t_{GO}}\int_0^{t} a_T(t)\,dt\right)\right] + \dot{\bar{\beta}}\left[\int_0^{t_{GO}}\int_0^{t} a_T(t)t\,dt - t_\beta \int_0^{t_{GO}}\int_0^{t} a_T(t)dt\right] \qquad (B.10)$$

$$\bar{r}_{GRAV} = \int_0^{t_{GO}} \int_0^{t'} \bar{g}\, dt\, dt' \qquad (B.11)$$

To simplify the calculation of $\bar{V}_{THRUST}$ and $\bar{r}_{THRUST}$, it is helpful to evaluate the following thrust integrals a priori:

$$I_1 = \int_0^{t_{GO}} a_T(t)\, dt \qquad I_1 = \int_0^{t_{GO}} \int_0^{t'} a_T(t)\, dt\, dt'$$

$$I_2 = \int_0^{t_{GO}} a_T(t)t\, dt \qquad I_2 = \int_0^{t_{GO}} \int_0^{t'} a_T(t)t\, dt\, dt'$$

$$I_3 = \int_0^{t_{GO}} a_T(t)t^2 dt \qquad I_3 = \int_0^{t_{GO}} \int_0^{t'} a_T(t)t^2 dt\, dt'$$

(B.12 a-f)

Then $\bar{V}_{THRUST}$ and $\bar{r}_{THRUST}$ may be written as:

$$\bar{V}_{THRUST} = \bar{\beta}_{VGO}\left[I_1 - \frac{1}{2}\left|\dot{\bar{\beta}}\right|^2(I_3 - 2t_\beta I_2 + t_\beta^2 I_1)\right] + \dot{\bar{\beta}}(I_2 - t_\beta I_1) \qquad (B.13)$$

$$\bar{r}_{THRUST} = \bar{\beta}_{VGO}\left[I_4 - \frac{1}{2}\left|\dot{\bar{\beta}}\right|^2(I_6 - 2t_\beta I_5 + t_\beta^2 I_4)\right] + \dot{\bar{\beta}}(I_5 - t_\beta I_4) \qquad (B.14)$$

Selection of a "best" set of linear tangent steering parameters depends upon the mission requirements for $\bar{V}_{THRUST}$ and $\bar{r}_{THRUST}$. For a mission in which the vertical component of the final position $\bar{r}_f$ is specified, along with the direction of $\bar{V}_{THRUST}$ (the velocity to be gained through thrust application), the linear tangent steering parameters may be chosen using the following procedure:

(1) Specify $\bar{\beta}_{VGO}$ to be colinear with $\bar{V}_{THRUST}$.

(2) Evaluate the thrust integrals I_1 through I_6.

(3) Examination of Equation (B.13) shows that in order for $\bar{V}_{THRUST}$ to be colinear with $\bar{\beta}_{VGO}$:

$$I_2 - t_\beta I_1 = 0 \tag{B.15}$$

Therefore choose:

$$t_\beta = I_2/I_1 \tag{B.16}$$

(4) Solve Equation (B.9) for the vertical component of $\bar{r}_{THRUST}$ that will carry the vehicle to the desired staging altitude.

(5) The downrange component of $\bar{r}_{THRUST}$ is not constrained. A value for the downrange component must be specified, however, in order to determine $\dot{\bar{\beta}}$. Ignoring second order terms in the right-hand side of Equation (B.14):

$$\bar{r}_{THRUST} = \bar{\beta}_{VGO} I_4 + \dot{\bar{\beta}}(I_5 - t_\beta I_4) \tag{B.17}$$

take the dot product of $\bar{\beta}_{VGO}$ with both sides of the above expression to find an approximate value for the downrange component of $\bar{r}_{THRUST}$ that will be produced if $\dot{\bar{\beta}}$ is perpendicular to $\bar{\beta}_{VGO}$:

$$\bar{\beta}_{VGO} \cdot \bar{r}_{THRUST} = I_4 \qquad \text{(B.18)}$$

(6) Now that $\bar{r}_{THRUST}$ is completely specified, use Equation (B.17) to solve for $\dot{\bar{\beta}}$:

$$\dot{\bar{\beta}} = \frac{\bar{r}_{THRUST} - I_4 \bar{\beta}_{VGO}}{I_5 - t_\beta I_4} \qquad \text{(B.19)}$$

LIST OF REFERENCES

1. Bonnice, William F., Steering of a Boost Vehicle to a Desired Flight Path Angle Trajectory Using Angle of Attack Control, Master of Science Thesis, 1983, Massachusetts Institute of Technology, C. S. Draper Laboratory Report T-802.

2. Bryson, A. E. and W. F. Denham, "The Solution of Optimal Programming Problems with Inequality Constraints," Institute of Aerospace Sciences paper, 1963, No. 63-78.

3. Bryson, A. E. and W. F. Denham, "Optimal Programming Problems with Inequality Constraints II: Solution by Steepest Ascent," AIAA Journal, 1964, pp. 25-34.

4. Dailey, James F., Steering and Roll Rate Control of a Boost Vehicle in the Atmosphere, Master of Science Thesis, 1985, Massachusetts Institute of Technology, C. S. Draper Laboratory Report T-895.

5. Fader, Leslie R., Altitude Steering of a Boost Vehicle, Master of Science Thesis, 1985, Massachusetts Institute of Technology, C. S. Draper Laboratory Report T-875.

6. Kelley, H. J., "Gradient Theory of Optimal Flight Paths," Journal of the American Rocket Society, Vol. 30, 1960, pp. 947-953.

7. Kirk, Donald E., Optimal Control Theory: An Introduction, Prentice-Hall, Inc., 1970.

8. Kulakowski, L. J. and R. T. Stancil, "Rocket Boost Trajectories for Maximum Burnout Velocity," Journal of the American Rocket Society, Vol. 30, 1960, pp. 612-619.

9. Lawden, D. F., Optimal Trajectories for Space Navigation, Butterworth & Co. Ltd., 1963.

10. Lietmann, G. E., Optimization Techniques, Academic Press, Inc., 1962.

11. McHenry, R. L., T. J. Brand, et al., "Space Shuttle Ascent Guidance, Navigation, and Control," Journal of the Astronautical Sciences, Vol. 27, 1979, pp. 1-38.

12. Northrop Corporation Technical Requirements and Compliance Unit, Product Description, Peacekeeper Inertial Measurement Unit (IMU) FSED-605 Configuration, July 1984.

13. Ozaki, Arthur H., Predictive/Adaptive Steering for the Atmospheric Boost Phase of a Space Vehicle, Master of Science Thesis, 1987, Massachusetts Institute of Technology, C. S. Draper Laboratory Report T-966.